



Multiband DRA for automotive applications with beam steering

Tzu-Ling Chiu

► To cite this version:

Tzu-Ling Chiu. Multiband DRA for automotive applications with beam steering. Electronics. Université de Limoges, 2017. English. NNT : 2017LIMO0112 . tel-01779130

HAL Id: tel-01779130

<https://theses.hal.science/tel-01779130>

Submitted on 26 Apr 2018

HAL is a multi-disciplinary open access archive for the deposit and dissemination of scientific research documents, whether they are published or not. The documents may come from teaching and research institutions in France or abroad, or from public or private research centers.

L'archive ouverte pluridisciplinaire **HAL**, est destinée au dépôt et à la diffusion de documents scientifiques de niveau recherche, publiés ou non, émanant des établissements d'enseignement et de recherche français ou étrangers, des laboratoires publics ou privés.

Université de Limoges

**École Doctorale Sciences et Ingénierie pour l'Information,
Mathématiques (ED 521)**

Laboratoire: Xlim

Thèse pour obtenir le grade de
Docteur de l'Université de Limoges

Discipline/spécialité: « Electronique de Hautes Fréquences, Photonique et
Systèmes »

Présentée et soutenue par
Tzu-Ling Chiu

Le 19 décembre 2017

Multiband DRA for automotive applications with beam steering

Thèse dirigée par Thierry Monédière et Laure Huitema

JURY:

Président du jury
Mme. Valérie Madrangeas

Professeur, Xlim, Université de Limoges

Rapporteurs
M. Fabien Ferrero

Maitre de conférences HDR, LEAT,
Université de Nice cote d'Azur
Professeur, IETR, Université de Rennes1

M. Ala Sharaiha

Examineurs
M. Olivier Pajona
Mme. Laure Huitema

Directeur R&D, Ethertronics
Maitre de conférences, Xlim, Université de
Limoges
Professeur, Xlim, Université de Limoges

M. Thierry Monédière



Thanks

This work was carried out at the lab of Ethertronics Inc, directed by Laurent Desclos. I would like to express my gratitude for supporting me and giving me the opportunity to join the company training program.

I would particularly like to thank Mr. Olivier Pajona, Chief Scientist of Ethertronics, who supervised my study during these years.

I want to thank Mr. Thierry Monédière, Professor at the University of Limoges. His patience leads me in my dedication to study.

I would like to express my gratitude to Ms. Laure Huitema, Associate Professor at the University of Limoges. She always gives me advice on how to analyze things from different perspectives.

I am grateful to my family for supporting me during my thesis, especially my husband Jimmy, forever the babysitter while I work on my thesis.

Finally, I would like to thank my colleague CC Heng, who supports me in pushing ahead.



Droits d'auteurs

Cette création est mise à disposition selon le Contrat:

« **Attribution-Pas d'Utilisation Commerciale-Pas de modification 3.0 France** »

disponible en ligne: <http://creativecommons.org/licenses/by-nc-nd/3.0/fr/>



Contents

Thanks	2
Droits d'auteurs	3
Contents	4
Introduction	7
Chapter I. Concept of beam steering for automotive application	9
I.1. Introduction	9
I.2. Concept of the global antenna system design	10
I.2.1. System structure	11
I.2.2. MIMO system	12
I.2.3. Beam steering system	12
I.3. Beam steering antenna	13
I.3.1. Switched beam system	13
I.3.1.1. Mechanical steerable antenna	13
I.3.1.2. Reconfigurable antenna	16
I.3.2. Adaptive array system	18
I.3.2.1. Analog beamforming	19
I.3.2.2. Digital beamforming	20
I.4. Key components of the beam steering system	21
I.4.1. Antenna selection	22
I.4.1.1. Wire antennas	22
I.4.1.2. Aperture antennas	23
I.4.1.3. Printed antennas	23
I.4.2. Phase shifter selection	25
I.4.2.1. Ferrite phase shifter	25
I.4.2.2. Electronic phase shifter	26
I.5. Objective of the thesis:	29
I.6. Conclusion	31
Chapter II. Compact and Multiband MIMO Dielectric Resonator Antenna for Automotive Application	33
II.1. Introduction	33
II.2. Development of the dielectric resonator antenna	34
II.2.1. Characteristics of a rectangular DRA	34
II.2.2. DRA excited mode	34
II.2.2.1. Coaxial probe excitation	34
II.2.2.2. Microstrip line and coplanar waveguide feeding	35
II.2.2.3. Aperture coupled feed	36
II.2.2.4. Dielectric image guide coupling	36
II.2.3. Selection of DR material	37
II.2.3.1. Different boundary conditions and resonant frequencies	37
II.2.3.2. Radiation Q factor	38
II.3. Multiband DRA structure	39
II.3.1. DRA development methodology – Initial antenna model	39
II.3.2. Final antenna structure	42

II.3.2.1. Impedance and S-parameter.....	47
II.3.2.2. 2D and 3D of antenna radiation patterns.....	48
II.3.2.3. Maximum realized gain and total efficiency	51
II.4. Antenna measurement on a vehicle	51
II.4.1. Measured results of vehicle rooftop DRA.....	52
II.4.1.1. 3D and 2D radiation patterns	52
II.4.1.2. Maximum realized gain	54
II.4.2. Measured results of dashboard and below vehicle rooftop DRA.....	55
II.4.2.1. 3D radiation patterns.....	56
II.4.2.2. Maximum realized gain	60
II.5. Conclusion	60
Chapter III. Global System Tunable Phase shifter design.....	61
III.1. Introduction	61
III.2. Development of the phase shifter for the thesis.....	61
III.2.1. 360° phase shifters on the market	61
III.2.2. The specifications of the phase shifter in this thesis	63
III.2.3. Phase shifter model and concept for thesis	64
III.2.4. Design for tunable phase shifter	69
III.2.4.1. One stage bandpass phase shifter	69
III.2.4.2. Two and Three stage bandpass phase shifter.....	70
III.2.4.3. Effect of the capacitor resistivity	72
III.2.4.4. Initial phase shifter concept.....	73
III.2.5. Phase shifter prototype development.....	74
III.2.5.1. First design of the phase shifter	74
III.2.5.2. Analysis of the initial phase shifter	76
III.3. Final structure and performance of the phase shifter.....	77
III.3.1. Prototype structure	77
III.3.2. SP4T-switched differential phase shifter	79
III.3.2.1. Reference line.....	79
III.3.2.2. Adjusting lines.....	79
III.3.2.3. Phase tuning result of SP4T-switched phase shifter.....	81
III.3.2.4. The effect of SP4T switch-loss	82
III.3.2.5. The effect of SP4T switch-ripples in the curve.....	83
III.3.2.6. Tunable 90° phase shifter only	86
III.3.2.7. Effect of different capacitance values	88
III.3.3. Manual-switched phase shifter: using metal strip lines	89
III.3.3.1. Reference line for manual-switched phase shifter	89
III.3.3.2. Adjusted lines with manual-switched phase shifter.....	90
III.4. Conclusion	92
Chapter IV. Beam Steering Global System for Automotive Introduction.....	94
IV.1. Beam steering DRA techniques.....	94
IV.1.1. Overview of beam steering methods for DRA.....	95
IV.1.1.1. Switched parasitic elements method.....	95
IV.1.1.2. Switched loading elements method	96
IV.1.1.3. Symmetry fed-in schematic method	96
IV.1.1.4. Three fed-in ports with different phase method	97
IV.1.1.5. Special design for fed-in with different phase method	98

IV.1.2. Proposed methodology for beam steering DRA	98
IV.2. MIMO system structure and performance	99
IV.2.1. Location of antennas	99
IV.2.2. Structure and performance of the MIMO antenna system	100
IV.2.3. ECC value for the MIMO system	102
IV.3. Beam steering system structure and performance	103
IV.3.1. Ideal system	103
IV.3.2. Global system with manual-switched phase shifter	104
IV.3.2.1. DRA with manual-switched phase shifter	104
IV.3.2.2. Global system with manual-switched phase shifter	105
IV.3.2.2.1. Different switched line paths	105
IV.3.2.2.2. Composite 3D gain	108
IV.3.2.3. Switching with different variable capacitance	112
IV.3.3. Global system with SP4T-switched phase shifter	114
IV.4. Beam steering system in automobile environment	114
IV.4.1. Measured results of global system located on vehicle rooftop	115
IV.4.1.1. Beam steering system gain	116
IV.4.2. Measured results of DRA located on dashboard	121
IV.4.2.1. Beam steering system gain	122
IV.4.3. Measured results of DRA located under the vehicle rooftop	123
IV.4.3.1. Beam steering system gain	124
IV.4.4. Summary for measurement in vehicle environment	125
IV.5. Conclusion	127
Conclusion	129
Reference	133
Annexes	138
Annex 1. Active steering result of SP4T-switched global system	138
Table of illustrations	141
Tables	148

Introduction

The progressive arrival of autonomous cars in the commercial market has led to a growing interest in wireless communication applications for connected vehicles from industry and the scientific community. Meanwhile, data transmission for vehicle location, video streaming, community network and big data analytics is becoming popular for vehicle digital audio and visual services. However, ensuring reliable data connectivity over the cell network is a challenge, particularly when the vehicles are moving fast and generating frequent cell changes.

Much research has been conducted on improving the transmission capacity of wireless access. For example, using diversity reception, the Multiple Input – Multiple Output (MIMO) technique or antenna beamforming are the most popular methods to obtain this goal. These methods allow improved data throughput and transmission distance compared to the performance of a single antenna. This is achieved without any need to increase the spectrum bandwidth and transmit power. When the main antenna has a poor signal, the system will switch to the diversity antenna, which provides a better quality signal. But the improvement provided by the antenna diversity technique is limited. The MIMO technique can help to overcome damaging multipath effects and increase the down-link and uplink data capacity rate without any additional spectrum. However, when the MIMO channel and the main antenna do not exhibit adequate orthogonal conditions, MIMO cannot be supported, thus limiting the benefits of the second antenna. Therefore, the technique of antenna beamforming has attracted much attention in recent years.

Initially, automotive antenna systems consisted of one single fixed antenna per communication service. But during high-speed transportation, communication links between the vehicle and the infrastructure are poor. This led to the start of MIMO systems being integrated into the automotive antenna module to improve the quality of the wireless communication. Moreover, the active steering of directional antennas allows a higher quality signal for both transmitter and receiver when the relative location between vehicle and the base station is changing. The objective of this study is to perform beamforming techniques with active steering capability using the original MIMO antenna elements for the vehicle rooftop environment.

The main challenge in designing the system on the vehicle rooftop is to obtain low correlation and high isolation between the antennas in a very confined space. Once there is interference between the antenna radio waves, the data throughput rate will be attenuated. This thesis will present a multi-band dielectric resonator antenna (DRA) which is designed for 800MHz to 2700MHz with a large grounding plane (vehicle rooftop). A significant advantage of using a dielectric resonator is that antenna dimensions can be shrunk to allow two antenna elements to be located in the limited space. Using a different DR excitation mode is another feature to increase the efficiency as well as wider operating frequency bands compared to the commercial FR4 material.

The purpose of this study is to obtain physical beamforming by antenna radiation pattern steering. Using a phase shifter integrated within the antenna array system is a common beamforming technique. The aim of the phase shifter in this study is to shift phase 0, 90, 180 and 270 degrees at 800MHz for the antenna system. But the off-the-shelf phase shifters for such low frequency with the ability of tuning a large phase range are always bulky and

expensive. It would be difficult to put them on the rooftop of the vehicle. So we decided to design and build a prototype phase shifter to target the phase shift degrees we needed.

The thesis is organized into four chapters:

Chapter One begins with a presentation of different types of beamforming antenna systems. To obtain smaller antenna dimensions and for easier fabrication, we adopted the analog beamforming method. We introduce our concept for the active steering system. Then we study which antenna structure and phase shifter is suitable for our system. We choose a DRA (Dielectric Resonator Antenna) and electrical control phase shifter as the base of the system elements. Furthermore, we integrate DRAs with an optimal 3dB power divider and optimal phase shifter to complete the beamforming phase array model. The architecture of a beamforming system is presented here.

In Chapter Two, we introduce and describe the DRA features. Further, we discuss selection of the DR material to fit the automotive environment criteria. Multi-band and high efficiency antennas are the most important subjects in this section. The procedure on how to obtain the final proposed DRA is presented. The measured result of the model realized is presented, which is in good agreement with the simulated one. To ensure the simulated antenna model is well matched to the antenna on the vehicle rooftop, the prototype antenna is also measured. We also performed the measurement at different positions of the vehicle.

In Chapter Three, we present a brief introduction of the phase shifter that is adopted in this paper. We use the IC switches to select the path we need and variable capacitor to accomplish the minor phase tuning. The features and advantages of the proposed phase shifter are shown in detail. We also analyze the phase shifter step by step and future related work is also discussed.

Finally, the complete model of a global system with the capability of active radiation pattern steering is presented in Chapter Four. We start the study with several beam steering DRA methods and we combine the different methods to generate one which can be suitable for the system. We then perform the relative distance optimization for the antenna elements in the MIMO system. We need to confirm that the global system works well with the MIMO technique. Then, we transfer the MIMO system as the beam steering system by integrating the 3dB power divider and phase shifter circuit. The measured results of the prototype are compared with the simulated models. Also, the measured results in the vehicle environments are discussed in the last section. The measured results of the global system placed on the vehicle rooftop, automotive dashboard and under the rooftop are presented.



Chapter I. Concept of beam steering for automotive application

I.1. Introduction

The automotive antenna has a long history which began in 1930s when car radios were commercially introduced by Galvin Manufacturing Corporation. In 1947, the name of manufacturing company was changed to “Motorola” to reflect the car radio brand name. Bringing wireless and broadcast systems into vehicles led to a requirement for more antennas. These needs were not only limited to antennas for AM/FM radio reception, but also for analog and digital radio, television, cell phone and navigation systems [1]. Also, connected vehicular applications started to receive more and more attention through wireless communication applications such as the autonomous car. This will soon appear on the commercial market [2]. Data connectivity will be one of the keys to enable these autonomous car services. Ensuring reliable data connectivity over a cellular network is a challenge when the vehicle is moving fast and changing cells frequently.

The explosive growth of smart phones and increasing demand for high data rate throughput for good wireless multimedia are pushing the deployment of Long Term Evolution (LTE) communication systems. From the beginning, the LTE standardization effort focused on enhancing Universal Terrestrial Radio Access (UTRA) and optimizing the Third Generation Partnership Project's (3GPP's) radio access architecture. Its initial release (Rel. 8) was finalized in 2008 for the basis of the LTE standard [3].

The Multiple Input – Multiple Output (MIMO) technique is one of the key technologies in the LTE system. The MIMO system can help overcome the damaging multipath effects and is now a common technique used for increasing throughput capacity of downlink and uplink data rate without additional spectrum. However, when the MIMO channel and main antenna exhibit inadequate orthogonal conditions, MIMO cannot be supported and the benefits of the second antenna are limited. Therefore, the beamforming technique can be an alternative method to provide better LTE service quality and can even be adopted in 3G or 2G systems.

In recent years, lots of research and development has targeted improving the support for machine to machine communication, also known as the Internet of Things, by achieving lower cost, lower battery consumption and high data quality. At high speed, communications between vehicle and infrastructure are poor. Much research is being done to solve (or to improve) the disconnection problem when the vehicles are moving.

In [4], it is indicated that directional antennas offer significant advantages over omnidirectional antennas. Also, with a beamforming technique one can achieve a higher quality signal for both transmitter and receiver sides when the relative location between the vehicles and base station are changing. The integration of a beam steering active antenna on the vehicle allows maximization of the gain in a specific direction while minimizing the interferences from other directions.

Conventionally, beam steering capability can be achieved through several methods. Analog beamforming antenna with phase shifters and combiner circuits can be fabricated at low cost, but these solutions require at least two antennas to create an antenna array that will act as a main antenna. It leads to a larger mechanical volume which brings design constraints regarding the location of the antenna system or the cosmetic appearance of the device.

The general scheme of a two-port MIMO antenna system is presented on the left side of Figure 1. The system comprises a Main antenna and a MIMO antenna which are connected to the RF front end module. When the performance of either antenna is insufficient to support MIMO due to environment variation or interference, the MIMO technique cannot improve the data throughput.

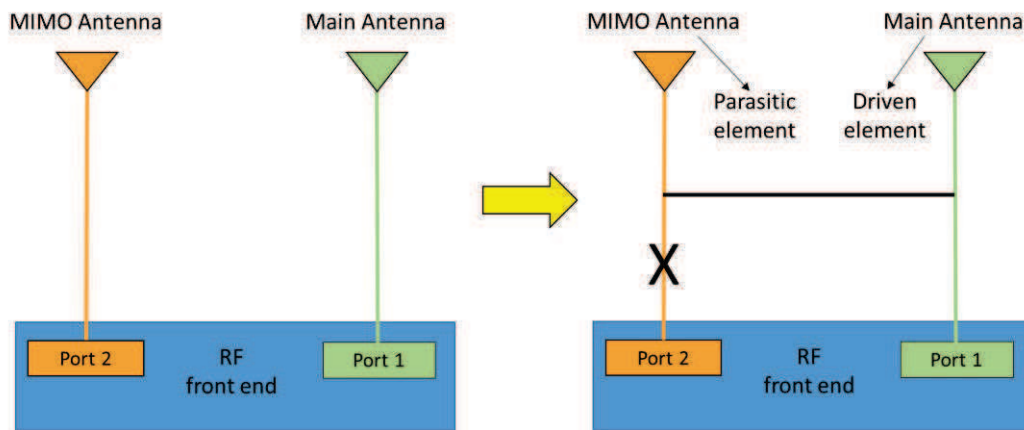


Figure 1: General schematic of a MIMO system and modified concept for a beam steering system.

If the MIMO antenna cannot properly support MIMO as a beam steering element, then the existing MIMO antenna is used as a parasitic element while the main antenna is the driven element in the active steering antenna system. (Figure 1). To achieve our target, we need to understand the concept of the current MIMO and beamforming antenna system. With this understanding, we propose combining the two systems.

First, the general scheme of an active steering antenna system architecture is detailed. The overview of the active beam steering methods is also presented. It introduces the background on the beamforming system. There are already many papers introducing the beamforming antenna system for mobile or access point routers [5]. This thesis focuses on finding the ideal solution that fits the automotive application.

Finally, in order to find the ideal solution, we analyze some of the antennas and phase shifters that play the key roles for active steering on the vehicle.

I.2. Concept of the global antenna system design

The mobile communication industry has recently moved rapidly towards LTE systems. LTE aims to provide improved service quality over 3G systems in terms of data throughput and spectrum bandwidth. The MIMO technique is one of the essentials of the LTE system for achieving these goals [3]. A classical commercial communication module has two connectors for the LTE function as shown in Figure 2 [4].

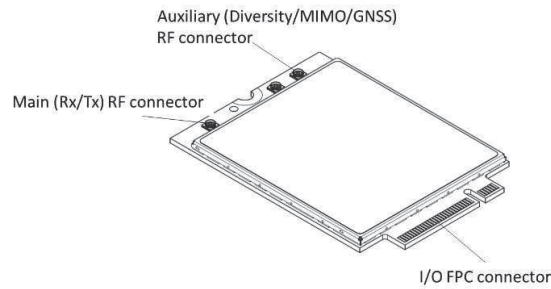


Figure 2: LTE module connectors.

Therefore, the antenna system for our investigation must also have only two elements in order to be used with the previous LTE module. This is to achieve beamforming without altering the original LTE system configuration (Figure 3).

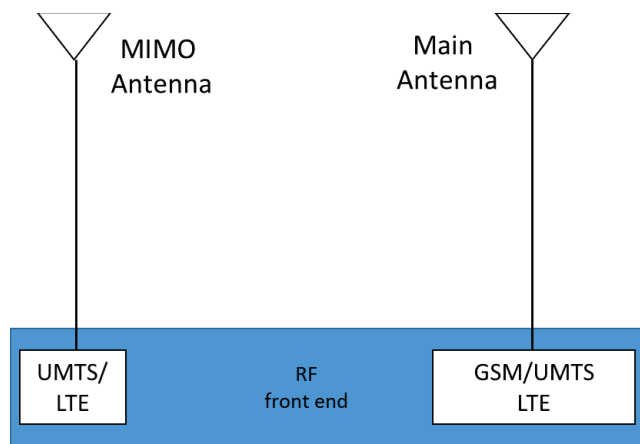


Figure 3: Basic antenna structure for fitting LTE commercial module.

I.2.1. System structure

Figure 4 shows the architecture of the proposed antenna system. The concept has been applied to a vehicle rooftop antenna system with Main and MIMO antennas. A phase shifter is implemented in the system with switches to select the working concept and to select the phase shifter path. A 3dB power divider is used when needed to provide the beamforming signal.

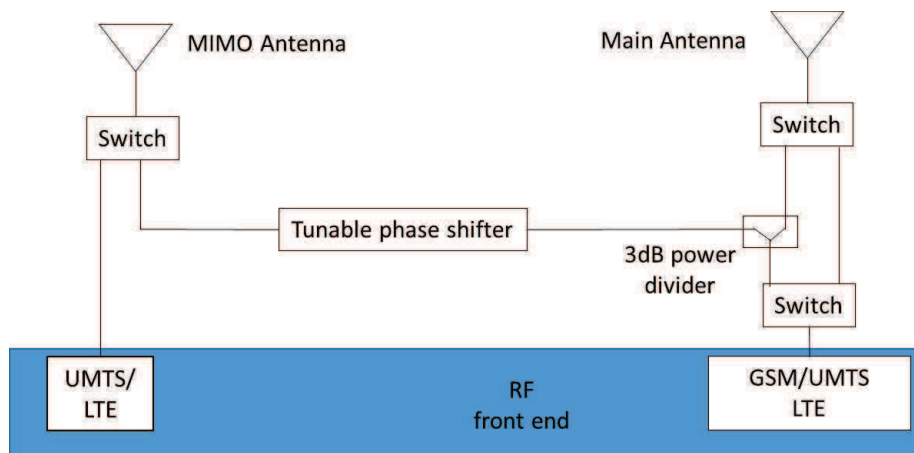


Figure 4: Architecture of the proposed antenna system.

When conditions allow, the Main and MIMO antennas are used independently. For LTE communication, the two antennas will be used independently as Main and MIMO antennas. For WCDMA and GSM communication, the MIMO antenna will be used as a diversity antenna in the system (using a switch). The Main and MIMO antennas will therefore create an antenna array that can be used to perform beamforming when designed correctly.

I.2.2. MIMO system

Dr. Claude E. Shannon developed the mathematical theory of communication, published in 1948. Shannon's theory contributed to the general model of communication, for example: source, channel, noise, codes, encoding, decoding, receiver and so on [8]. Digital wireless communications often use channel codes to improve link performance between a single transmitter and receiver. In the late 1990s, Telatar and Foschini independently proposed a method to extend Shannon's capacity limits for wireless systems by using multiple antennas at one or both ends of the communication link [9]. The limitations for multiple channels exceeded Shannon's single antenna proposal. MIMO wireless communications were born [3].

Therefore, using just two antennas in the system is a basic configuration that can be connected to form a compact MIMO system (Figure 5, green path and orange path) with switches to support the LTE work.

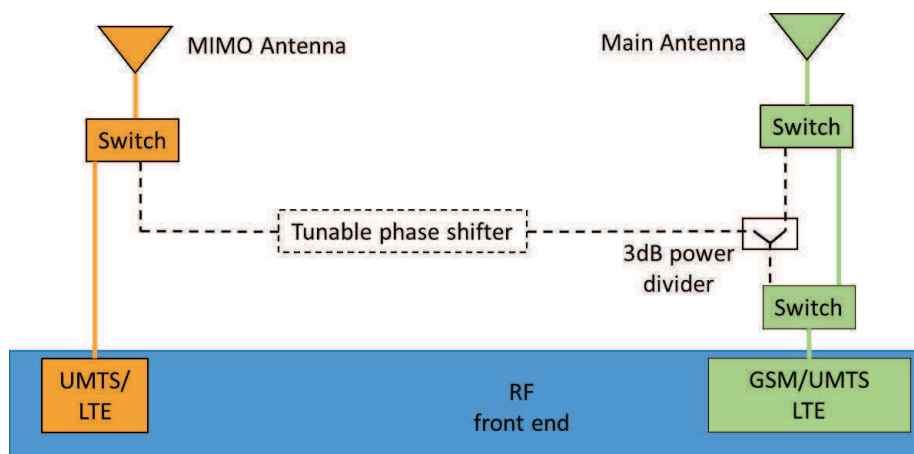


Figure 5: MIMO antenna system concept for LTE.

I.2.3. Beam steering system

In order to form the beam steering system, a switch is used to change the RF path as shown in Figure 6. The simple two-antenna array system is then complete.

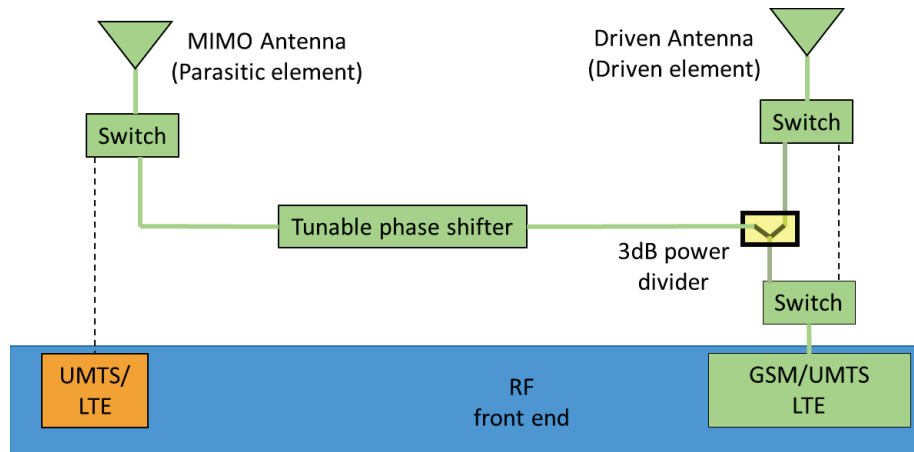


Figure 6: Beamforming antenna system concept.

The Main antenna becomes a driven element and the MIMO antenna becomes a parasitic element in the beam steering array. When the beam steering system is needed, the switch changes the path to provide the RF signal through the power divider to connect both Main and MIMO antennas. The beamforming function is achieved by using the phase shifter to change the phase of the RF signal applied to the MIMO antenna. In this study, the MIMO antenna is used as a second antenna element to allow the main antenna to exhibit active steering capability.

Several beam steering methods are studied to find the ideal solution for our concept.

I.3. Beam steering antenna

In wireless communication standards, the beamforming technique is employed through WCDMA. Even in next generation wireless broadband technology, the beamforming technique is more commonly applied to access point or mobile instruments than few years ago. Also, wireless propagation issues such as interference, energy loss, noisy environment and shadowing need to be solved by using appropriate methods. In such a scenario, the capability of an antenna with beam steering to transform signal propagation to the desired direction can overcome the effect of these issues. Different methods to steer the beam are described in this section.

I.3.1. Switched beam system

I.3.1.1. Mechanical steerable antenna

Some popular commercial smart antennas use a mechanical (electrical) switched beam system. The system can choose between many predefined patterns in order to enhance the received signal. The space will be divided up into different sections for different antennas [10] (Figure 7).

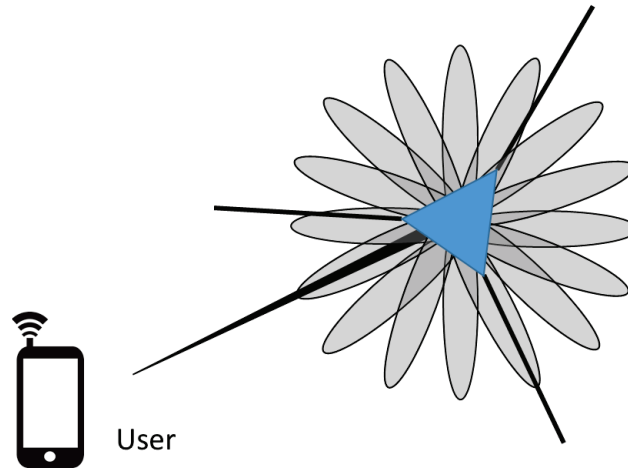


Figure 7: Switch beam system.

There are various recognized methods to achieve the performance by switching the pattern. The simple structure switches the feeding point to radiate in different sections (Figure 8). This is the basic antenna array design for beamforming. In [11], the antenna has eight feeding points in the system. The structure uses a double square loop antenna. This antenna allows beam steering with a step of 45° for full coverage.

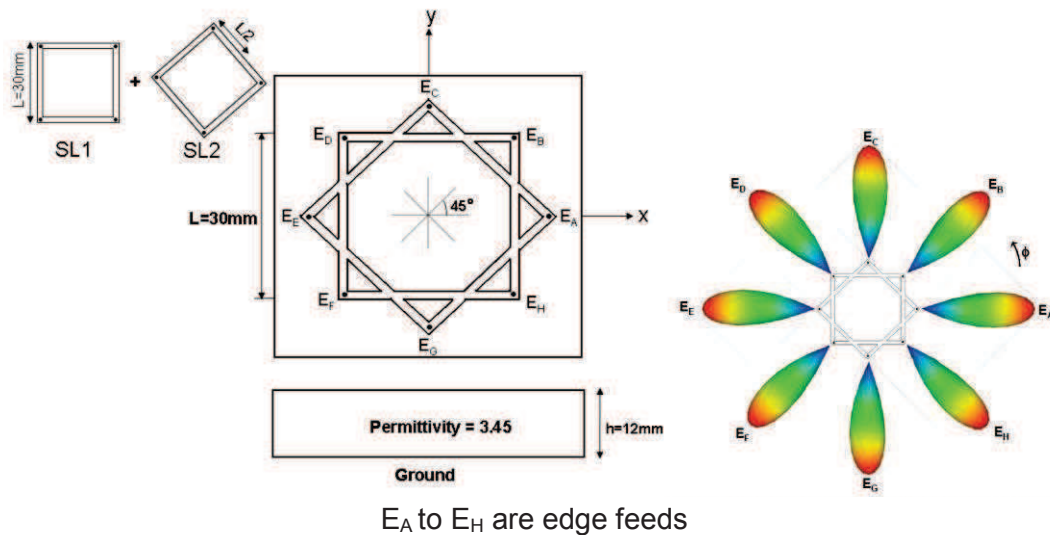


Figure 8: Switch feeding antenna system and 3dB radiation cone.

Using one signal feeding antenna and switching between many parasitic elements is another frequently used solution. [12] introduces the design of broadband circular switched parasitic arrays (SPAs) for portable DVB-T receiver applications in the VHF/UHF bands. The system is made of an active central element and a uniform ring of five parasitic elements. When operating, only one parasitic element is open-circuited, while the others remain short-circuited (Figure 9).

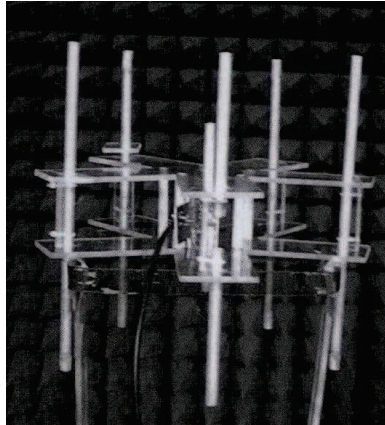
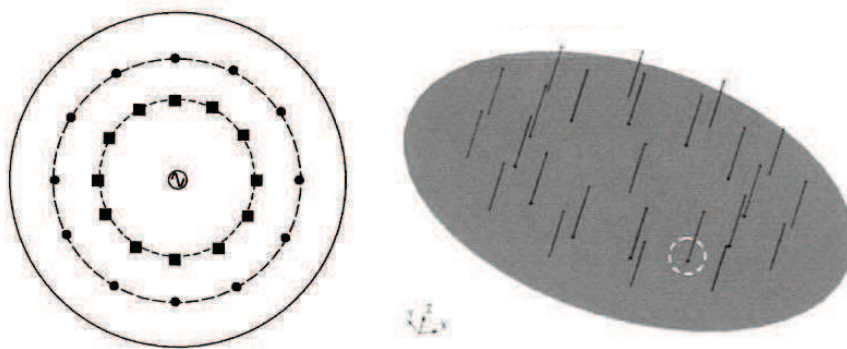


Figure 9: switched parasitic elements in DVT-T antenna system.

Through suitable design, the array is able to select between the five horizontal radiation patterns and cover the entire horizontal plane. The advantage of the switching-parasitic elements model is that the RF port is always connected to the central element, unlike the switching-feeding method, which has a high risk if there are switch problems, meaning the signal may not be properly transmitted.

Another kind of system is switching the antenna loading elements [13]. This system switches the loading between the feed and parasitic elements. The only element to be fed is the central one. The other elements are all parasitic. Compared with the previous case, the load on each parasitic element is changed. Each parasitic element is placed with a variable capacitor that can be controlled electronically. The variable capacitance can change the electrical length of the loaded “antenna” in order to tilt the beam over a 360° scan angle (Figure 10).



⊙: Source (driven element)

■: Reactively loaded parasitic element; ●: Parasitic element

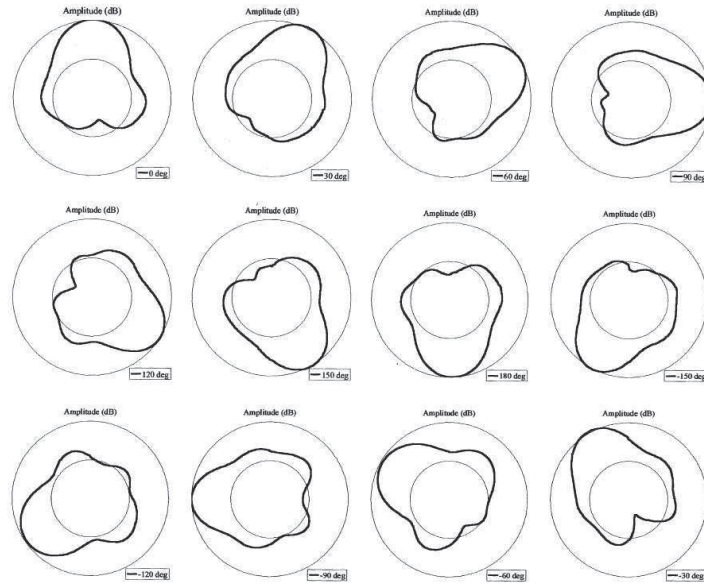


Figure 10: Switch loading elements antenna system and beam steer pattern.

The above methods are simple and just require the appropriate antenna section to be selected to switch the beam.

I.3.1.2. Reconfigurable antenna

Reconfigurable antenna systems focus on changing the radiation patterns while maintaining the operating frequency and bandwidth for enhancing the system performance. The system adopts the active component such as PIN diode, varactor and MEMs to control the radiation pattern of the antenna. Figure 11 shows an example of a reconfigurable antenna for GPS application [14]. The beam configuration is achieved by switching the PIN diodes. The switched element is able to control the beam pattern to achieve a different main lobe angle at a specified location without degrading the antenna performance or shifting the frequency.

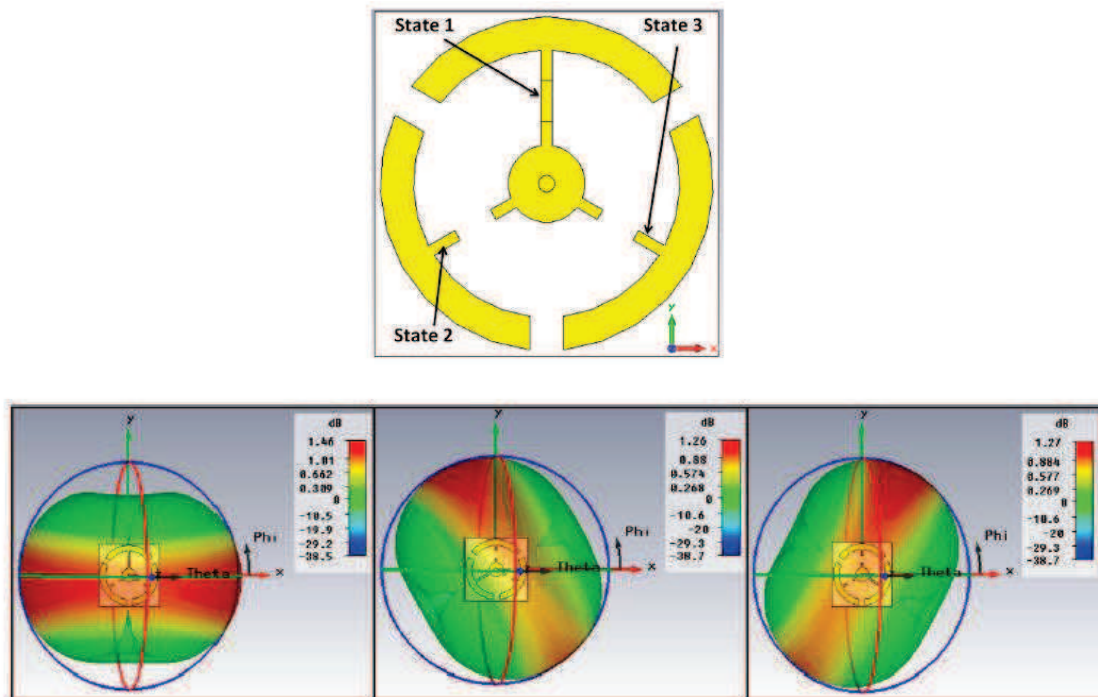


Figure 11: Geometry and radiation pattern of a reconfigurable GPS antenna.

This kind of solution allows an antenna to be smaller than an array because only a single antenna element is used. However, this kind of design is only suitable for single frequency band antenna with beam steering capability and is hard to implement on a multi band antenna.

A reconfigurable beam steering antenna can also be obtained by using a specific patch antenna design [15]. The feed is directly connected to the U-shaped slot which is designed to match the operation frequency. The two switches are implemented inside the U-shape slot (Figure 12). There are three states (S0, S1 and S2) obtained by controlling the on-off condition of the switches. Such an antenna is able to steer the maximum beam direction in the y - z plane (+30°, 0°, -30°) (Figure 12) when the states of the switches are changed. By using this type of design, it is not necessary to reserve more space to accommodate several elements to switch the radiation pattern.

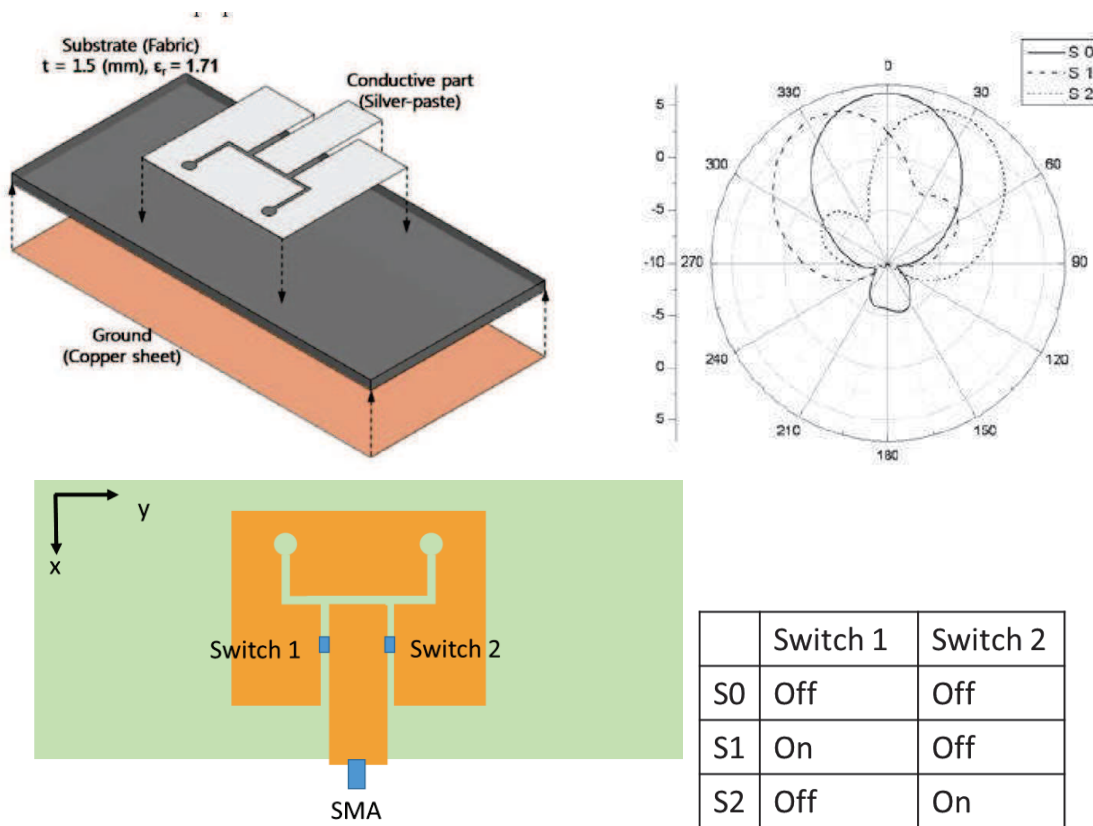


Figure 12: Geometry and radiation pattern of a reconfigurable patch antenna.

Using the parasitic array to reconfigure a linearly polarized pattern is another approach. An example is shown in [16] using four switches to reconfigure the radiation pattern into three directions (Figure 13). The antenna has an SMA fed centre microstrip with parasitic element strips on both sides. Each parasitic element has two connected switches. There are also three working modes for this concept of antenna:

- the switches of the right side are turned-on,
- the switches of the left side are turned on,
- all the switches are turned-off.

This antenna has a maximum radiation direction of between +35°, 0° and 35°.

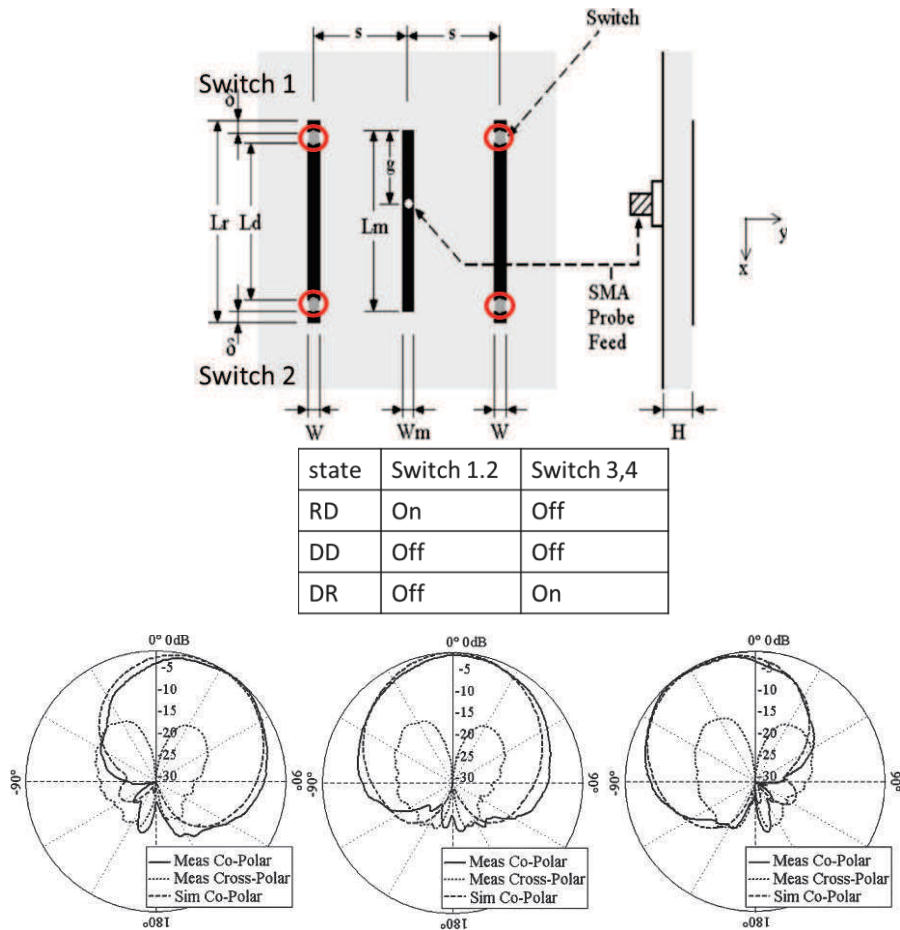


Figure 13: Geometry and radiation pattern of a reconfigurable microstrip parasitic array.

I.3.2. Adaptive array system

Adaptive array systems provide more freedom for beam scanning because they have the real time ability to adapt the radiation pattern when the environment changes. They can customize an appropriate radiation pattern for an individual user. They can also avoid the interferer by controlling the beam. Especially in a high interference environment, the interference rejection capability of the adaptive systems provides significantly more coverage than conventional or switched beam systems. [10] (Figure 14).

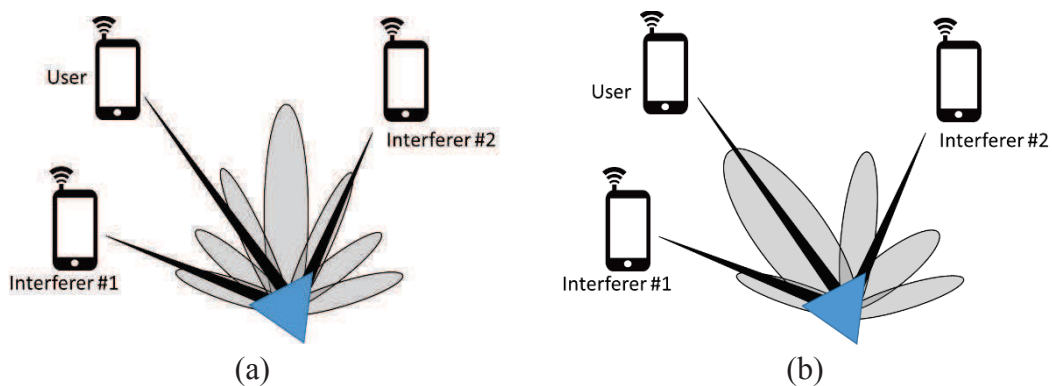


Figure 14: Comparison of radiation pattern: (a) switched beam scheme; (b) adaptive array scheme.

Adaptive array systems can locate and track signals by adjusting the antenna pattern dynamically to enhance reception. For this kind of beam steering system, signal processing algorithms are very important for good system performance.

Generally, this requires a narrow main beam with high gain in the desired direction combined with low side lobes for all other directions. The fundamental procedure for beamforming is weighting the individual signals of each antenna element and then summing all these weighted signals [17]. The desired radiation direction is obtained thanks to phase weighting (Figure 15). Then the maximum signal-to-noise ratio (SNR) is achieved for the desired directions.

The phase rotations are usually provided by microwave phase shifters. In principle, phase shifting may also be achieved by multiplying the received signal with a corresponding complex number. The way to provide the phase shifting can be classified into two groups: analog and digital.

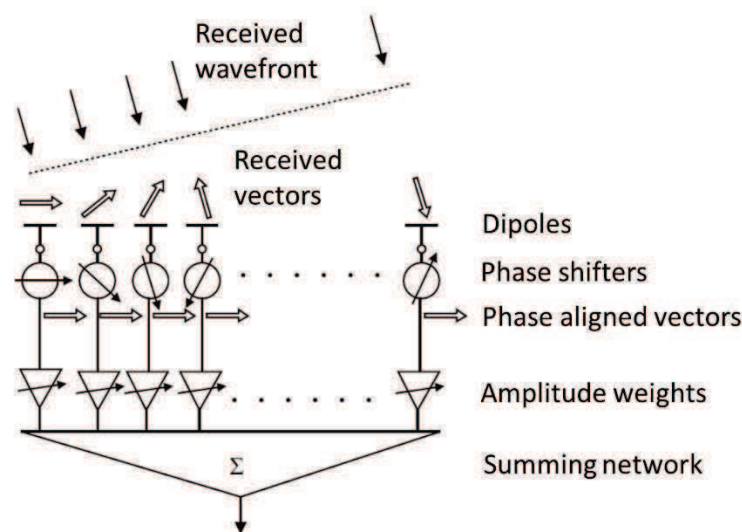


Figure 15: Basic beamforming principle: phase alignment, amplitude weighting and summing.

I.3.2.1. Analog beamforming

Implementing the phase shifter element in the antenna system is the most conventional method of achieving beamforming.

There are several methods for the combination of a transmitter and a receiver with the antenna elements array and the phase shifters. The most popular is called “central feed” configuration (Figure 16) [18]. The phase shifters are placed behind the radiating elements and the beams are steered in the desired direction. The direction of the antenna elements can be controlled in the desired direction.

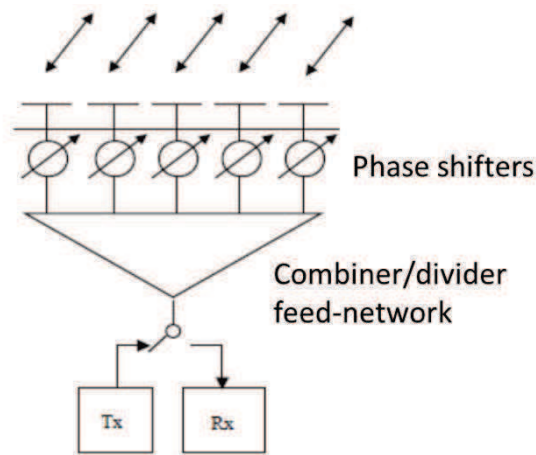


Figure 16: Central feed array

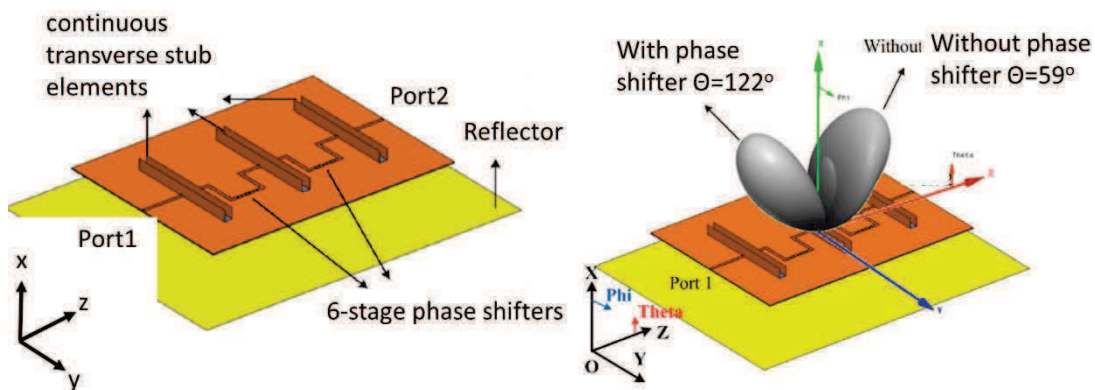


Figure 17: Beam steering by phase shifter element

[19] is an example where phase shifters are used to steer the radiation pattern (Figure 17). However, the phase tuning steps and angle ranges of the phase shifter will affect the beamforming capability.

1.3.2.2. Digital beamforming

Digital beamforming (DBF) was initially developed mainly for military applications. It consists of a digital signal processor (DSP) to calculate and apply a weight factor to each data sample. The DBF technique became a common approach for smart antenna systems with growing interest in low-cost wireless local area networks (WLANs). The DBF system provides several advantages over analog beamforming techniques. First, analog array systems often use phase shifters and attenuators, each element of which is expensive. Second, when considering the signal processing capability, analog beamforming is usually more limited [20]. However, DSP has a speed bottleneck in data I/O depending on the CPU speed that it can offer [21].

Phase array antennas with digital beamforming have revolutionized the capabilities for wireless communications. For a high throughput system, hybrid analog–digital beamforming techniques have been used to successfully demonstrate adaptive beamforming, adaptive nulling, and improved signal-to-interference ratio [17], [21]. Figure 18 illustrates the concept of partial digital beamforming with analog phase shifter. The summing of the subarray antenna channels is performed at microwave frequency by a microstrip combining network. Each subarray output has its own receiving channel with a mixer to IF and a bandpass IF-amplifier. This is followed by the mixer to the baseband to obtain the two orthogonal

components I and Q. Finally, the signal is converted from analog to digital format for both components.

Next, it is digitally processed. DSP calculates all the data from each element. Then the special computed weights can be applied to form the adapted beams in order to eliminate jammers or to change the beam direction.

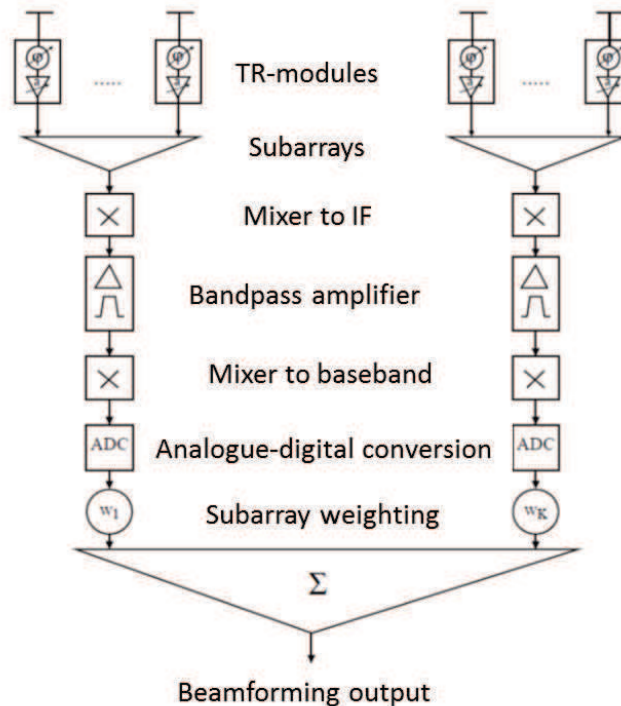


Figure 18: Concept of digital-analog hybrid beamforming

From the above analysis, we can see that it is very important to have an antenna capable of adjusting its radiation pattern. It is a highly important feature, which allows flexibility and can increase the throughput capacity for modern communication systems. The adaptive antenna array is used as the most common type of steerable antenna system and offers better antenna gain.

However, the conventional adaptive array antenna system requires a larger space to accommodate multiple antenna elements. The trend is to reduce the dimensions of the adaptive array antenna system by using small electrical components to replace large volume components. The extra cost in terms of volume used is negligible.

1.4. Key components of the beam steering system

When implementing a beam steering system for automobile application, we have two considerations to take into account. First, the space within the system is limited. Second, the beam steering system is designed for an LTE communication service that needs to support a broad range of frequency bands (800MHz to 2700MHz).

From analysis done of the several beam steering methods, we can understand that the selection of the antenna type and the integrated components are two important factors. Now an overview of the critical components will take place.

I.4.1. Antenna selection

A wide variety of antennas have been developed for different applications (Figure 19). They can be classified in different categories, such as by shapes or geometries: wire antennas, aperture antennas and printed antennas [22] and [23].

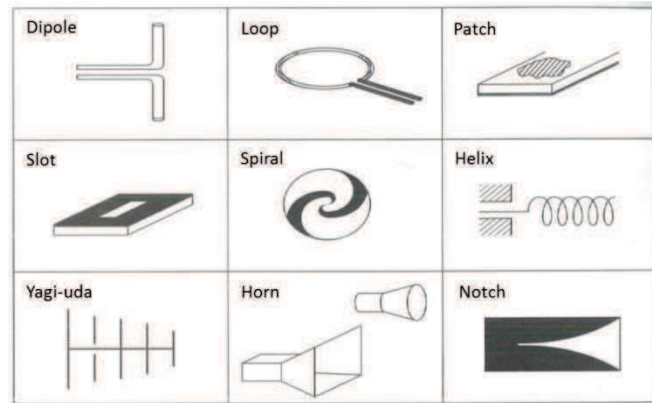


Figure 19: Various antennas

We need to select the best solution from the categories of different antennas. We are aiming for small antenna dimensions for automotive application, with high antenna efficiency at 800MHz and which can be easily manufactured.

I.4.1.1. Wire antennas

The list of wire antennas includes dipoles, monopoles, loops and Yagi-Uda arrays. This kind of antenna generally has low gain. They are light weight, low cost and of simple design. Figure 20 shows monopole and dipole antennas. They are the most commonly used antenna for wireless communications due to their omnidirectional radiation pattern.

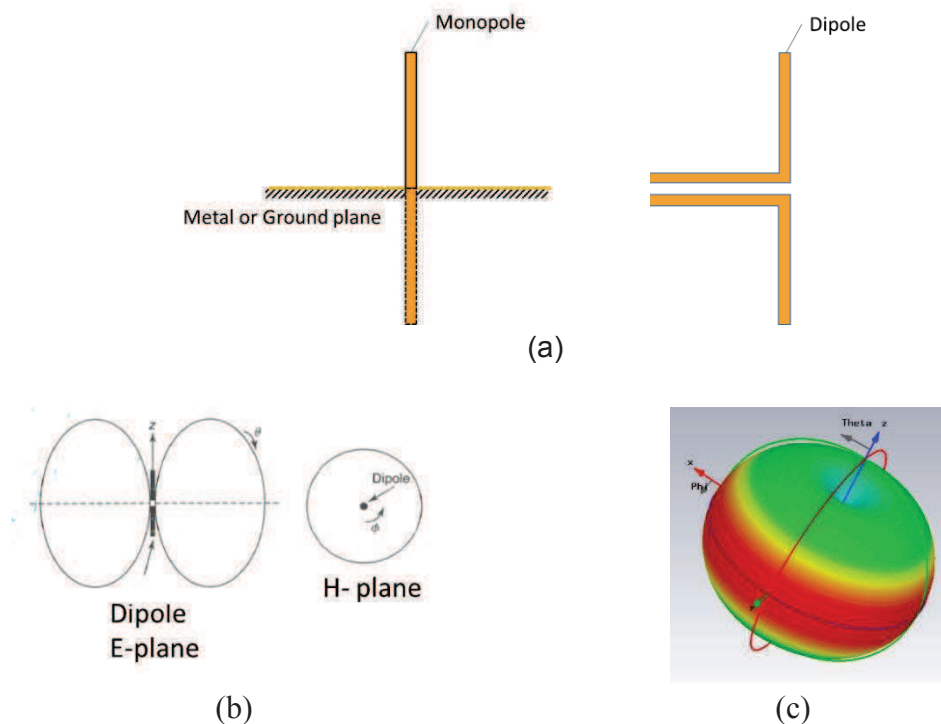


Figure 20: (a) Wire dipole and monopole antenna, (b) E-and H-plane radiation patterns (c) 3D diagram of the radiation pattern

A loop antenna could also be considered as a magnetic dipole with an axis perpendicular to the plane of the loop (Figure 21) [23].

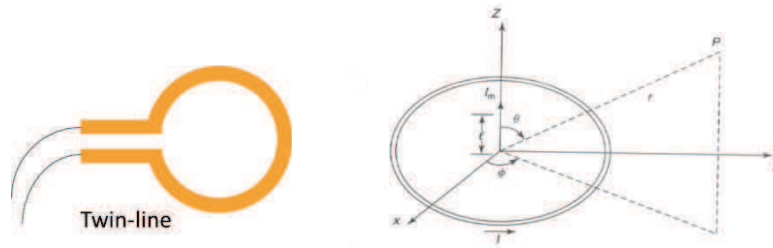


Figure 21: Configuration of full loop antenna and its equivalent magnetic dipole at the centre

To achieve 800MHz resonance, the dimension for this kind of antenna is around 19cm ($\lambda_0/2$) which is huge and is difficult to implement in an automotive environment. Most also do not exhibit multi band broad bandwidth characteristics, which is a requirement for the study.

I.4.1.2. Aperture antennas

This kind of antenna includes open-end waveguides, horn antennas, reflector antennas and lens antennas. They are commonly used at microwave and millimeter wave frequencies for high gain antennas [22].

We can take the horn antenna as an example. It is a transition between a waveguide and free space (Figure 22). The horn antenna is commonly used as a feed for a parabolic antenna or like a gain standard device for the antenna gain measurement. Since its gain can be calculated to within 0.1dB accuracy from its known dimension, it could be a gain standard in antenna measurement systems [23].

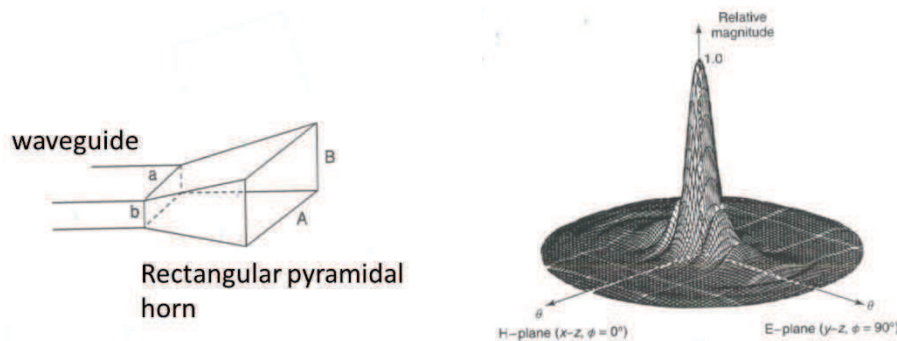


Figure 22: Configuration of rectangular horn and 3D radiation pattern.

Aperture antennas can achieve high antenna peak gain, high directional beam and also support broad bandwidth. However, the antenna dimension to support 800MHz resonance is also over 20cm.

I.4.1.3. Printed antennas

The list of printed antennas includes printed slots, printed dipoles, microstrip patch antennas and dielectric resonator antennas. These antennas can be fabricated using photolithographic methods with radiating elements and associated feed circuit fabricated on substrates. They can be easily used in high gain arrays and can be mounted on the surface of aircraft, spacecraft, satellites, cars and handheld mobile devices.

Patch antennas can be fed in many ways, for example, a coaxial probe or a microstrip line. Figure 23 illustrates a rectangular patch antenna and its radiation pattern [23].

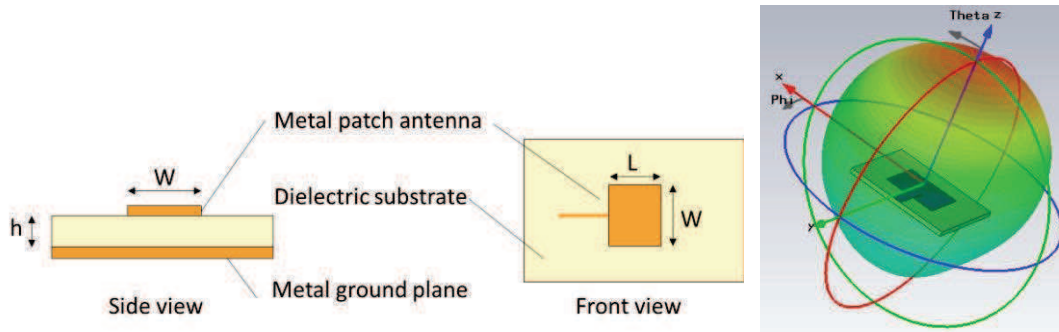


Figure 23: Rectangular patch antenna and radiation pattern.

Patch antennas always have narrow beam direction as shown in Figure 23. They are often used in arrays [24] with adaptive technologies (diode, MEMs...) which allows variation of both phase and amplitude, which is applied to each radiating element in order to obtain a steerable radiation pattern.

Apart from patch antennas, dielectric resonator antennas can also be fabricated by photolithographic technique. Dielectric resonators were used for circuit elements such as compact filters and oscillators in 1939 [25]. The first dielectric resonator antenna was demonstrated by Professor S.A. Long [26]. A dielectric material excited and placed in an open environment has a boundary condition at its interface allowing evanescent mode to exist and to radiate (Figure 24). This important property can form a dielectric resonator antenna (DRA). If the chosen dielectric constant is high, we can have impact antenna size.

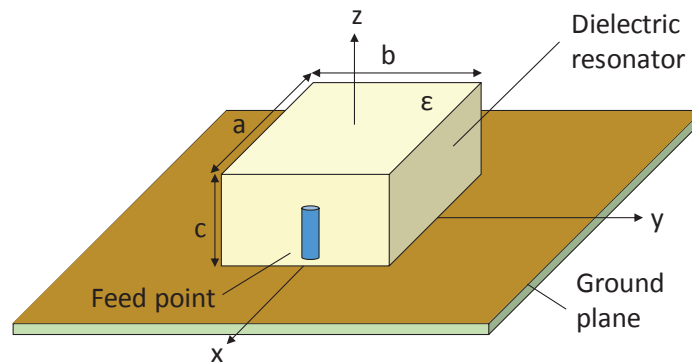


Figure 24: Geometry of dielectric resonator antenna.

DRAs can take different shapes such as cylindrical, rectangular, pyramidal, spherical and hemispherical. The shape of the DRA, its feeding mechanism and its wall boundary condition play an important role in working frequencies and bandwidths.

Since DRAs have similar advantages to printed antennas in the manufacturing process: easy feeding method, low profile.... it can be easily fabricated and duplicated. The duplication uses the photolithographic technique. We also can choose different high electric material to obtain correct antenna size to implement on a vehicle rooftop. Based on these characteristics, we will select DRA as the key component for our beam steering system for automobile application.

I.4.2. Phase shifter selection

When the condition or propagation environments do not allow the use of MIMO, or when the communication protocol does not support MIMO, the MIMO antenna can be switched (as previously explained) in order to support beamforming.

For our case, the method for beam steering must satisfy the below criteria:

- It should be controlled easily, using an electronic circuit.
- The radiation pattern must be steered for low frequency: 800MHz.
- The signal coverage range should be as large as possible.
- The whole system can be placed in an automobile, especially on the rooftop.

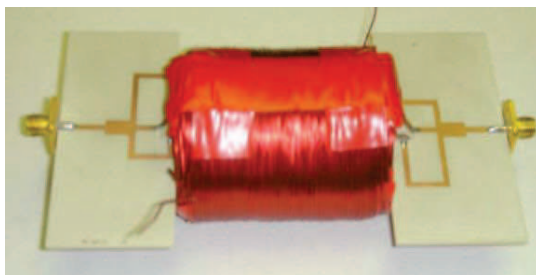
From Section I.3.2, the switched beam antenna size using mechanical matrix switches is very large for 800MHz and impractical for the commercial market. Apart from this, the configurable antenna only points out in a few specified directions; the radiation pattern does not cover all the space. Therefore, an adaptive array method for beamforming will be investigated.

Digital beamforming is the most flexible approach and can give best system performance due to its ability to optimize the beam pattern. But the major disadvantage of digital beamforming is its high cost associated with the RF chains and signal processing units. To the contrary, analog beamforming is a less expensive approach with the use of phase shifters and combiners located before the active device.

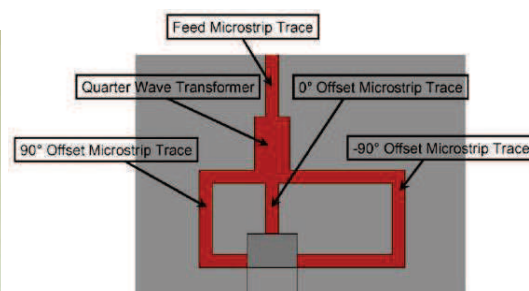
Based on Figure 6 in the global antenna system concept, it appears that this structure could be extended to integrate a DBF technique in the future. If we want to obtain an analog beamforming system, a phase shifter and a 3dB power divider have to be added. The 3dB power divider could be replaced by a direct connection with the RF front end. The phase shifter can provide the signal to the MIMO antenna. **Therefore, an appropriate phase shifter should be assessed.** Two well-known phase shifters with a wide phase shifting range are the ferrite phase shifter and the electronic phase shifter.

I.4.2.1. Ferrite phase shifter

Different types of phase shifters have been developed, both reciprocal and nonreciprocal phase shifters. Of the most useful designs that use ferrite material are the Faraday rotation phase shifter and the Reggia-Spencer reciprocal phase shifter [22]. However, these are relatively bulky and heavy compared to diode phase shifters and they required significant switch power [27] (Figure 25).



(a)



(b)



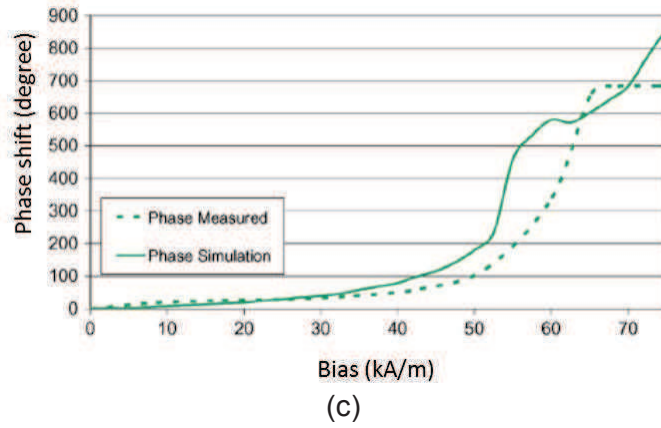


Figure 25: Ferrite phase shifter. (a) Fabricated microstrip-line-based ferrite phase shifter prototype with a bias coil; (b) Feed network; (c) Bias vs. phase shift result

I.4.2.2. Electronic phase shifter

Modern phase shifters are usually electronically controlled. They are designed as a two-port network with at least two different states. They are controlled by using PIN diodes, transistors or MEMS. This kind of design with fixed configurations has two lines: a reference line and a phase shifting line. The existing topologies in the literature are: switched line, reflection-type, loaded-line, high-pass, low-pass and all-pass filter network [28] - [35]. Their benefits are:

- (a) Switched line: very low power requirement to switch the state, high power handling, low RF insertion loss (within 1dB), high linearity and dynamic range. Figure 26 shows a device using MEMS to switch for different phase shift paths [28]. For the same path, the phase shift depends on frequency.

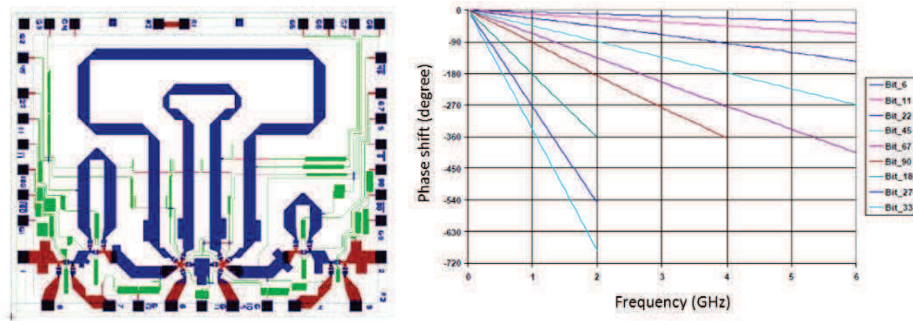


Figure 26: Example for switched line and phase shift result

Figure 27 and Figure 28 are also examples of switched lines phase shifter [29] and [30].

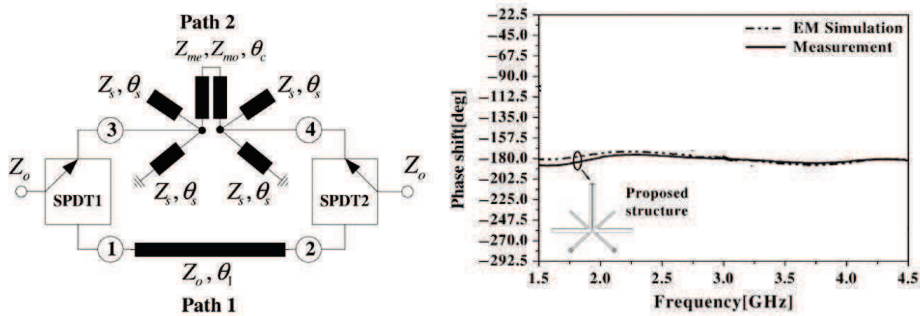
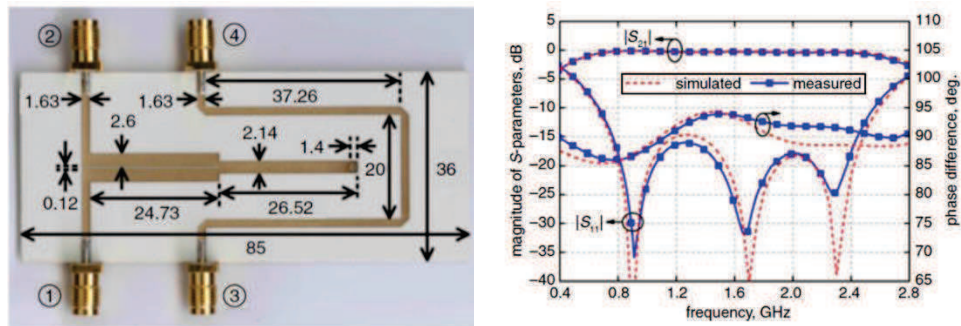
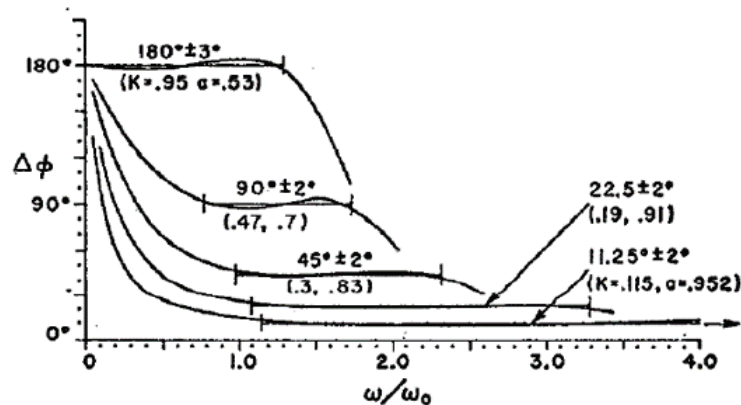
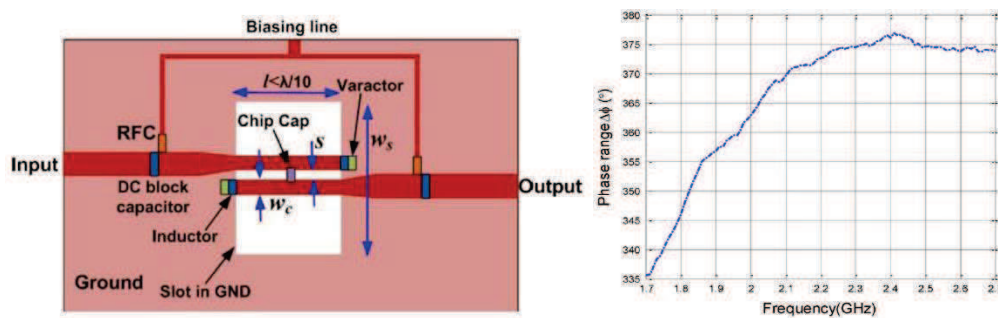


Figure 27: Switched line phase shifter for 180°



(b) Reflection-type: The phase shifter is made with a circulator or 3dB coupler. The characteristic of the circulator or coupler will define the phase shifting performance [31]. In a reflection-type phase shifter, the coupler structure can be designed using less than $(\lambda_0/10)$ one tenth of the target frequency. The mode impedances can be changed if we correctly change the coupler structure [32] (Figure 29). The insertion loss of this type is within 1.5dB. However, the band width is also limited as shown in Figure 30.



(c) **Loaded line:** The device uses PIN diodes or switches to change the loads of a line [33]. This type of phase shifter is flexible in achieving different phase shifts for the same loaded line and has low insertion losses (Figure 31). The insertion loss is lower than 0.5dB but the bandwidth is not very broad.

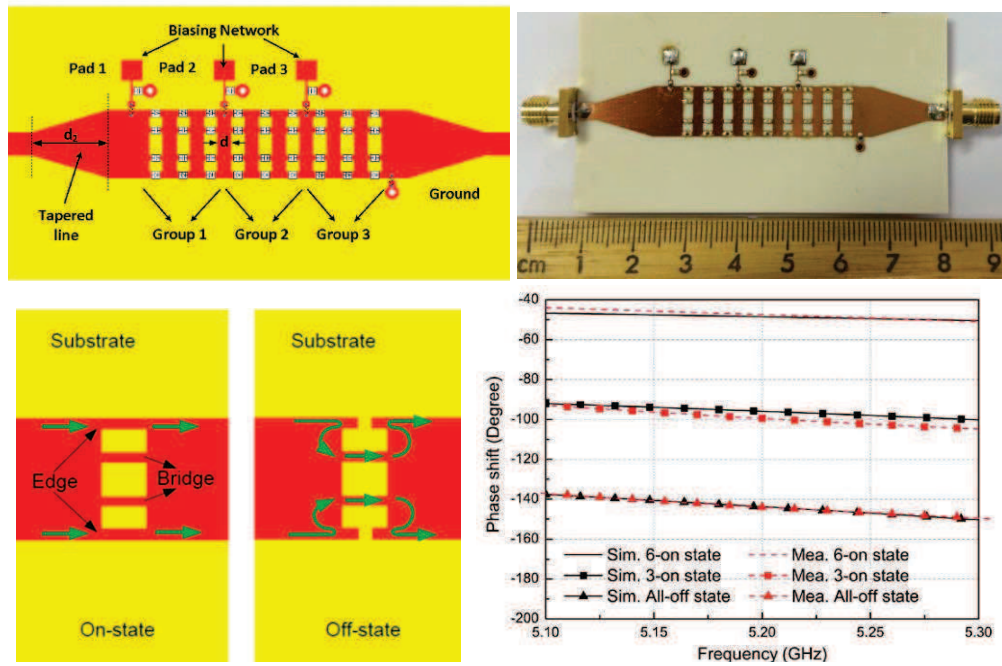


Figure 31: Photo of loaded line phase shifter and phase shifter result.

- (d) High-pass, low-pass and all-pass filter networks: minimized space, easily developed via lumped element and can be developed using MMIC. The frequency range can be as high as 6GHz [34] or as low as around 500MHz [35] depending on the component and circuit type selection. Figure 32 and Figure 33 illustrate the performances of phase shifters using discrete components.

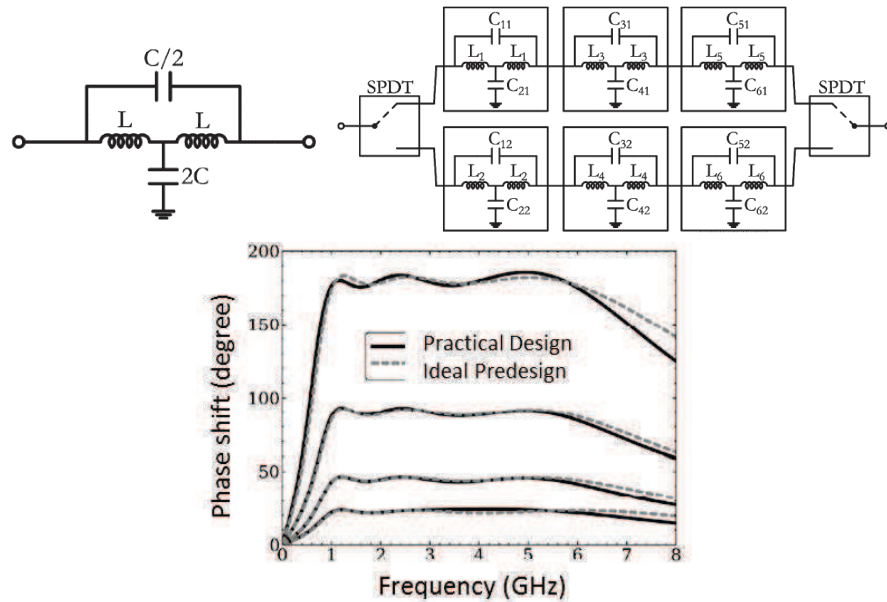
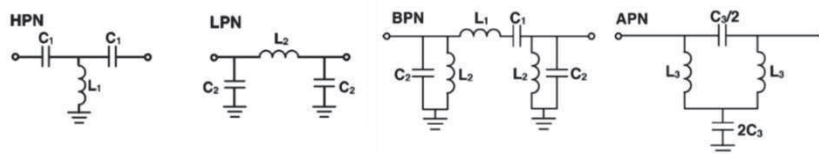


Figure 32: Filter phase shifter with series-C filter configuration and three-stage all-pass filter configuration with phase shift result.



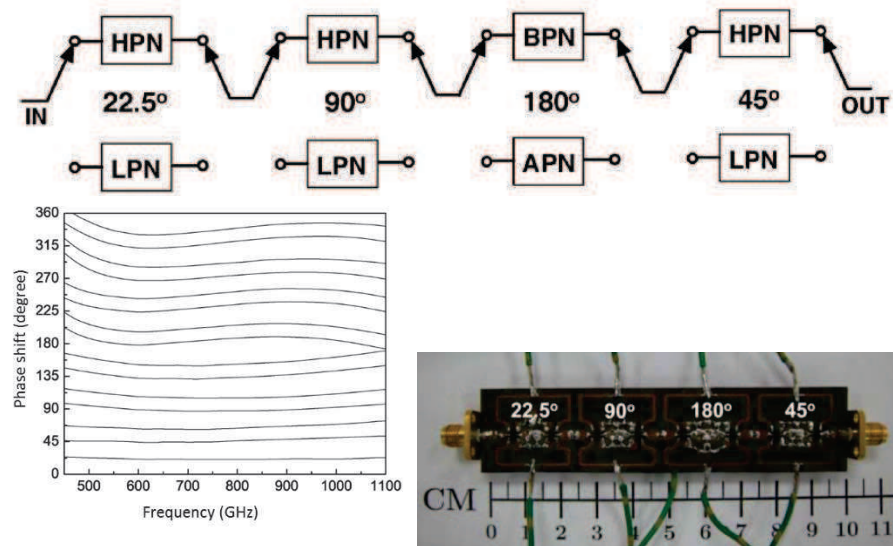


Figure 33: High-pass and low-pass hybrid phase shifter and phase shift result.

The advantages and comparisons of the above discussed electronic phase shifter are shown in Table 1.

Table 1: [Comparison between different electronic phase shifting technologies]

Parameter	MEMS digital delay line	switched line	reflection-type	loaded line	filter network
RF loss	Low	Low	Low	Middle	High
Linearity	Good	Not bad	Not bad	Bad	Not Bad
Production Cost	Low	Low	Low	High	Low
Frequency range	Wide	Wide	Middle	Narrow	Middle

The different kinds of phase shifter characteristics have been summarized. The desired functions for the phase shifter in the thesis should be:

- Good performances at the lowest LTE frequency such as 800MHz.
- Minimum fabrication cost.
- An easy control method.
- A 360° shifting phase.

To achieve these goals and to also obtain a phase shifter that works in broadband for LTE, GPS and Wi-Fi networks, a combination of all-pass filter and switched line phase shifter (Figure 34) will be studied in the thesis. This is the tunable phase shifter structure which takes advantage of different kinds of phase shifters. This work will be detailed in Chapter Three.

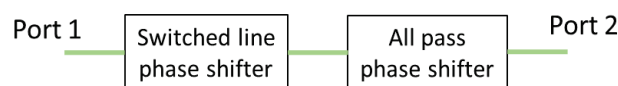


Figure 34: Adopted phase shifter structure.

I.5. Objective of the thesis:

As described earlier, the trend in antennas for automotive applications is towards implementing wireless communication systems on vehicles. The development of car antenna

systems is becoming increasingly diverse. In the beginning, radio reception for AM and FM was obtained by a monopole mounted on the roof. Then Bluetooth and DVB antennas became commonplace in vehicles. Nowadays, Wi-Fi and LTE communications modules are increasingly integrated into cars.

With respect to the vehicle environment, the limited space on the vehicle rooftop and its large metal sheet is well understood. In the automotive environment, communications links between the vehicle and the infrastructure are poor at high speed [36] [37]. It is also indicated that a directional antenna in the automobile can improve data throughput rate for the communication service. We want to design a MIMO system with directional antenna to improve the quality of the wireless system.

Considering all the factors and the target of commercializing the antenna design, we decided to use a dielectric resonator antenna (DRA) as the leading candidate for the MIMO and beamforming system. The use of the dielectric resonator material offers advantages such as diversity excitation, wide range of permittivity material, compact size with very low loss, high radiation efficiency, high directive gains and various shapes. In addition, we can use printed-circuit technology to fabricate the antenna for mass production. We would adopt a rectangular shape, which is simple and easy for manufacture.

To cover the LTE standard frequency bands that are used all around the world, the DRA will be designed to cover the LTE spectrum operated on four distinct frequency bands: LTE 800DD (band 20), LTE 1800+ (band 3), LTE 2100 (band 1) and LTE 2600 (band 7). With specific design procedure for the DRA, we will design an efficient, relatively compact, multiband antenna.

Since the relative position between the vehicle and the infrastructure is always changing in a high-speed situation, we can benefit if we can adapt the antenna radiation pattern. Even though beam steering technology has significant advantages in wireless communication systems, it is still not implemented in the commercial automotive industry. This thesis is focused on the design of the LTE beam steering antenna system by using the original MIMO automotive system. The vehicle environment space is limited; therefore we want to integrate these two techniques within the same system. They will be integrated in the proposed antenna system as shown in Figure 35.

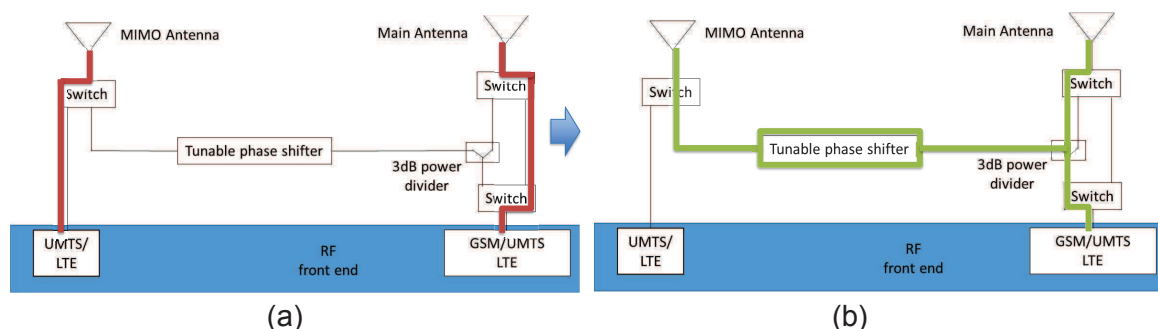


Figure 35: Concept of MIMO system (a), transfer to beam steering antenna system (b)

An appropriate miniature and multiband DRA will be developed. Also, a tunable phase shifter (which covers almost 360° at 800MHz) will be designed. Indeed, the phase shifters on the market are not suitable for our requirements. We therefore decided to design our own phase shifter. The one proposed must have basic 0° , 90° , 180° and 270° phase shifting. The possibility of obtaining minor phase tuning using a variable capacitor will also be studied. The

tunable phase shifter design can be achieved using electronically controlled switches and a variable capacitor.

To simplify, the simulated and measured global system models are illustrated in Figure 36 and Figure 37.

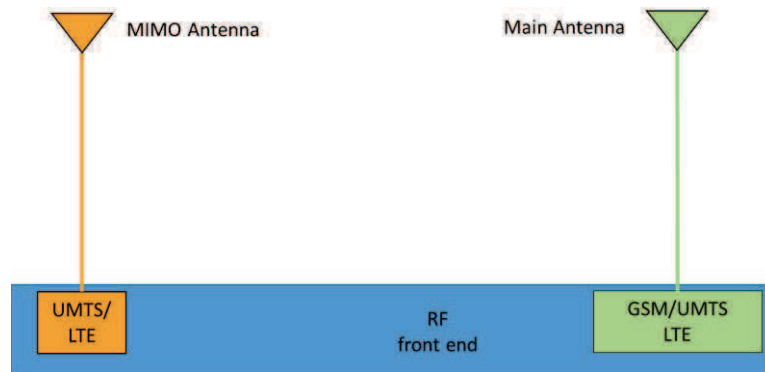


Figure 36: MIMO antenna system model in the thesis

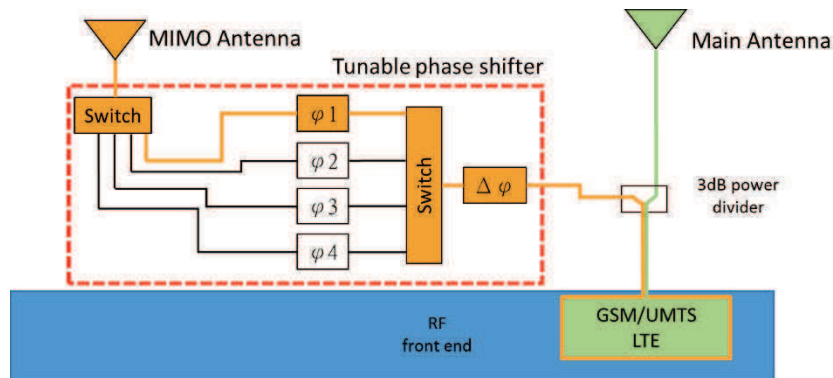


Figure 37: Active steering antenna system model in the thesis

The simulation tool for the thesis is CST Microwave Studio 2013.

I.6. Conclusion

This chapter provides a clear picture of the active steering global array system with commercial communication module.

The first part introduces and illustrates the principle of different beamforming systems. Beamforming systems have many advantages, such as improving the quality of transmitting and receiving signals, raising the throughput data rate and increasing the base station or antenna system signal coverage.

The second objective is to introduce basic antenna types and our considerations for selection of the antenna to fit the automobile application. The selected antenna structure is the rectangular DRA which can be easily commercialized. The shape of the DRA, its feeding mechanism and its wall boundary condition play an important role in working frequencies and bandwidths. By using a high permittivity material, DRA can be used for compact size at the lowest desired frequency while covering higher frequencies [38].

Several phase shifter structures have been presented and compared in terms of performances and working frequency range. The detail regarding switching in two working models, the MIMO system and the beam steering system, are explained in the final part.

The end of this first chapter highlighted the beam steering system on the vehicle. The next chapter discusses and presents the study of DRA to achieve broad band, miniaturization and ease of fabrication. The antenna focuses on the multiband design for the now popular LTE communication service.

Chapter II. Compact and Multiband MIMO Dielectric Resonator Antenna for Automotive Application

II.1. Introduction

The explosive growth of wireless communications and the increasing demand for high data rate throughput are pushing the deployment of Long Term Evolution (LTE) communication systems. In Chapter One we showed that the Multiple Input – Multiple Output (MIMO) technique is one of the key technologies in the LTE system. Indeed, a MIMO system can help to overcome the multipath damage effects and is now a common technique used for increasing the capacity of downlink and uplink data rate throughput without additional spectrum. In this context, we study resonance frequencies within a rectangular shaped DRA according to whether a part of the faces are coated with a metal or not. This shape is easy to fabricate and for commercial use, only one face will be partially covered. The DRA will be designed to cover the LTE spectrum operated on four distinct frequency bands: LTE 800DD (band 20), LTE 1800+ (band 3), LTE 2100 (band 1) an LTE 2600 (band 7). In order to have a MIMO system for the LTE standard, the antenna needs to cover all these four frequency bands while possessing reconfigurable radiation patterns.

Based on the commercial LTE wireless module specifications, we aimed for an $|S_{11}|$ value lower than -6dB with a minimum total antenna efficiency of 50% on the four frequency bands. Furthermore, the MIMO antenna system performances will be evaluated with the envelope correlation coefficient (ECC) with a value of under 0.5 required.

The proposed MIMO system is designed to be integrated on the rooftop of a vehicle within a limited space of 120mm × 70mm × 65mm corresponding to $\lambda_0/3 \times \lambda_0/5 \times \lambda_0/6$ at 800MHz and defined in Figure 38.



Figure 38: Dedicated space of the automotive antenna

The roof of the car is considered a large ground plane but for easy measurement and fabrication, we are using a 200mm × 200mm-FR4 substrate coated entirely with copper.

A lot of literature has been published on dielectric materials used for antenna applications. The dielectric resonator characteristics are introduced in the first part of this chapter. We would like to take the advantages of a rectangular shape for dielectric resonator antenna development and fabrication. In the second part, different feeding mechanisms are introduced and the properties of a dielectric resonator are described. Finally, the basic antenna structure is formed by using a monopole with a probe feed which is attached on one of the rectangular dielectric resonator surfaces. Finally, the DRA is mounted on a real automobile and measured to determine the antenna efficiency and its radiation patterns in an

anechoic chamber. The result from testing the DRA mounted in different locations of the vehicle is shown at the end of this chapter.

II.2. Development of the dielectric resonator antenna

The development of dielectric resonators began with circuit elements such as compact filters and oscillators in 1939 [25]. Using a dielectric material to create the first dielectric resonator antenna was demonstrated by Professor S.A. Long [26]. Indeed, a dielectric material excited and placed in an open environment has a boundary condition at its interface allowing evanescent mode to exist and to radiate. This important property is thus applied to make an antenna element in dielectric resonator antenna (DRA) form. This can be highly compact when the chosen dielectric constant is high.

DRA can be employed in different shapes such as cylindrical, rectangular, pyramidal, spherical and hemispherical. Since we need to use a simple fabrication method for commercialization, the antenna structure chosen is rectangular. This section will focus on a general study of a rectangular DRA.

II.2.1. Characteristics of a rectangular DRA

Main DRA characteristics are summarized as follows:

- The dimension of a DRA is proportional to $\lambda_0 / \sqrt{\epsilon_r \cdot \mu_r}$ where λ_0 is the wavelength in free space at resonant frequency, and ϵ_r and μ_r are the dielectric and magnetic constant of the material, respectively. For dielectric materials, $\mu_r = 1$ implying that the main dimension of DRA is proportional to $\lambda_0 / \sqrt{\epsilon_r}$ [38].
- The DRA can achieve better radiation efficiency, since the material can be selected with a minimum loss tangent with no metal losses.
- For a given resonance frequency, the aspect ratio of a rectangular DRA (height/length and width/length) can be chosen independently. Also, the higher eigenmodes can be properly chosen according to the three dimensions of the resonator [39].
- Furthermore, based on the wide choices of available dielectric material, the impedance bandwidth and dimensions of the DRA provide the best approximation of the expectation.
- There are different excitation methodologies for a DRA, which can avoid or allow some eigenmodes.
- Different boundary conditions applied to the dielectric resonator interface can reduce its overall dimensions.

II.2.2. DRA excited mode

Before developing the DRA, we need to study different feeding methods so as to choose the best mechanism for our design. There are several feeding methods used to excite different resonance modes inside the DRA, we will detail them in this section.

II.2.2.1. Coaxial probe excitation

The probe can be located within the DRA or adjacent to it. If the probe is inside the DRA, it can excite the electric field of the DRA mode through a good coupling [40] (Figure 39).



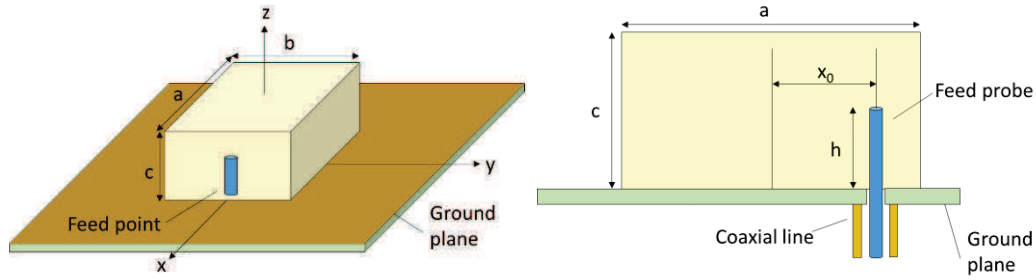


Figure 39: Internal coaxial probe feed

When the probe is inside the DRA, it implies an air gap between the probe and the dielectric material which involves a lower effective dielectric constant for the antenna. Therefore, resonance frequencies are shifted at upper frequencies and the Q factor is decreased.

The probe can also be located outside the DRA. This uses the coupling of the magnetic field to generate the DRA modes (Figure 40).

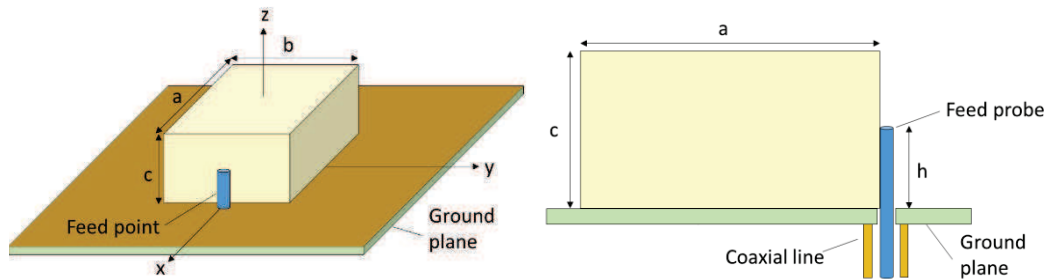


Figure 40: External coaxial probe feed

This allows a great deal of freedom to adjust the antenna characteristics by modifying the probe length and its height. For this feeding mechanism, we could use a strip line to replace the coaxial probe.

II.2.2.2. Microstrip line and coplanar waveguide feeding

This is also a simple and direct coupling feeding method between the DRA and the microstrip line. In this design, the end of the microstrip line is terminated in an open condition. The DRA needs to be close to the open end of the microstrip line to obtain the maximum coupling. The coplanar waveguide method uses a similar scheme to the microstrip line [41] (Figure 41).

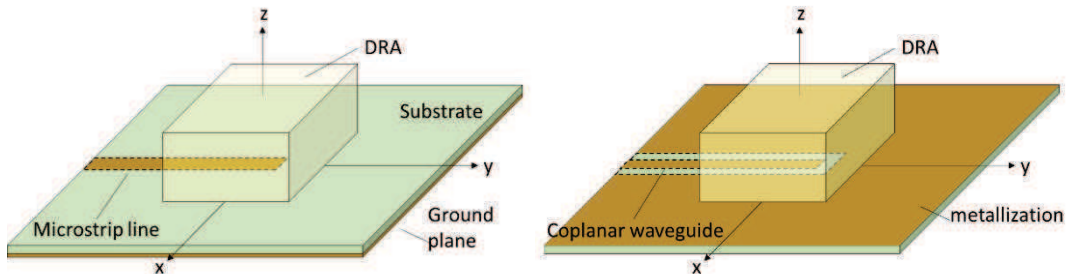


Figure 41: Microstrip feeding and coplanar waveguide feeding

The microstrip line feeding method can obtain the coupling of the TE_{111}^z and TE_{111}^x modes of a rectangular DRA. In both these case, the mode coupling can be optimized by changing the resonator position and/or its dielectric permittivity. However, this kind of coupling is critical for a DRA with a low dielectric constant value ($\epsilon_r \leq 20$) [39].

II.2.2.3. Aperture coupled feed

Another common method for exciting the DRA is to use a microstrip line with an aperture at the end of the transmission line (Figure 42). In effect, the DRA is placed above a narrow slot that is etched in the ground plane. The slot length is small enough to ignore the self-resonant effect.

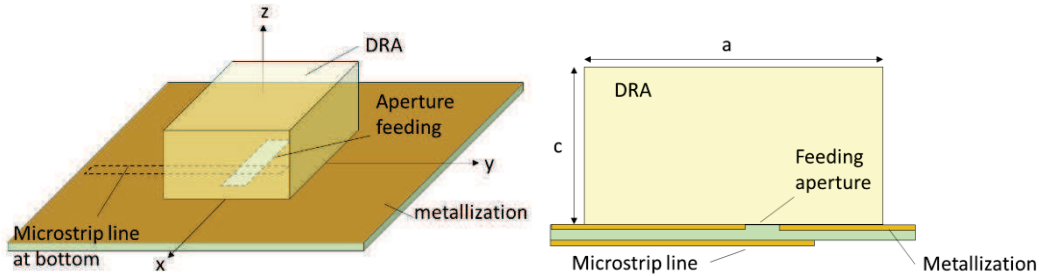


Figure 42: Aperture coupled feed

When the DRA is kept symmetrical with respect to the slot, the TE_{111}^z mode is excited. The coupling between the DRA and the slot can be easily adjusted by changing the length and /or the width of the slot.

II.2.2.4. Dielectric image guide coupling

This mechanism uses a dielectric material as a guide to transmit the power from the waveguide to a DRA array. DRAs are placed at some specific distance from the dielectric image guide in order to get the coupling energy from the dielectric image guide ([41], [42], Figure 43). The advantages of the dielectric image guide are its low loss at high frequencies and the ease of coupling energy into the DRA. With this method it is also easier to apply the power to the array elements at the same time.

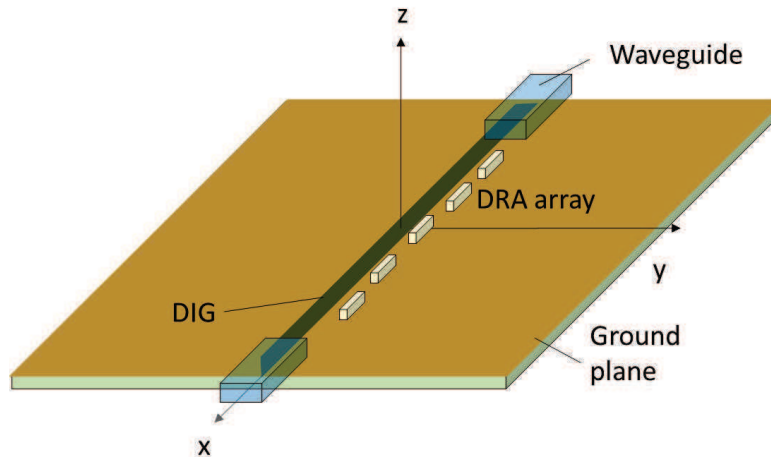


Figure 43: Dielectric image guide feed

In our study, we will develop an antenna for LTE automotive solutions. To cover the LTE standard frequency bands that are used all around the world, the antenna needs to be matched at around 800MHz, 1800MHz, 2100MHz and 2600MHz. The aperture coupled method requires a length of approximately half of the wavelength. This is therefore a difficult requirement to obtain a miniature antenna at the lowest frequency. Thus, a coaxial probe feed will be used for the antenna design since it is flexible and can be easily fabricated.

II.2.3. Selection of DR material

II.2.3.1. Different boundary conditions and resonant frequencies

This section presents a detailed study of an isolated rectangular DR (Figure 44). The dimensions of the rectangular DR are formed with a length (l), width (w) and height (h), which are independent of each other. Here the rectangular dielectric waveguide model is used to analyze the rectangular DRA. Typically, only TE modes exist [39]. As the DRA dimensions are independent, TE modes can be along the three directions in x, y and z. The modes with lower order indexes are $TE_{x_{111}}$, $TE_{y_{111}}$ and $TE_{z_{111}}$.

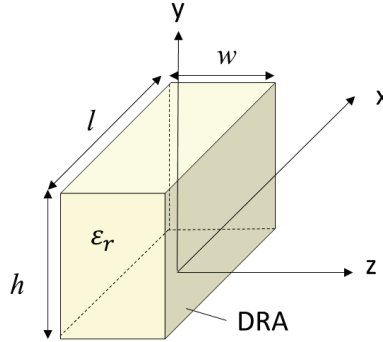


Figure 44: Isolated rectangular dielectric resonator antenna

The resonant frequency can be obtained by satisfying the following equations.

$$f_0 = \frac{c}{2\pi\sqrt{\epsilon_r\mu_r}} \sqrt{k_x^2 + k_y^2 + k_z^2} \quad (1)$$

$$k_z \tan\left(\frac{k_z w}{2}\right) = \sqrt{(\epsilon_r - 1)k_0^2 - k_z^2} \quad (2)$$

$$k_x = \frac{\pi}{l}, k_y = \frac{\pi}{h}, k_x^2 + k_y^2 + k_z^2 = \epsilon_r k_0^2 \quad (3)$$

Where k_x , k_y and k_z denote the wavenumbers along the x, y, z directions inside the DR. k_0 is the free space wavenumber corresponding to the resonant frequency. For a given resonator parameter ϵ_r , l , w and h , the resonant frequencies of the DRA can be predicted. If the dimensions of DR are such that $h > w > l$, the resonant frequency of the mode in increasing order is $TE_{x_{111}}$, $TE_{y_{111}}$, $TE_{z_{111}}$ [39].

In this study, the DRA is mounted on a near infinite ground plane (rooftop of a vehicle) implying that the bottom surface could be assumed to be an electric wall (Figure 45). In this case, by applying the image theory, the DR height is divided by two and thus formed by the length (l), width (w) and height ($h/2$).

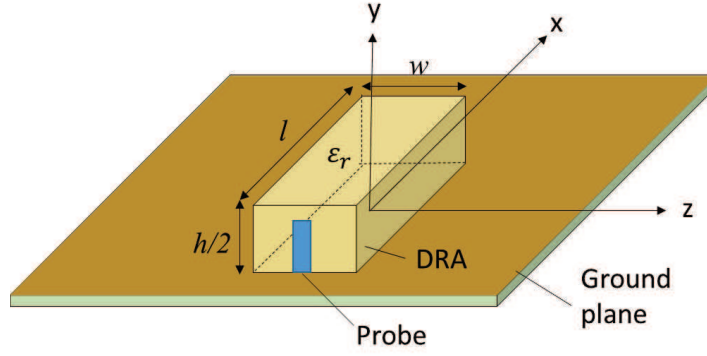


Figure 45: Rectangular DRA placed on a ground plane excited by a strip probe.

The TE_{x111}^x and TE_{z111}^z modes of this DR are equivalent to an isolated DR of double height (Figure 44). It means that the resonant frequency of these two models is the same [42]. Also, [43] illustrated that using another metallic plate as a different boundary condition can increase the hybrid mode inside the DRA (Figure 46). This characteristic is useful for increasing the bandwidth for our application.

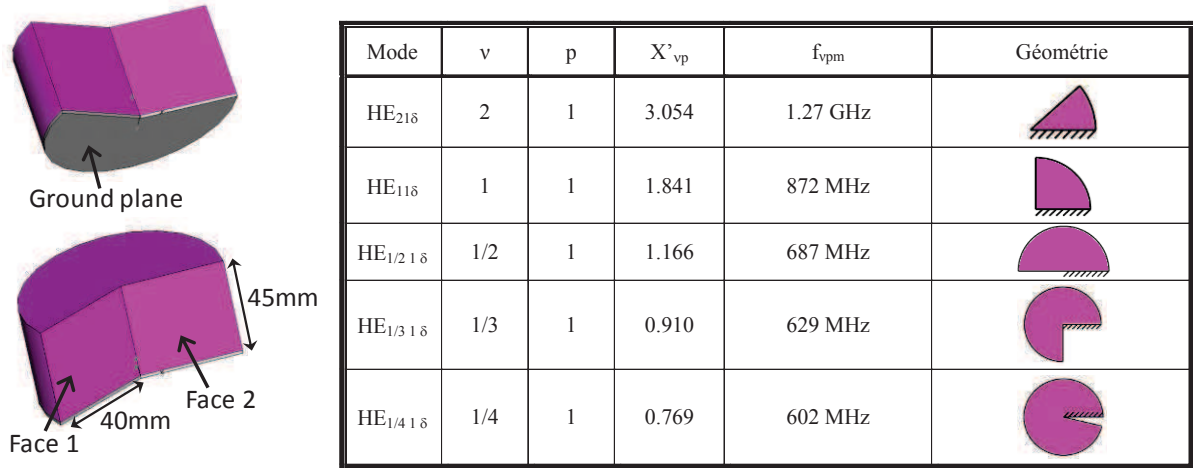


Figure 46: Adding extra metallic plate for hybrid mode [43].

II.2.3.2. Radiation Q factor

The Q factor of the rectangular DRA is proportional to the ratio between the total stored energy in the DR and the power radiated by the DRA. In TE_{111} mode, a DRA radiates like a magnetic dipole of moment \mathbf{p}_m given by [44]:

$$\mathbf{p}_m = -\frac{j8A\omega\epsilon_0(\epsilon_r-1)}{k_x k_y k_z} \sin\left(\frac{k_z d}{2}\right) \mathbf{a}_z \quad (4)$$

A is an arbitrary constant and k_x , k_y and k_z denote the wavenumbers along the x, y and z directions inside the DRA. The power radiated by a magnetic dipole of moment \mathbf{p}_m is given by the following standard relation:

$$P_{rad} = 10k_o^4 |\mathbf{p}_m|^2 \quad (5)$$

Most of the stored electric energy lies inside the resonator due to its high dielectric constant. The expression for the stored electric energy is found from

$$W_e = \frac{\varepsilon_0 \varepsilon_r l w h A^2}{32} \left(1 + \frac{\sin(k_z w)}{k_z w}\right) (k_x^2 + k_y^2) \quad (6)$$

Finally, the radiation Q factor of the antenna can be determined using the relation

$$Q_{rad} = 2\omega_0 W_e / P_{rad} \quad (7)$$

where ω_0 denotes the angular frequency. When ε_r is high, the Q factor is proportional to:

$$Q_{rad} \propto (\varepsilon_r)^{3/2} \quad (8)$$

For both models, the Q factor is the same (Figure 44 and Figure 45).

With reference to these equations, the resonant frequency decreases when dielectric permittivity increases, meaning that the antenna becomes physically smaller. However, it implies also the decrease of its bandwidth [38]. Indeed, for low dielectric permittivity DRA, fields are less confined by the resonator and for high dielectric permittivity material, although strong coupling is achieved inside the resonator, Q increases while the bandwidth decreases.

Moreover, the loss tangent and the bandwidth of an antenna are linked to the Q factor as well as the antenna total efficiency. The aim for our antenna performance is to maintain efficiency of over 40% in all the LTE frequency bands. The antenna efficiency is also more affected by the losses when the dielectric permittivity increases [38]. Also, the lowest frequency for the proposed antenna is 800MHz, the best trade-off between miniaturization, Q factor and efficiency is to choose a relative DR permittivity of around 10.

II.3. Multiband DRA structure

II.3.1. DRA development methodology – Initial antenna model

The aim of the antenna design is to be not only multi-band, but also to produce a more compact antenna. Designing a compact DRA with multi-band properties can be achieved by integrating several antenna theories and concepts [45]. The literature explains that DRA can use the advantages of the DR to resonate and radiate at different frequencies determined by the DR shape and boundary conditions. However, most DRA designs are able to cover only some parts of the frequencies supported by LTE communicated services. And many DRA shapes are designed with specific structures that are difficult to manufacture at low-cost.

To integrate two antennas within the allocated space, each radiating element needs to be miniaturized. With this intention, we set the dimensions of one dielectric resonator (DR) at 22mm×13mm×50mm to be vertically placed on a finite FR4 substrate (Figure 47). The antenna's characteristics (dimensions, quality factor, bandwidth, gain and efficiency) are influenced by both the permittivity and the loss tangent of the dielectric material. To obtain the widest impedance bandwidth, but with small dimension, the selected DRA permittivity is close to 10. Therefore, the DR material chosen was the TMM10 material from Rogers with a relative permittivity of 9.2 and a loss tangent of 0.0022.

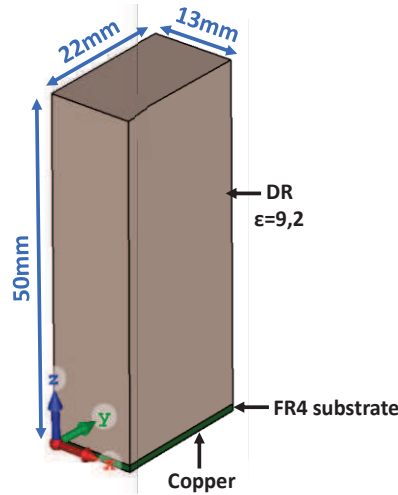


Figure 47: Maximum dimensions of the antenna to be integrated within the dedicated space presented in Figure 38.

For the modal analysis, the FR4 substrate is considered to have the same lateral dimensions as the dielectric resonator (see Figure 47) with a copper metallic ground on the bottom side. Its permittivity equals 4.1 with a loss tangent of 0.012 at 1GHz. Within these dimensions, and considering a dielectric resonator placed on an FR4 copper coated substrate, the first resonant mode is the TE_{101} at 2GHz (Figure 48). It should be noticed that this resonant frequency has been determined considering evanescent modes at the interface between the dielectric resonator and the air, i.e. without considering a perfect magnetic condition (PMC).

Moreover, metallic conditions are based on the use of copper layers. For doing that, a vacuum cavity surrounded by PMC conditions, is integrated around the DRA during the eigenmode analyses. The thickness of the cavity is chosen such that we obtain a convergence of the resonance frequency of the mode with eigenmode analyses. These eigenmode analyses are then validated by the electromagnetic simulation by integrating an excitation port and checking both the resonance frequencies and the 3D shapes of each mode.

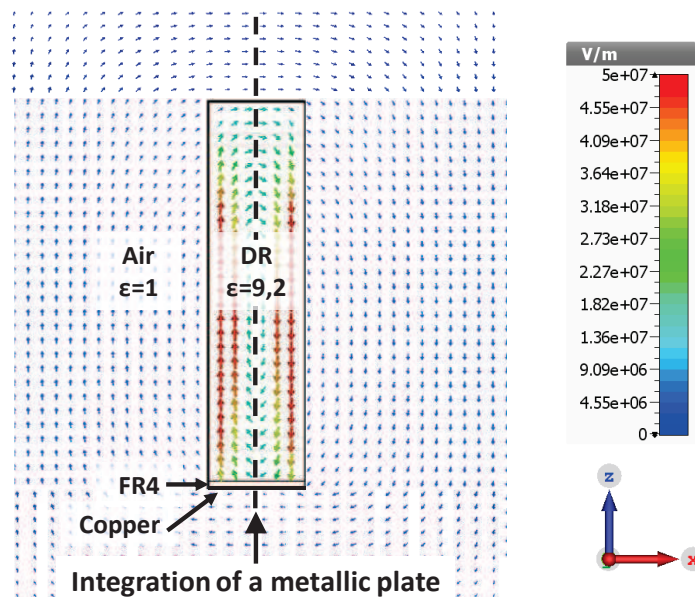


Figure 48: E-field on the $y=11$ mm plane of an isolated DRA placed on FR4 copper coated substrate.

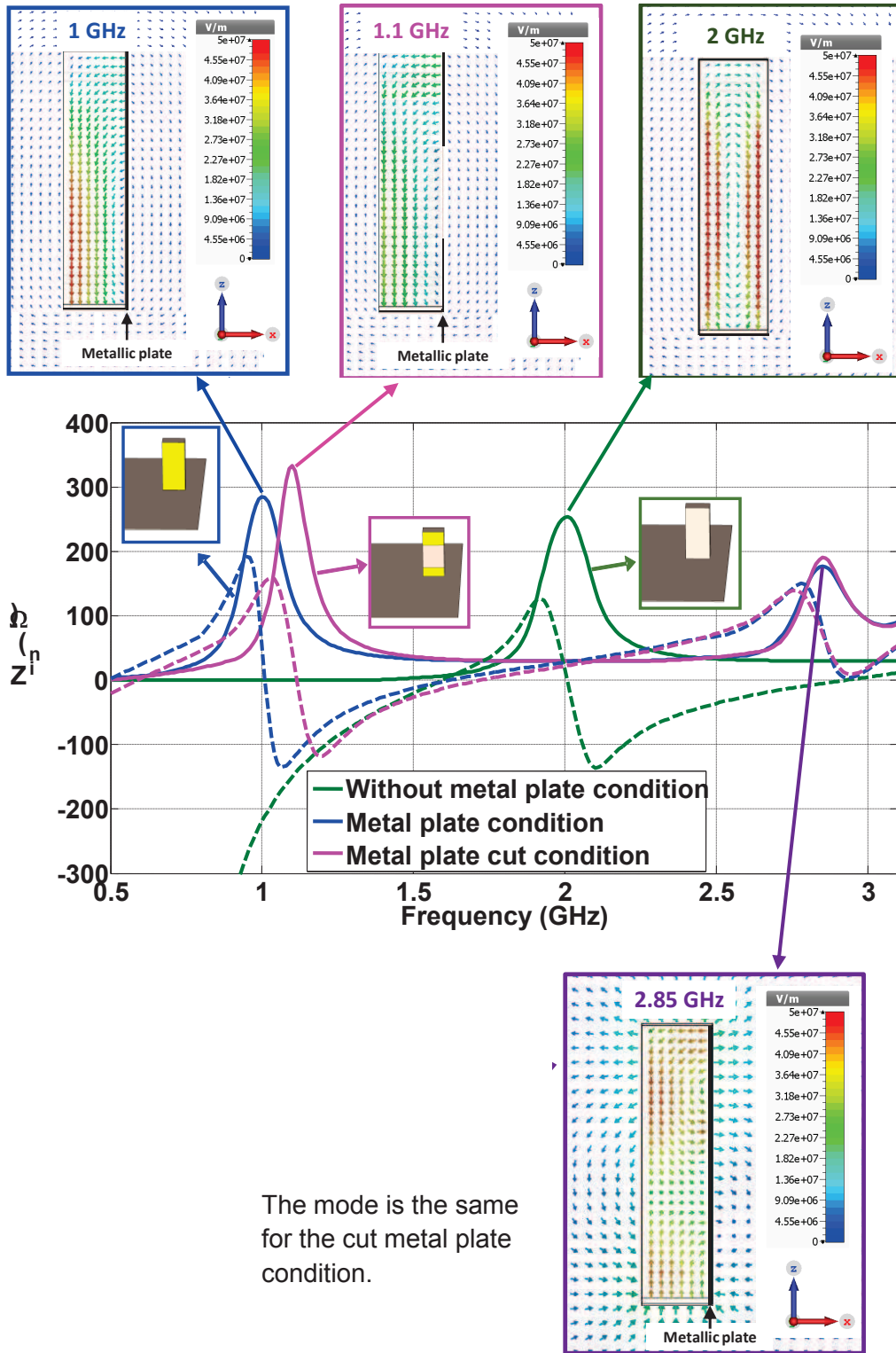


Figure 50: Input impedances with the modal analyses for three different cases.

II.3.2. Final antenna structure

The final proposed antenna structure is detailed and shows the face where metallic areas are integrated (Figure 51).

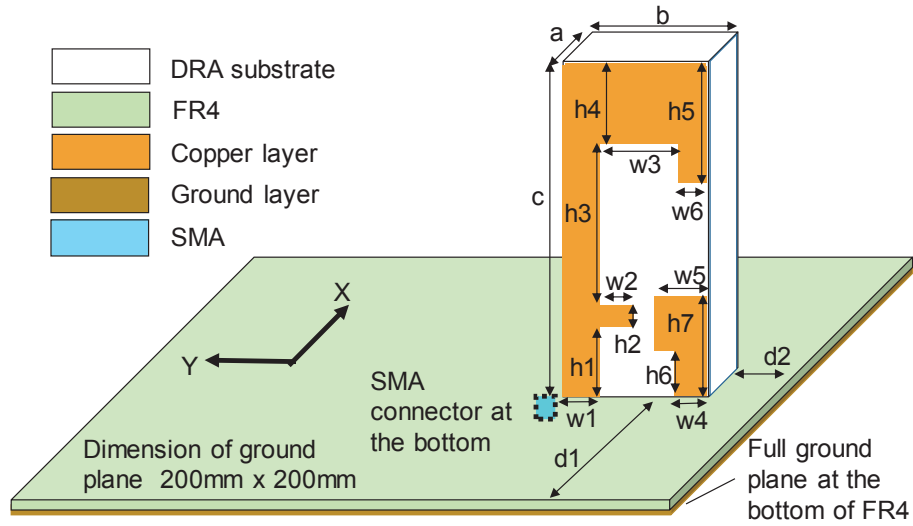


Figure 51: Final DRA cell dimensions.

For practical reasons, the ground plane dimensions are 200mm×200mm. The antenna design is targeted to satisfy the LTE spectrum operated on distinct frequency bands: LTE 800DD (band 20), LTE 1800+ (band 3), LTE 2100 (band 1) and LTE 2600 (band 7). GPS L1 band is also included. Based on commercial LTE wireless module specifications, we aimed for an $|S_{11}|$ value lower than -6dB with a minimum total antenna efficiency of 50% on the four frequency bands.

The rectangular shape is easy to fabricate and for commercial purposes, only one face will be partially covered. Table 2 details DRA dimensions.

Table 2: [Detailed dimensions of the DRA metal part (unit: mm)]

Parameter	a	b	c	d1	d2		
Value	13	22	50	109	20		
Parameter	w1	w2	w3	w4	w5	w6	
Value	4.5	6.3	13.5	3.4	7	4	
Parameter	h1	h2	h3	h4	h5	h6	h7
Value	9.7	2	24.3	14	20.5	8	14.5

The FR4 substrate used is 1mm thick with a dielectric permittivity of $\epsilon_r=4.1$ and a loss tangent equal to 0.012 at 1GHz.

The distance, from the DR to the FR4 edge, $d1 = 109\text{mm}$ and distance $d2$ is 20mm.

The input impedance of the optimized design alone is presented in Figure 52. Since this antenna is developed to be integrated on an automobile rooftop, it will be studied on a 200mm×200mm-FR4 substrate, entirely copper coated. Therefore, Figure 52 also includes the DRA response on the considered 200mmx200mm ground plane. For higher frequencies, both eigenmode analyses of the DR and the input impedance presented in Figure 53 show

that the parasitic strip on the side wall creates hybrid modes at 1.8GHz and 2.4GHz respectively. The resonance frequency of the fundamental mode is only slightly shifted compared with the cut metal plate condition since it is equal to 1.18 GHz. The fourth mode of this DRA structure is the same as the previous second cut metal plate mode condition.

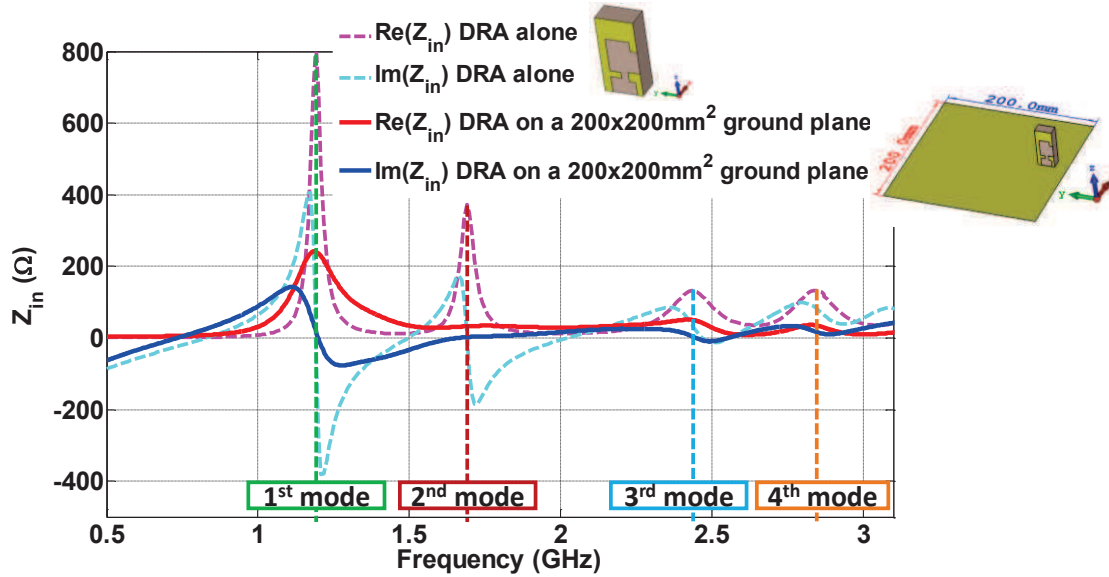


Figure 52: Input impedance variation of the final DRA alone and integrated on a $200 \times 200 \text{ mm}^2$ ground plane.

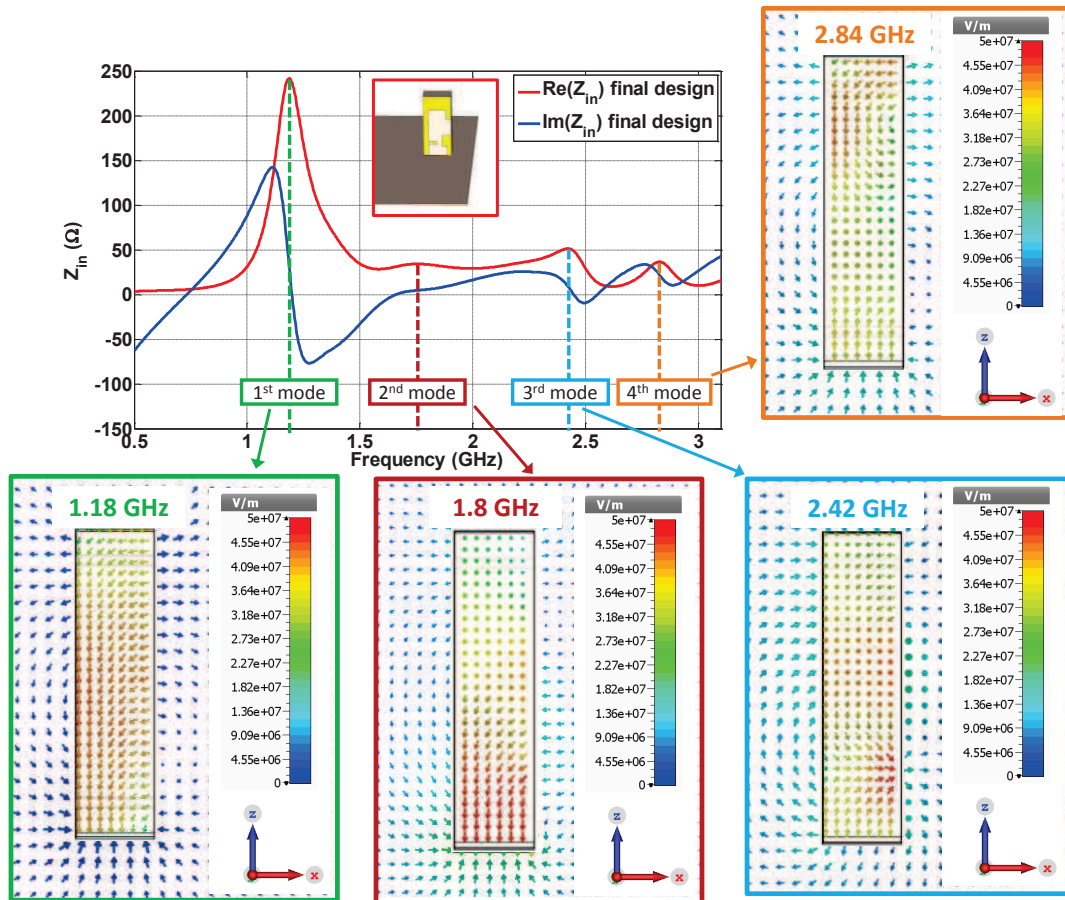


Figure 53: Input impedance with the modal analyses for the final design on $200 \times 200 \text{ mm}^2$ ground plane.

The benefit of exciting hybrid modes in this design is that the real part of the input impedance stays at around 50Ω while the imaginary part is around 0Ω between 1.4GHz and 2.6GHz. A wider frequency bandwidth is therefore obtained compared to the other cases, as presented by the $|S_{11}|$ parameters in Figure 54.

Combining the previous three cases and with partial metallic plates optimized in the final design (total four cases), we can deduce that:

- The shapes of the first resonating modes for the three cases with lateral metallic part conditions are almost the same. The resonance frequency of the fundamental mode for the two metallic conditions presented in Figure 50 is a little bit different since it equals 1GHz when the lateral face is totally metal coated while it equals 1.1GHz for the cut metal plate condition. For the final design it is shifted at 1.18GHz (Figure 53).
- The fundamental mode of the DRA without any metallization on its lateral face is TE_{101} and it resonates at 2GHz (twice as high as the totally coated case, as expected). That means that without the matching circuit, our DRA has been miniaturized halved.
- Two hybrid modes are excited for the final design case at 1.8GHz and 2.42GHz, these modes exist and are created by the optimized metal shape on the lateral face of the final design.
- The second mode excited for the metal plate and cut metal plate conditions at 2.85 GHz corresponds to the fourth mode of the final design at 2.84 GHz as shown by their respective shapes (Figure 50 and Figure 53).

Now, from these input impedances, we can plot the $|S_{11}|$ parameters (Figure 54) for the four above cases.

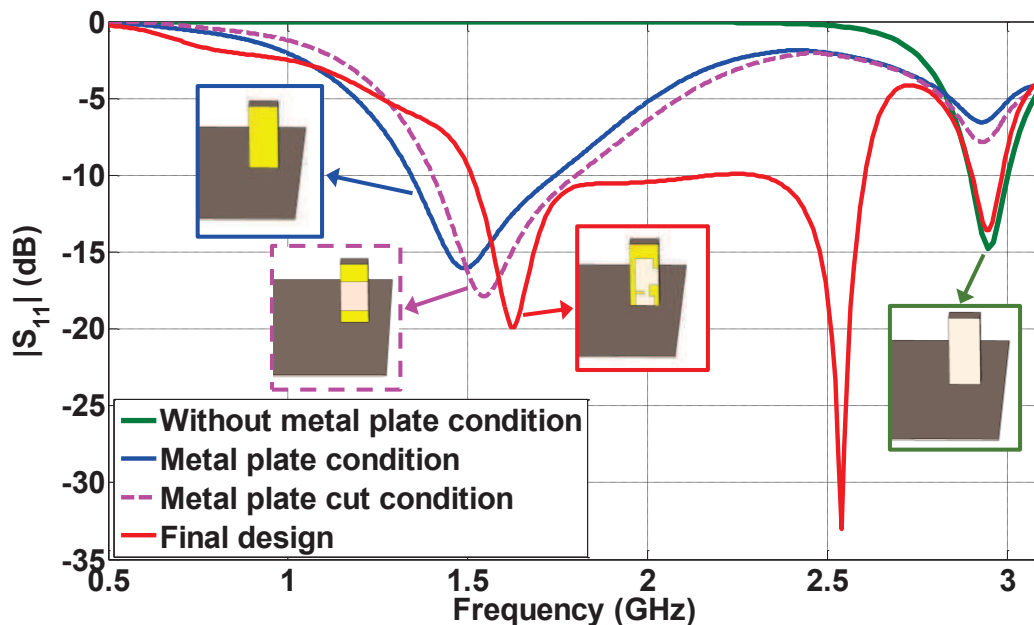


Figure 54: $|S_{11}|$ parameters for the four studied cases.

For all cases, antennas are matched above their resonances: for example, for the final design, the first resonance frequency is equal to 1.18GHz (see the input impedance in Figure 53) while its matching band starts at 1.5GHz. It is the same for the DRA without metal plate on its lateral faces: the resonance frequency of the first mode equals 2GHz while its

matching frequency is around 2.8GHz (i.e. when the real part of the Z_{11} is around 50Ω and the imaginary part around 0Ω).

Moreover, since the first mode is resonating around the same frequency for the metal plate condition, for the cut metal plate condition and for the final design, the first matching band starts around the same frequency.

The most important conclusion here is that for the final design, the two hybrid modes, excited at 1.8GHz and 2.42GHz, allow the antenna to be matched on a larger frequency band from 1.34GHz to 2.64GHz if we consider an $|S_{11}|$ lower than -6dB.

Until this step the matching network has not been integrated, which means that the antenna is not matched around 800 MHz.

The integration of a large ground plane means that the global dimensions of the radiating element are increasing, which implies the decrease of the Q factor. Indeed, from the input impedance, we can determine the antenna quality factor from the equation (9) [46] where ω_0 is the resonant angular frequency, R_0 is the resistance and Z_0 is the impedance of the resonant frequency.

$$Q(\omega_0) = \frac{2R_0(\omega_0)}{\omega_0|Z_0'(\omega_0)|} \quad (9)$$

The Q factor reaches a maximum value of 30 at 1.04GHz for the antenna on the $200 \times 200 \text{mm}^2$ ground plane while it equals 100 for the DRA alone (without a large ground plane). It is lower than 5 for the other resonance modes for the antenna mounted on the ground plane. A high Q factor implies that it is difficult to match the antenna on a wide bandwidth.

It should be remembered that the antenna needs to work on the lowest LTE band between 790 MHz and 860 MHz. Therefore, a T-type matching circuitry is placed on the FR4 substrate just before the DRA to match the antenna on the serial resonance of the first mode, i.e. at 825 MHz. This matching circuit is presented in Figure 55 which is provided the conjugate $Z_{in}=8+25j$ at 825MHz. Measured touchstone files with a homemade TRL kit for inductor and capacitor from Murata LQG and GRM series are used in the electromagnetic simulation and the SMA connector is placed under the ground plane.

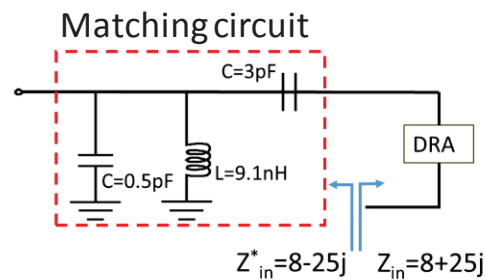


Figure 55: Final DRA matching circuitry.

The prototyped antenna is visible in Figure 56. The feeding point is between the ground plane and the edge of the DR wall which has the copper plane routing on the surface. A parasitic element is located at the corner which is on the same side of the monopole and the SMA connector is placed at the bottom of the matching circuitry.

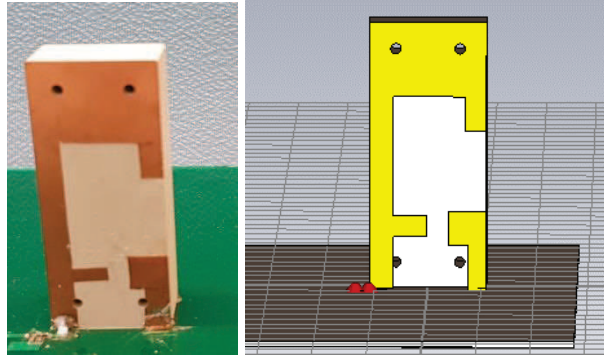


Figure 56: Photography for DRA cell.

To validate the design, the prototype of the proposed DRA has been measured in an anechoic chamber. It has been also simulated with the Frequency Domain Solver in CST Microwave Studio.

II.3.2.1. Impedance and S-parameter

Figure 57 shows the simulated and measured input impedance of the DRA with the matching circuitry implemented. As expected, the matching circuit has created a new resonance around 800MHz showing that the antenna is well matched at this frequency (Figure 58). The DRA is also well matched where the hybrid resonant modes are excited, i.e. around 1800MHz and 2600MHz.

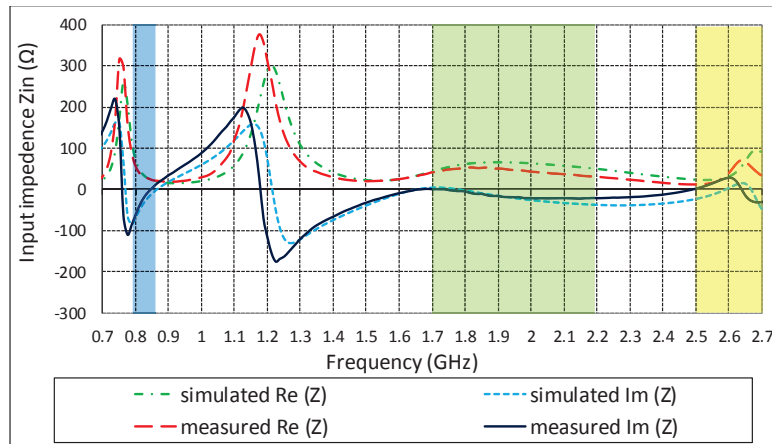


Figure 57: Input impedance variation of DRA with matching circuitry

Indeed, the measured $|S_{11}|$ is shown in Figure 58 and agrees with the electromagnetic analysis. The antenna is matched on the target bands- LTE 800DD, GPS L1 and LTE 1800+, LTE2100 and LTE2600. Indeed, results exhibit a broadband and multiband DRA since it covers [790MHz-860MHz], [1575MHz-2200MHz] and [2500MHz-2700MHz] frequency bands with a $|S_{11}|$ value lower than -6dB.

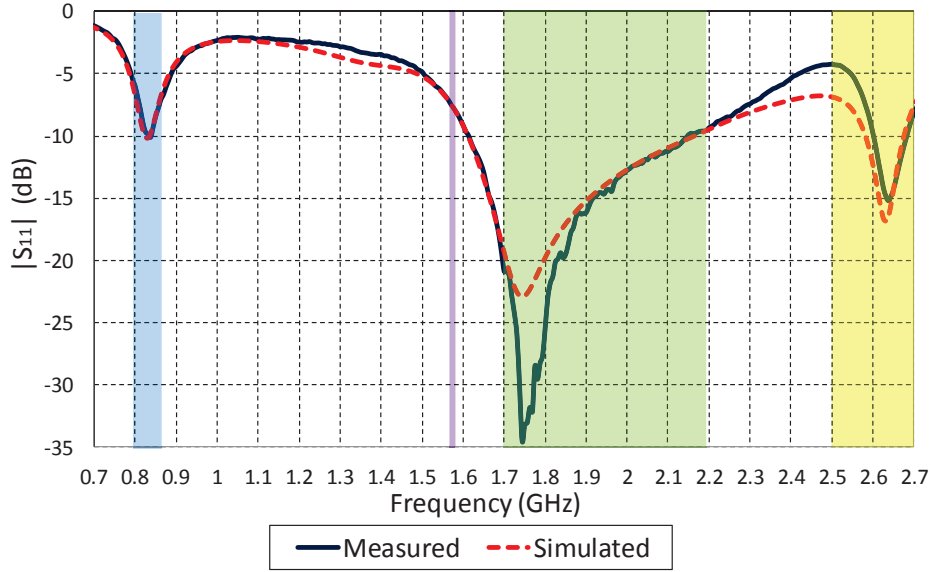


Figure 58: Measured and simulated $|S_{11}|$ parameters of the DRA

II.3.2.2. 2D and 3D of antenna radiation patterns

2D cut radiation patterns on both the xOz and yOz planes are shown in this section. We can observe that the measured results are very close to the simulated ones. Also, peaks and nulls of the 3D radiation pattern are similar between the measured and simulated results (Figure 59 and Figure 60). The axis of orientation is the same as Figure 51. These results showed good agreement with the CST simulation model.

The cross polarized field is high and the antenna does not exhibit a linear polarization due to the DRA location, close to the edge of the ground plane. However, a pure polarization in this design is not needed since LTE specifications depend on the total radiated field $E_{tot} =$

$$\sqrt{E_{\theta}^2 + E_{\phi}^2}, \text{ including both the co- and the cross-polarizations.}$$

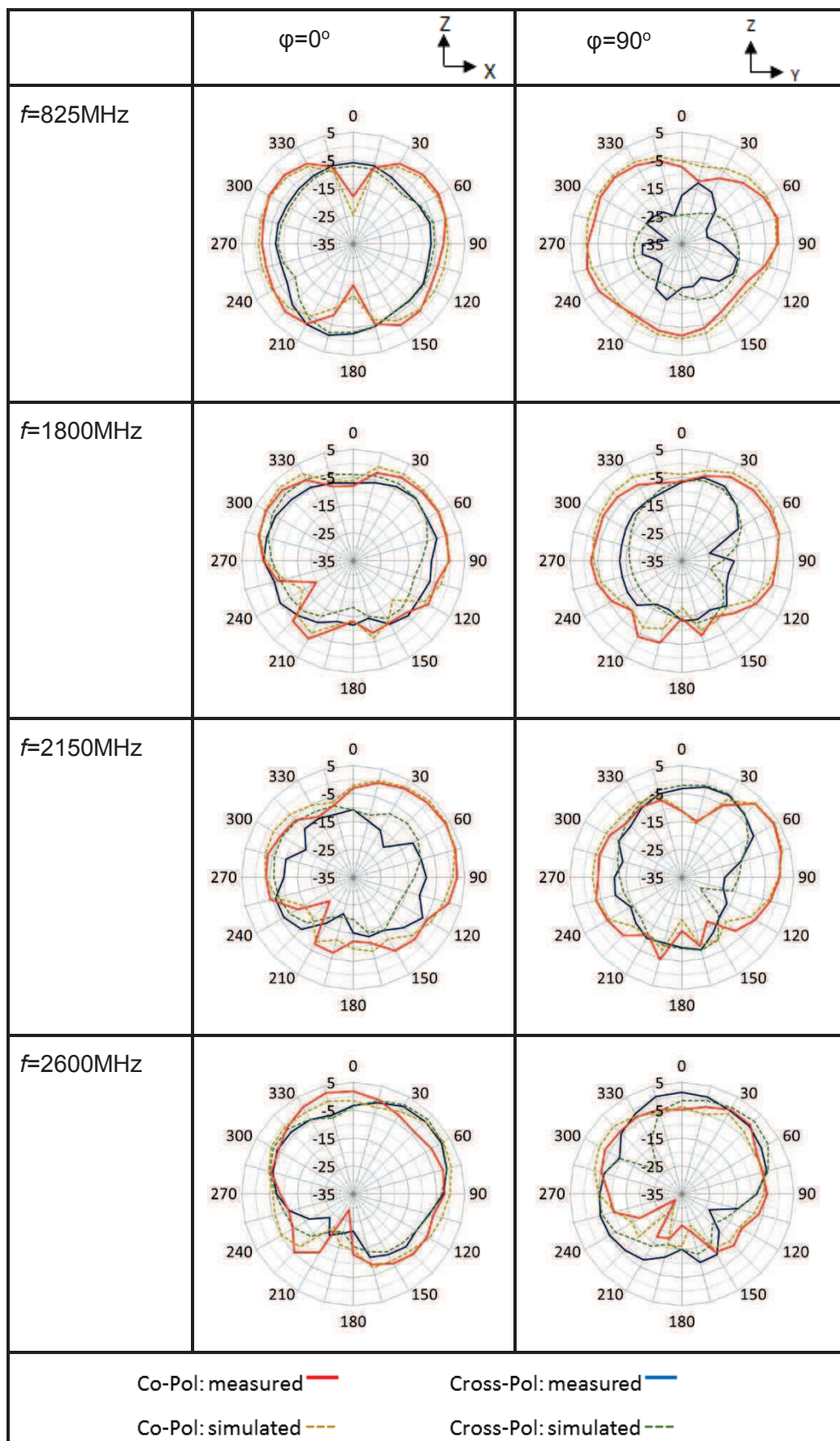


Figure 59: 2D radiation pattern for the DRA.

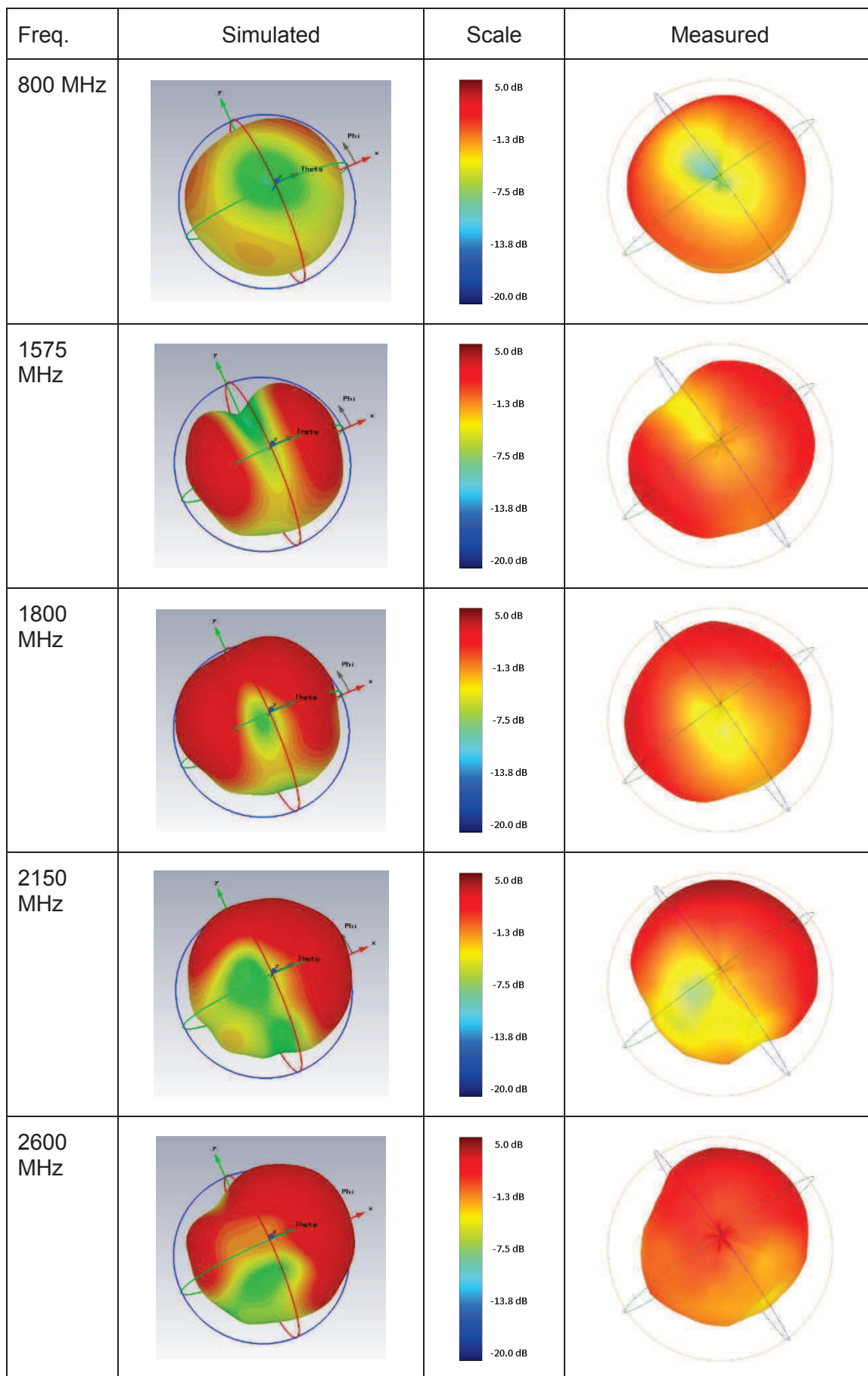


Figure 60: 3D radiation pattern for the DRA.

II.3.2.3. Maximum realized gain and total efficiency

From the 3D radiation patterns, we can deduce both the maximum realized gain and the total efficiency according to the frequency. The comparison between the simulated and measured result is presented in Figure 61. Measurements and simulations are in good agreement, with some of the resulting measured points a little higher than the simulated ones due to the expanded measurement uncertainty of the anechoic chamber calibration.

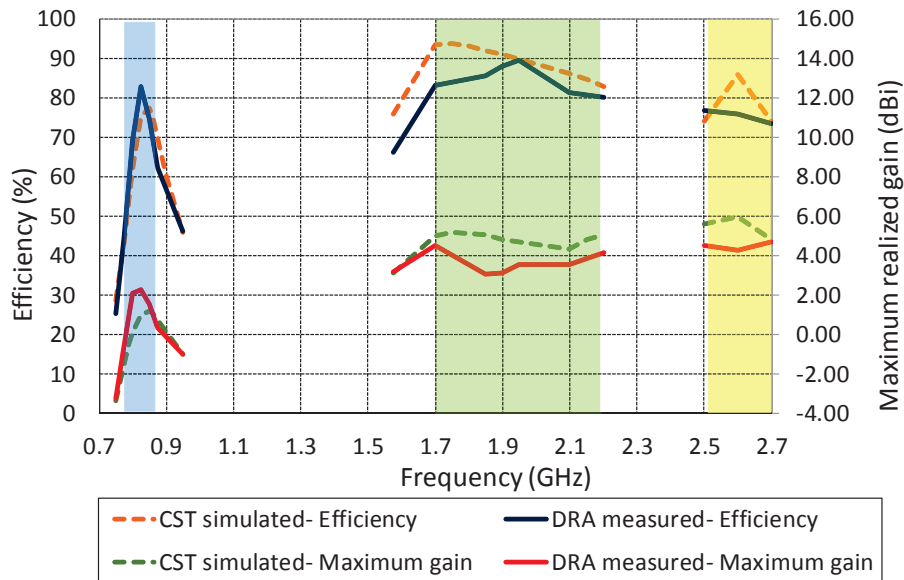


Figure 61: Measured and simulated efficiency and maximum realized gain of the DRA

Measurement results are in good agreement with the simulated ones. The antenna efficiency is greater than 50% for the first LTE band around 800MHz and better than 75% for the three others.

II.4. Antenna measurement on a vehicle

Since the antenna in this thesis is designed for automotive use, the antenna prototype is placed on the rooftop of a vehicle and its characteristic is measured in an anechoic chamber (Figure 62) which is specially designed for automobiles at the Ethertronics Nice office. Measurement is not only done using the traditional location of the antenna (Figure 63), but also done for the dashboard location and under the rooftop.



Figure 62: 3D anechoic chamber for the automobile.

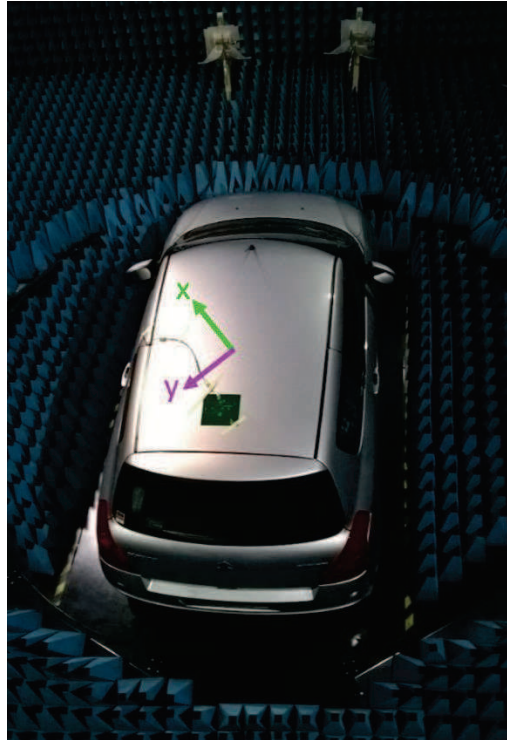


Figure 63: Top view of the antenna located on the rooftop

It should be noted that the following radiation patterns are measured and calculated only for the upper hemisphere because the antenna reception chamber cannot go under the ground plane. We use the standard dipole antenna to calibrate the upper hemisphere radiation pattern from 800MHz to 2700MHz.

II.4.1. Measured results of vehicle rooftop DRA

The measurement setup is shown in Figure 64. It should be noted that the metal surface of the DRA is not facing the x or y-axis. It has a 45-degree rotation compared to the simulated CST coordination. The metal surface of the DRA is at the back of the photo view.

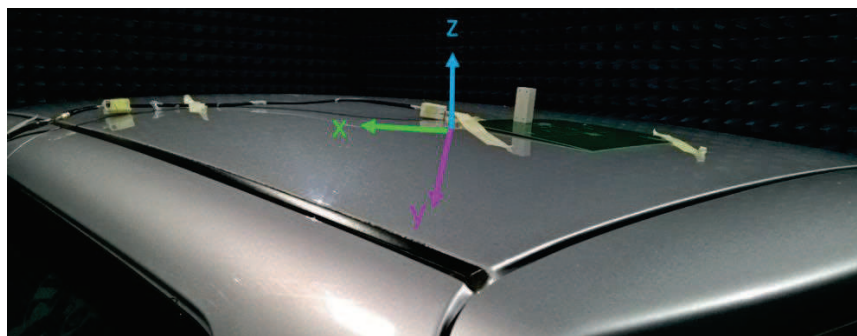


Figure 64: Photo of rooftop located DRA.

II.4.1.1. 3D and 2D radiation patterns

3D radiation patterns on the upper hemisphere of the anechoic chamber are presented in Figure 65. They are rotated to align them with the vehicle direction as presented in Figure 63. The front of the car is directed to the upside and the rear of the car is directed to the downside. Comparing with the antenna placed on the 200mm×200mm ground plane, radiation patterns are disturbed due to the large ground plane represented by the vehicle

rooftop. Moreover, Figure 65 shows clearly that the proposed DRA has more directional radiation patterns compared with the previous case. This is an important feature for the beam steering system since the radiation patterns could be better reconfigured when antennas are placed on the vehicle rooftop. This will be presented in the following chapters.

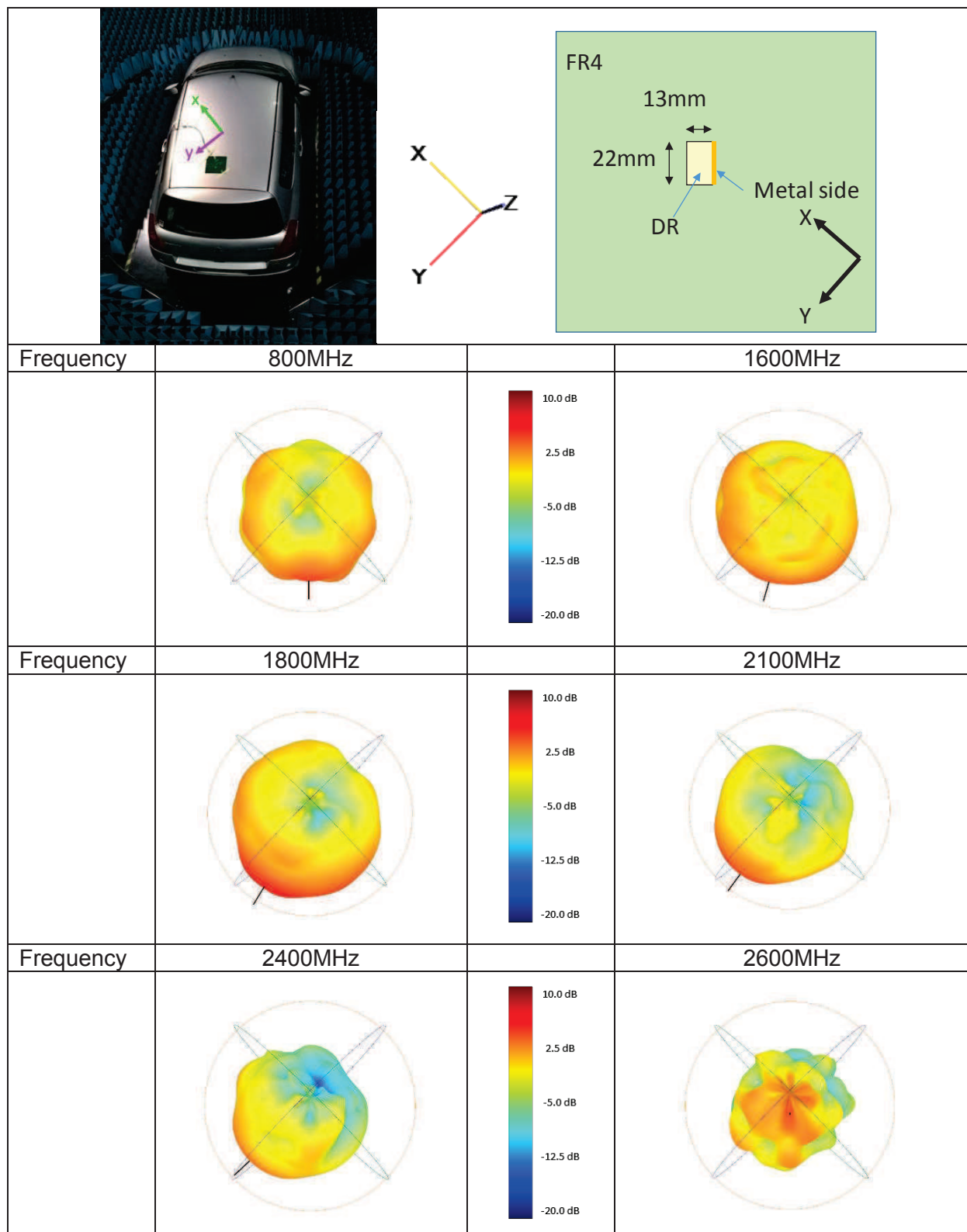


Figure 65: Measured 3D radiation patterns at different frequencies on vehicle rooftop.

Figure 67: Comparison of measured maximum realized gain for the DRA.

This higher value for the realized gain is due to better antenna matching at this frequency. In the plot in Figure 68, the $|S_{11}|$ chart for a larger ground plane of 500mm×500mm is compared with the 200mm×200mm ground plane case.

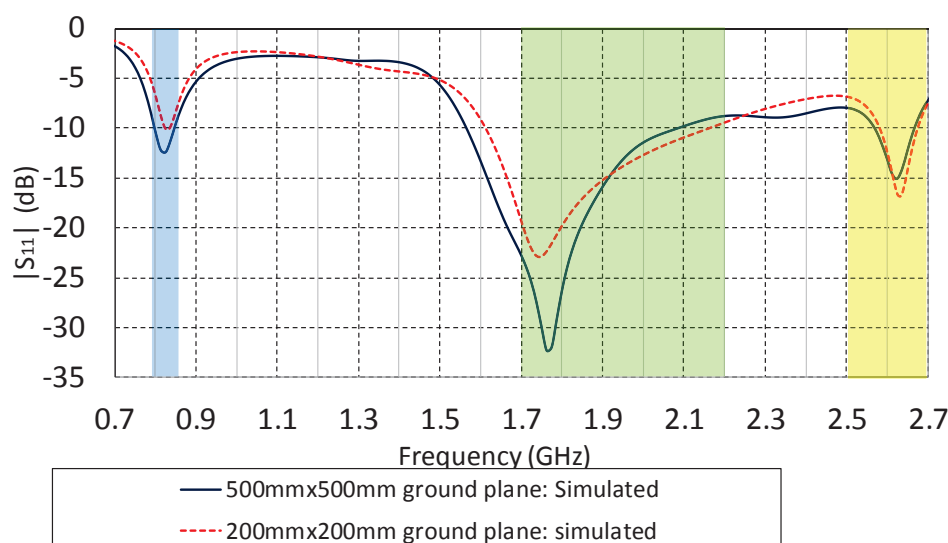


Figure 68: simulated $|S_{11}|$ parameters of different ground plane size.

This figure shows that the matching is better for the large ground plane since it increases the global dimensions of the radiating element.

II.4.2. Measured results of dashboard and below vehicle rooftop DRA

There are possibilities for placing the antenna in other positions of the vehicle. Since the in vehicle antenna environments are very complex, i.e. with metal parts, the location of the antenna may be located on the dashboard or below the centre of the rooftop. Figure 69 and Figure 70 show the DRA positions and test board setups in the vehicle.

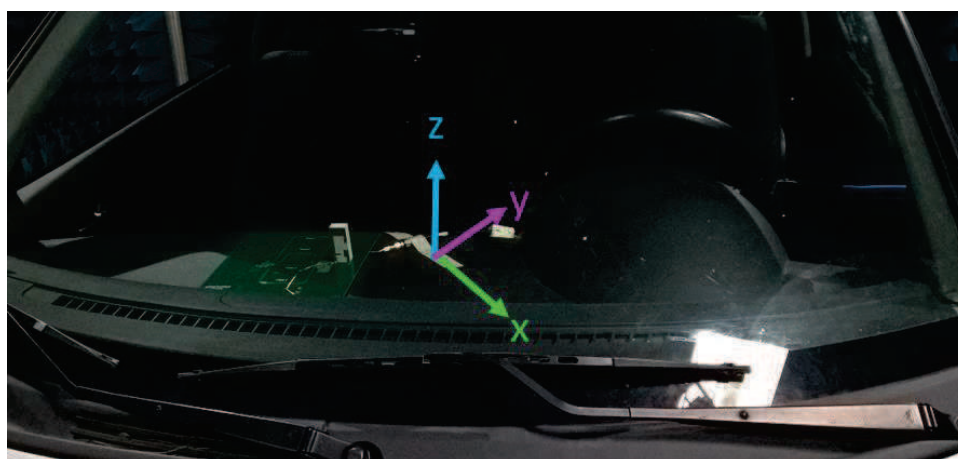


Figure 69: Photo of dashboard located DRA.



Figure 70: Photo of DRA located below the vehicle rooftop.

II.4.2.1. 3D radiation patterns

From II.3.2.2, the 3D radiation pattern of pure DRA is radiated towards the monopole strip and opposite side. For the dashboard location, the metal strip side of the DRA is placed toward the front of the vehicle (Figure 69). Figure 71 shows the measured antenna results.

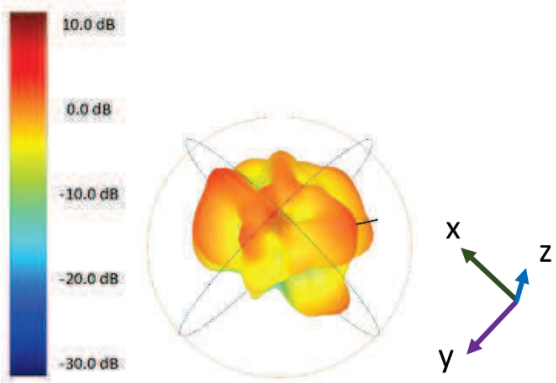
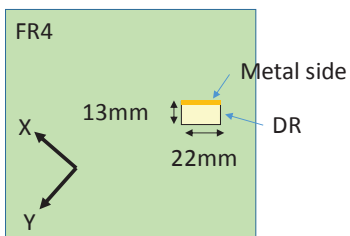
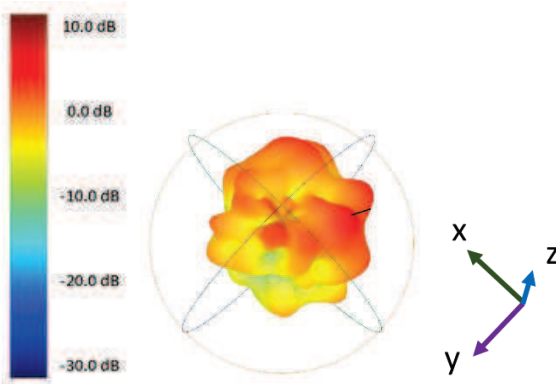
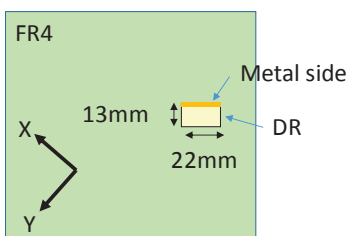
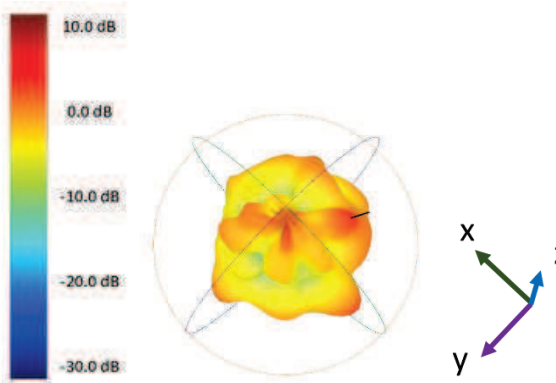
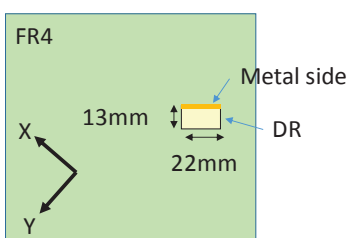
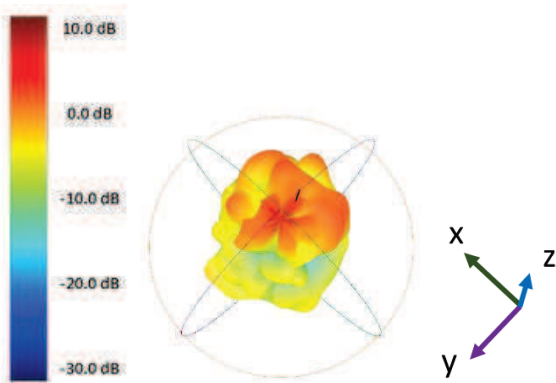
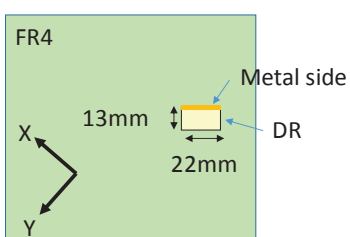
1		<p>Freq: 800MHz Peak Gain: 2.99dBi</p> 
3		<p>Freq: 1800MHz Peak Gain: 5.99dBi</p> 
4		<p>Freq: 2100MHz Peak Gain: 4.42dBi</p> 
5		<p>Freq: 2600MHz Peak Gain: 3.47dBi</p> 

Figure 71: Measured 3D radiation patterns at different frequencies on the dashboard

Observing the radiation pattern in Figure 71, most of the radiated energy is towards the front of the vehicle while the gain is lower toward the rear of the vehicle. The antenna performs as

expected: strong radiated energy toward the outside of the vehicle with less energy toward the driver.

Normally, vehicle antennas are placed on the vehicle rooftop or dashboard. But, some Multi-Purpose Vehicles (MPV) or Sport Utility Vehicles (SUV) have room for the antenna to be placed below the roof. This extra space is a reason to place the antenna in this location even though the antenna efficiency and gain is not as good as the previous cases.

The vehicle rooftop has a curve and bending at the edge. Since the DRA height is 50mm, the rooftop could be considered as an obstruction to the antenna radiation. (Figure 72)

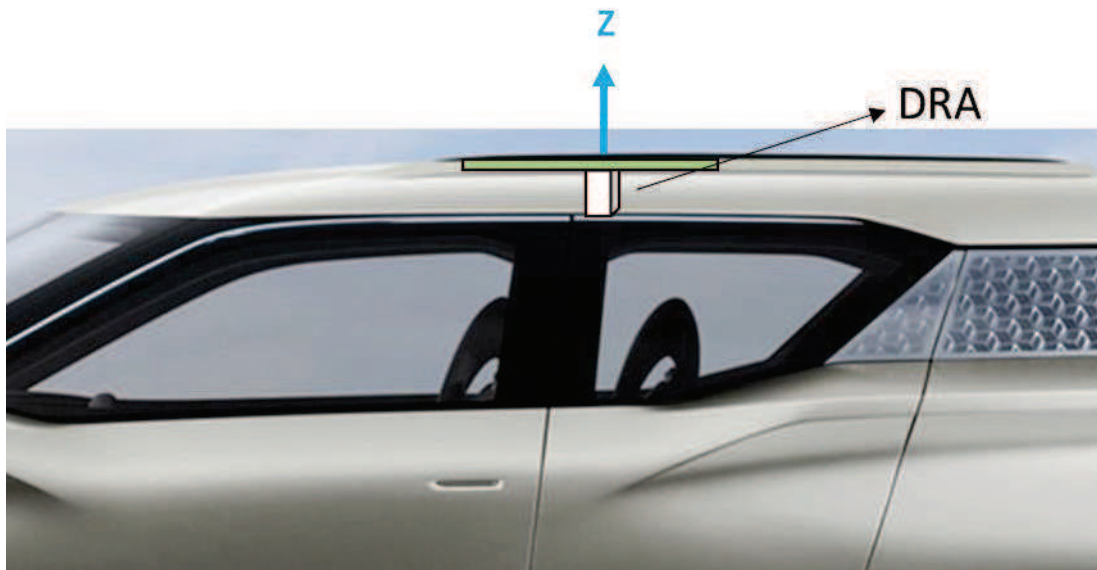


Figure 72: Photo of the related DRA location below the vehicle rooftop.

Figure 73 clearly shows that the automotive metal environment alters the antenna radiation pattern.

Indeed, the 3D radiation patterns show that at 800MHz, the antenna has good performance with a peak realized gain of 4.2dBi but this decreases when frequencies increase. Indeed, it is well known that the penetration inside buildings, vehicles, and so on is even more difficult to achieve for higher frequencies.

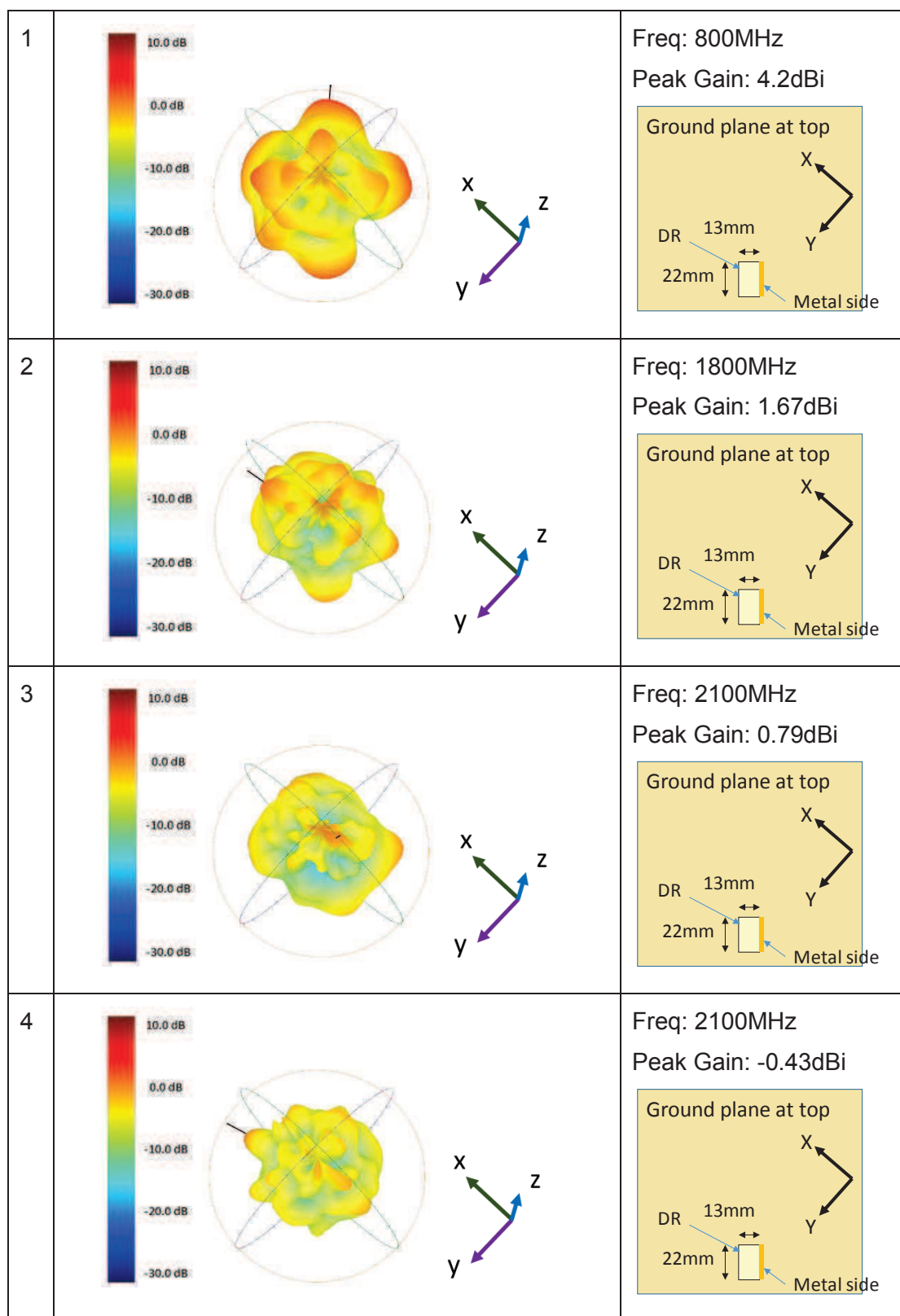


Figure 73: Measured 3D radiation patterns at different frequencies for the DRA under the vehicle rooftop.

II.4.2.2. Maximum realized gain

We can compare the three positions for the DRA located on or within the vehicle. The $|S_{11}|$ parameter is not really disturbed by the environment while radiation patterns are clearly affected by implementation in the real environment. In particular, when the working frequency is increasing the maximum realized gain dropped to 2dB for the case of the antenna integrated under the rooftop. When the DRA is put on the dashboard, the maximum realized gain is almost the same as on the rooftop. This indicates that the dashboard could be another good position to locate this antenna system. (Figure 74).

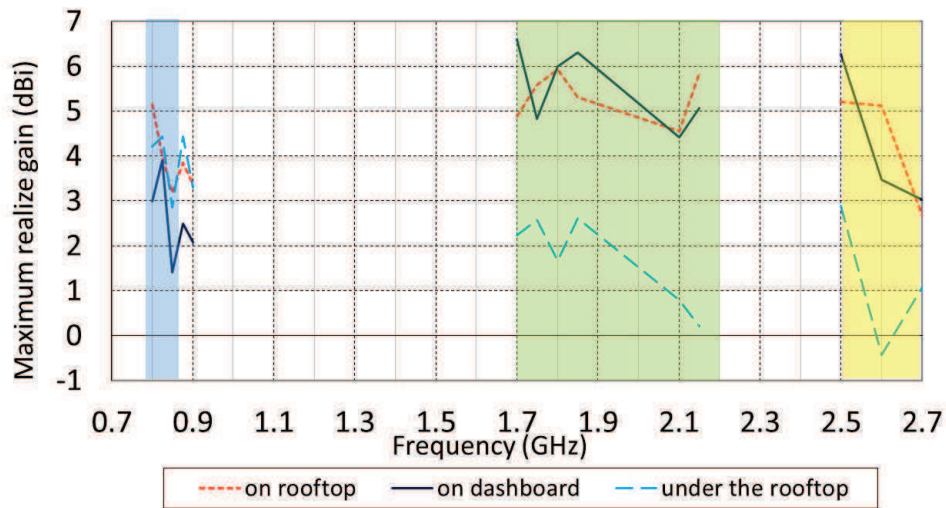


Figure 74: Maximum realized gain comparing different locations

II.5. Conclusion

A compact and multiband DRA has been designed for automotive application. The proposed antenna exhibits the advantages of using a dielectric resonator as an antenna by covering LTE 800DD, LTE 1800+, LTE 2100 and LTE 2600. The DRA design satisfies the -6dB impedance bandwidth for four distinct frequency bands. The antenna achieved 50% efficiency in LTE 800DD band and 75% in higher frequency bands while being miniature given its global dimensions of $\lambda_0/8 \times \lambda_0/17 \times \lambda_0/29$ at 790MHz.

In this chapter, we showed the development progress of a multiband antenna by using dielectric material which plays the most important role for our antenna system. Indeed, the antenna used the distinguishing feature of the dielectric material with high dielectric permittivity and low loss to achieve high efficiency and good performance. The design methodology focused on achieving a low profile, compact and easily fabricated antenna. In fact, the thickness of the dielectric material is selected from a normal commercial product and the antenna is rectangular for mass production. Combining all these requirements, the antenna design uses metal strips to decrease resonance frequencies inside the dielectric resonator while creating hybrid modes for the higher frequencies.

The study of the multiband DRA has been done with successful modeling in simulation and building of a prototype. All the measurements are well matched to the simulations.

Since in a full system, the antenna will be used at different locations in the vehicle, we also studied the DRA in other vehicle environments in section II.4 and showed the measured results. The next step will be integration of a phase shifter for the active steering system.

Chapter III. Global System Tunable Phase shifter design

III.1. Introduction

Phase shifters play an important role in many microwave systems, such as smart antennas, microwave instruments, modulators and radar. In research, the phase shifter is a key component in completing the active steering antenna system. The requirement of the phase shifter in this thesis is to be able to apply 360° phase shifting. Also, it needs to have minimum insertion losses and must be able to support a broad frequency band (800MHz to 2700MHz). Many choices of phase shifters exist in the market. However, we also need to consider in our choice the controlling methods and the manufacturing cost. In the first part of this chapter, we will analyze existing market phase shifters in order to choose the best direction for the suitable phase shifter in the study. Various papers have already been published on the theme of phase shifter designs for antenna application. The differential phase shifter is the most commonly used because of its ease of realization and development. We would like to take advantage of different types of differential phase shifter to achieve the needed 360° phase shift.

In the second part of the chapter, the basic theory for the differential phase shifters is introduced and their main properties are described. We would also like to design a phase shifter with a tunable ability. We will simulate and evaluate variation of the capacitance and resistance which will affect the performance of the bandpass phase shifter models.

First, and based on these results, the type of the tunable phase shifter is defined.

After checking the characteristics of the first phase shifter prototype, we start to optimize its layout. It is targeted to have 0° , 90° , 180° and 270° phase shifting at 800MHz. For the phase adjustment, $\pm 10^\circ$ at 800MHz is the expectation. The behavior of the proposed phase shifter, which is electronically controlled, is demonstrated. The detailed analysis of the influence of each component's value on the phase shifter is shown and discussed.

Secondly, another phase shifter prototype with manual control is presented and discussed in the final section. The goal is to remove the circuit effect.

III.2. Development of the phase shifter for the thesis

III.2.1. 360° phase shifters on the market

In Chapter One Section IV.3, we saw that the active steering system requires a phase shifter with 90° per step to complete the 360° phase shifting. A lot of commercial off-the-shelf products exist. For our application, we focused on 360° phase shifters, which operate from 800MHz to 2700MHz to fit our antenna design requirements. The main products are shown below:

- **MMIC phase shifter**

It is common to use a GaAs PHEMT process to provide a 6-bit digital phase shifter. It has low RMS phase error, around 3 degrees. It has low insertion loss variation of ± 1 dB across all phase states (Figure 75) and can be easily voltage controlled (0/-5V or 5/0V) [47]. Its dimension is smaller compared to other types of phase shifters. The MMIC phase shifter can be part of a QFN package for an SMT process [48] (Figure 76). This type of phase shifter provides us a phase step of 6° using an electronic control.

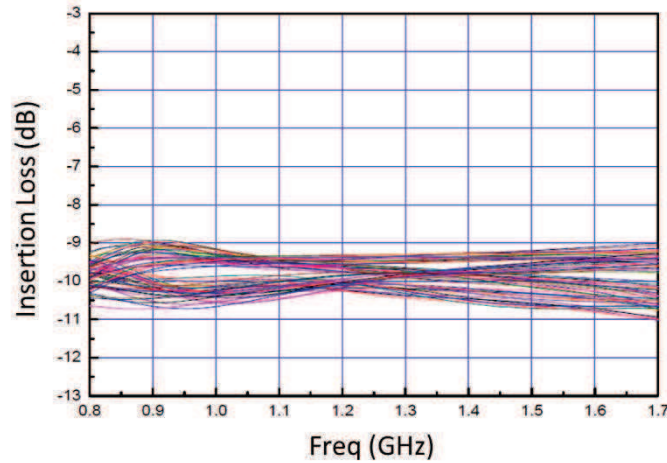


Figure 75: MMIC phase shifter: Insertion loss

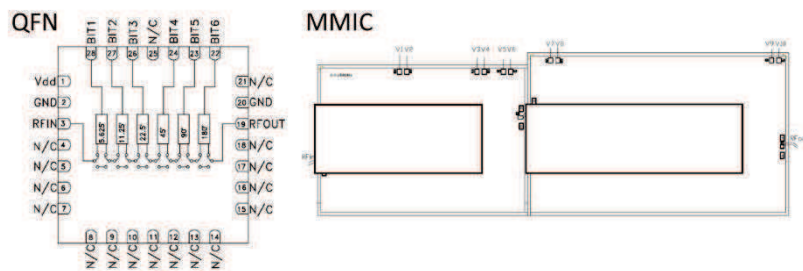


Figure 76: Phase shifter pin definition for QFN package and MMIC die

However, this kind of phase shifter has many disadvantages. The wider the working frequency bandwidth is, the worse the return loss. The return loss is close to 9dB if the phase shifter operates from 0.8 to 1.7GHz; the return loss is close to 12dB if the phase shifter operates from 0.8-2.4GHz. We need to combine at least two ICs to cover all bands. We also need to use switches to integrate the components. The overall loss of the device will then be increased, and as such will not be suitable in our application.

● Surface mount phase shifter module

Another type of phase shifter uses voltage control and is packaged as a PCB module. In the market, we can find voltage variable phase shifters providing precise 180° or 360° phase control. This type of phase shifter performs well with low insertion loss of 2.8 dB and VSWR of 1.2:1. Housed in a shield, the module offers a space efficient and low-cost alternative. Although it is bigger than an MMIC, it is still small enough for most applications. (Figure 77)

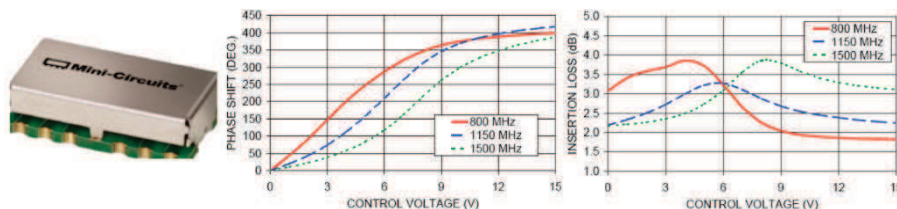


Figure 77: Photo of surface mount phase shifter and its RF characteristics

It needs a control voltage with a range from 0 to +15V or above. Based on the requirement for 360° phase control, [49] is the only broad band surface mount phase shifter found, but it only works from 800MHz to 1500MHz. This is still not enough for our application. The high voltage supply requirement will also make the system development more complex.

● SMA phase shifter

The use of an SMA phase shifter means the use of an SMA connector to connect the RF signal in the product interface (Figure 78). Using an SMA connector is easier for experiments. We can find three types of device:

- The first kind is voltage controlled which is similar to the surface mount phase shifter. The control voltage range is around 0-20V. The advantage is an accurate phase shift control over 360°. On the other hand, the workable frequency range is only 200MHz for each product [50]. In order to be used for broadband applications, it is necessary to combine at least 4~5 devices.

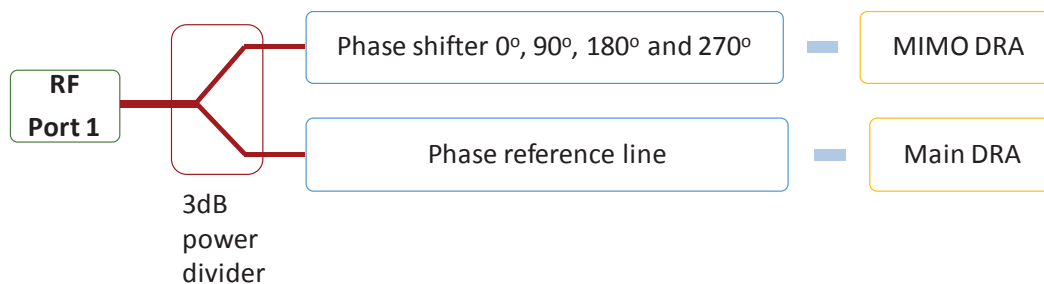


Figure 78: Photo of surface mount phase shifter and its RF characteristics

- The second kind is a passive phase shifter which does not need any power for the control. It has low insertion loss (around 1dB) and can be used for broadband coverage (from DC to 18GHz). However, it is difficult to find a 360° phase shift product. [51]
- The third kind (Figure 78) is the motor controlled phase shifter. It can provide 360° phase shift. By providing 28V DC to the motor drive control box and using a D-sub connector to give the command to the unit, the phase shifter can offer a 360° / GHz phase shift. The insertion loss is only 0.5dB which is very good compared to other types. The main disadvantages are that this device needs a high voltage supply and it is bulky (60cm in length) [52]. All the SMA phase shifters are expensive. Their cost is in thousands of dollars. It is also difficult to put them on the vehicle rooftop.

III.2.2. The specifications of the phase shifter in this thesis

As was explained in Chapter One (Section I.5), we need a phase shifter with a 360° phase excursion. This is our target. It will be integrated with the MIMO system in order to achieve the beam steering. To simplify the beam steering structure, we will use a power divider to provide the signal to both Main and MIMO DRA with the different phases (Figure 79a).



(a)

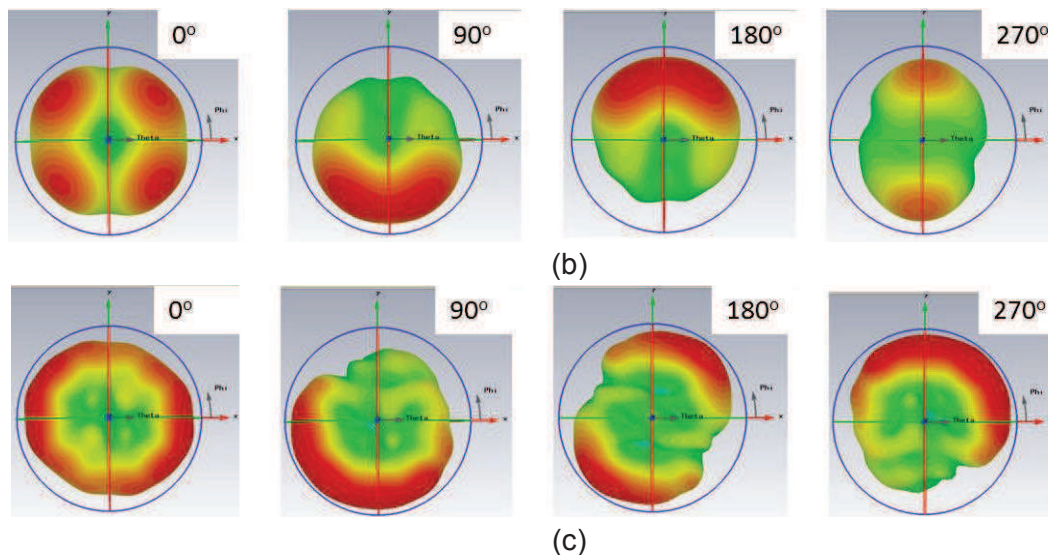


Figure 79: (a) Beam steering architecture; Radiation pattern in different phases (b) 800MHz and (c) 1800MHz

Figure 79 (b) and (c) show that the radiation pattern can be steered in different directions by providing the RF signal with different phases to the antennas. The minimum target is to obtain 0° , 90° , 180° and 270° phase shift. This chapter will start with the study of the phase shifter. The design will also consider the difficulty of the controlled method and the possibility of commercialization. The 360° phase shifters on the market mostly require around 15Volt for electrical control. We want to use a lower voltage power supply. We will detail the study and then analyze the phase shifter performances during the development.

III.2.3. Phase shifter model and concept for thesis

After surveying these commercial phase shifters, it appears that there is no suitable solution on the market for our application. Therefore, designing the proper phase shifter is an important target and the design must have the benefits of being cheap, easy to control, small and have low insertion loss.

● Differential phase shifter

Of the electronically controlled phase shifters, the differential phase shifter is the most commonly used design for antenna systems. It includes a phase adjusting line and a reference line (Figure 80) with four-port network which makes it suitable for our two paths Main/MIMO antenna system.

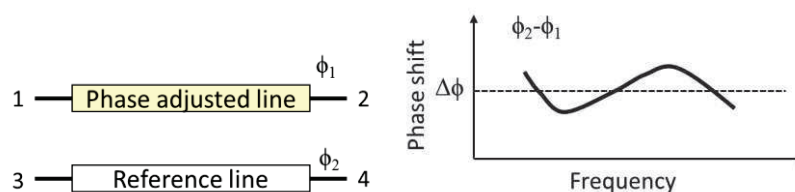
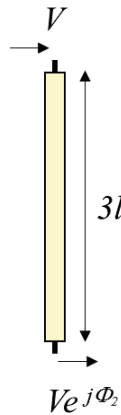


Figure 80: Topology of differential phase shifter

The SCHIFFMAN paper first introduced the differential phase shifter using the parallel-coupling line design in 1958 [53]. It demonstrated several differential phase shifters which could exhibit 90° phase shift from 300MHz to 1500MHz. Here we simply introduce this kind of phase shifter which uses two kinds of lines:

- ✓ A “uniform” strip line



- ✓ A special coupling line

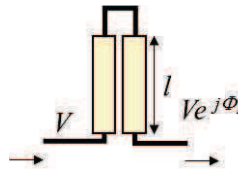


Figure 81 presents the phase response curves for the example of a 90° phase shifter. [53] indicates that using two lines, a strip line and a special coupling line, it is possible to increase the frequency bandwidth.

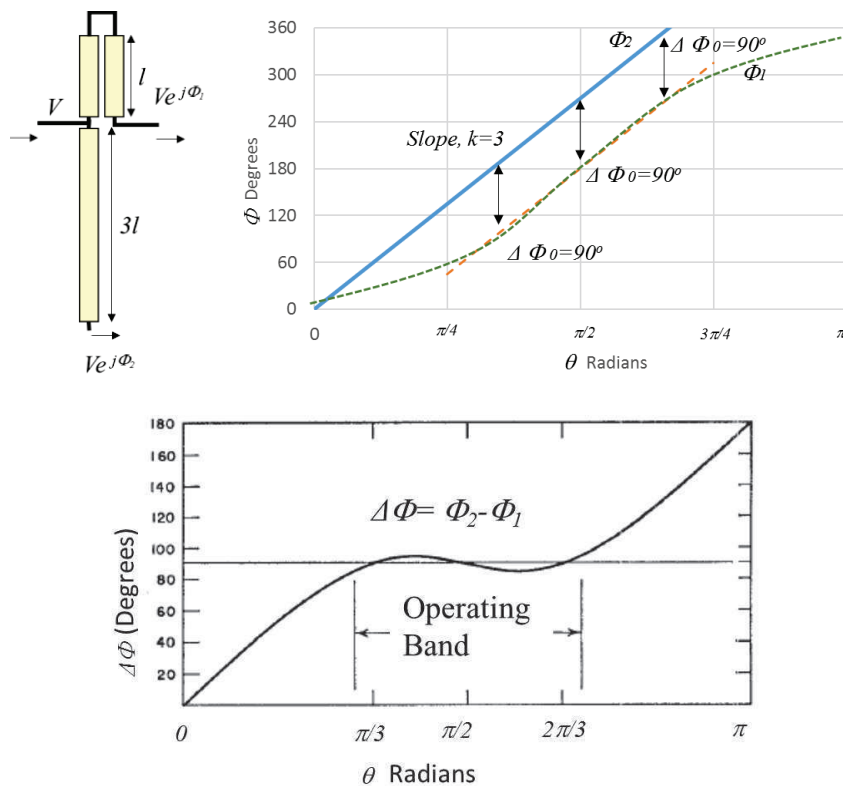


Figure 81: The phase response for an example of a Schiffman phase shifter and differential phase response curve

Unfortunately, the length of a standard Schiffman phase shifter working at 800MHz is close to half a meter which is not acceptable for our application. Many studies were published subsequently to improve this kind of device. In 1971, diodes were integrated to switch different load lines or different traces of the bandpass network to achieve a broad band phase shifter [54]. It opened a new research area for phase shifters and increased the possibility of reducing their size and cost. Also, a digital control method for such a device could also be interesting.

● Bridged T-type high pass filter phase shifter

There are a few kinds of high-low bandpass networks that could achieve 90° phase shifting. It is for example easy to implement metal strip lines on FR4 substrate and have discrete components mounted over it. [55, 56].

[56] applied a new proposed bridged T-type bandpass network with only one stage. A 90° phase shifter is achieved. Figure 82 is the schematic of a one stage 90° phase shifter.

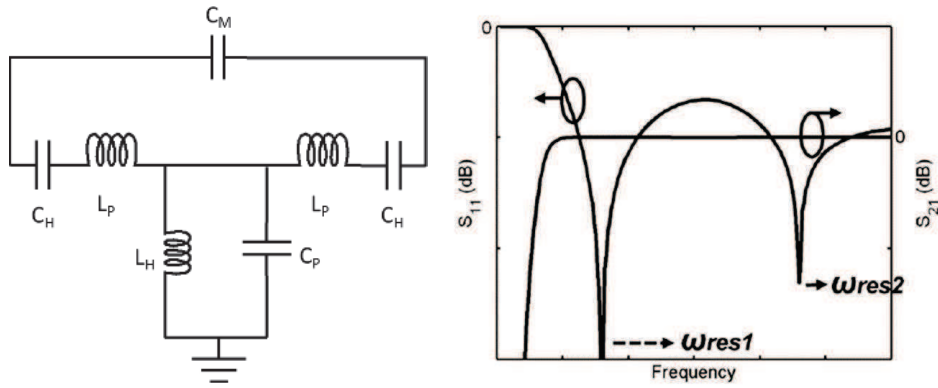


Figure 82: Bridge T-type bandpass network and its magnitude response [56].

Here ω is the frequency and Z_0 is the impedance of the system. Based on [56], by using this type of filter it is possible to obtain two resonant frequencies (Figure 82) as follows:

$$\omega_{res1} = \sqrt{\omega_P \omega_H} \quad (10)$$

$$\omega_{res2} = \frac{\omega_{res1}}{\sqrt{1-4k}} \quad (11)$$

which are defined by:

$$k = \frac{C_M}{C_P}, \quad \omega_H = \frac{\sqrt{2}}{\sqrt{L_H C_H}} = \frac{2}{C_H Z_0}, \quad \omega_P = \frac{1}{\sqrt{2 L_P C_P}} = \frac{1}{C_P Z_0}$$

For the differential phase shifter, the local minimum phase shift should be satisfied by:

$$\varphi_{ad}(\omega_{min}) - \varphi_{ref}(\omega_{min}) = \Delta\varphi_{min} \quad (12)$$

$$\left. \frac{d(\varphi_{ad}(\omega))}{d\omega} \right|_{\omega_{min}} = \left. \frac{d(\varphi_{ref}(\omega))}{d\omega} \right|_{\omega_{min}} \quad (13)$$

where φ is the phase degrees of the line, $\Delta\varphi$ is the phase shift, *ad* denotes “phase adjusted line,” and *ref* denotes “reference line.” Since the reference line is the microstrip, we could define the physical length of the microstrip as l and V_g as the phase velocity:

$$\varphi_{ref}(\omega) = -\frac{l}{V_g} \quad (14)$$

Using (14) into (12) and (13) to obtain Equation (15):

$$\varphi_{ad}(\omega_{min}) - \left. \frac{d\varphi_{ad}}{d\omega} \right|_{\omega_{min}} \omega_{min} = \Delta\varphi_{min} \quad (15)$$

($\sqrt{2L_H/C_H}=Z_0$), and having placed these conditions into Equation (15), this results in:

(16)

$(\omega_2 - \omega_1)$ becomes narrower.

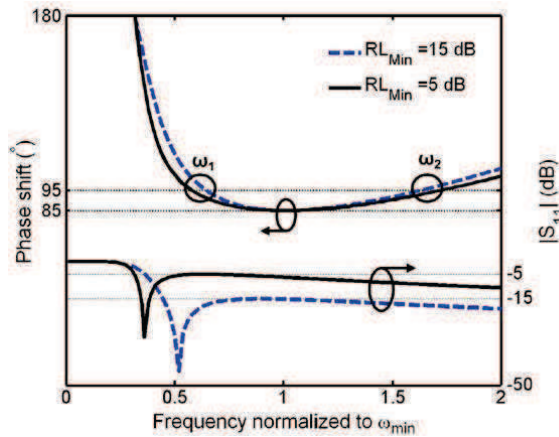


Figure 83: The plot for different return losses to the phase shifter bandwidth [56]

increased by changing the C_M value and the local maximum phase shift should satisfy:

(17)

shows the result of different k values in the design a 90° phase shifter with error +/- 5°.

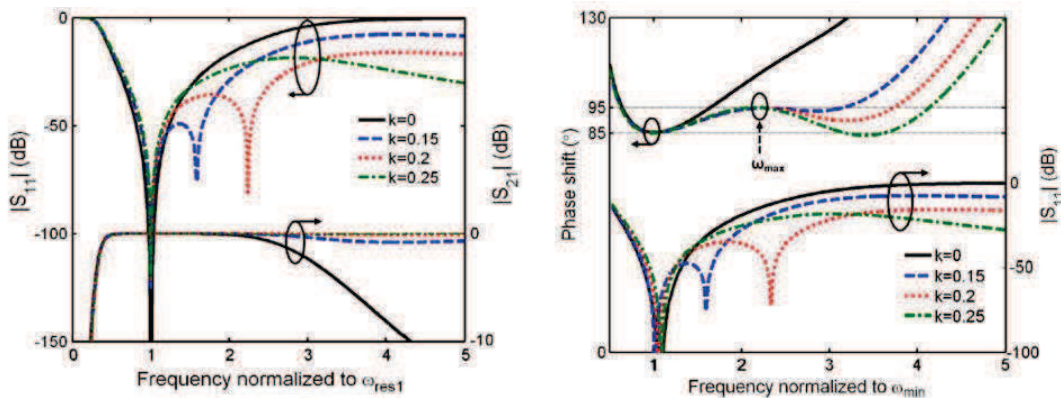


Figure 84: $|S_{11}|$, $|S_{21}|$ and phase shift of bridge T-type bandpass network for different k [56]

After understanding the relationship of the filter components with phase shifters, we prepared the 90° phase shifter step by step:

1. We already know the target phase shift is 90°. A phase error of 10° and minimum frequency of 700MHz is allowed.
2. We started with the value of k from 0.25 as recommended by the paper.
3. We obtained ω_{res1} and ω_P from Equation (15) and (17) with known k , ω_{min} , phase shift 90° and phase error 5°. L_H , C_H , L_P and C_M can be calculated with known k , ω_{res1} , and ω_P .
4. The electric length of the reference line can be obtained with Equation (16).
5. Varying the k value to balance the return loss and bandwidth of the phase shifter.

Following the above steps, we obtained the values presented in Table 3. Simulations with suitable discrete component values were done using CST Design Studio. Results are presented in Figure 85.

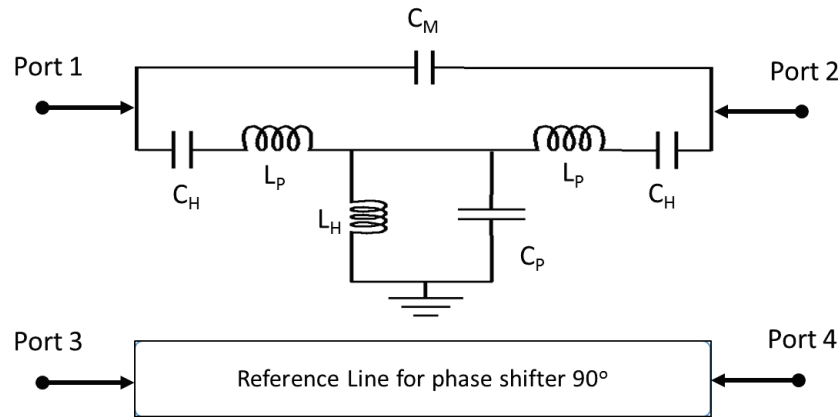


Figure 85: Initial simulation model for 90° phase shifter

Table 3: [Initial optimized values for bridged T-type bandpass filter 90° phase shifter]

Phase shift	L_P	L_H	C_M	C_H	C_P
90	1.6nH	12nH	0.5pF	7.2pF	1.8pF

The bridged T-type bandpass filter model for 90° phase shifting is simulated. Figure 86 shows an $|S_{11}|$ under -15dB and insertion loss lower than 1dB which is acceptable for us.

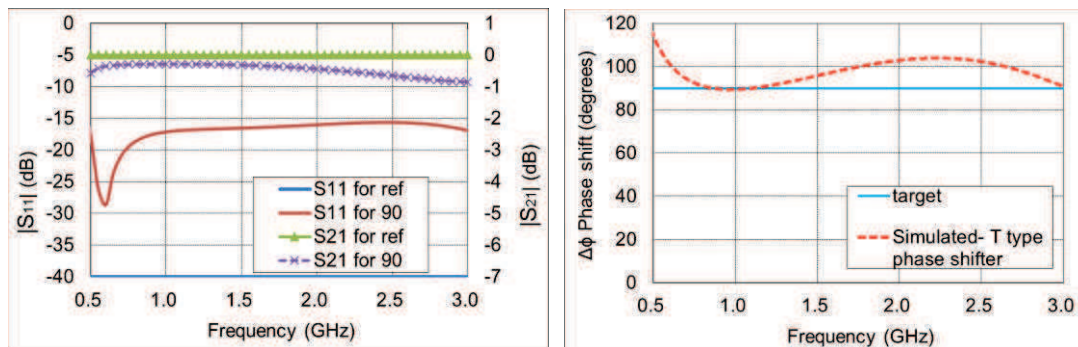


Figure 86: Design characteristic of 90° phase shifter for 90° with phase error 10°

We also realized that by using the value from Table 3 we could obtain phase shift close to our target with an error within $\pm 10^\circ$ (Figure 86). Therefore, the type of phase shifter is determined to be a bridge T-type bandpass filter phase shifter. The design for 180° and 270° phase shifters can be continued.

III.2.4. Design for tunable phase shifter

The phase shifter in the previous section can be integrated in the antenna system. It is also interesting to design a tunable device in order to have variable and accurate shifting of the radiation lobe. This work is the subject of the following paragraphs.

III.2.4.1. One stage bandpass phase shifter

To make the tunable phase shifter, we replaced all the capacitors with variable capacitors in the T-type bandpass phase shifter. The phase shifter characteristics may be altered by variable capacitors. The modified T-type bandpass circuit model is presented in Figure 87. We used the ideal capacitor model in the CST Design Studio. The tunable capacitor ranges in the simulation are: C_H - from 4.3pF to 7.2pF; C_M - from 0.3pF to 0.5pF; C_P - from 0.3pF to 3pF. The capacitor model in the simulation used ideal capacitor with 3 Ohms resistance which is the value shown in the datasheet of the market product [58].

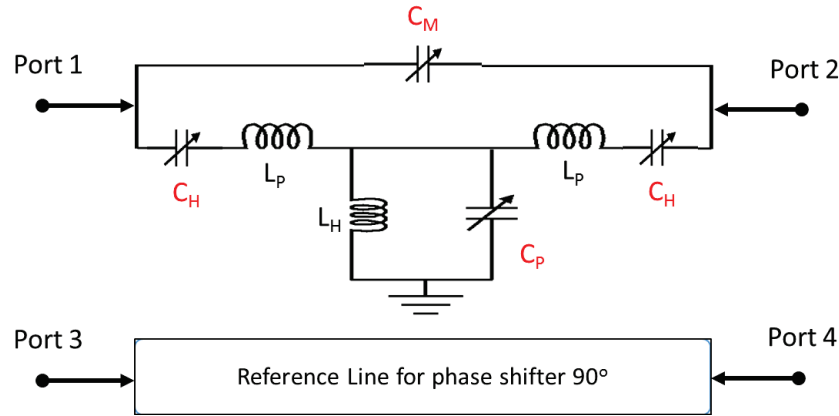


Figure 87: Initial model of the tunable 90° phase shifter

The labels in the following graphs, “Lowest capacitance”, mean C_H : 4.3pF, C_M : 0.3pF, C_P : 0.3pF; “Highest capacitance” means C_H : 7.2pF, C_M : 0.5pF, C_P : 3pF.

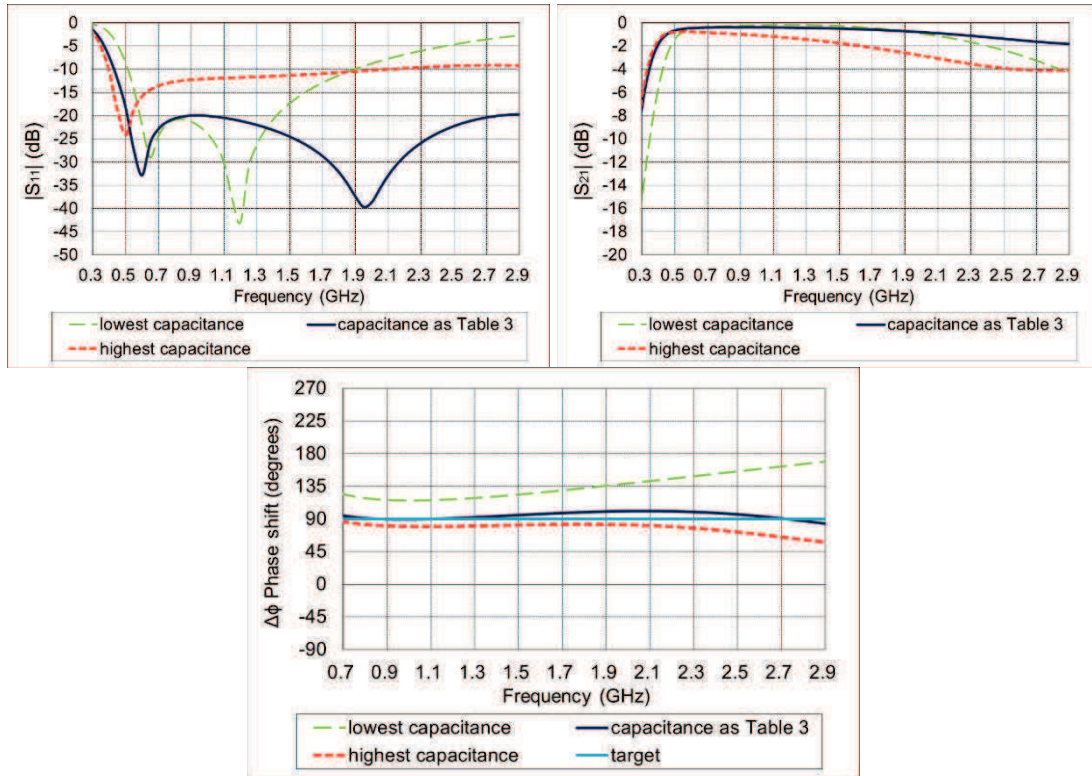


Figure 88: Characteristics of the initial tunable 90° phase shifter

Figure 88 shows that the phase shifter tunable range can reach approximately 38° at 800MHz, 47° at 1800MHz and 97° at 2600MHz. However, the $|S_{11}|$ and $|S_{21}|$ are also affected by the change in capacitance. It means we need to choose the balance between these factors.

III.2.4.2. Two and Three stage bandpass phase shifter

From the previous section, a variable capacitor could offer the phase shifter a tunable phase. To see if the phase tuning range can be increased, we integrated two stage and three stage bandpass circuitries (Figure 89). The simulated results for these phase shifters are shown in Figure 90 and Figure 91.

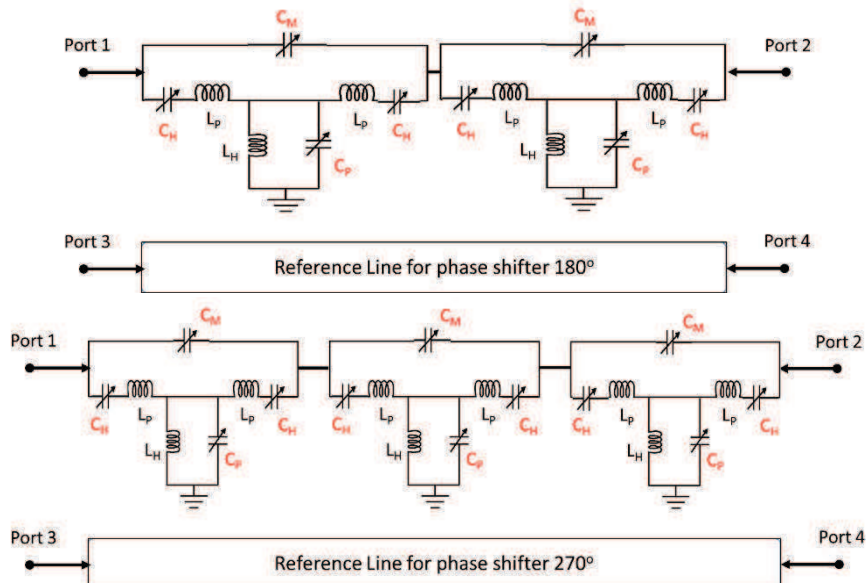


Figure 89: Two stage and three stage tunable phase shifters

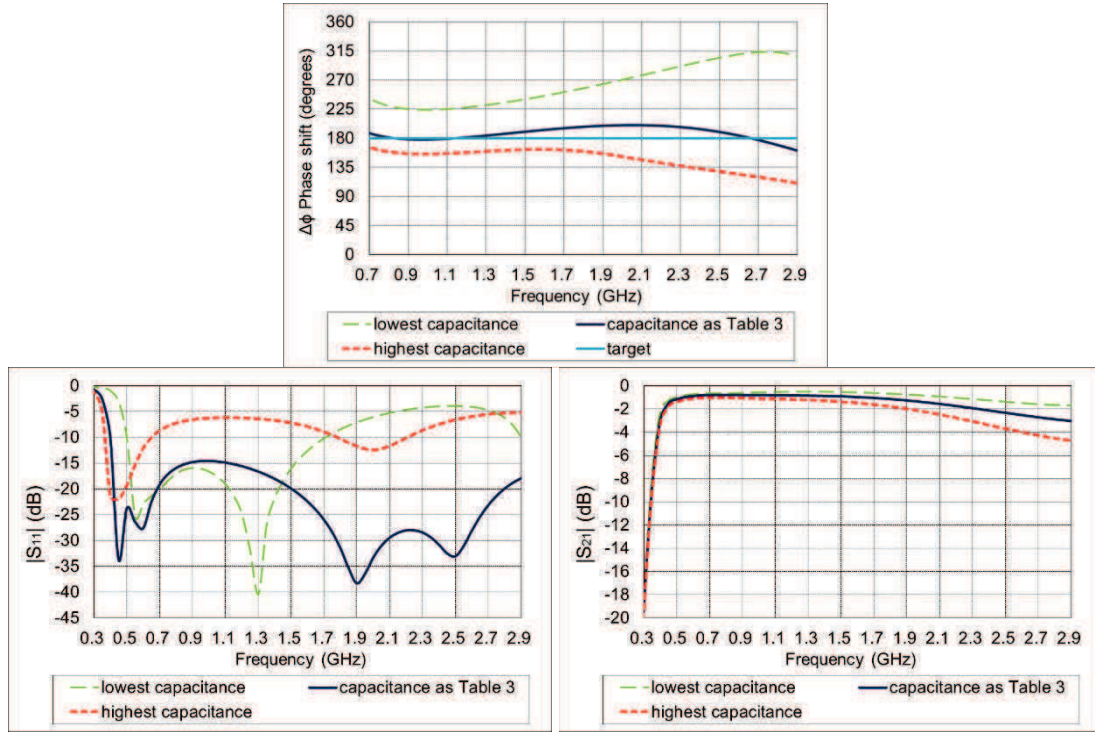


Figure 90: Characteristics of the two stage 180° tunable phase shifter

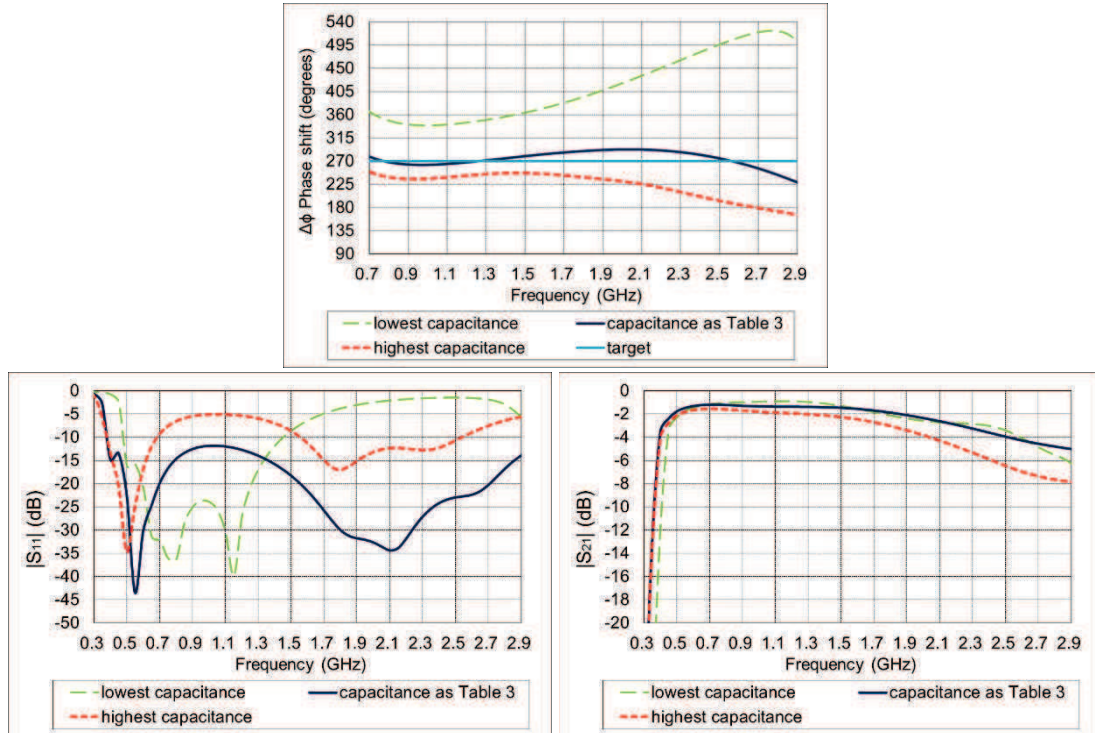


Figure 91: Characteristics of three stage 270° tunable phase shifter

If we compare Figure 88, Figure 90 and Figure 91, it appears that the phase shifts are almost double (62° at 800MHz) for the two stage bandpass phase shifter and triple (110° at 800MHz) for the three stage bandpass phase shifter. However, the $|S_{11}|$ became greater than -15dB at 800MHz and insertion loss worse than -3dB when the frequency is higher than 2GHz in the

three stage device. We considered that using the three stage tunable phase shifter is not a good option even if the phase tuning range is increased.

III.2.4.3. Effect of the capacitor resistivity

Some differences appear in the simulation of the one stage bandpass phase shifter if we use the ideal capacitor model with a resistance 3 Ohms or the SMD components. $|S_{11}|$ and $|S_{21}|$ are quite different (Figure 92).

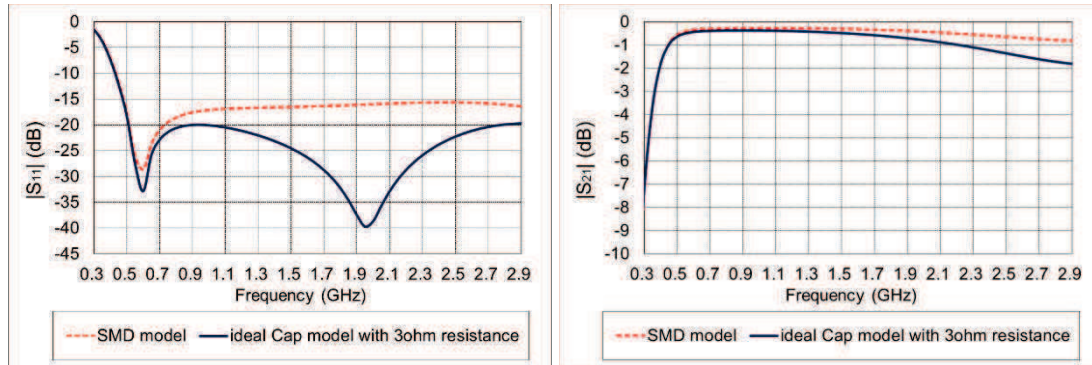


Figure 92: Comparison of the different capacitor models in simulation

Since the model in simulation uses 3 Ohms resistance for the capacitor, we tried to study the resistor effect. In the variable capacitor datasheets [58, 59, 60], the series given resistance of the variable capacitor varies from 1.4 Ohms to 5.6 Ohms.

Here we only considered the one and two stage bandpass tunable phase shifter. From the simulation, the phase is not changed during the altered resistance.

Figure 93 indicates that $|S_{11}|$ is almost the same and $|S_{21}|$ is within 0.4dB for frequencies lower than 1.3GHz even if the resistance is increased by 6 Ohms.

We can see, particularly in the two stage design, that $|S_{21}|$ can decrease more than 1dB when the resistance increases (Figure 94). However, even if the phase shift tuning range can be increased by using a two stage tunable phase shifter, the benefit for our application is insufficient due to the introduced insertion loss. Later, only the one stage bandpass phase shifter will be kept using variable capacitors with 3 Ohms resistance [60]. The other stages will use SMD to keep the insertion loss to a minimum.

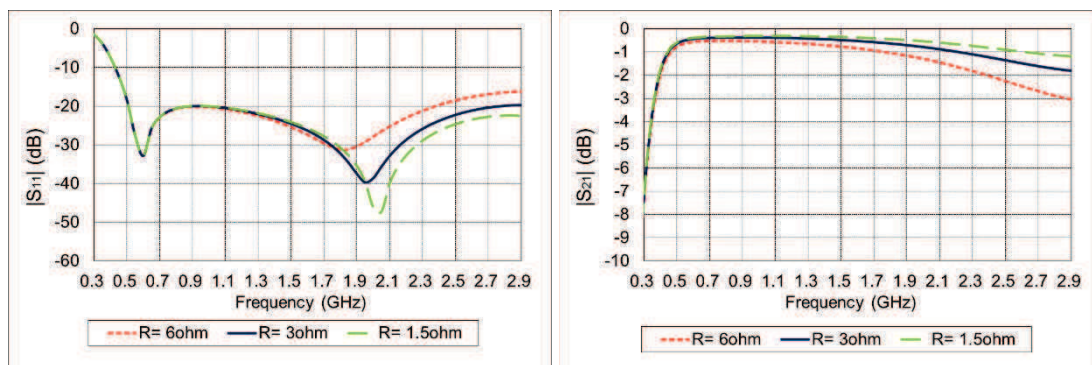


Figure 93: The resistor effect on $|S_{11}|$ and $|S_{21}|$ for 90° phase shifter

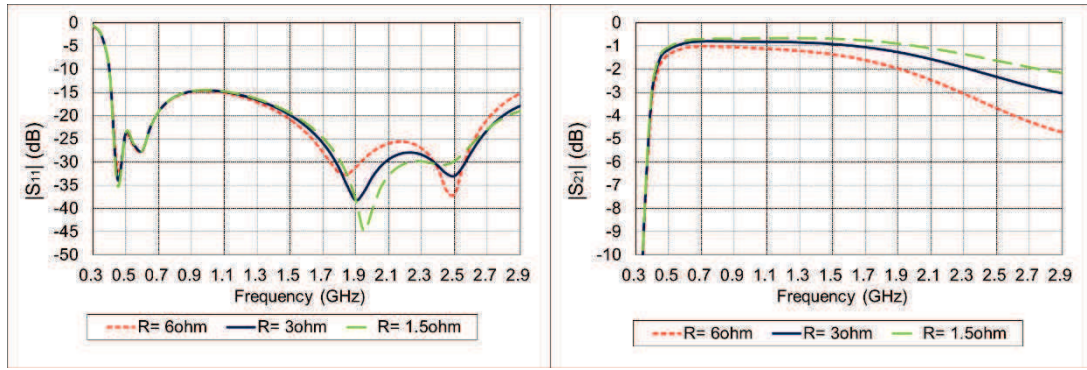


Figure 94: The resistor effect on $|S_{11}|$ and $|S_{21}|$ for 180° phase shifter

III.2.4.4. Initial phase shifter concept

The general scheme of the proposed phase shifter is presented in Figure 95. It has been simulated with CST microwave studio.

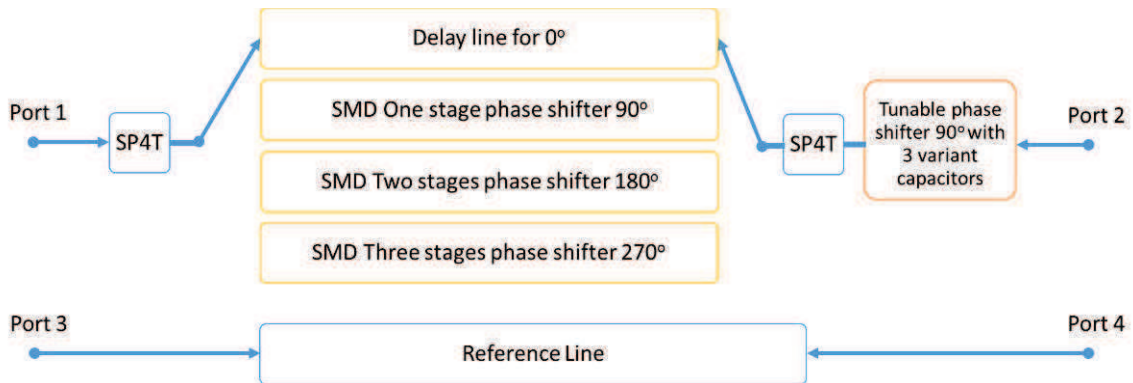
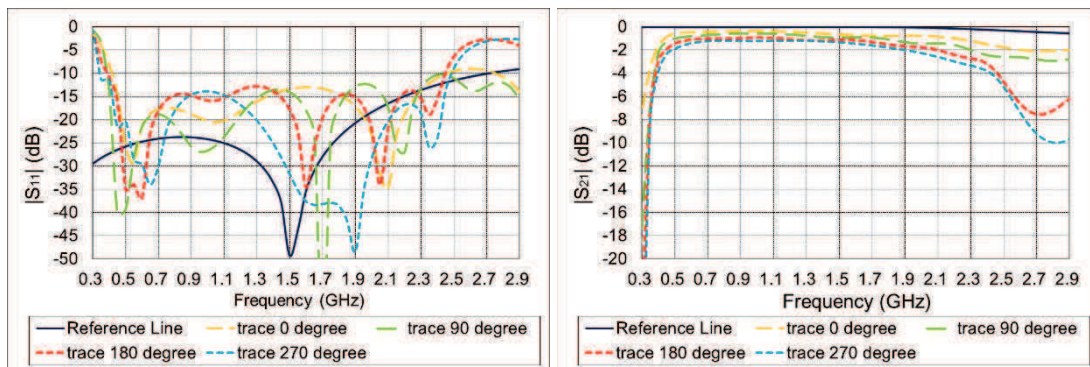


Figure 95: Initial diagram for the phase shifter

To combine four paths of the bandpass phase shifter circuits, we implement two SP4T switches. We simulated the whole differential phase shifter with ideal SP4T model without losses in CST. For the simulation of different lines, we used the microstrip line model. An FR4 substrate with dielectric constant of 4.1 is used. The results are presented in Figure 96.



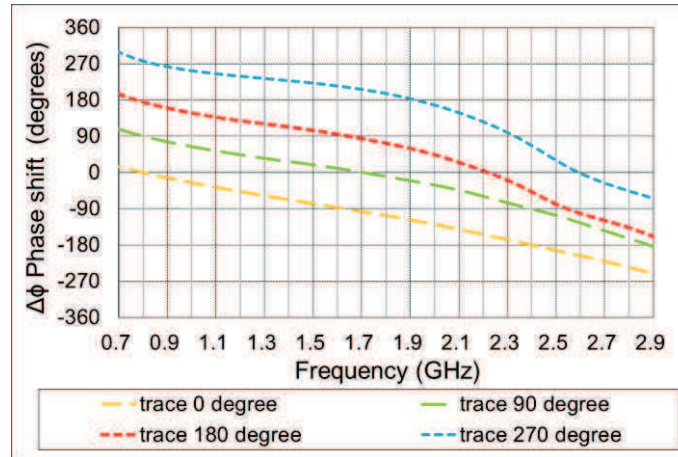


Figure 96: Characteristic of the initial tunable phase shifter for the antenna system

Figure 96 clearly illustrates the phase shift can be achieved for 0°, 90°, 180° and 270°. However, for frequencies greater than 2.3GHz, $|S_{11}|$ becomes higher than -15dB and insertion loss is worse than -3dB for the 180° and 270° paths. We still develop this type of phase shifter because we can choose not to use the 180° and 270° paths if the losses are too bad to use.

III.2.5. Phase shifter prototype development

III.2.5.1. First design of the phase shifter

We decided to realize the previous simulated phase shifter even if simulated results are not very good for frequencies greater than 2GHz.

Figure 97 shows the topology of the first prototype design. This design concept is based on the model in Figure 95. We can observe that there are four paths with different bandpass SMD components between the SP4T switches. After the switches, we have a tunable phase shifter with three variable capacitors. Figure 98 shows the 1st PCB prototype design.

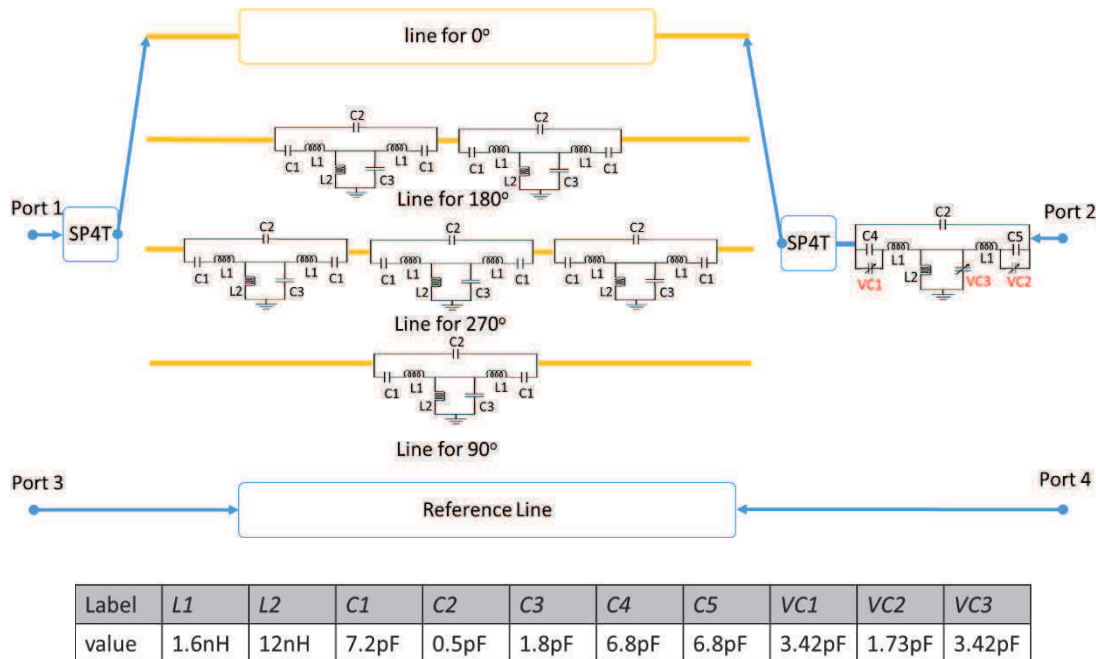


Figure 97: The topology of the 1st prototype phase shifter.

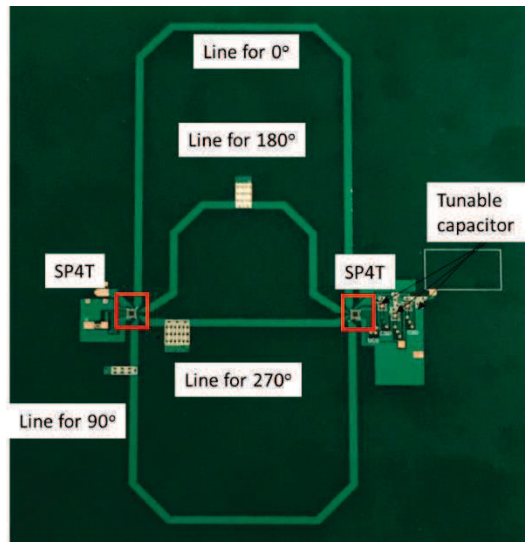


Figure 98: The layout of the 1st prototype phase shifter.

Figure 99 demonstrates the measured results for the 1st prototype.

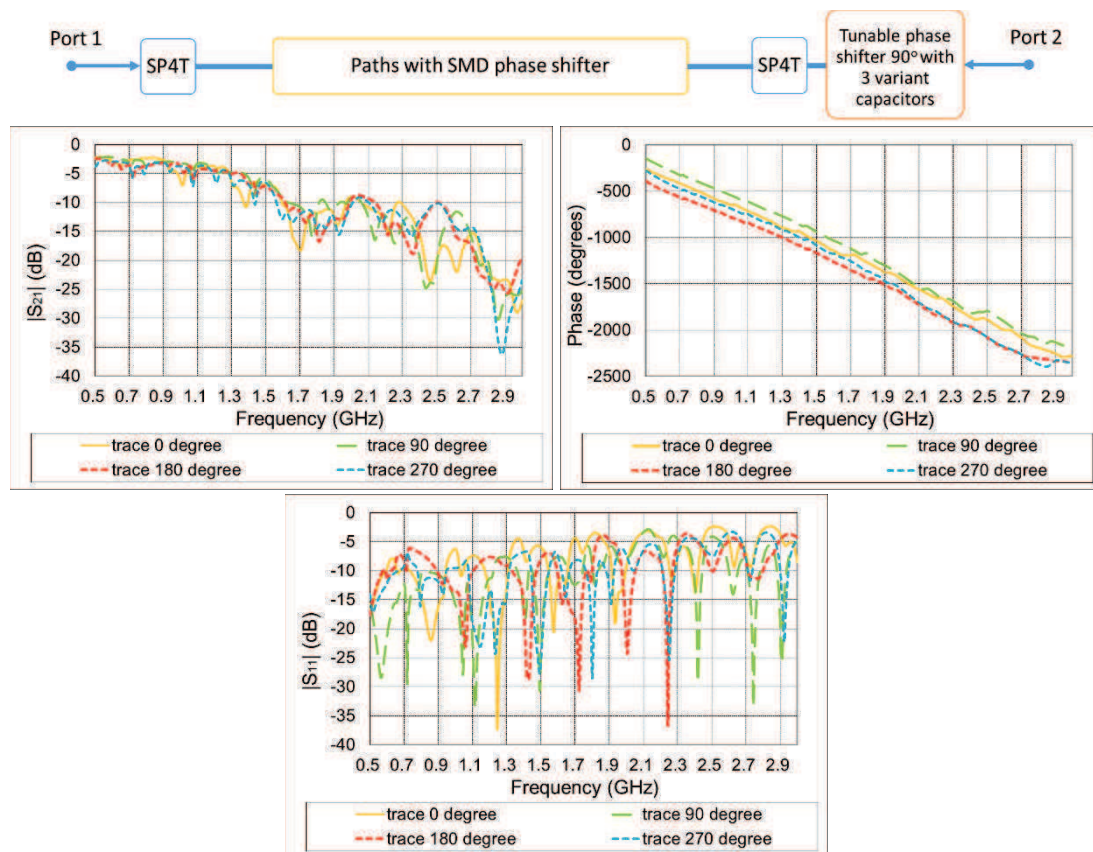


Figure 99: Measured results of the phase adjusting lines of the 1st phase shifter design

Figure 99 demonstrated there are lots of ripples in the measured results. There is also a mismatching of the device.

We must investigate the factors that influence the operation of the phase shifter.

III.2.5.2. Analysis of the initial phase shifter

First, we measured and simulated results for the 4 paths keeping the SP4T (Figure 100) and removing the tunable phase shifter.

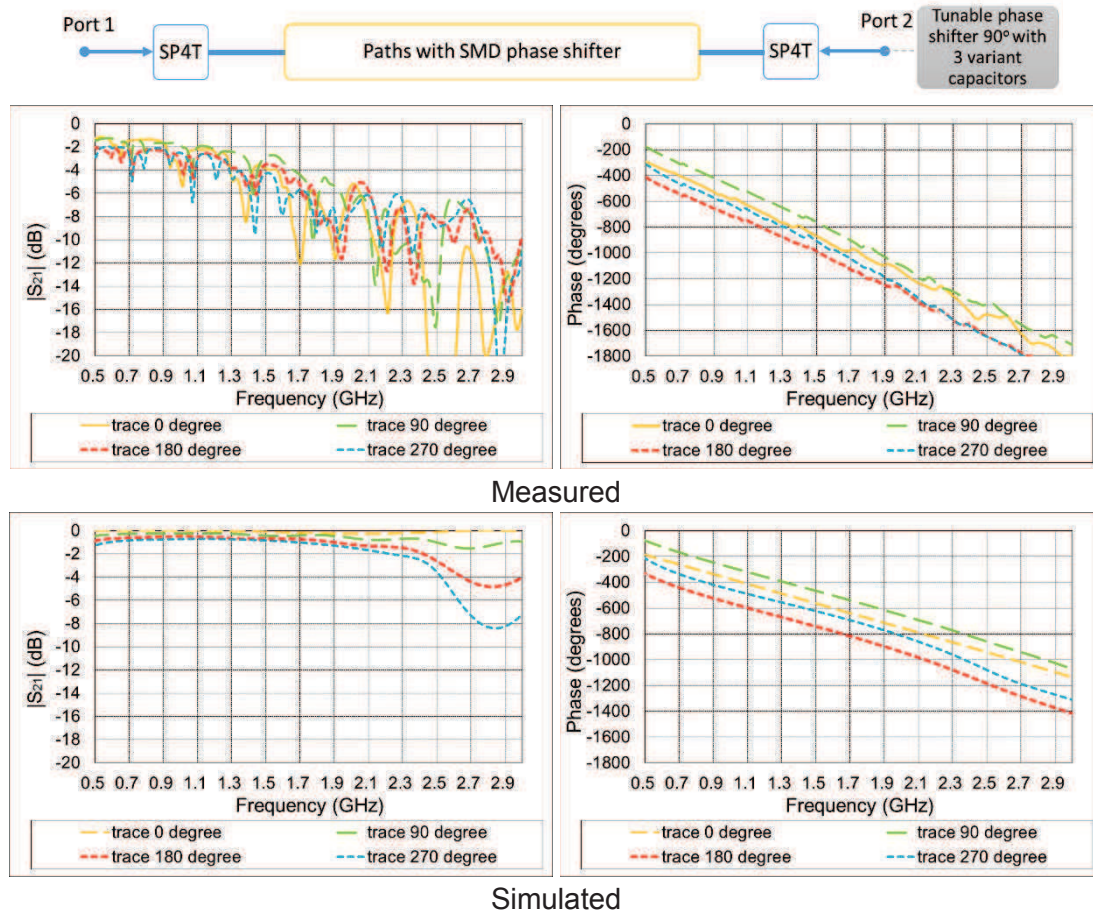


Figure 100: Measured and simulated results for the paths between SP4T switches of 1st design phase adjusting lines

Comparing with Figure 99, insertion loss in measurement is improved, 10dB (Figure 100) but is still very high.

We need to reduce the losses from this part in the new phase shifter model for the next step. Also, the results of the phase degree measurement are still bad, especially for the priority 800MHz band.

However, we can observe that the $|S_{21}|$ and line phase between the simulation and measurement are much different in Figure 100.

Also, we found that even if we skipped the tunable phase shifter, we still have a lot of the ripples in the $|S_{21}|$ measurement. These ripples can be due to the SP4T or the trace design (SMD components layout). In order to verify this, we removed two paths (Line for 180° and 90°) in order to reduce the interferences between the different paths. The measured $|S_{21}|$ are presented in Figure 101. Results are improved but losses are again too high.

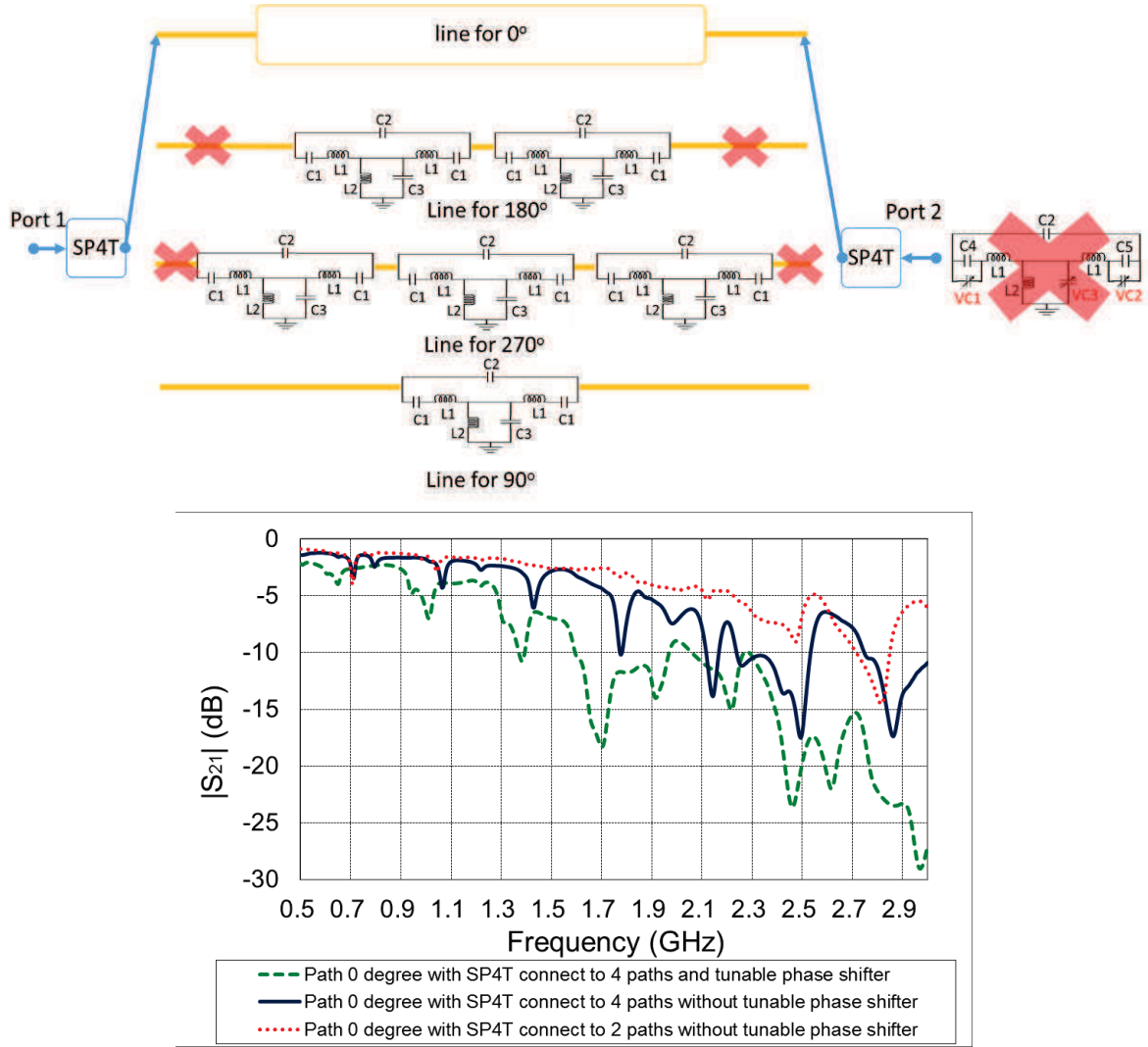


Figure 101: Measured result to compare the $|S_{21}|$ when two of the paths between SP4T and tunable phase shifter are removed

Therefore, we need to redesign the phase shifter paths to improve these defects. When the frequency is higher than 1.5GHz, the insertion loss increased significantly and is worse than in any other devices on the market. We need to optimize the phase shifter in order to improve insertion loss and to reach the targeted phase shift.

III.3. Final structure and performance of the phase shifter

III.3.1. Prototype structure

From the previous section, we see the measurement of the initial phase shifter is still not good enough to be used. We want to improve the insertion loss $|S_{21}|$ to within 5 dB and the phase shifting range to have the 360° coverage in 800MHz which is the target for our global system requirements. To avoid the effect of the SMD components between the traces, we simplify the phase shifter structure by using delay lines to replace the bandpass phase shifter and so reduce the number of variable capacitors (Figure 102).

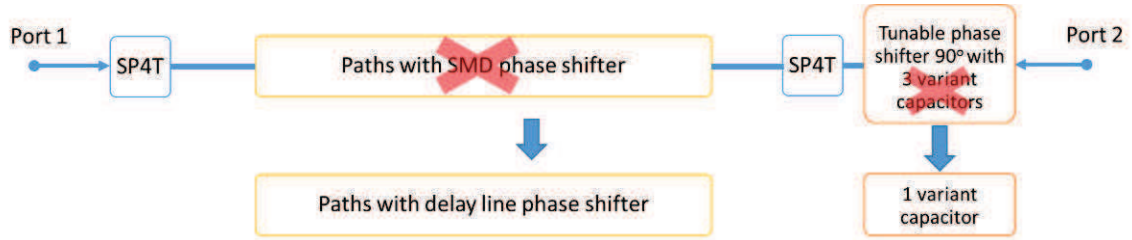


Figure 102: The difference between the initial and final phase shifter structure

The architecture of the “new” phase shifter, as shown in Figure 103, uses a pair of SP4T from Ethertronics EC686 [61] and four RF lines for 0°, 90°, 180° and 270° (at 800MHz), that will be used as phase offset delay lines. A tunable 90° phase shifter also appears for fine phase tuning.

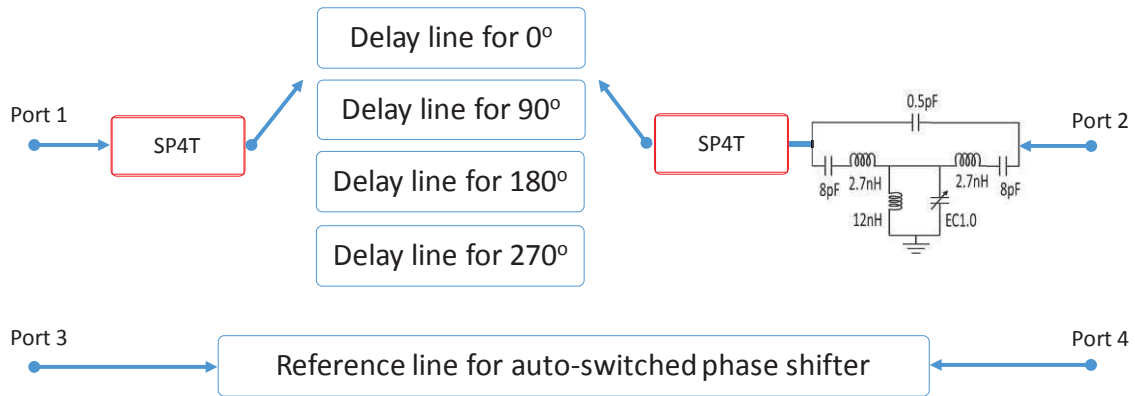


Figure 103: Topology of final differential phase shifter for the thesis

This phase shifter design has two portions for the phase tuning. Firstly, it uses a MIPI to control the EC686 [61] to select the basic phase delay line. Secondly, the variable capacitance is controlled using an SPI. Figure 104 is a photograph of the final phase shifter.

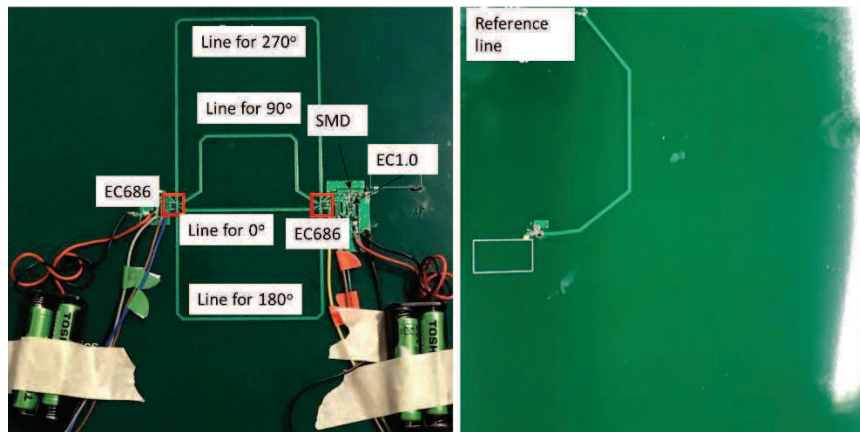


Figure 104: Photograph of the final phase shifter and its reference line

The tunable 90° phase shifter is based on a bridged T-type bandpass circuit and modified as in Figure 105. The tunable phase shifter feature is obtained by using only one variable capacitor (C_P). We chose Ehertronics EC1.0 chip [60] used in the T-type bandpass networks. The final discrete component values in the tunable phase shifter are shown in Table 4. The capacitance range of EC1.0 goes from 0.78pF to 3.47pF. The phase shifter layout is placed on the same FR4 substrate with a dielectric constant of 4.1 and a thickness of 1mm.

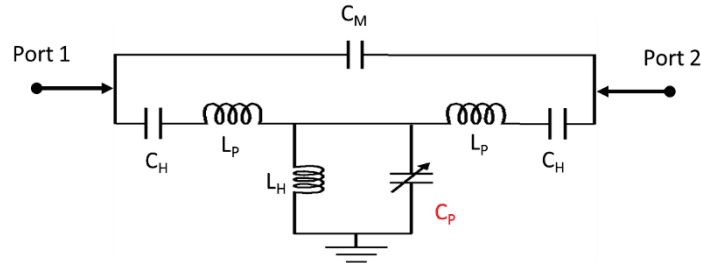


Figure 105: Final circuitry for the tunable phase shifter

Table 4: [Final optimized values for the 90° tunable phase shifter]

Phase shift	L_p	L_H	C_M	C_H	C_P
90	2.7nH	12nH	0.5pF	8pF	EC1.0

The following section will indicate the detail of the differential phase shifter design and measurements.

III.3.2. SP4T-switched differential phase shifter

III.3.2.1. Reference line

The reference line is designed by through delay line (Figure 106) and will be compared with the whole phase adjusting lines.

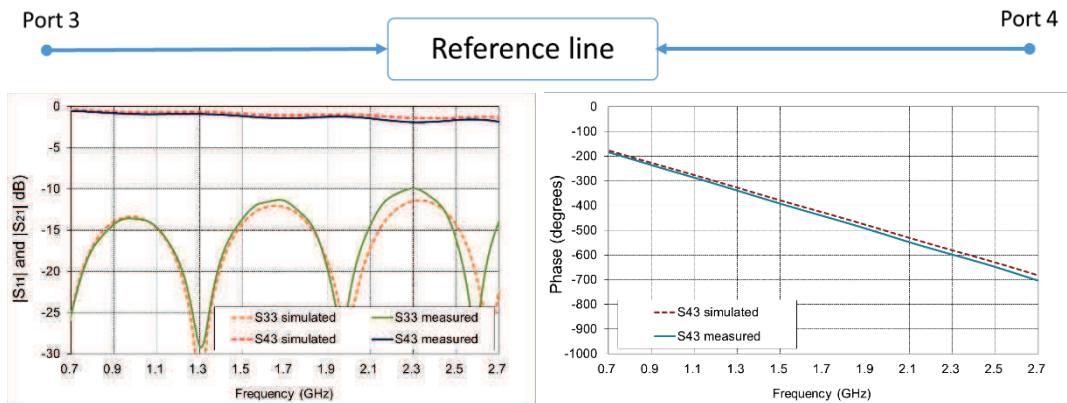
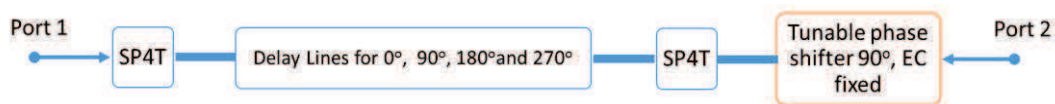


Figure 106: Simulated and measured result of reference line for SP4T-switched phase shifter

III.3.2.2. Adjusting lines

The adjusting lines are composed of the switches, delay lines and one stage 90° tunable phase shifter. The obtained results are presented in the following paragraphs.

The capacity of the tunable 90° phase shifter was set to be fixed at 1.73pF at 900MHz, which is closest to 90° matching value of [56]. The SP4T switches were operated for different selected paths. The simulated and measured phase shifts obtained for the different paths are presented in Figure 107.



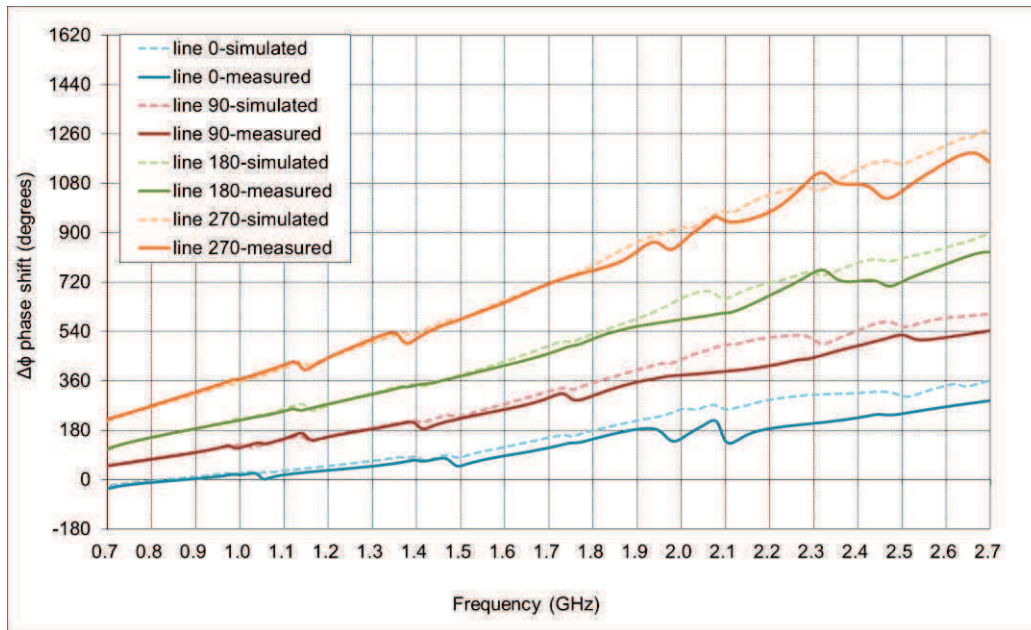
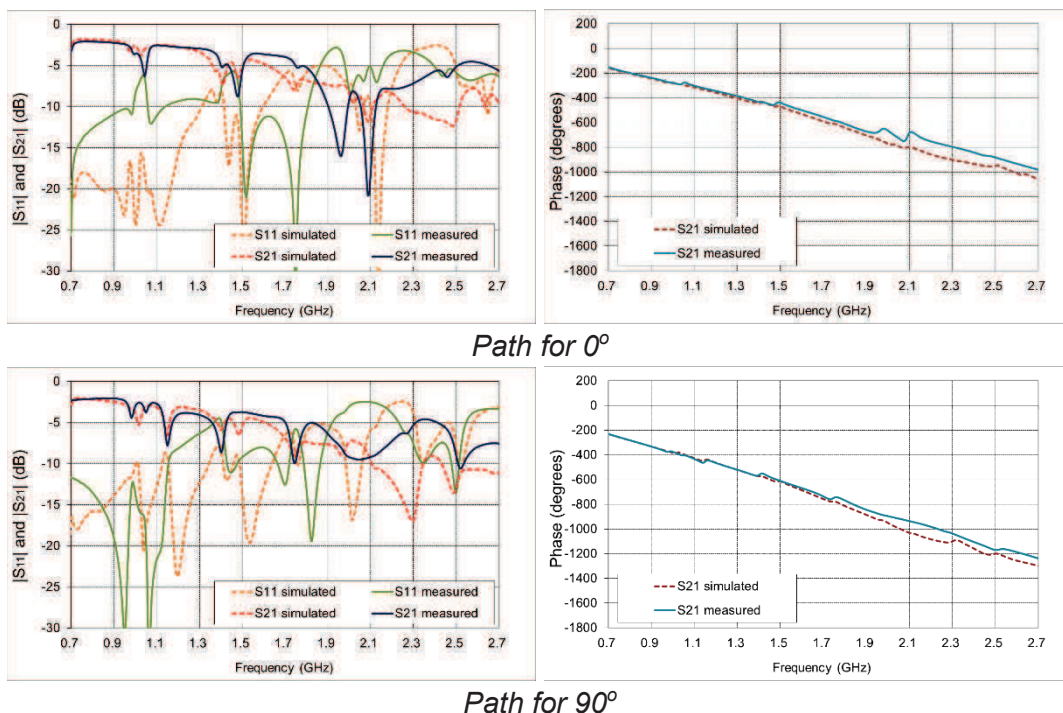


Figure 107: Phase shift result of SP4T-switched phase shifter with tunable phase shifter fixed at 90°

Figure 107 shows the measured results are in good agreement with the simulation when the frequency is lower than 1.5GHz. When the operating frequency is higher than 1.8GHz, the phase shifter did not perform as good as the simulation. Especially, when the frequency is higher than 2.1GHz, the measurement is 90° lower than the simulation. In the following pages, the characteristics of the SP4T-switched adjust line are shown in detail (Figure 108).



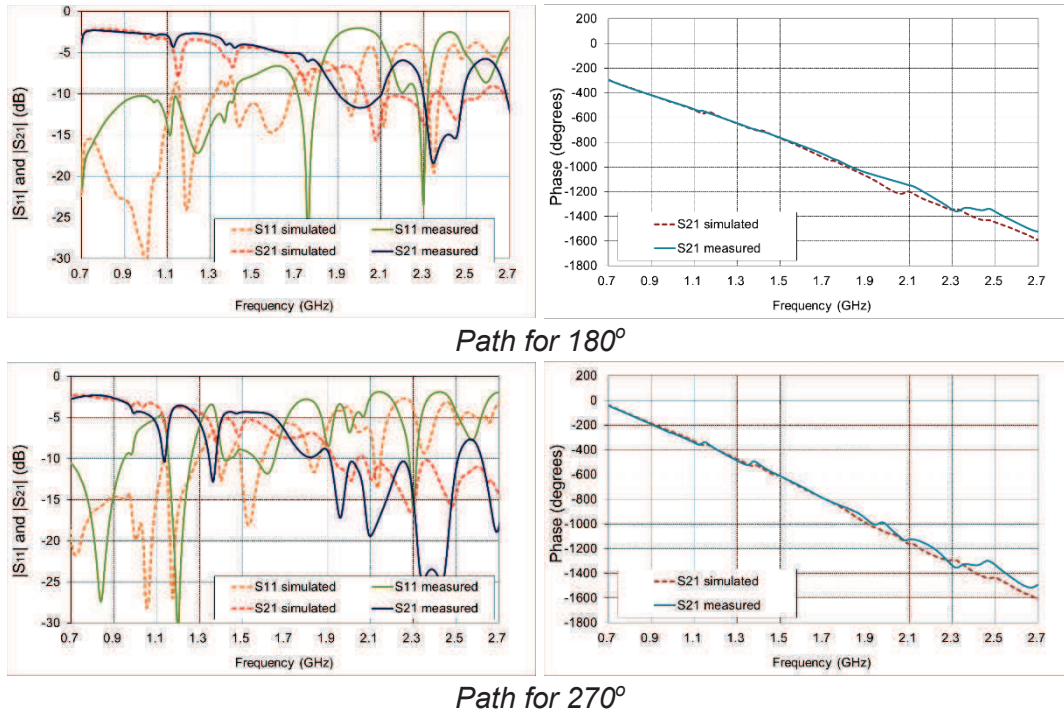


Figure 108: Simulated and measured results of SP4T-switched phase shifter in different paths

It could be observed that there are some repeatable ripples in the $|S_{11}|$ and $|S_{21}|$ measured result (Figure 108). Also, when the frequency is higher than 1.7GHz, the measurement showed some significant and unexpected increase in insertion losses. For the phase of each trace, the simulated result is close to the measured one. Also, the matching for these paths is not good when the frequency is higher than 1.1GHz. We assume that the problem could come from the SP4T switch or from the tunable phase shifter. We need to investigate this.

III.3.2.3. Phase tuning result of SP4T-switched phase shifter

To summarize the above simulations and measurements, based on the schematic in Figure 109, we obtain the SP4T-switched phase shifter performance shown in Figure 110.

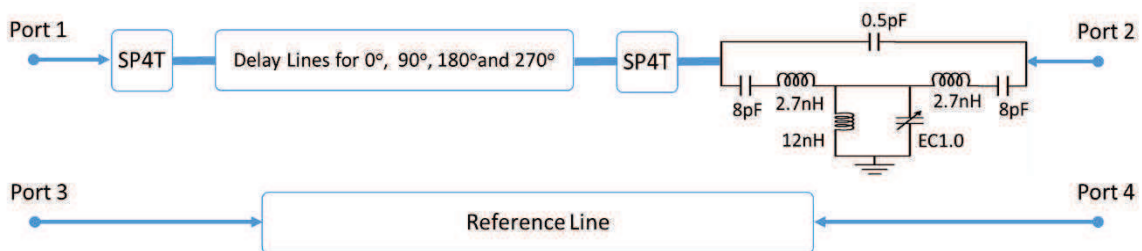


Figure 109: Schematic of the final SP4T-switched phase shifter

Since the prototype phase shifter will be implemented in the global system where the operating frequencies of the system focuses only on [790MHz to 860MHz], [1710MHz to 2170MHz] and [2500MHz to 2700MHz], the phase shifter operating frequency is therefore concentrated on the same frequency bands. Figure 110 also illustrates the ability of the differential phase result using SP4T-switching at these frequencies. In the 800MHz frequency bands, we were able to achieve phase differences in 80°, 160°, 275° and 340°.

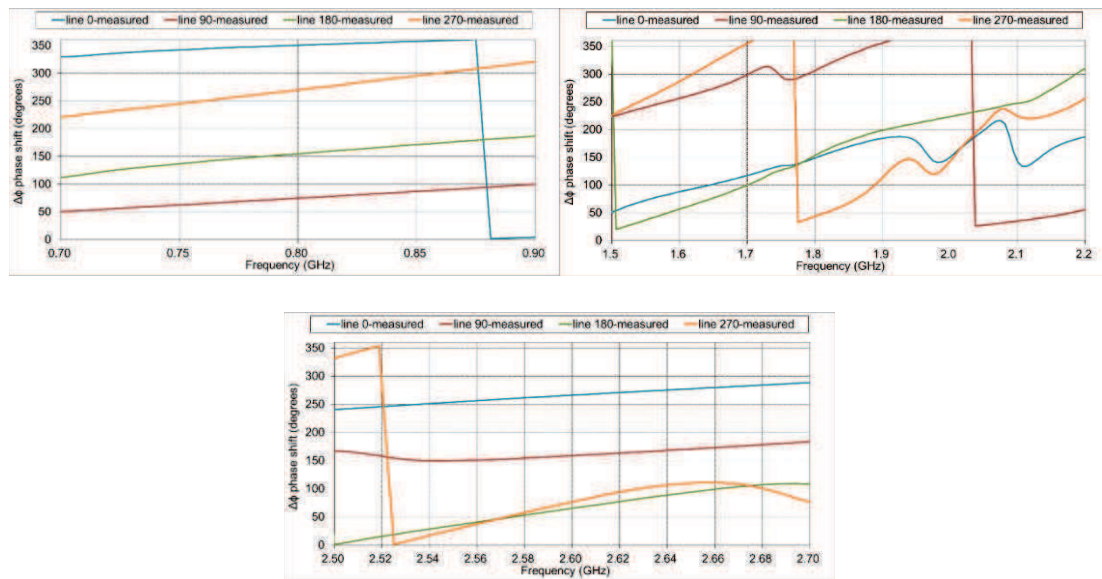


Figure 110: Performance of the SP4T-switched phase shifter at system target band

However, the behavior of the SP4T-switched phase shifter for high frequency is not as good as in simulation, we need to find out the root cause. We already know that the tunable phase shifter portion did not change the slope of the phase shifting curve from section III.2.5.1. To make comparison easier, we start with the SP4T analysis.

III.3.2.4. The effect of SP4T switch-loss

The S-parameters measurement of the SPT4 is defined in Figure 111. In this section, we focus on switch losses for each RF pin.

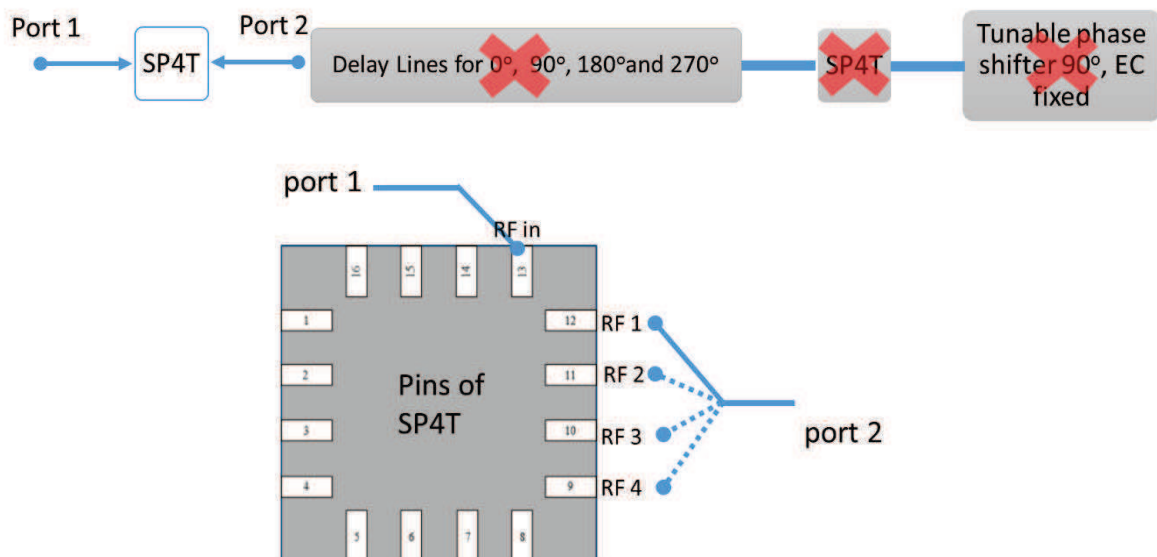


Figure 111: Measured port for the SP4T switch

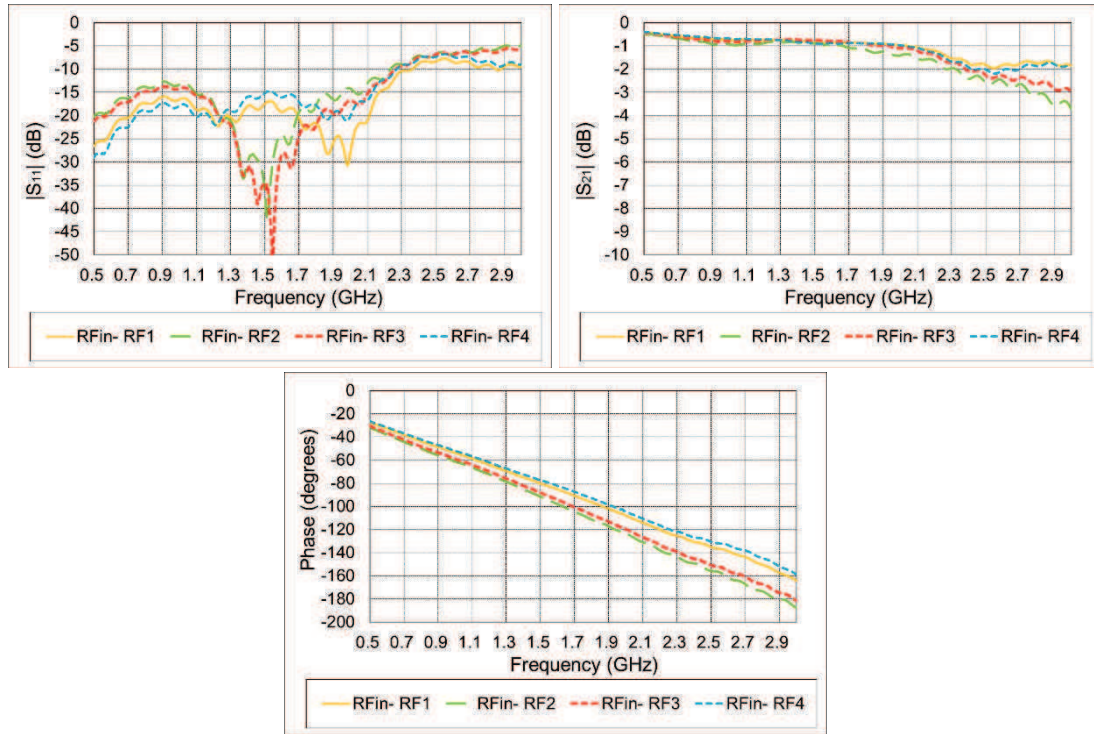


Figure 112: Measured result for a single SP4T

From Figure 112, it can be clearly observed that the $|S_{11}|$ and $|S_{21}|$ parameters perform worse when the frequency is higher than 2GHz. Since there are two SP4T switches implemented, the loss effect will be increased. For the phase shifting in the RF ports, they are separated by two groups (Figure 112). This means that if we connect the same length of the metal line, the phase shifting is different for each port. Figure 113 indicates how the pins have been connected to the paths of the phase shifter. Therefore, the phase shifting degrees in RF2 and RF3 are more important than in RF1 and RF4 (Figure 112). According to the phase shifter path, the difference between the measurement and simulation for the phase in the 0° and 90° paths is worse than for the phase in 180° and 270° .

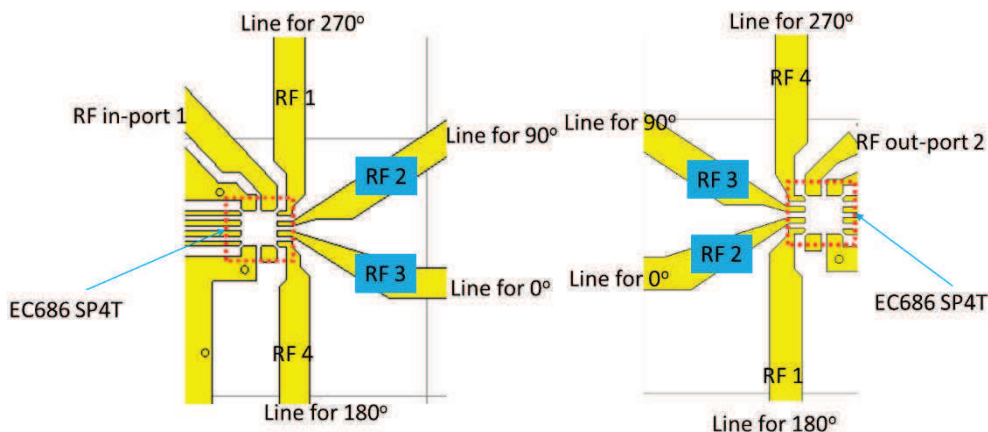


Figure 113: The connection for switches and the paths

III.3.2.5. The effect of SP4T switch-ripples in the curve

From Figure 108, we can observe repeatable ripples in the $|S_{11}|$ and $|S_{21}|$ curves. To confirm the source of these ripples, each path is simulated and measured individually. We

use the PCB with the final phase shifter layout and we remove the switches. We took four measurements with four separate independent traces with the tunable phase shifter as shown in Figure 114. There are four lines on one PCB. The characteristics of the true delay lines are recorded in Figure 115.

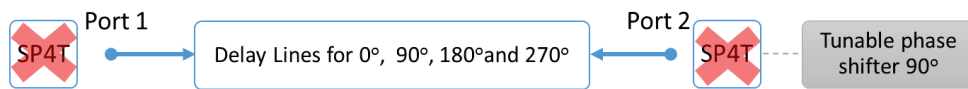


Figure 114: Topology of the four traces line only measurement

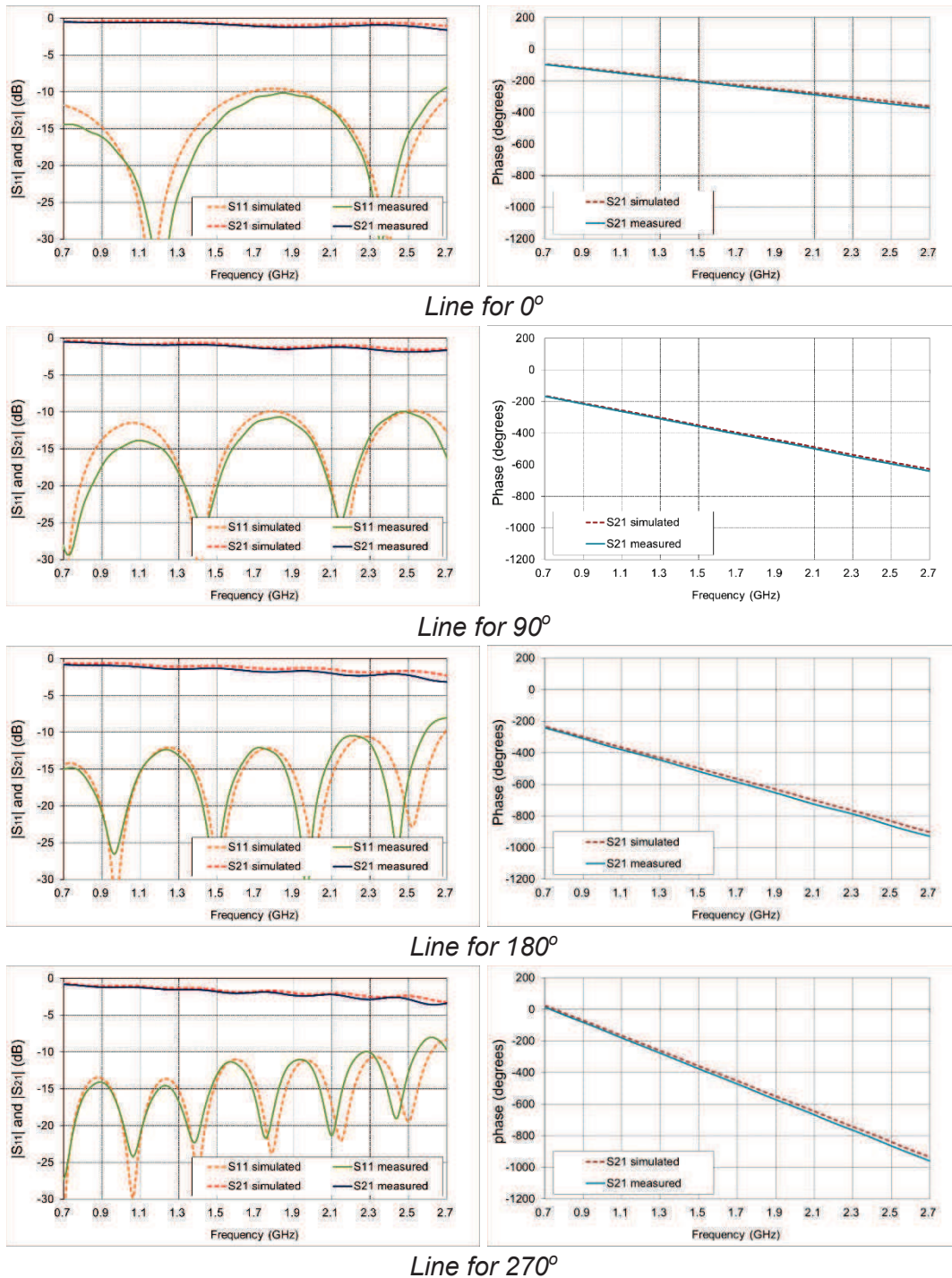


Figure 115: Simulated and measured result for delay lines only

Therefore, the experiment was continued with the integration of the SP4T switches in the circuit but the tunable phase shifter part removed in this case, as shown in Figure 116. Figure 117 shows the result of simulations and measurements between SP4T switches.

Block diagram of the proposed 90° tunable phase shifter. The circuit consists of two SP4T (Single-Pole Four-Through) blocks connected by four delay lines. The delay lines are labeled "Delay Lines for 0°, 90°, 180° and 270°". The input is Port 1 and the output is Port 2. A red 'X' is placed over the "90°" label, indicating the selected phase shift.

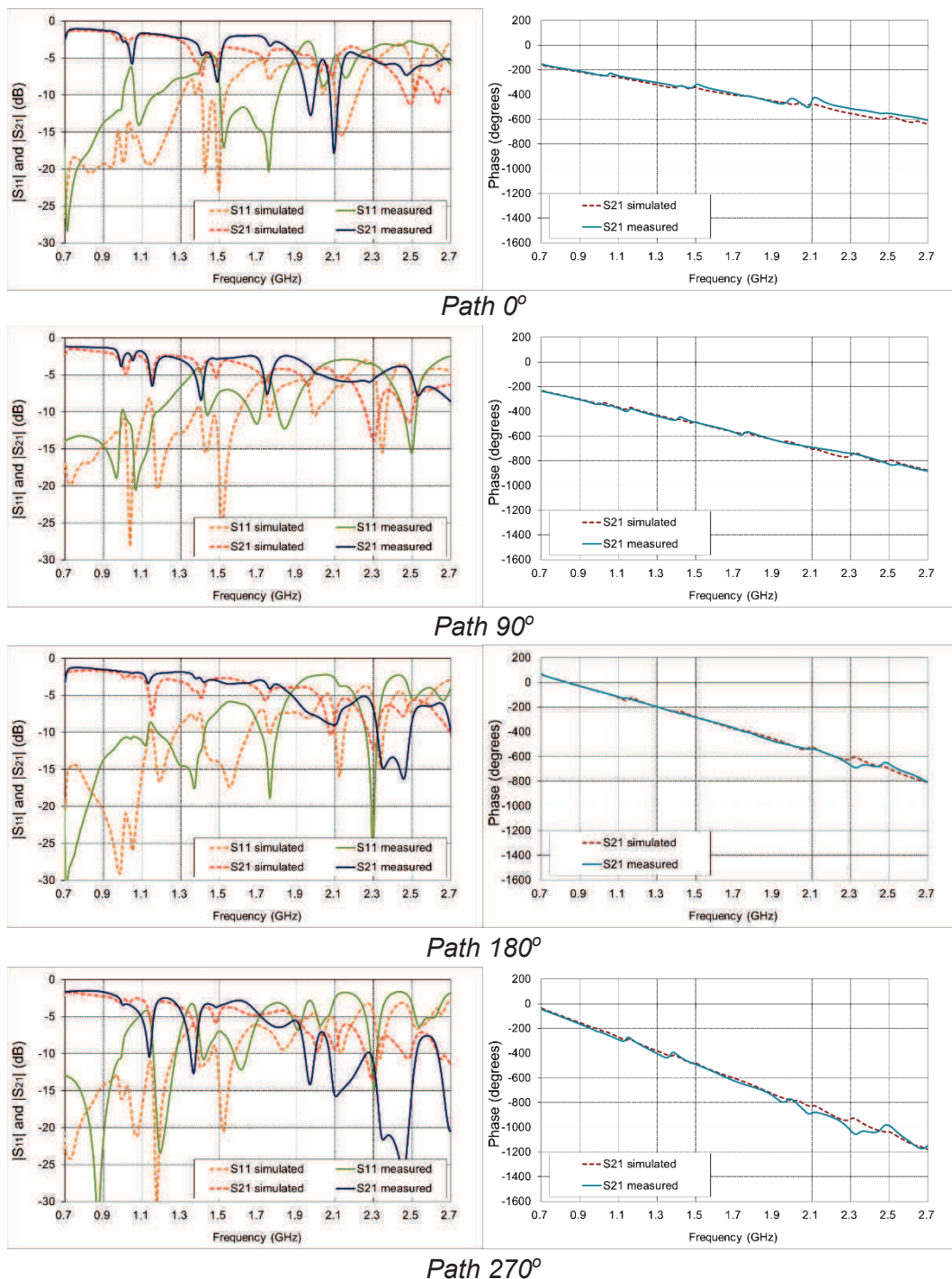


Figure 117: $|S_{11}|$ and $|S_{21}|$ Simulated and measured result for switches with lines

The S-parameter charts indicate that some repeated ripples occurred once we integrated the switches to the pure delay line (Figure 117). Especially for the 270° path, the insertion loss is 10dB worse than the other lines. If we ignore the repeatable ripples and only focus on the antenna system frequency band, there is good agreement between simulation and measurement for $|S_{21}|$ when frequency is lower than 1.8GHz. The $|S_{11}|$ measurement is not very close to the simulation.

In the simulation, we get the SP4T touchstone files (s2p) coming from the measurement. But in the real situation, the non-working traces are still coupled to the working trace. Moreover, when the frequency is over 2GHz, significant losses are observed on all the traces.

Some of the paths have larger insertion loss (over 12dB) for some specific frequencies, which may not be suitable for the application. Our global system must work in three bands: [790MHz to 860MHz], [1710MHz to 2170MHz] and [2500MHz to 2700MHz].

With reference to Figure 110, when the frequency is higher than 2.5 GHz, using the 180° path and the 270° path will obtain similar phase shifting. But the insertion loss of the 180° path is much better than the 270° path. Therefore, we will not use 270° path when the frequency is higher than 2.5GHz. Also, the 180° path will not be adopted for 1.7GHz to 2.2GHz because the 0° path already has a similar phase shifting result. These could be done by programming to select the best path for the different testing conditions.

Our global system has to be placed on the rooftop of the vehicle. We need to consider the facility to control the system.

Considering the ripple phenomenon, the losses may come both from the cross interaction between delay lines or from the SP4T characteristics effect. To investigate the cause of the spikes, we removed the SP4T ICs and used metal strips to connect all the lines. The analysis will help us to decide if we need to change the delay lines to reduce the cross interaction or minimize the SP4T effect for system integration.

SP4T is not the only factor which may impact the performance significantly, the variable capacitor is another factor. Both of them use semiconductor design with digital control which may also influence phase shifter behavior through some unknown parasitic effect inside the IC. We therefore analyze the tunable phase shifter in the following paragraph.

III.3.2.6. Tunable 90° phase shifter only

For our phase shifter design, we need to check the performance for the tunable phase shifter portion. We fixed the path and changed the variable capacitance to achieve a tunable phase shifter. The setup for the measurement is changed as shown in Figure 118.

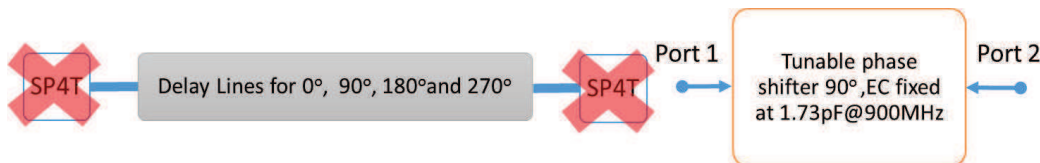


Figure 118: Measurement and simulation condition for tunable phase shifter only

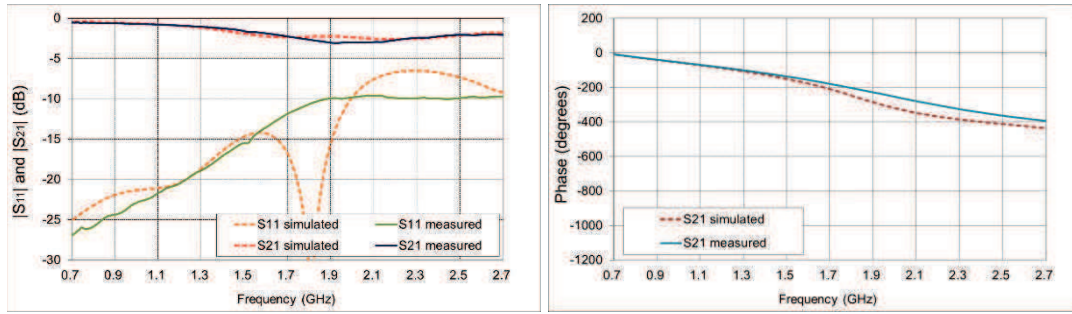


Figure 119: Simulated and measured result of EC capacitance= 1.73pF @900MHz for tunable 90° phase shifter

For $|S_{11}|$, when the frequency is under 1.5GHz the result is close to the literature [56] (Figure 120). In the $|S_{11}|$ chart, most frequency bands could be under -10dB. We can observe that $|S_{11}|$ is worse at high frequency (Figure 119) than the simulated SMD result (Figure 86).

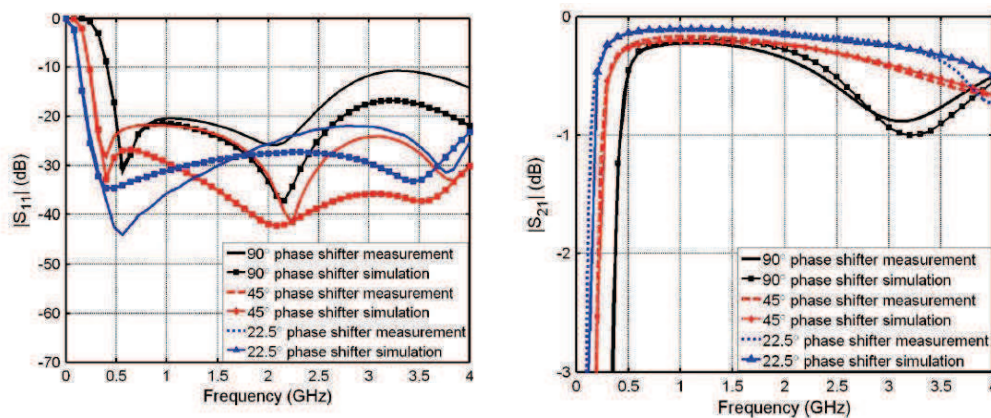


Figure 120: All SMD phase shifter result from [56]

However, measurements and simulation of $|S_{11}|$ and phase are quite different when the frequency is higher than 1.5GHz.

We believe that one of the reasons for this difference is due to the fact that capacitance varies with frequency (Figure 121). In the simulation, we have only used a fixed value of the capacity provided in the datasheet for some target frequency. Another reason is that this variable capacitor uses a semiconductor process and needs some digital lines for signal control. The parasitic effect between the capacitor structure and these controlled lines may affect the tunable phase shifter performance.

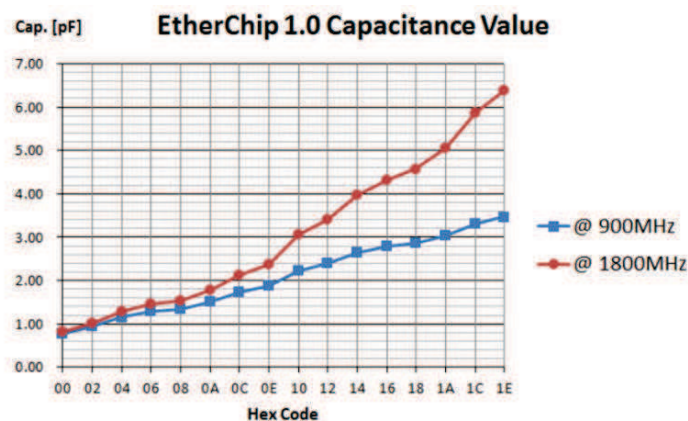


Figure 121: variable capacitance chart and table for the SPI controlled by Hexadecimal code for EC1.0

III.3.2.7. Effect of different capacitance values

Figure 122 shows the effect of the tunable capacity on the phase and insertion losses.

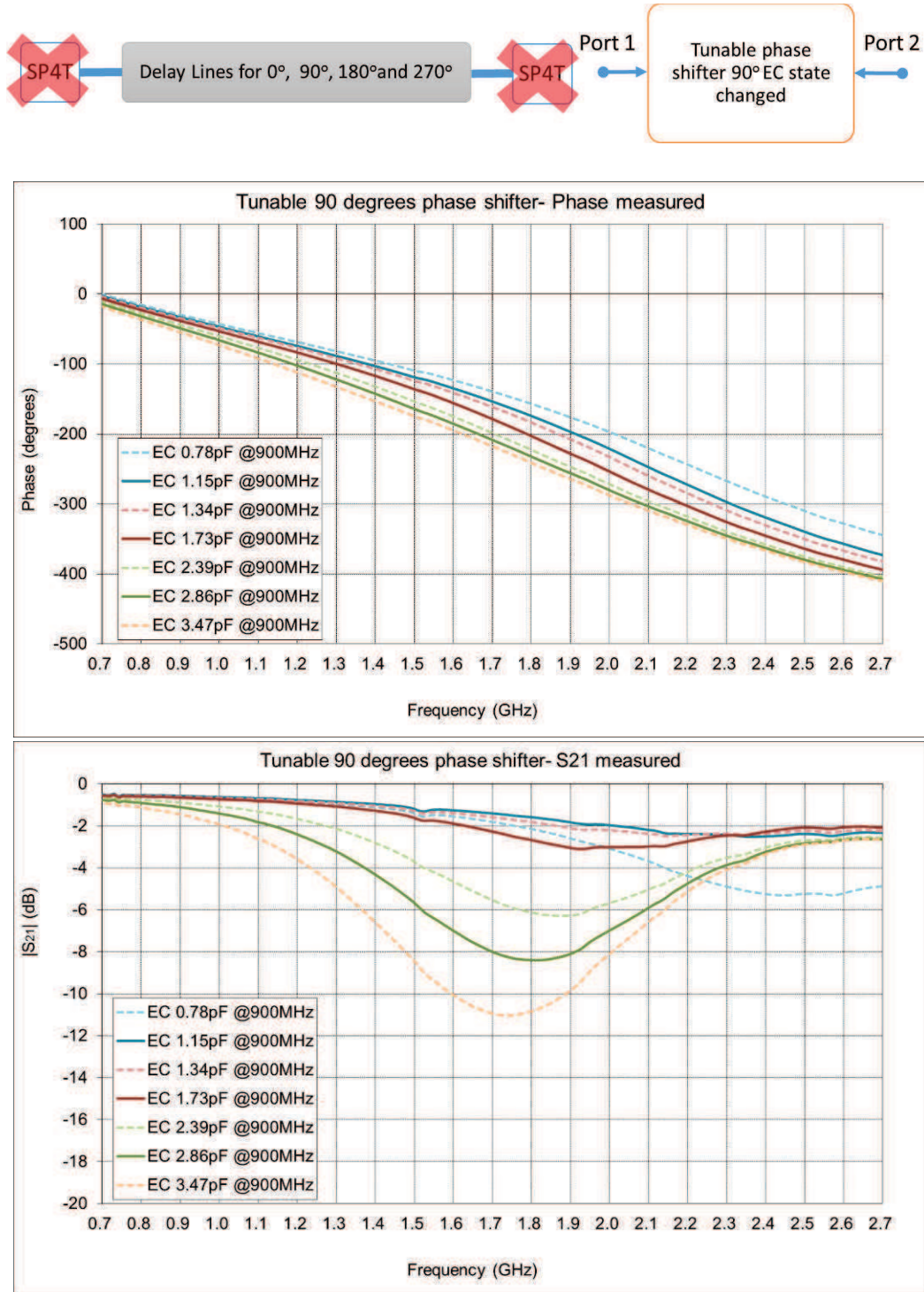


Figure 122: $|S_{21}|$ and phase measurement of the tunable 90° phase shifter with different values of the capacity

It appears that the value of the $|S_{21}|$ is sometime worse than -3dB. One solution to avoid this problem is to choose a capacitor value for good operation for the target frequencies.

From the above charts, the designed phase shifter has the ability for phase shifting of 16° at 800MHz, 100° at 1800MHz and 60° at 2600MHz. This measured result showed the possible

phase tuning range with the tunable phase shifter. We observed that when the capacitance value is higher, the insertion loss is also higher. So, for better performance, we decided to set the capacity value to 1.73pF.

For the SP4T-switched phase shifter, we have seen that only the low frequency band (790MHz to 860MHz) can work well. This phase shifter is not good enough to be used. For the higher frequency bands, we need to find a better solution to reduce the insertion loss. Therefore, we move on to the development of a manual-switched phase shifter.

III.3.3. Manual-switched phase shifter: using metal strip lines

In this part of the study, the SP4T switches were removed and we used copper lines to complete the trace as presented in Figure 123 and Figure 124. When the copper lines are connected to the target delay line, the other lines are floating. Since the switches also have a phase delay effect, we redesigned the reference line for four new paths without SP4T switches.

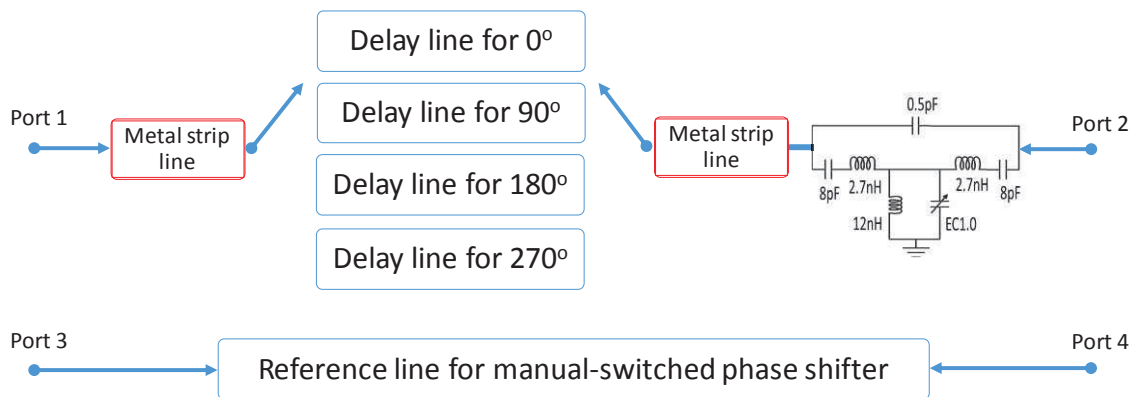


Figure 123: Topology of manual-switched phase shifter

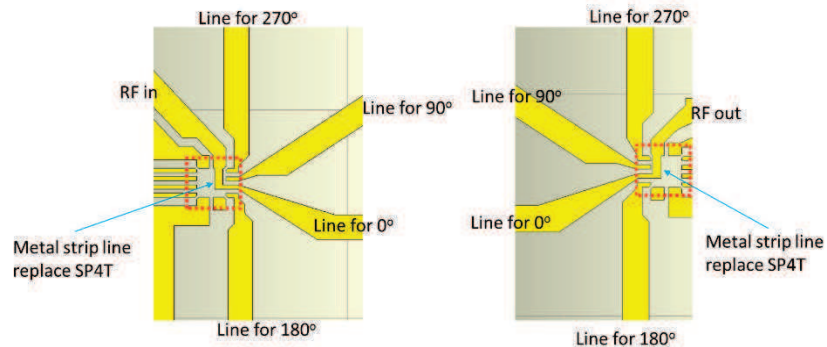
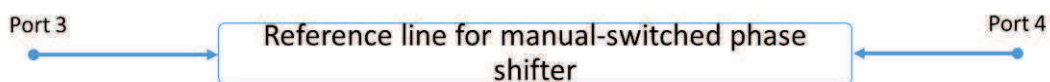


Figure 124: Diagram of metal strip line connection at manual-switched phase shifter

III.3.3.1. Reference line for manual-switched phase shifter

Figure 125 shows the redesigned reference line characteristics. The measured results are in good agreement with the simulation.



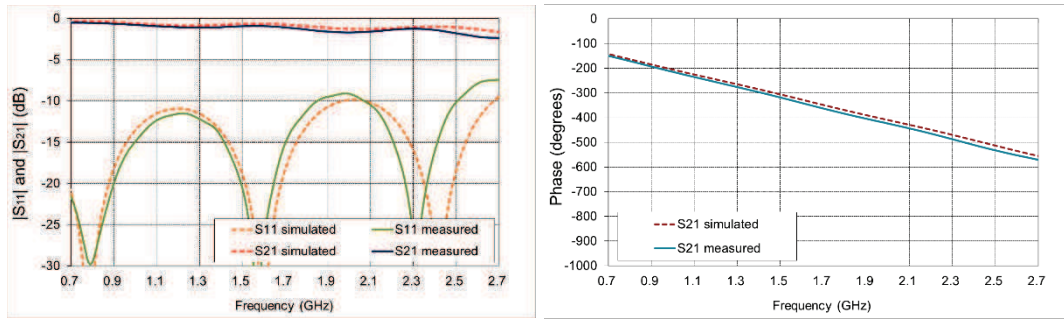
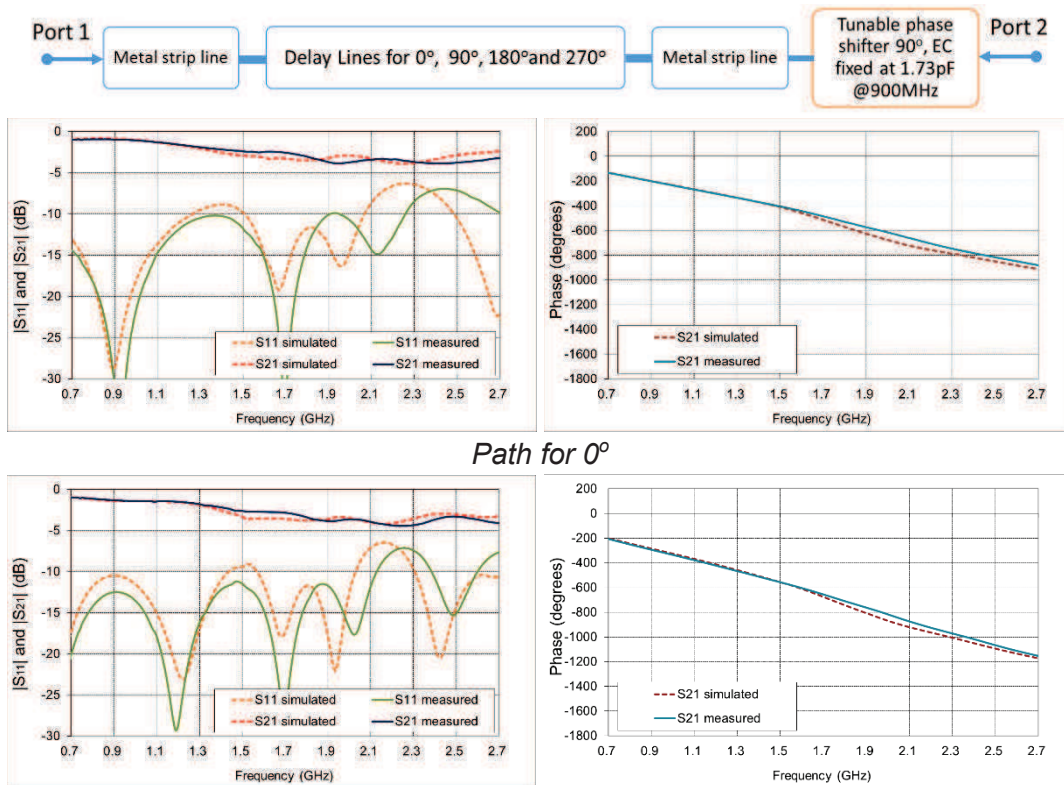


Figure 125: Simulated and measured result of the reference line for manual-switched phase shifter

III.3.3.2. Adjusted lines with manual-switched phase shifter

Initially, the traces of the adjusted lines were measured and simulated for the manual-switched phase shifter. The variable capacitor in the tunable phase shifter part was kept at the same state, maintaining a capacitance of 1.73pF at 900MHz. Figure 126 shows the results. There is good agreement between measurement and simulation for the insertion loss with a difference of less than 1dB. For the phase chart, the simulations and measurements give similar results for all traces. However, the return loss of the measured results is worse than the simulation for frequencies higher than 1.9GHz.



Path for 90°

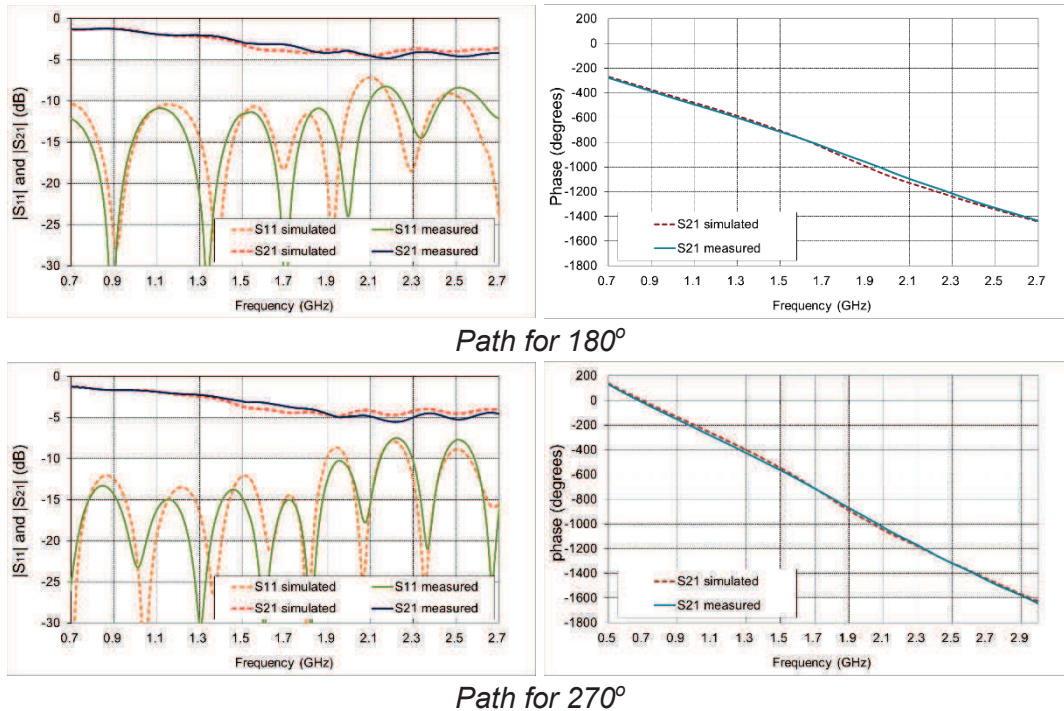


Figure 126: Simulated and measured results of the adjust line for manual-switched phase shifter

The mismatching is coming from the simulation for the tunable phase shifter. In the tunable phase shifter portion, $|S_{11}|$ is quite different from 1.7GHz to 1.9GHz (Figure 119) which impacts the simulation in the manual-switched phase shifter. However, the curve of the phase is quite close to the measurement for this type of phase shifter.

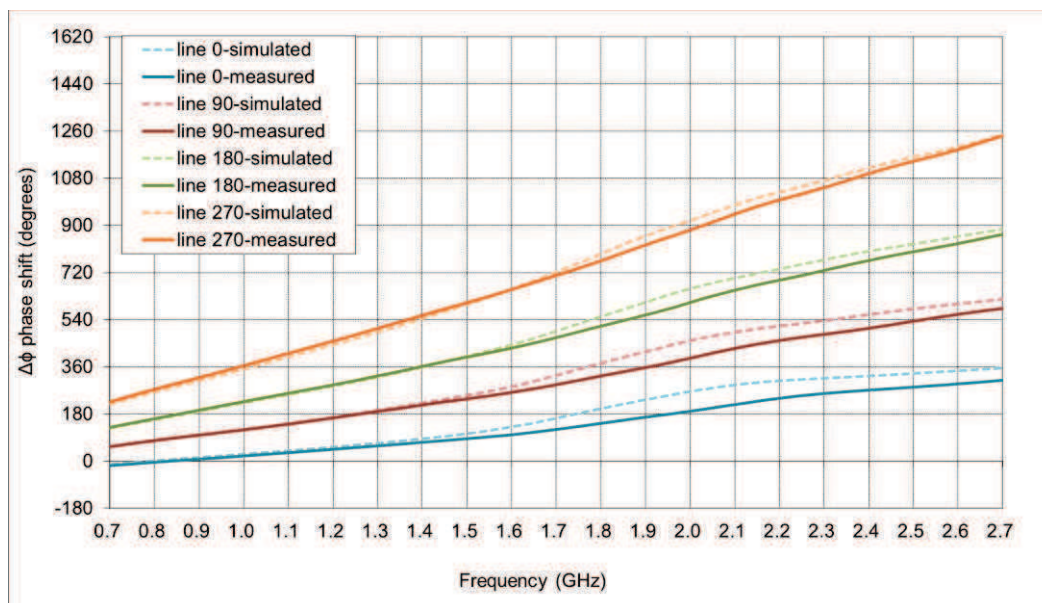


Figure 127: Simulated and measured result for the manual-switched phase shifter

The measured result for the manual-switched phase shifter exhibited good linearity without any spikes for the system (Figure 127). And the insertion loss of the manual-switched phase shifter was under 5dB (Figure 126).

Now the trace was fixed for 0° (at 800MHz). Only the variable capacitance for the tunable phase shifter part was changed. Also, the $|S_{21}|$ is better in this case than with the SP4T-switched phase shifter (Figure 128).

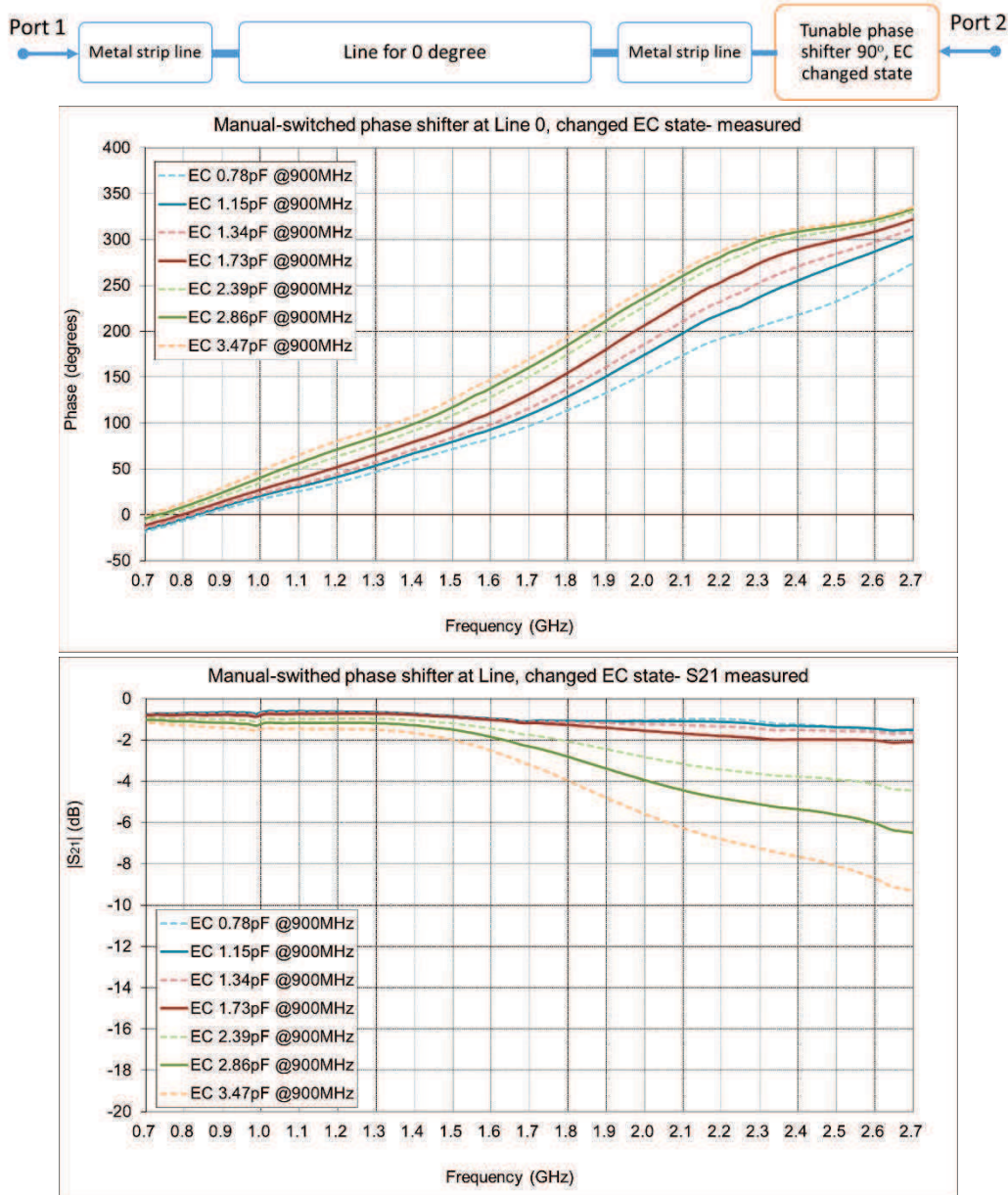


Figure 128: Measured result of the manual-switched phase shifter by changing capacitance in tunable phase shifter part

III.4. Conclusion

In the global system, the phase shifter is the key component in completing the antenna radiation pattern steering. It is easy to find one on the market for each separate frequency band. But phase degree coverage, close to 360° for 800MHz with low insertion loss, is always difficult to obtain and needs a high voltage supply. On the other hand, a miniature phase shifter such as the IC has high insertion losses (over -12dB) at 800MHz. Here we presented the phase shifter which could cover the wanted phase range with acceptable insertion losses (-3dB @800MHz).

The proposed phase shifter used a simple structure made of two parts:

- four lines for every 90° phase shift.
- T-type bridge bandpass circuit with SMD components and variable capacitor.

The reason for using true delay lines for the main phase shifter part is to minimize the insertion loss and interference between the lines. The tunable part of the phase shifter provides the capacity for more tuning steps for the phase shifter. It also only requires 5V for the tunable IC and controlling switches.

The proposed phase shifter could offer phase shifts close to 0°, 86°, 164° and 271°. This result is close to the objective. The measured result is very close to the simulated result. Table 5 demonstrates the value of this work. At approximately 0.8GHz, both the auto-switched and manual-switched phase shifter exhibit good performance.

Table 5: [Performance comparison of market available 360° phase shifter]

Reference	Frequency (GHz)	VSWR (:1)	Insertion loss (dB)	Type
[47], NEDI technology Co	0.7-1.5	1.4	7	IC
[49], Mini-Circuits	0.8-1.5	2	4	module
[50], Sigatek Microwave LLC	0.8-0.9	2	4.2	SMA
This work: manual-switched	0.7-0.9	1.92	1	SMD on PCB
This work: auto-switched	0.7-0.9	1.7	2.5	SMD on PCB
[47], NEDI technology Co	1.6-3.2	1.4	9.5	IC
[50], Sigatek Microwave LLC	1.8-2	2	4.4	SMA
This work: manual-switched	1.5-2.2	1.6	3	SMD on PCB
This work: auto-switched	1.5-2.2	4.4	12	SMD on PCB
[50], Sigatek Microwave LLC	2-2.5	2	4.8	SMA
[52], L3 Narda-ATM	DC-2.5	1.5	1.6	SMA with motor
This work: manual-switched	2.5-2.7	3.5	5	SMD on PCB
This work: auto-switched	2.5-2.7	5	8	SMD on PCB

However, considering the insertion loss and return loss effect, the phase shifter range would be limited by SP4T integration when the frequency is higher than 1.5GHz. Even if we change to other switches, the phenomenon is still similar. We obtained good results with the manual-switched phase shifter from Section III.3.3. In the future work, the design of the auto-switched phase shifter needs to be modified in order to reduce the ripple and improve the performance of the overall device.

However, we will use both auto-switched and manual-switched in the global beam steering system presented in the next chapter.



Chapter IV. Beam Steering Global System for Automotive Introduction

We saw in Chapter One that there are several methods for achieving beamforming to improve the quality of the wireless communication. We selected the design of an adaptive array with phase shifter to form the analog beamforming mechanism. To achieve this goal, we proposed an architecture with a tunable phase shifter to provide different phases of the radio signal to complete the antenna array.

In Chapter Two, a multiband DRA design was proposed to satisfy the spectrum operating on the distinct frequency bands: LTE 800DD (band 20), LTE 1800+ (band 3), LTE 2100 (band 1) and LTE 2600 (band 7). In Chapter Three, a switchable phase shifter with an electronic control was designed. By using both the phase shifter and variable capacitance, we could obtain a good phase shifting degree range from 780MHz to 2700MHz.

In this chapter, we will begin with a brief overview of beam steering DRAs in order to take the benefit of different methods for our own analysis. Then, we will propose our global system, in which we aim to achieve beam steering with only two antennas. We are using CST to figure out and analyze the optimization of both the distance and the direction between the main and the MIMO DRAs within the limited space on the automotive rooftop. We are aiming at two kinds of system reconfiguration:

- Reconfigurable radiation pattern using the spatial diversity technique, i.e. the system will perform as a DRA MIMO system on the vehicle rooftop.
- Beam steering system by adding a phase shifter and power divider circuits.

After having detailed the MIMO system performance in the second part of this chapter, we will show the multiband DRA integrated with the differential phase shifter to confirm the antenna performances. Results will be shown for both auto-switched phase shifter and manual-switched phase shifter.

Finally, we will integrate the 3dB power divider to realize the antenna radiation pattern steering. During the analysis process, we also compared manual-switched phase shifter and auto-switched phase shifter impact on system performance. We will measure the system in the real vehicle environment. The system was placed in different locations on and in the automobile and comparison was made.

For the study, the difficulty is not only to build a MIMO system in such a small space, it is also in that we need to enable the radiation pattern as low as 800MHz to have beam steering and to cover almost 360 degrees. This frequency band is the most challenging for beam steering because of its low frequency and is often not addressed in the literature.

IV.1. Beam steering DRA techniques

Beam steering antennas have been developed for many applications as introduced in Chapter One. For the objective of the thesis, the beam steering antenna will use the DRA as the array element. A few methods for achieving the DRA beam steering are presented in the literature, and they will be summarized in this paragraph.

IV.1.1. Overview of beam steering methods for DRA

IV.1.1.1. Switched parasitic elements method

When a parasitic element is placed close enough to the main active element, a current is induced on the parasitic element by mutual coupling, implying that both the input impedance and radiation characteristics are modified. In [62], the authors demonstrated the changing of the parasitic patch array current distribution by shorting the parasitic elements for a GPS patch antenna. It showed the beam steering in the different directions with this method (Figure 129) with operating frequency at 1.55 GHz.

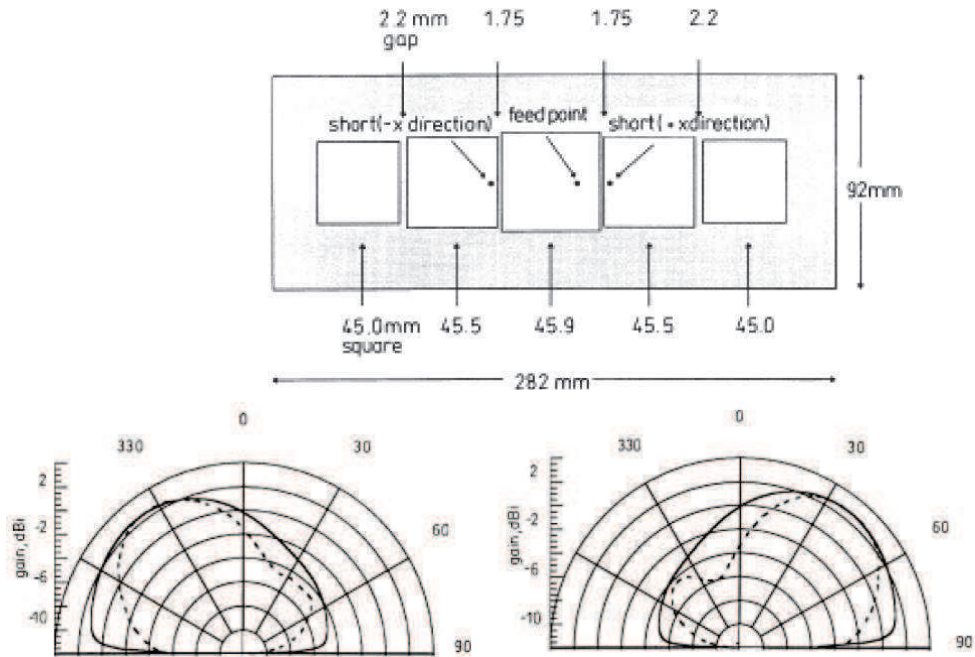


Figure 129: Beam steering by switching parasitic patch elements

This method took up a large space since it requires the implementation of five patches in the system. Therefore, the length of the system is around $28\text{cm} \times 9.8\text{cm}$ ($0.74\lambda_0 \times 0.24\lambda_0$ to 800MHz), which is not easy to implement for the automotive environment.

In [63], the authors illustrated an easier method to achieve beam steering by switching parasitic elements. This paper describes a concept employing a wideband DRA structure with four parasitic strip lines at the corner of the DR. The rectangular DR is excited on both its TE_{111} and TE_{112} modes by two vertical metal strips connected to the microstrip lines on the substrate.

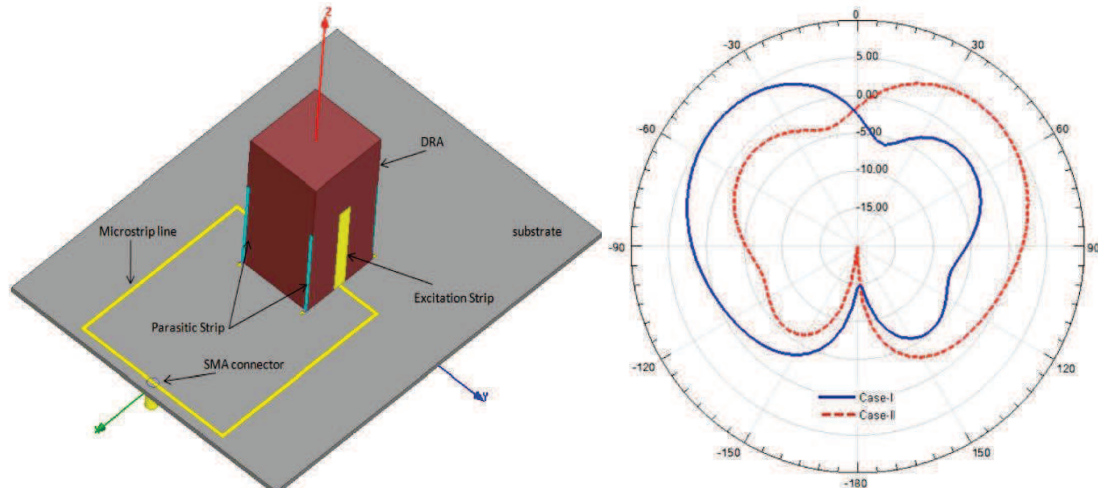


Figure 130: Beam steering by switched parasitic elements

The antenna beam is steered in the azimuth plane by switching the parasitic strips as a short or an open connection. The beam steering result is shown in Figure 130 which illustrates the radiation pattern switched at the frequency of 1.6GHz. It can obtain 5.04dB at $\theta=45^\circ$ and 5.14dB at $\theta=-45^\circ$ with antenna beam width of 80° for switching the parasitic elements in two conditions.

IV.1.1.2. Switched loading elements method

In [64], another phased array DRA for analog beam steering is introduced. The phased array consisted of three elements where the DRA placed at the centre is the driven element, fed by a microstrip line. The other two parasitic DRs are coupled to the driven element while having the same dielectric constants and dimensions as the ones of the driven dielectric resonator. The phase shift between elements is adjustable by changing the reactive loading with two small capacitors between the microstrip lines and the ground plane. The scan coverage of the phased array antenna is at 2.8 GHz (Figure 131).

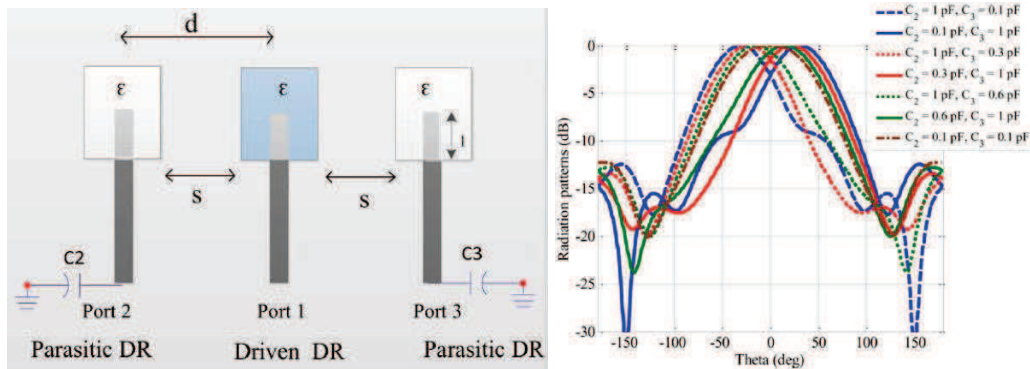


Figure 131: Beam steering by switched capacitor loading

Since the scanning phase is based on using mutual coupling and capacitor loading, the distance between the DRs therefore affects the performance of the beam steering.

IV.1.1.3. Symmetry fed-in schematic method

Providing a phase shifting signal to the DR feed is another common method for achieving beam steering. A method to obtain phase shifting using a cylindrical DRA is presented in [65].

The maximum radiation direction is not aligned to the z axis because of the non-central feeding of the DRA (Figure 132).

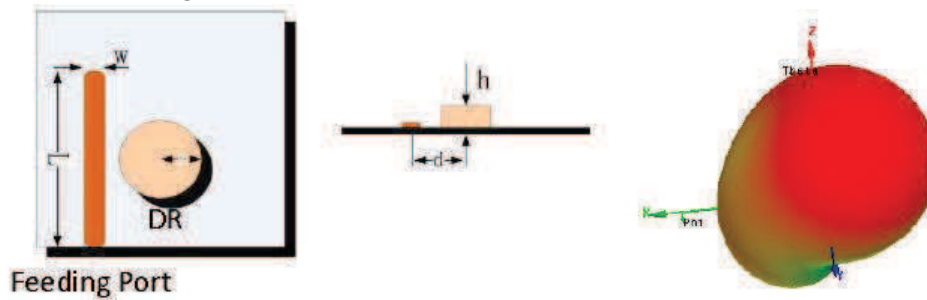


Figure 132: A single port of a cylindrical DRA and its radiation pattern

Another microstrip line is added to obtain a phase shifted signal [65]. The configuration is therefore a dual-port microstrip transmission line fed DRA (Figure 133). All the elements are placed symmetrically with dual port feeding. When the phase difference is 0 degree, the dual port DRA can realize the radiation toward the z -axis. With a phase difference of 180 degrees, the radiation is similar to an omnidirectional radiation pattern. Therefore, by changing the phase difference between the dual feeding ports, the DRA can easily realize beam steering.

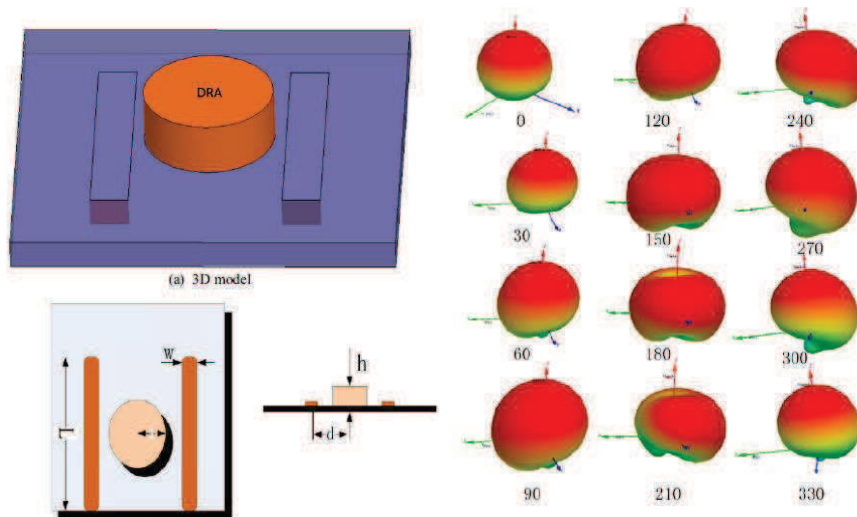


Figure 133: Dual ports of a cylindrical DRA and its radiation pattern with different phase differences

IV.1.1.4. Three fed-in ports with different phase method

The combination of different antenna structures with symmetric shapes to provide different phase shifting signals has been studied in recent years. [66] presents a beam steering system with a single fed omnidirectional dielectric resonator antenna and a directional dual fed patch antenna. By exciting three orthogonal radiating modes, the resulting beam peak and null can be steered continuously by adjusting the port relative phase (Figure 134).

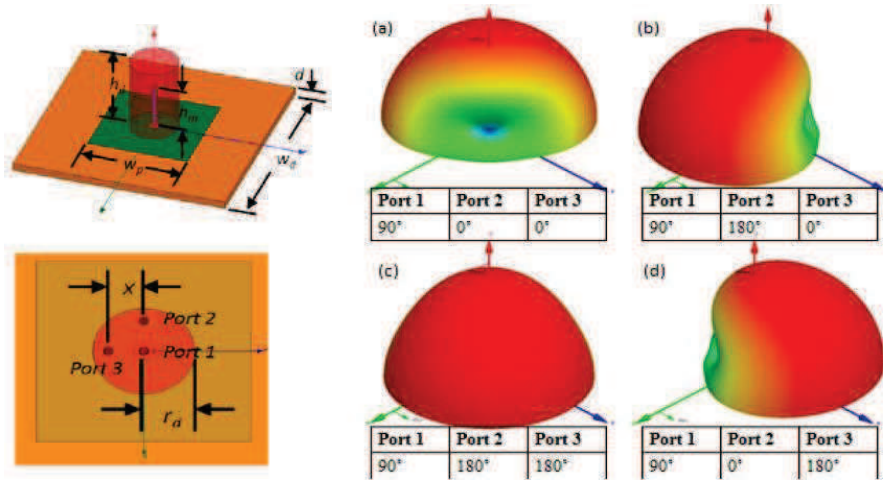


Figure 134: A three fed-in ports antenna system and its radiation pattern

IV.1.1.5. Special design for fed-in with different phase method

In [67], the authors introduced a similar concept to the previous one but it only adopted two feeding ports. The geometry of the antenna structure uses a monopole implemented in the centre of a patch antenna. The feeding of port 2 must be designed to excite two orthogonal modes. The beam steering is achieved by the superposition of the radiation from monopole and patch components (Figure 135).

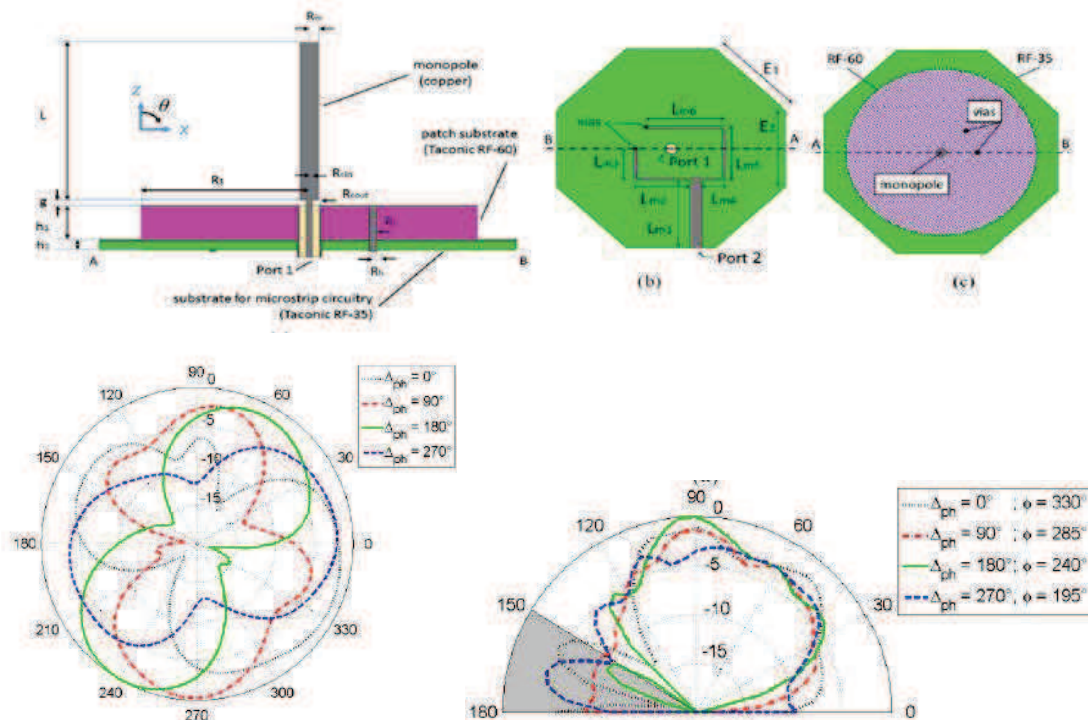


Figure 135: A dual port with orthogonal excited fed-in system and its radiation pattern

IV.1.2. Proposed methodology for beam steering DRA

In Chapter One, the global system is defined as only two antenna elements to be integrated within the allocated and dedicated area for antennas on the vehicle roof. Figure 136 is to re-highlight the two main objectives of our study, where a miniature MIMO system with only two elements will be developed, after which both antennas will be used as an adaptive array for

beamforming. This global system must satisfy both MIMO and beam steering system requirements.

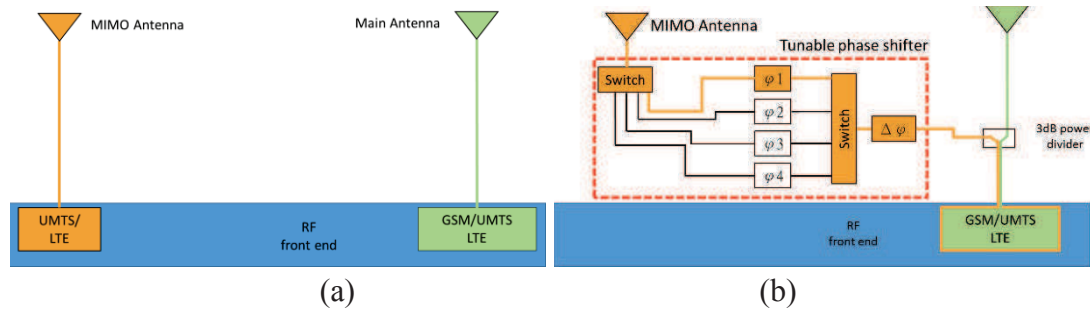


Figure 136: The miniature antenna array for: (a) MIMO system working diagram; (b) beam steering working diagram

The antenna will be based on the DRA developed in Chapter Two, which covers LTE standard frequency bands used all around the world. Our beam steering method will take the MIMO antenna, while using a phase shifter to provide the required phase signal to complete the adaptive array.

Also, the relative antenna locations must be investigated in order to reach the best radiation pattern coverage by providing the different phase signals for an adaptive array system. For the whole system, the most challenging target for the beam steering system is the lowest working band of 800MHz.

IV.2. MIMO system structure and performance

IV.2.1. Location of antennas

At 800MHz, the radiation pattern can exhibit beam steering from 10° to -80° . Also at 1800MHz, the beam can steer from 195° to 110° . For the next step, we continue to optimize the detailed distance between the two antenna elements.

There are different methods for the relative orientation between the main DRA and MIMO DRA. To reduce the coupling between the two antennas while having the best pattern reconfigurability, the proposed system integrates two DRAs placed face-to-face in such a way that they can be embedded in the dedicated automotive space. Therefore, the distance between the DRAs is 18mm along the x-axis and 40mm for the y-axis. Figure 137 demonstrates the optimized distance between the antenna elements. The global antenna system can perform well for both MIMO and beam steering systems and the final model will be based on this model.

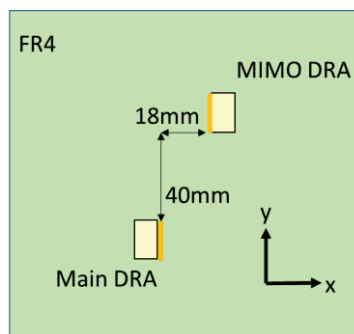


Figure 137: Relative distance of the antenna array elements in the system

IV.2.2. Structure and performance of the MIMO antenna system

For the MIMO system, each DRA is independently fed with a 50 Ω - coaxial cable and the system shape and element locations are symmetric as presented in Figure 138. The ground plane size is 400mm \times 200mm which comprises two sets of DRA models as in Chapter Two.

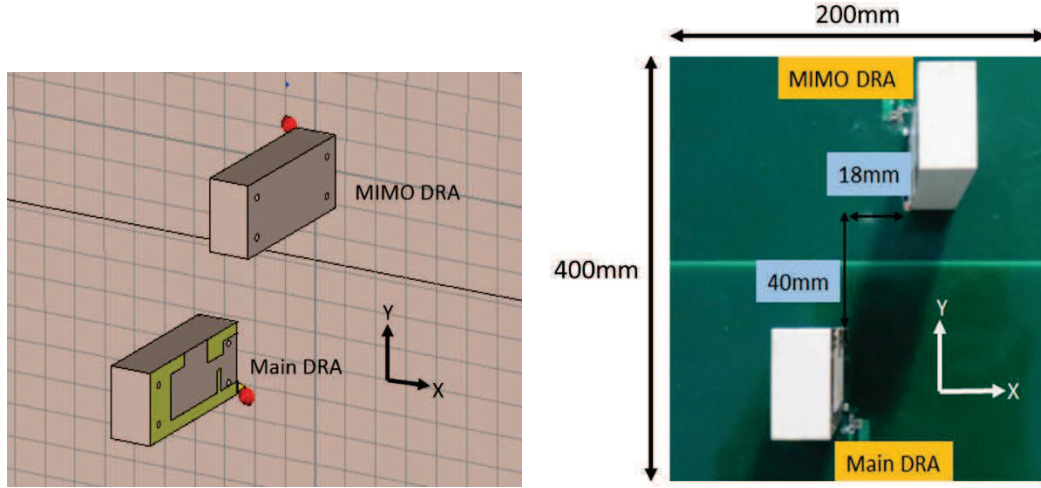
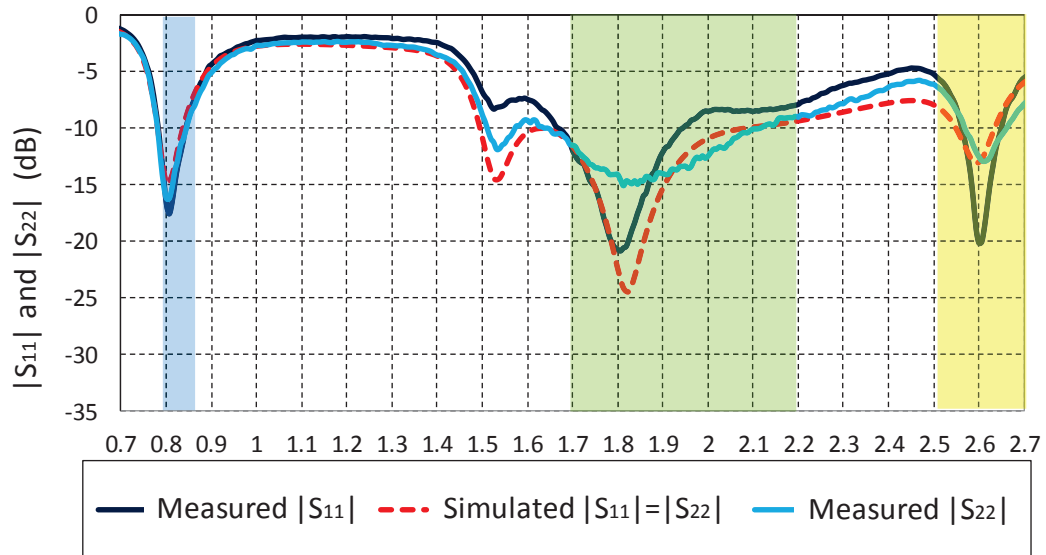


Figure 138: MIMO antenna system in CST and prototype

The S-parameters are presented in Figure 139. Since the DRAs are similar and the structures are symmetric, the $|S_{11}|$ and $|S_{22}|$ parameters are very similar and they are well matched on the four LTE frequency bands. Moreover, the system reciprocity implies that the $|S_{21}|$ parameter is equal to the $|S_{12}|$ parameter. Since the distance between the two radiating elements equals $\lambda_0/8.5$ at 800MHz, the coupling reaches its maximum of -6dB on this frequency band. This coupling will therefore result in a lower realized gain and thus a lower efficiency compared with the case when the antenna is studied alone in Chapter Two.



(a)

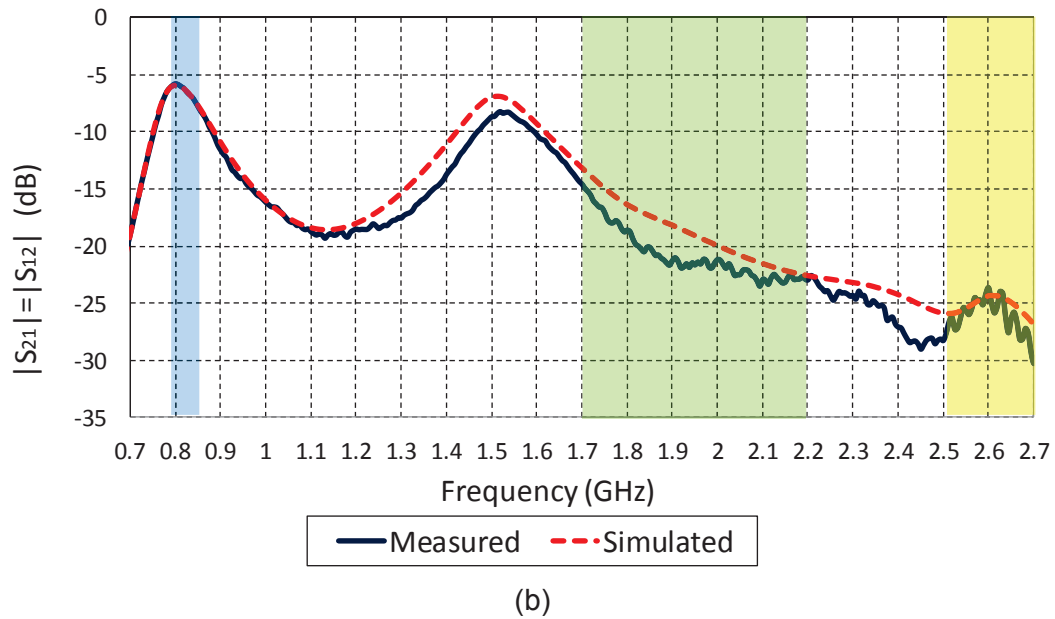


Figure 139: (a) Measured and simulated $|S_{11}|$ parameter. (b) Measured and simulated $|S_{22}|$ parameter. (c) Measured and simulated $|S_{21}|$ parameter.

Figure 140 plots the total efficiency and maximum realized gain according to the frequency. As expected, it demonstrates that the antenna efficiency is lower for frequency bands where the coupling is higher than 10dB. However, this efficiency remains more than acceptable since it is higher than 50% around 800MHz, higher than 70% between 1.7GHz and 2.2 GHz and better than 60% for the highest LTE frequency band.

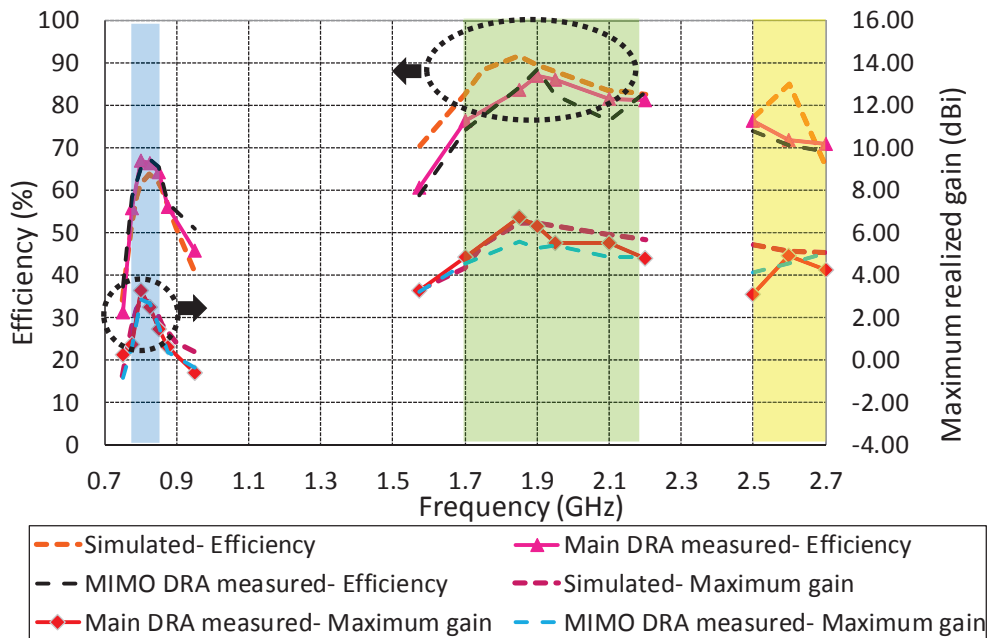


Figure 140: Measured and simulated maximum realized gain and total efficiency for the proposed DRA in the MIMO system

Figure 141 shows the 3D simulated radiation patterns for the Main and MIMO antennas at 800MHz, 1575MHz, 1800MHz, 2150MHz and 2600MHz. It can be observed that the radiation patterns are dependent on the excited DRA.

However, these results are not sufficient to conclude that the radiation pattern is reconfigured. To check whether the radiation pattern is reconfigured, the most widely used parameter is the Envelope Correlation Coefficient (ECC).

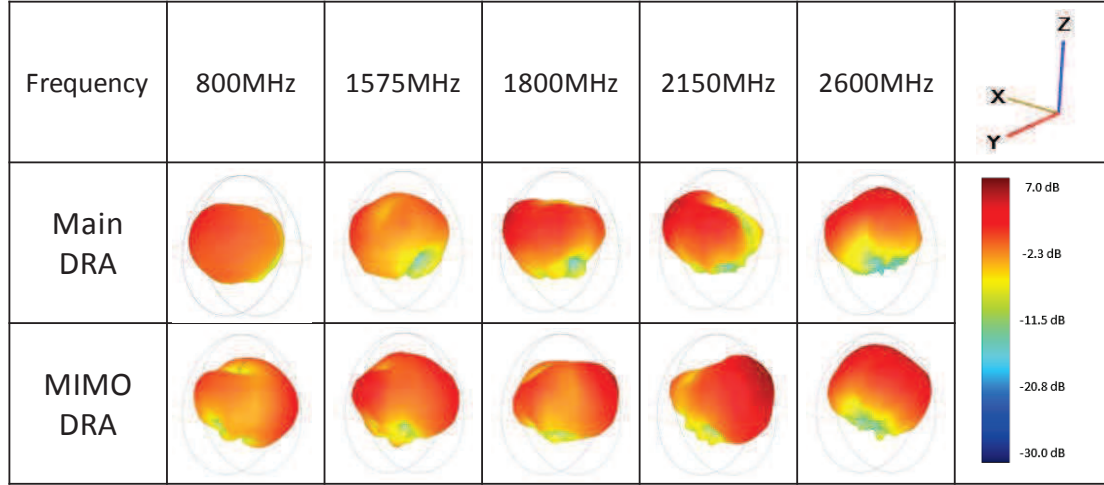


Figure 141: Measured 3D radiation pattern at different frequencies for the MIMO system

IV.2.3. ECC value for the MIMO system

The ECC evaluates the correlation between the signals received by the two antennas and defines if the diversity antenna system could operate properly. The ECC can be calculated using either the far field radiation patterns or S-parameters [68].

An important parameter to evaluate the diversity performance of a system is the Envelope Correlation Coefficient (ECC). In effect, it evaluates the correlation between the signals received by the two antennas and defines if the diversity antenna system could operate properly. The ECC can be calculated using either the far field radiation patterns or the S-parameters [68], [69]. However, using S parameters for the ECC calculation is valid only for highly efficient antennas [70]. In this antenna design, using S parameters could cause inaccurate results, particularly around 800MHz (efficiency around 50%). Therefore, in this study, ECC values are obtained by using the far field radiation patterns (Equation 18) and Figure 142 plots the ECC on each LTE frequency band.

$$\rho_e = \frac{|\iint_{4\pi} [\vec{F}_1(\theta, \phi) \cdot \vec{F}_2(\theta, \phi)] d\Omega|^2}{\iint_{4\pi} |\vec{F}_1(\theta, \phi)|^2 d\Omega \iint_{4\pi} |\vec{F}_2(\theta, \phi)|^2 d\Omega} \quad (18)$$

$\vec{F}_n(\theta, \phi)$ is the field radiation pattern of the antenna system when port 1(n=1) or 2(n=2) is excited.

The ECC value range is between 0 and 1 with 1 corresponding to similar radiation patterns. The necessary diversity requirement is a value lower than 0.5.

For the antenna system, the ECC is lower than 0.25 meaning that the radiation pattern is well reconfigured and the MIMO system has good pattern diversity for the four LTE bands.

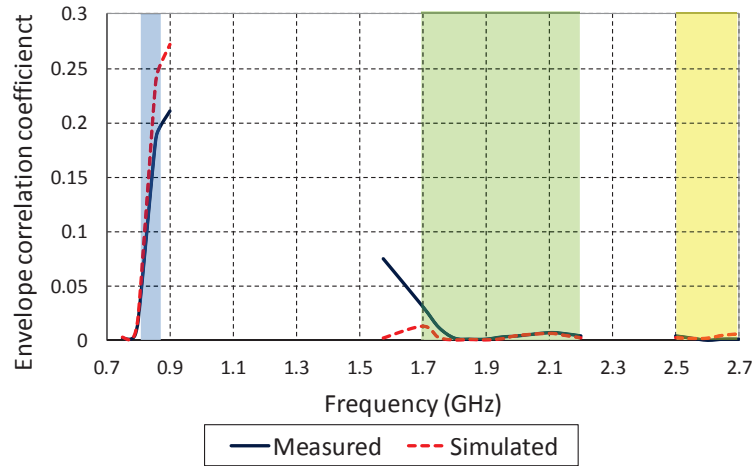


Figure 142: ECC value of the MIMO system

IV.3. Beam steering system structure and performance

IV.3.1. Ideal system

We can obtain the beam steering radiation pattern through different phase signals by integrating an ideal phase shifter and a 3dB divider with the global system described in Figure 136. Figure 143 shows the ideal steering far field radiation patterns which we would like to obtain.

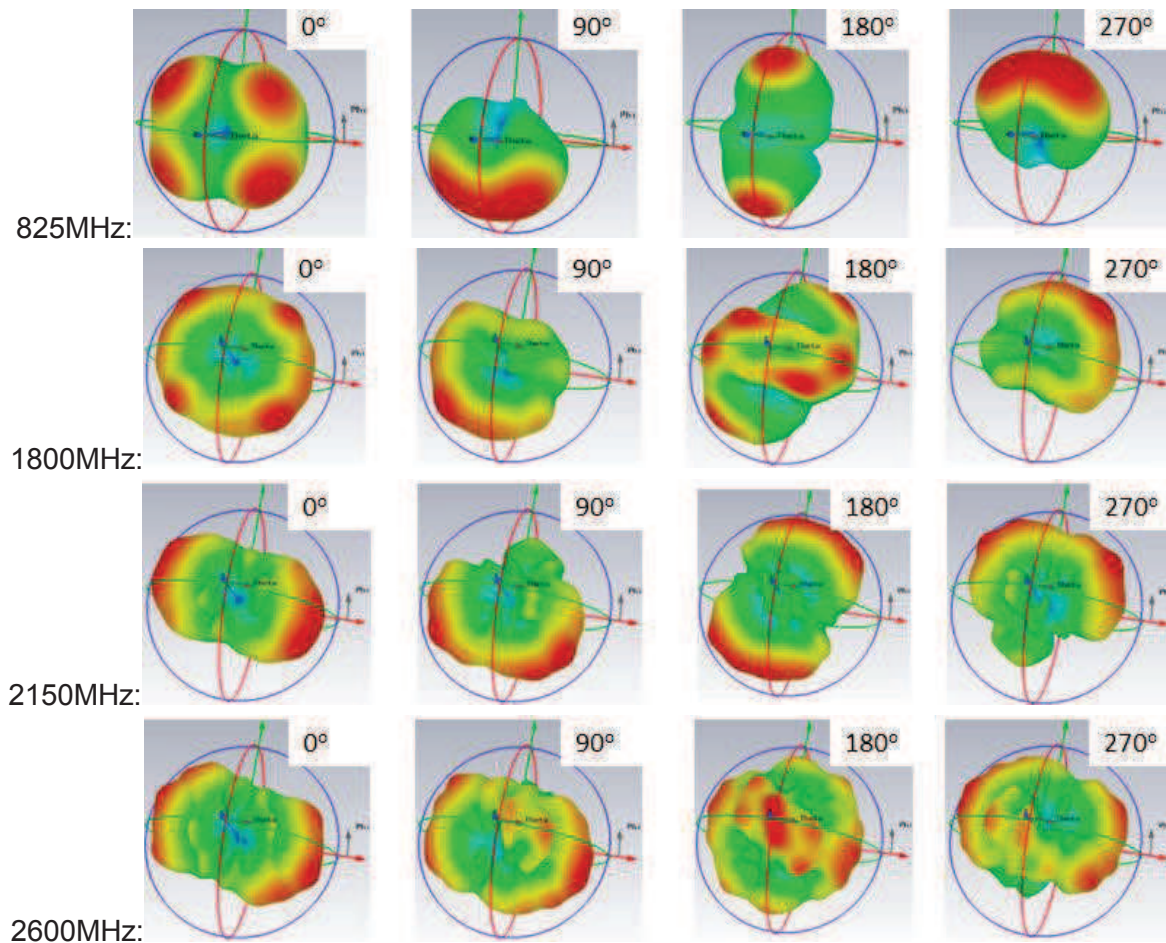


Figure 143: Ideal radiation pattern of proposed global system

IV.3.2. Global system with manual-switched phase shifter

We built the prototype of the global system integrated with a 3dB power divider, a phase shifter, reference line and DRA array. Since the SP4T-switched phase shifter realized in Chapter Three degraded performances with ripples on the S parameters of our system, a manual-switched phase shifter is therefore adopted in this section.

Both the $|S_{11}|$ and efficiency of the DRA with phase shifter is shown at the beginning of the paragraph. Then the global system performances are demonstrated. After that, we change the variable capacitance to observe beam steering results.

IV.3.2.1. DRA with manual-switched phase shifter

It is important to check the DRA performances step by step before integration into the global system. Hence, we simulated and measured the DRA with manual-switched phase shifter and reference line as described in Figure 144. Figure 145 presented the $|S_{11}|$ parameter of the reference line with DRA and efficiencies charts according to the chosen line.

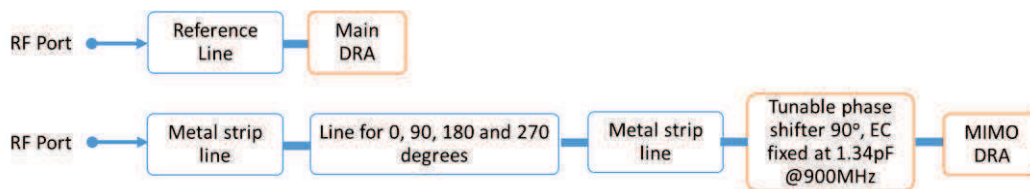
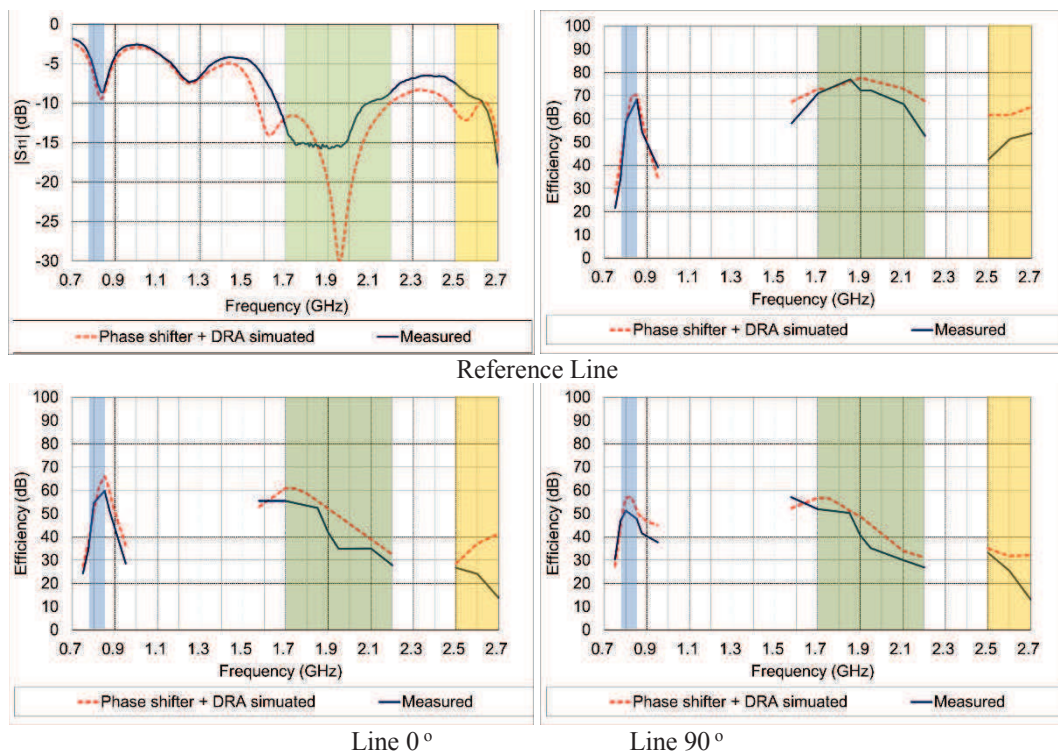


Figure 144: Setup for measuring different paths in the manual-switched global system



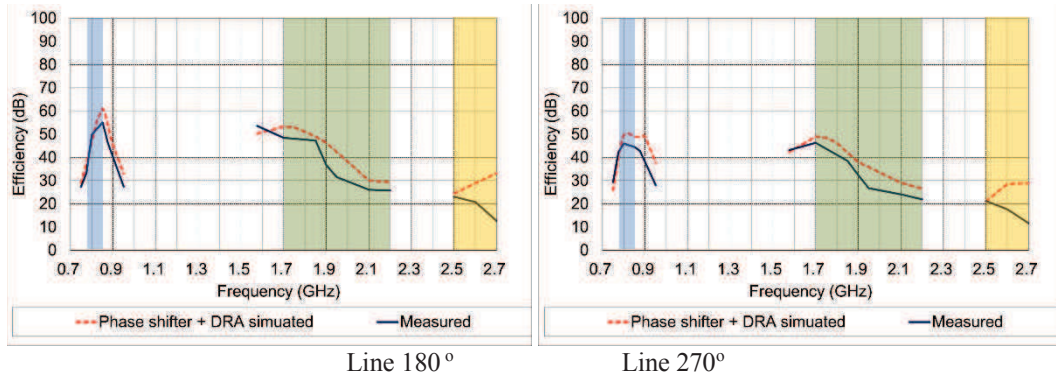


Figure 145: Performance of DRA with manual-switched lines

Simulations predict the system performances well since they are in good agreement with the measurement. The efficiency is higher for the lowest LTE band. The length of the lines are measured from 70mm to 220mm implying attenuation transmission losses of more than 2.6dB at 3GHz for the longest line since the substrate used is an FR4 with a loss tangent of 0.025.

IV.3.2.2. Global system with manual-switched phase shifter

The global system is composed of a DRA with a reference line and a DRA with phase shifter lines developed in Chapters Two and Three. We also implemented a commercial 3dB power divider (Woken Technology Inc) to measure all parameters. Figure 146 shows the prototype of the global system. In this section, we use a metal strip to replace SP4T switches as a manual-switched method.

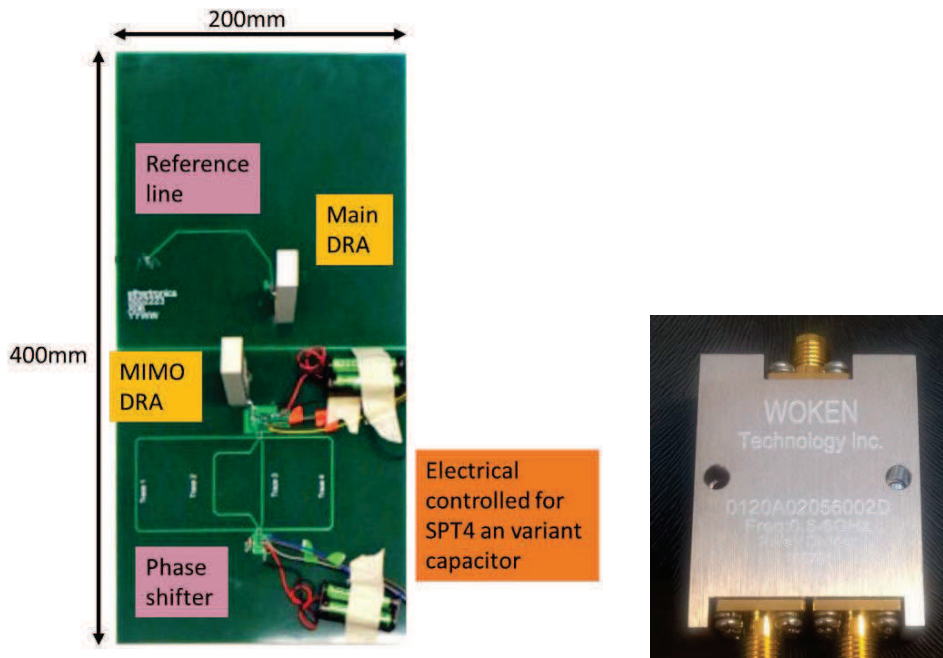


Figure 146: Geometry of the global system and its 3dB power divider

IV.3.2.2.1. Different switched line paths

As the system is using manual-switches rather than the SP4T, the ripples and interferences from the circuit are not substantial. The system measurement condition is shown in Figure 147 and analyzed in a 2D cut (Figure 148).

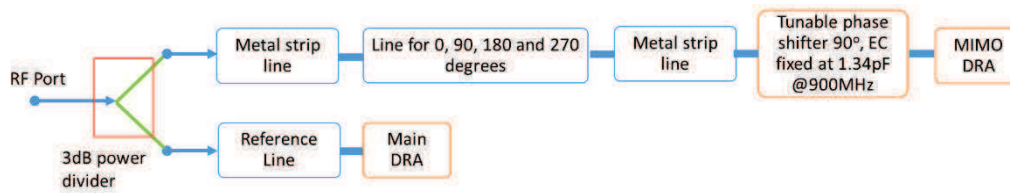


Figure 147: Measurement setup for manual-switched global system with fixed variant capacitance

Around the 825MHz frequency band (LTE800DD), the beam is steered by switching different phase shift lines. We can use the maximum gain direction to define the beam steering range, these results are illustrated in Table 6.

Table 6: [Beam steering range in different planes]

	xOy plane ($\theta=90^\circ$)	xOz plane ($\varphi=0^\circ$)	yOz plane ($\varphi=90^\circ$)
Path Line	270- 0- 90- 180	270- 180- 90- 0	0- 270- 180- 90
825MHz	315° - 15° - 15° - 90°	300° - 0° - 75° - 120°	345° - 300° - 60° - 75°
Range	105°	180°	90°

Based on the objectives, the system using the proposed phase shifter provides the benefit of having all the radiation patterns being steered by different traces in the DRA on all the LTE frequency bands – LTE 800DD, LTE 1800+, LTE 2100 and LTE 2600. Therefore, we want to demonstrate with composite 3D gain charts to show the benefit of our global system.

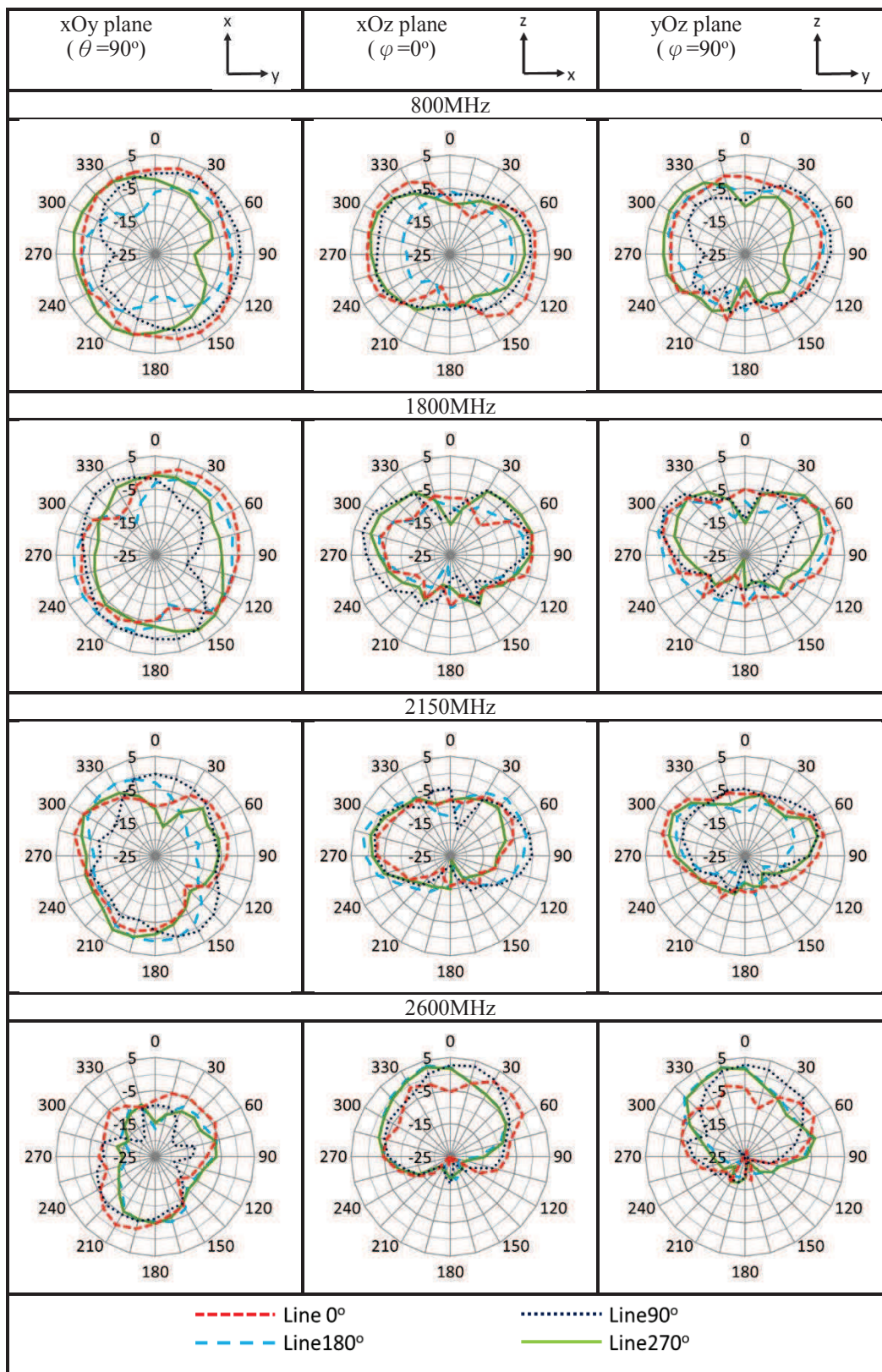


Figure 148: Performance of global system with manual-switched lines

For both LTE 1800+ and LTE 2100 bands, frequencies of 1800MHz and 2100MHz also have obvious beamforming results in xOy planes. For the LTE 2600 band, xOz and yOz have clearer beam steering performances.

IV.3.2.2.2. Composite 3D gain

To show the benefit of using the beam steering system, using a composite 3D gain chart is an appropriate approach method. The composite 3D gain is contributed from the 3D radiation power of each different path to the sum of all the maximum gains at each angle.

We need to understand the total power radiated by integrating the Poynting vector over the surface of a sphere. The radiated power of the antenna is calculated by integrating the radiation intensity over a unit sphere [71]:

$$P_{rad} = \int_{\theta=0}^{\pi} \int_{\varphi=0}^{2\pi} U(\theta, \varphi) \sin(\theta) d\varphi d\theta \quad (19)$$

Where $U(\theta, \varphi)$ is the radiation intensity at each angle in Watts per solid angle.

An antenna that is radiated equally in all directions is called an isotropic antenna. This antenna will have $U(\theta, \varphi)=1$ and

$$\int_{\theta=0}^{\pi} \int_{\varphi=0}^{2\pi} \sin(\theta) d\varphi d\theta = 4\pi$$

The effective isotropic radiated power to the measured antenna, we define as $EiRP$:

$$EiRP(\theta, \varphi) = P_T G_T(\theta, \varphi) = 4\pi U(\theta, \varphi) \quad (20)$$

Where $P_T G_T$ is the product of the power delivered to the antenna and the antenna's power gain. Therefore,

$$P_{rad} = \frac{1}{4\pi} \int_{\theta=0}^{\pi} \int_{\varphi=0}^{2\pi} EiRP(\theta, \varphi) \sin(\theta) d\varphi d\theta \quad (21)$$

The total $EiRP$ will be measured, having two orthogonally polarized components, $EiRP_{\theta}(\theta, \varphi)$ and $EiRP_{\varphi}(\theta, \varphi)$.

$$P_{rad} = \frac{1}{4\pi} \int_{\theta=0}^{\pi} \int_{\varphi=0}^{2\pi} (EiRP_{\theta}(\theta, \varphi) + EiRP_{\varphi}(\theta, \varphi)) \sin(\theta) d\varphi d\theta \quad (22)$$

We assumed that the data is available at uniform angular intervals in theta and phi. In practical measurement, the angular interval is set at 15 degrees which is specified in the CTIA test plan [72]. So, the *radiated power* of the antenna is calculated with the following equation:

$$P_{rad} \cong \frac{\pi}{2NM} \sum_{i=1}^{N-1} \sum_{j=0}^{M-1} [EiRP_{\theta}(\theta_i, \varphi_j) + EiRP_{\varphi}(\theta_i, \varphi_j)] \sin(\theta_i) \quad (23)$$

N = number of angular intervals in the nominal theta range from 0 to π

M = number of angular intervals in the nominal phi range from 0 to 2π

i = index for each theta sample, i ranges from 0 to N

j = index for each phi sample, j ranges from 0 to M

The anechoic chamber radiation pattern is used for sample calculation at every 15 degrees. N is 12 and M is 24 for gain measurement setup.

To calculate the composite gain, we measured the radiated power $EiRP_{\theta}(\theta_i, \varphi_j) + EiRP_{\varphi}(\theta_i, \varphi_j)$ at every 15 degrees for four different paths. Then we selected the maximum value from the four paths compositing a new radiation pattern as equation (22) which means the 3D composite gain becomes $P_{rad-composite}$.

The antenna composite efficiency can be obtained by this equation.

$$\eta = \frac{P_{rad-composite}}{P_A} \quad (24)$$

P_A is the power delivered to the antenna.

In future related work, we can use a program to select the path based on the parameters of wireless communication quality related to our antenna system. Indeed, if there is no interference during the wireless transmission, the best path selected should be the highest gain in each sample angle from the gain result of the four paths.

The 3D radiation pattern for different paths and the composite radiation patterns are shown in Figure 149 and Figure 150.



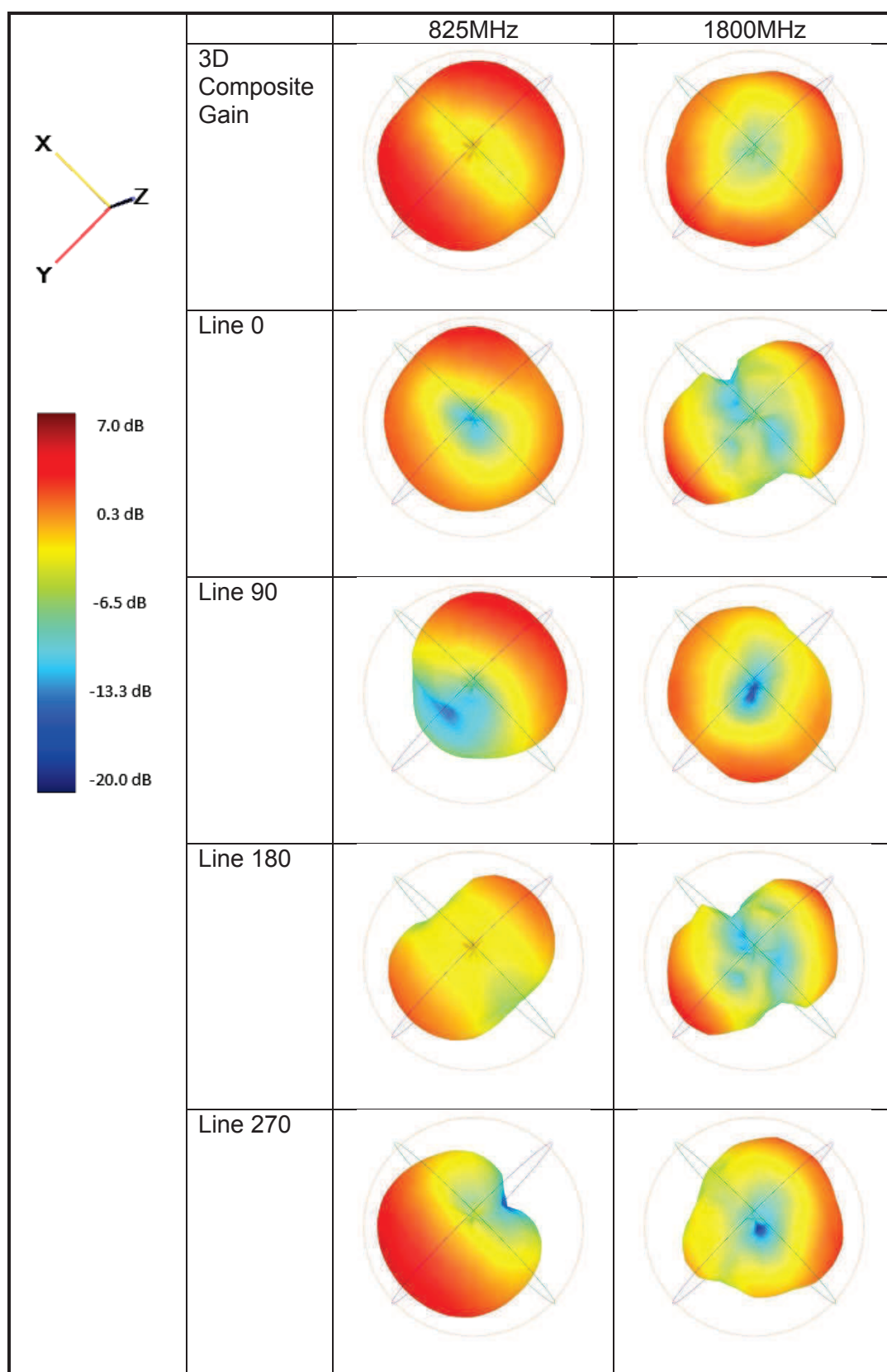


Figure 149: 3D radiation pattern and composite radiation pattern for manual-switched lines - 825MHz and 1800MHz.

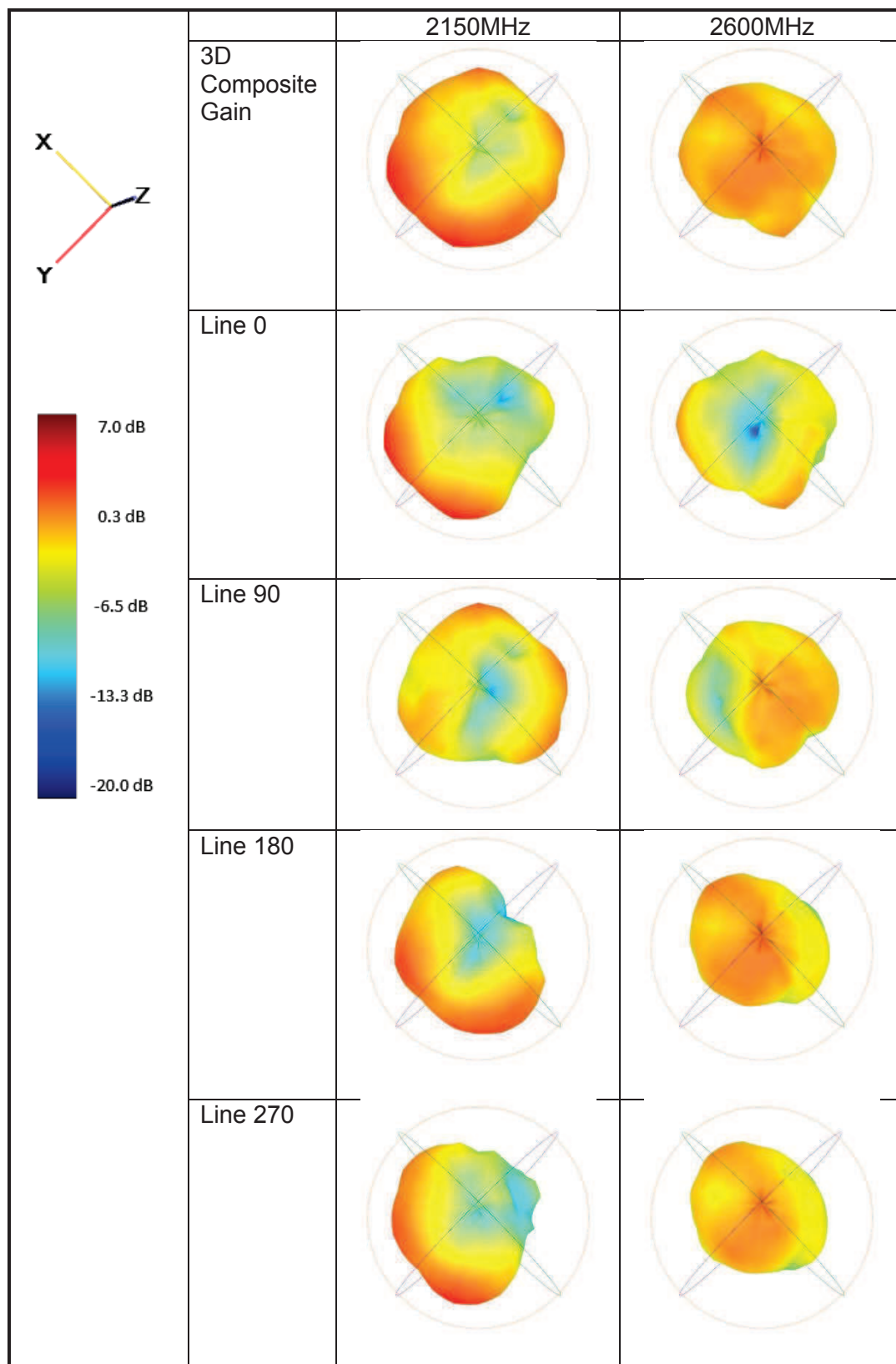


Figure 150: 3D radiation pattern and composite radiation pattern for manual-switched lines - 2150MHz and 2600Hz.

Figure 151 plots the 3D composite gain in a 2D map at 800MHz and demonstrates the benefits from a beam steering system. This figure compares two cases: (1) Using of one path (0 degree), which meant that there is no beam steering; (2) Combining the maximum realized gain from different lines. We can observe that the null areas are reduced when the phase shifter is used. Therefore, the coverage of the wireless communication service is increased by switching different traces of the global system.

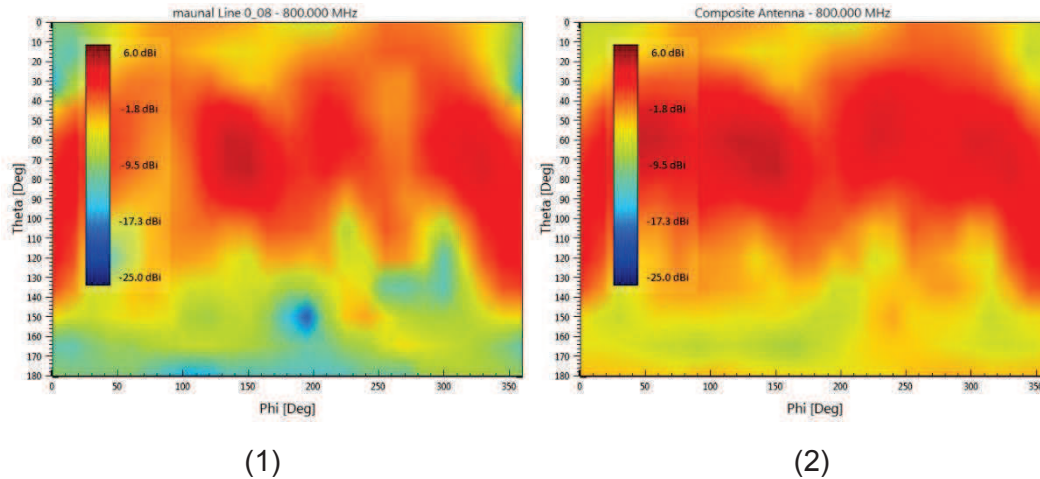


Figure 151: Composite gain for manual-switched global system at 800MHz

IV.3.2.3. Switching with different variable capacitance

In Chapter Three, we presented the integration of a variable capacitance in order to improve the phase shifter for the LTE 1800+, LTE 2100 and LTE 2600 frequency bands. We demonstrated that the insertion losses increased for specific states of the variable capacitances. Therefore, in this paragraph, we use some specific and lower capacitance states to verify the beam steering performance. The setup presented in Figure 152 is investigated with capacitance values from 0.78pF to 2.34pF. The 2D cut results are presented in Figure 153.

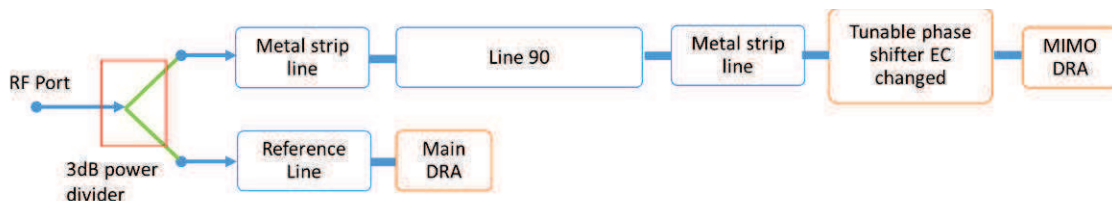


Figure 152: Measurement setup for global system while varying the capacitance

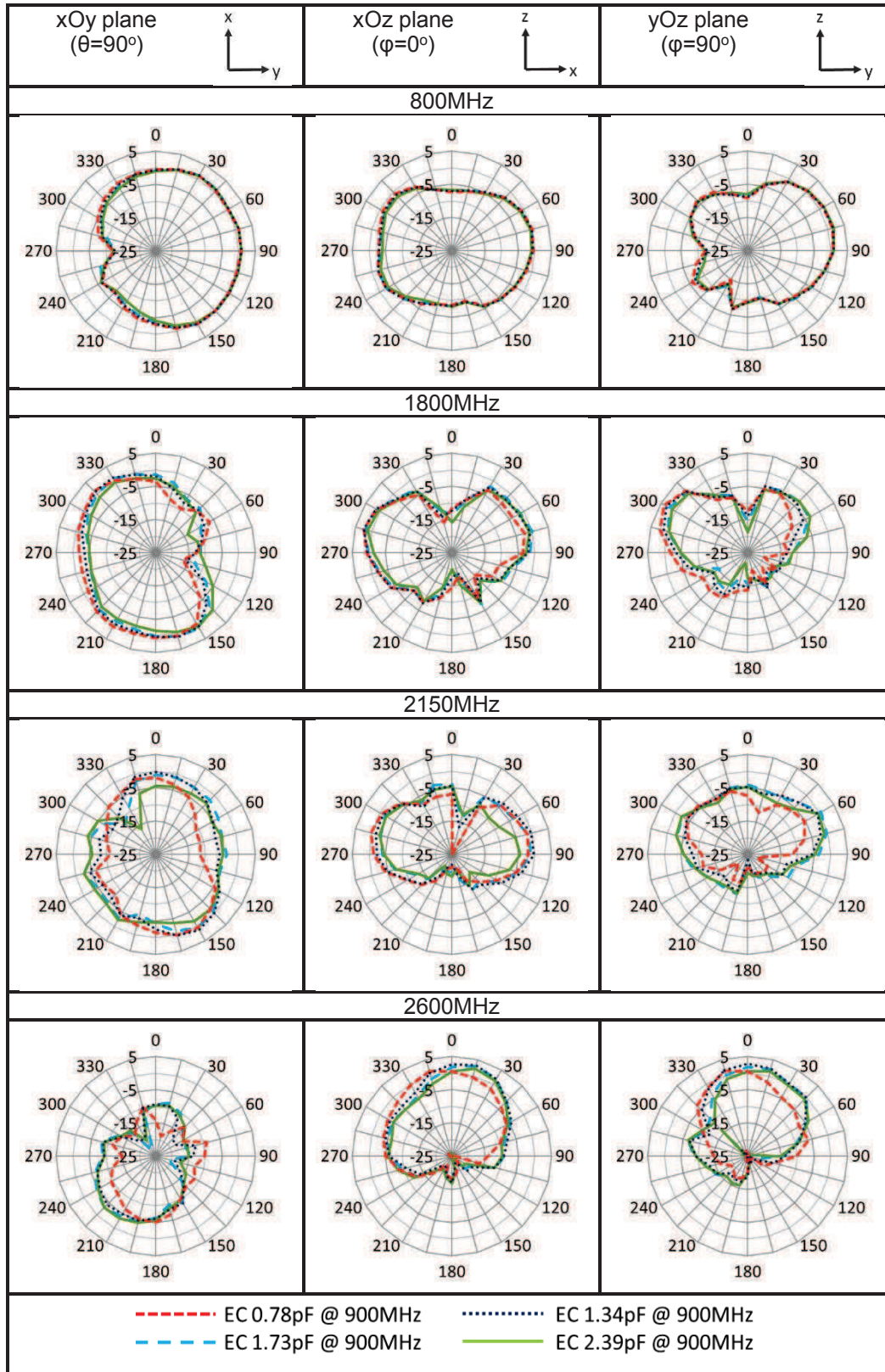


Figure 153: Variable capacitance impact on 2D radiation

From the above results, the radiation beam is steered clearly when the frequency is higher than 1.8GHz. These results show that the tunable phase shifter is dedicated from the 1.8GHz to 2.6GHz frequency range as mentioned in Chapter Three.

IV.3.3. Global system with SP4T-switched phase shifter

In Chapter Three, we showed that using SP4T-switches added more losses and ripples to the system. Nevertheless, it is worth evaluating whether the radiation pattern could steer toward the expected direction.

Figure 154 shows a diagram of the global system with an active SP4T-switch. We integrated the differential SP4T-switched phase shifter with our antenna system. For comparison to the manual-switched system, we also fixed the variable capacitance value.

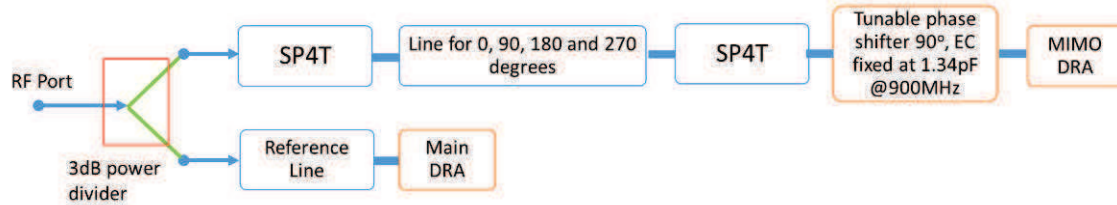


Figure 154: Setup for IC-switched global system

Compared to the manual-switched system, the antenna efficiency is 1dB lower when the frequency is below 1.9GHz. When the frequency is higher than 1.9GHz, the system performance is lower by around 2dB. This phenomenon can be mapped to different phase shifter characteristics with the $|S_{11}|$ higher than -10dB at a frequency higher than 1.9GHz. However, the composite efficiency of the SP4T-switched global system is good as it is over 50% at 800MHz. Although the efficiency is lower than our expectation, the beam direction is still changed by using an SP4T-switched phase shifter. The radiation patterns are shown in Annex I.

Since this global system is proposed for use in a vehicle, the next step is to implement it in the vehicle environment.

IV.4. Beam steering system in automobile environment

As already presented for the DRA alone in Chapter Two, Figure 155 presents the global system measured within its real context, i.e. in an automotive environment. The full active beam steering global system is placed at different locations: on the rooftop, on the dashboard and under the roof top. The efficiency and radiation pattern are all calculated for the upper hemisphere only, since the chamber receive antennas cannot go under the ground plane. The chamber is calibrated from 800MHz to 950MHz and from 1600MHz to 2700MHz. The global system uses a SP4T-switched setup for the radiation pattern measurement.

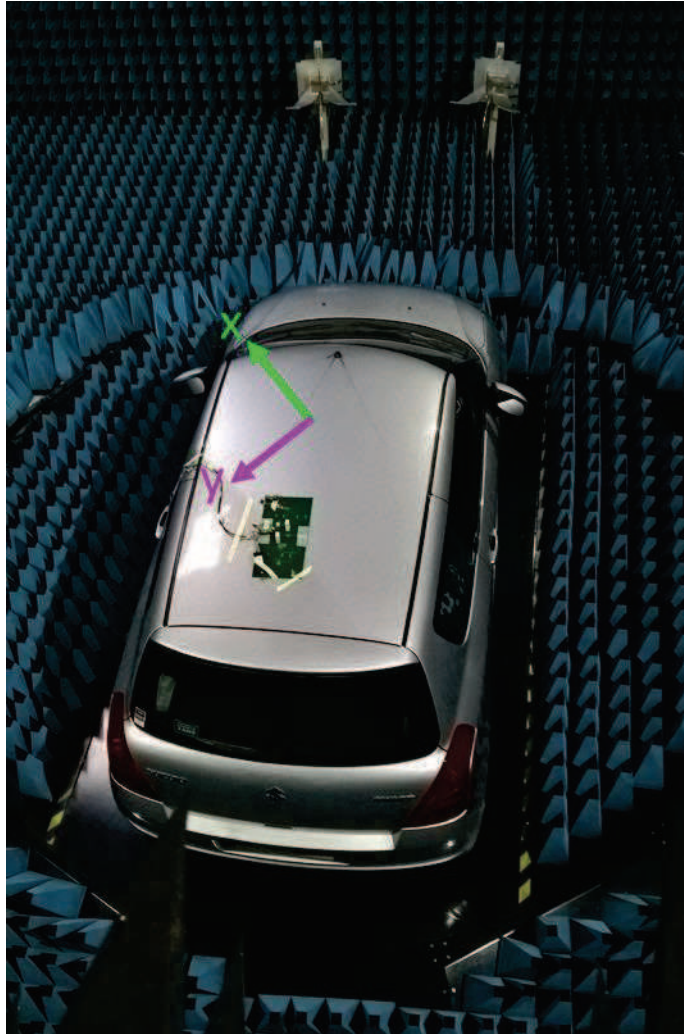


Figure 155: Photo of 3D chamber for measuring the global system.

IV.4.1. Measured results of global system located on vehicle rooftop

The measurement setup is presented in Figure 156. The global system is located on the rooftop and has a 45° rotation compared to the previous free space measurement.

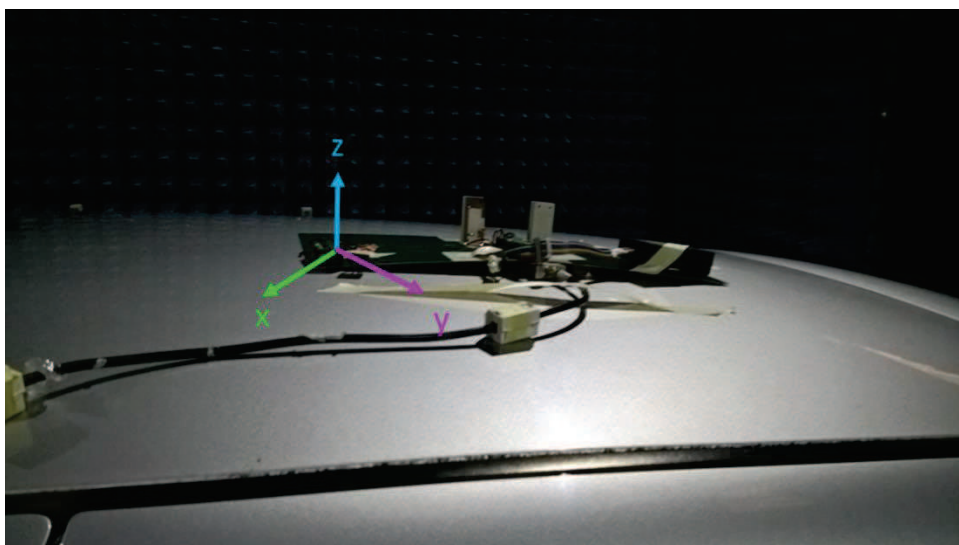


Figure 156: Photo of global system located on the rooftop.

IV.4.1.1. Beam steering system gain

Figure 157 demonstrates the global system composite gain by combining measured results when the SP4T is switched between different traces. At 800MHz, the gain is improved by the proposed system.

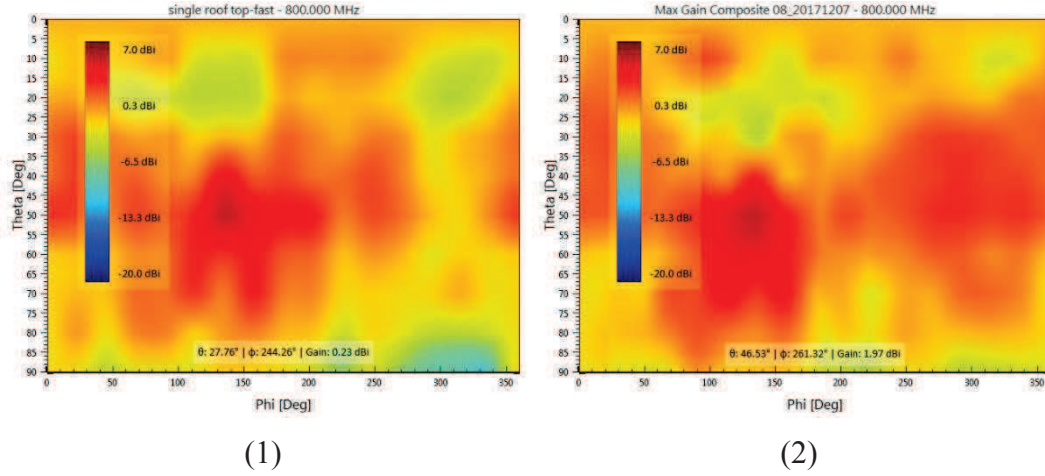


Figure 157: Gain improvement for global system located on the vehicle rooftop at 800MHz: (1) single antenna (2) beam steering system

The global system also gets the benefit of obtaining a higher maximum gain from different traces (Figure 158) at 1800MHz. The global system can always select the best mode based on different situations.

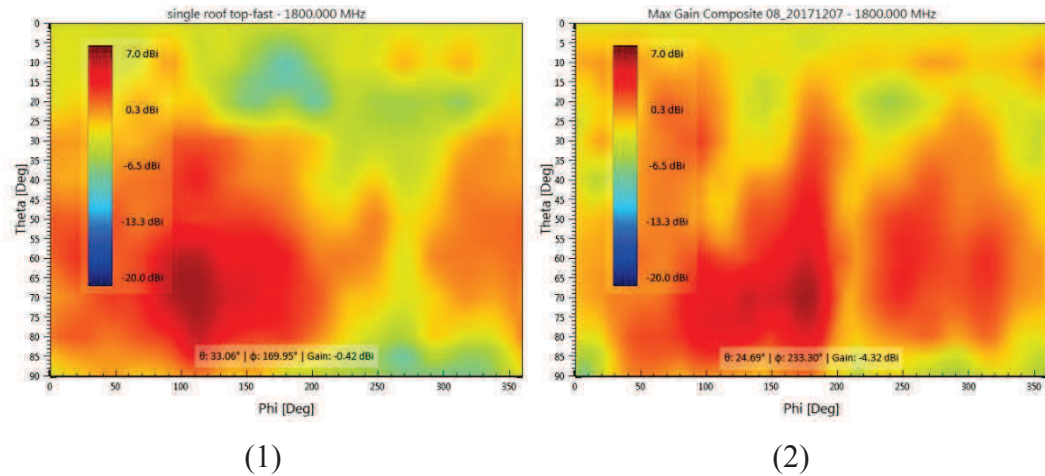


Figure 158: Gain improvement for global system located on the vehicle rooftop at 1800MHz: (1) single antenna (2) beam steering system.

From these results, we can compare the global system measured in free space with the real use case, i.e. on the vehicle. Figure 159 demonstrates the result of the composite efficiency comparison. The two measured results are similar and mapped to each other. Since the global system ground plane is 200mm×400mm (2 sets of DRA with SP4T-switched system), the measured results are similar to the actual vehicle rooftop area.

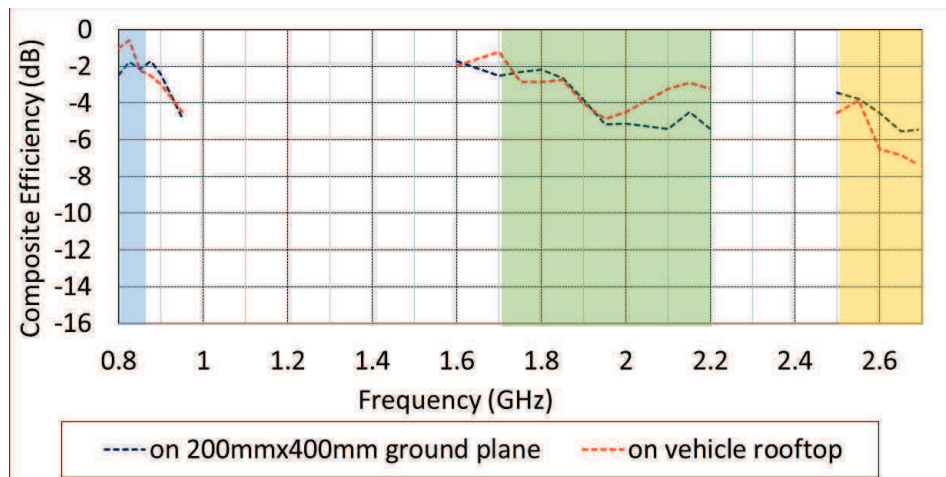


Figure 159: Compared composite efficiency in free space and on vehicle rooftop

Thus, the global system performed well on the vehicle rooftop for all the targeted bands. Typical frequency points are demonstrated here: 800MHz, 1600MHz, 1800MHz, 1900MHz, 2150MHz and 2600MHz. (Figure 160, Figure 161 and Figure 162)

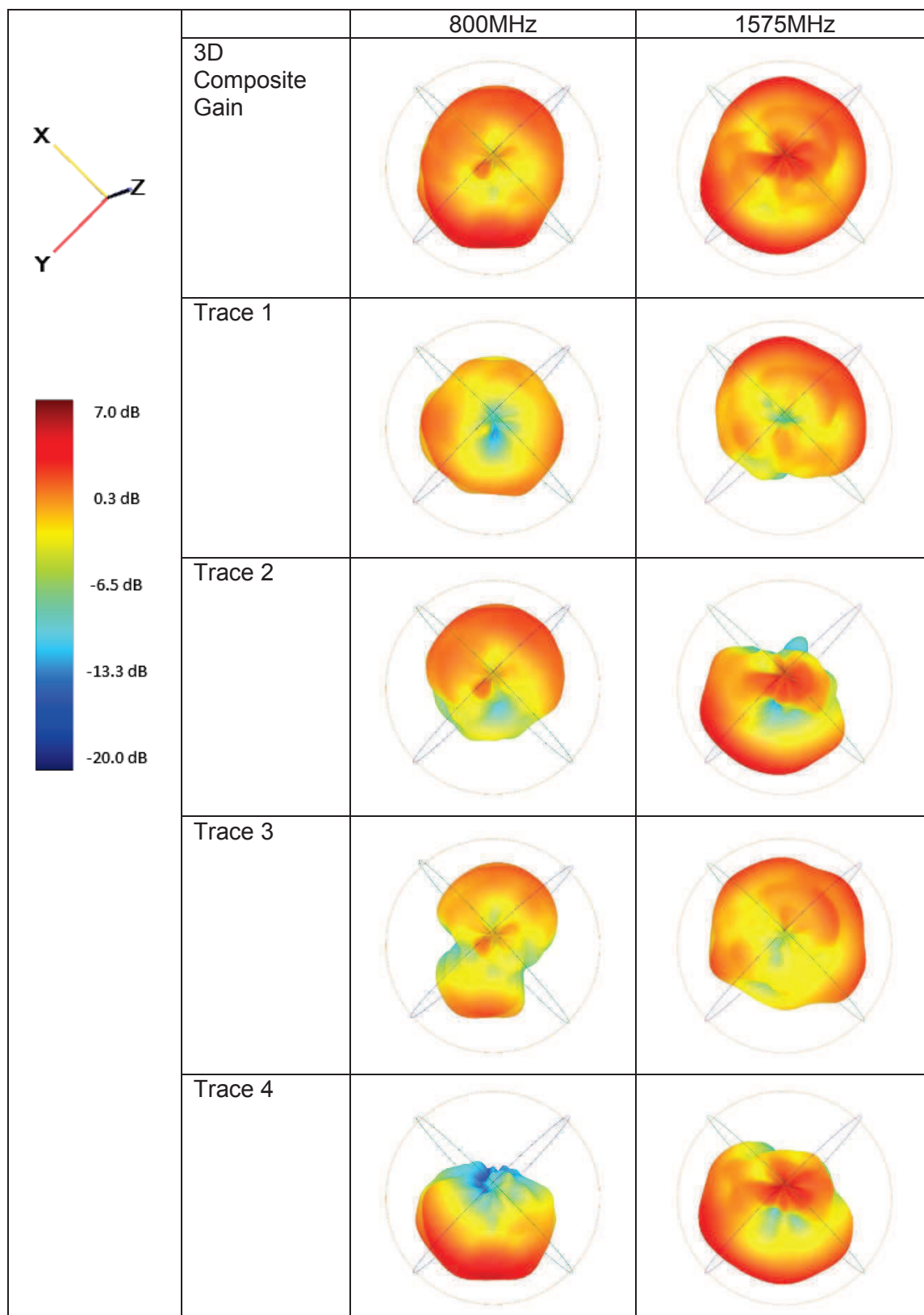


Figure 160: 3D radiation pattern and composite radiation pattern for global system on vehicle rooftop- 800MHz and 1600MHz.

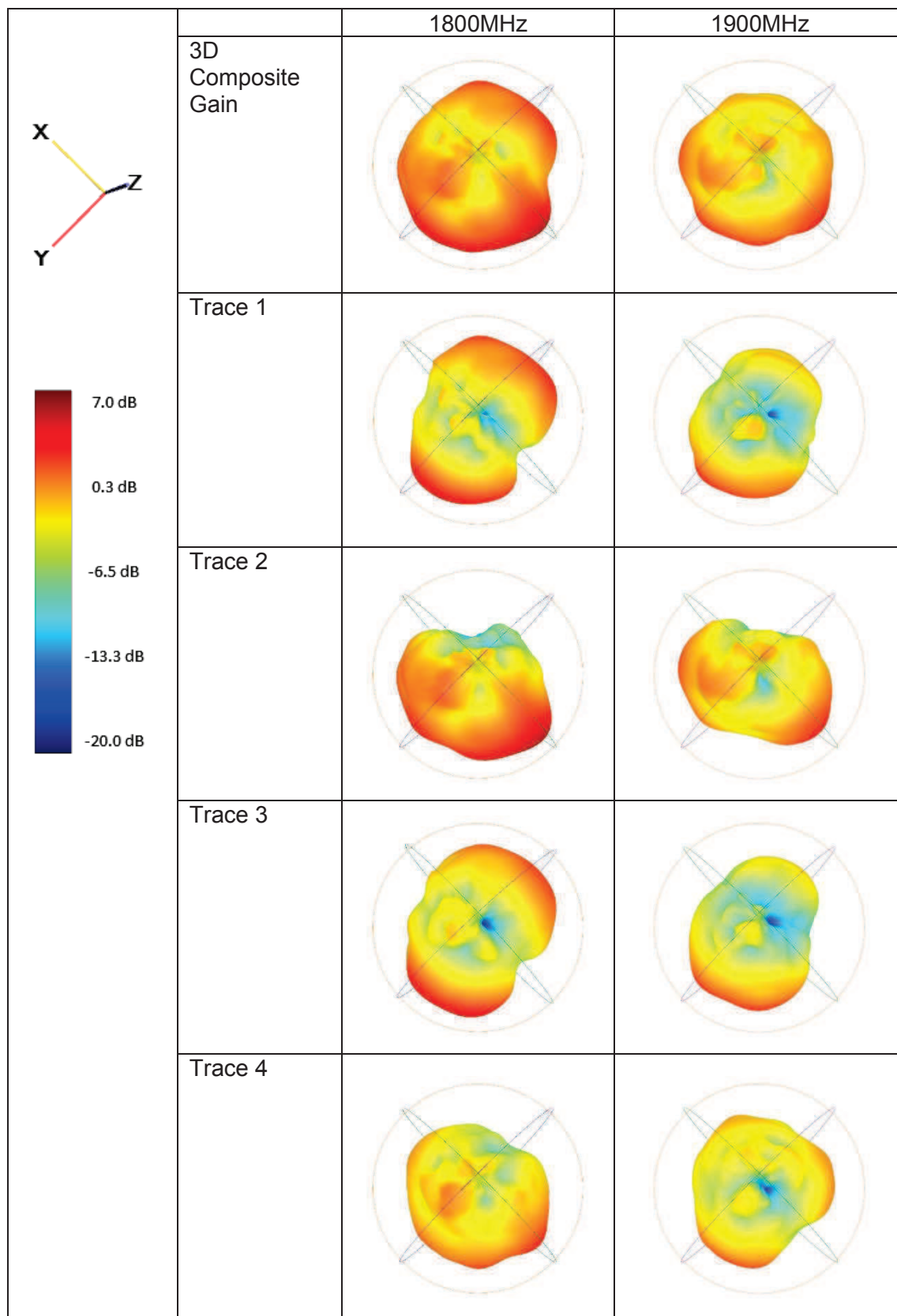


Figure 161: 3D radiation pattern and composite radiation pattern for global system on vehicle rooftop-1800MHz and 1900MHz.

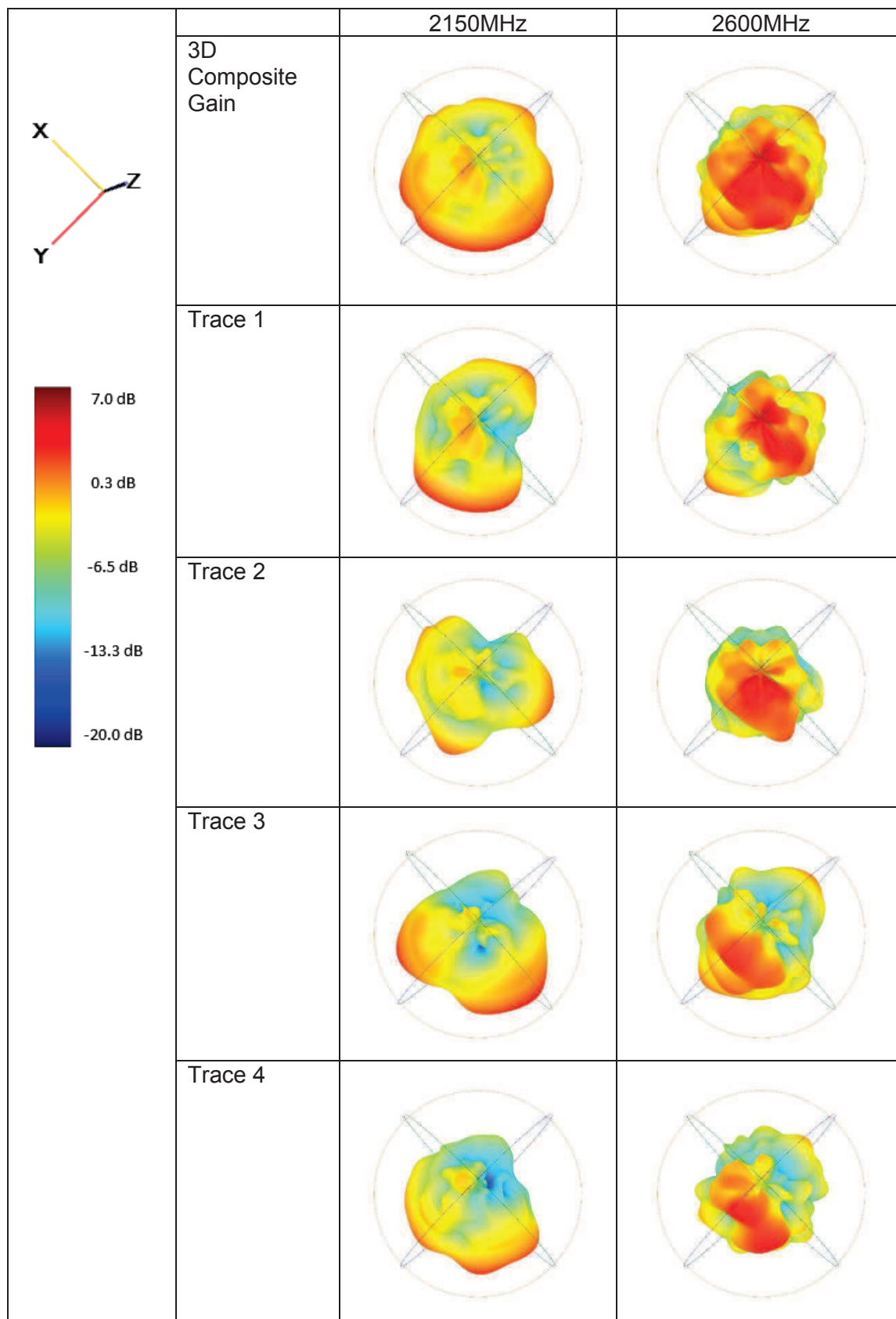


Figure 162: 3D radiation pattern and composite radiation pattern for global system on vehicle rooftop- 2150MHz and 2600MHz.

Previous results can be summarized by plotting the 3D composite radiation pattern. Figure 163 therefore illustrates the advantage of using the global system to steer the radiation pattern. From these radiation pattern results and the composite efficiencies, our system on the vehicle rooftop corresponds closely to the IC-switched global system measured in a normal anechoic chamber.

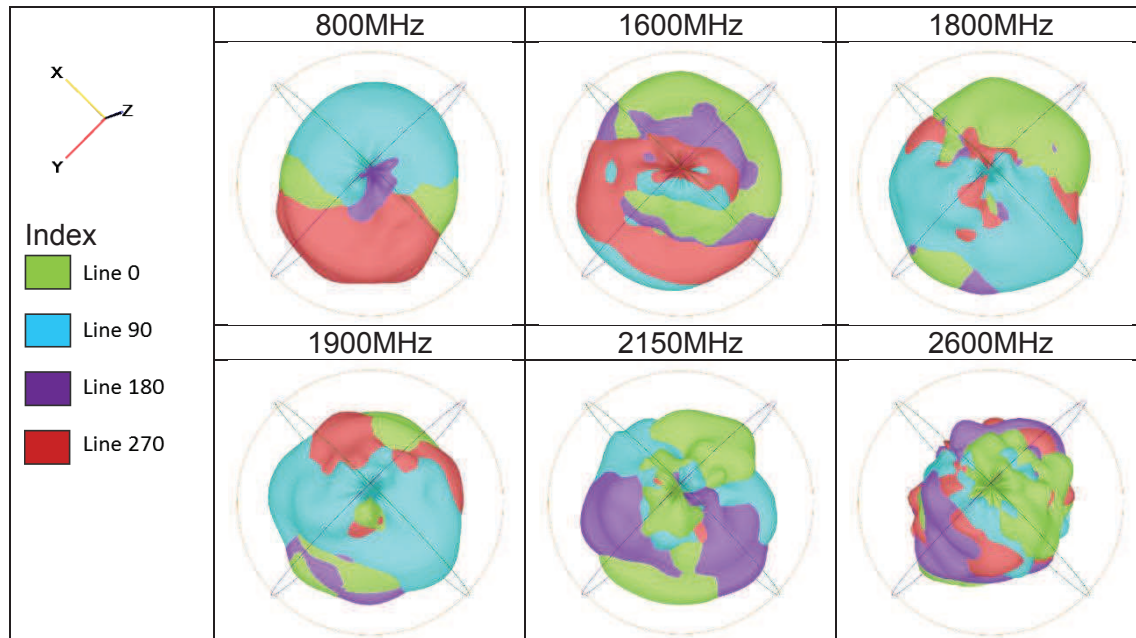


Figure 163: Composite maximum gain by trace index for global system on vehicle rooftop.

IV.4.2. Measured results of DRA located on dashboard

Since the rooftop is not the only location to place the antenna system, the dashboard location is also evaluated. Figure 164 is the photo for the IC-switched global system testing setup on the dashboard of the vehicle. It needs to be understood that the system orientation is set for the easiest method of implementation. These measurements are expected to maintain the benefit of active beam steering of the proposed global system even in such inhospitable environments- lots of metal shielding around the antenna system.

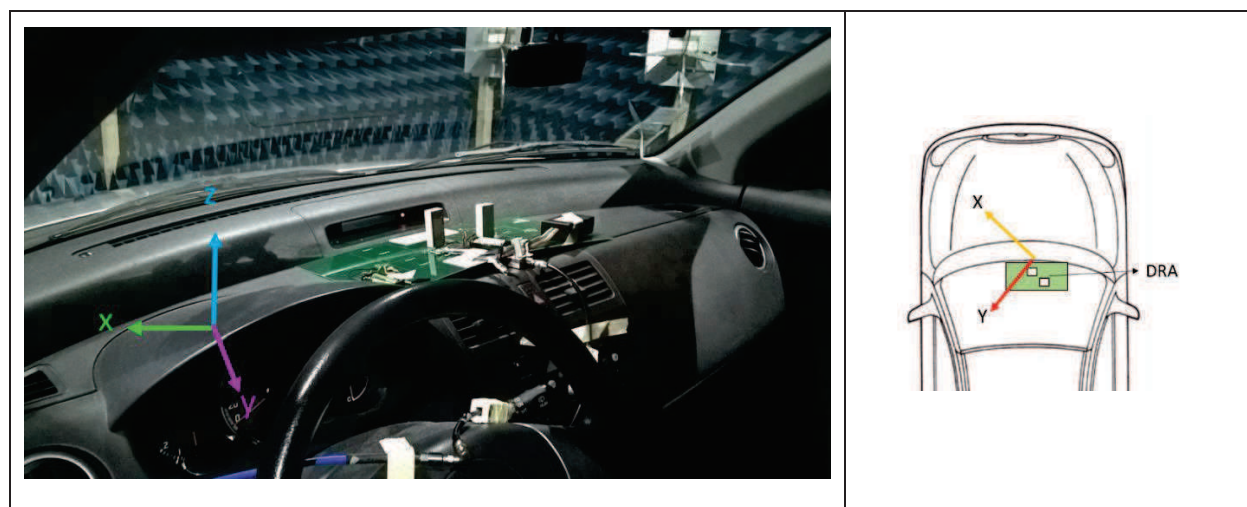


Figure 164: Photo of the global system located on the dashboard.

IV.4.2.1. Beam steering system gain

Figure 165 shows the low frequency and high frequency simple 3D radiation pattern versus the traces. It is clear that the beam steering of the global system on the dashboard has real benefit for both low and high frequency bands.

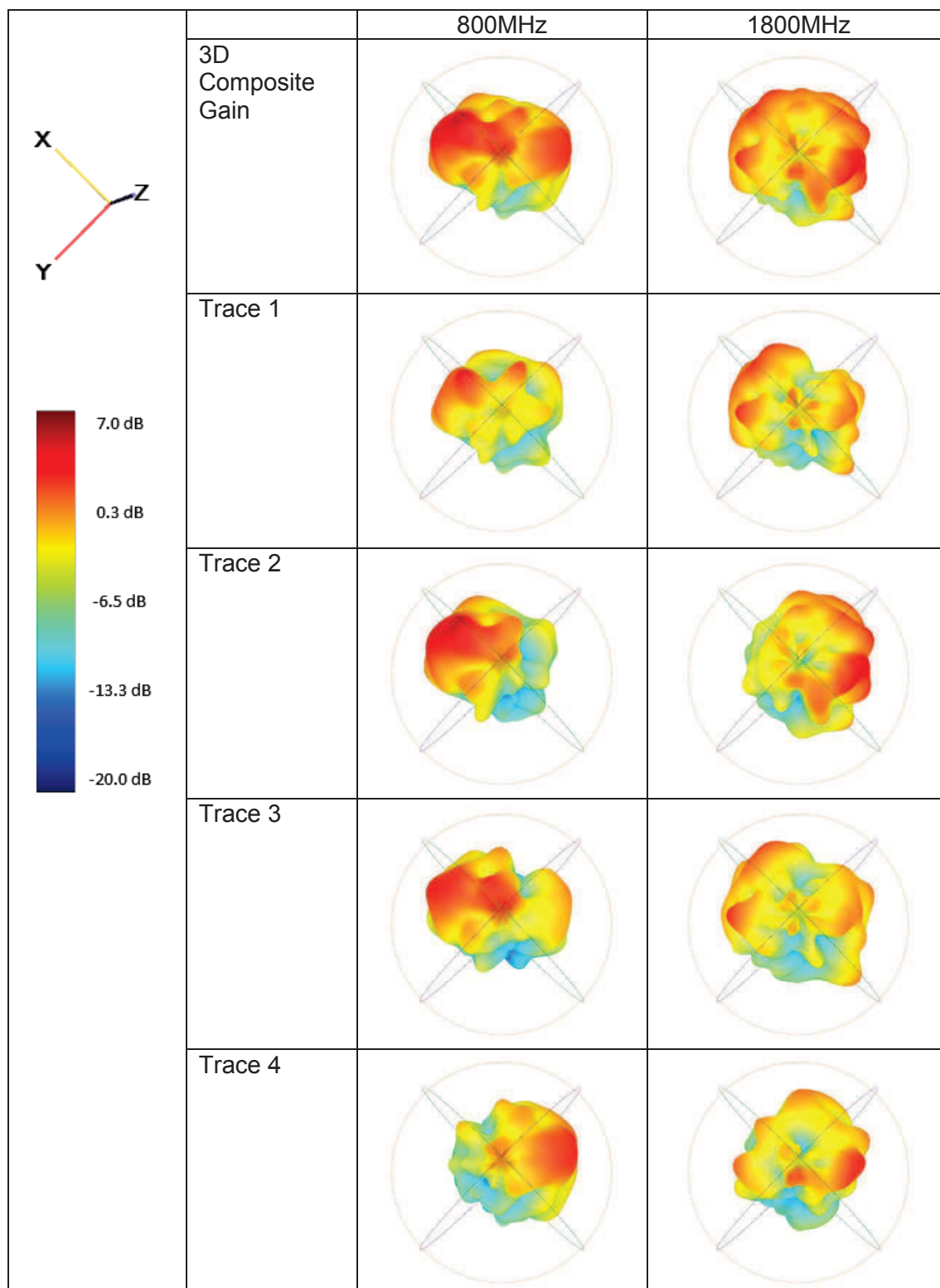


Figure 165: 3D radiation pattern and composite radiation pattern for the global system on the dashboard- 800MHz and 1800MHz.

Since the global system is placed on the dashboard, the radio frequency signal in the direction of the windshield, driver, passenger and so on is disturbed. Therefore, measured radiation patterns are destroyed by the vehicle environment.

Figure 166 shows the benefit in gain improvement by using the beam steering system in such a complex environment- some null angles have better gain by using the system.

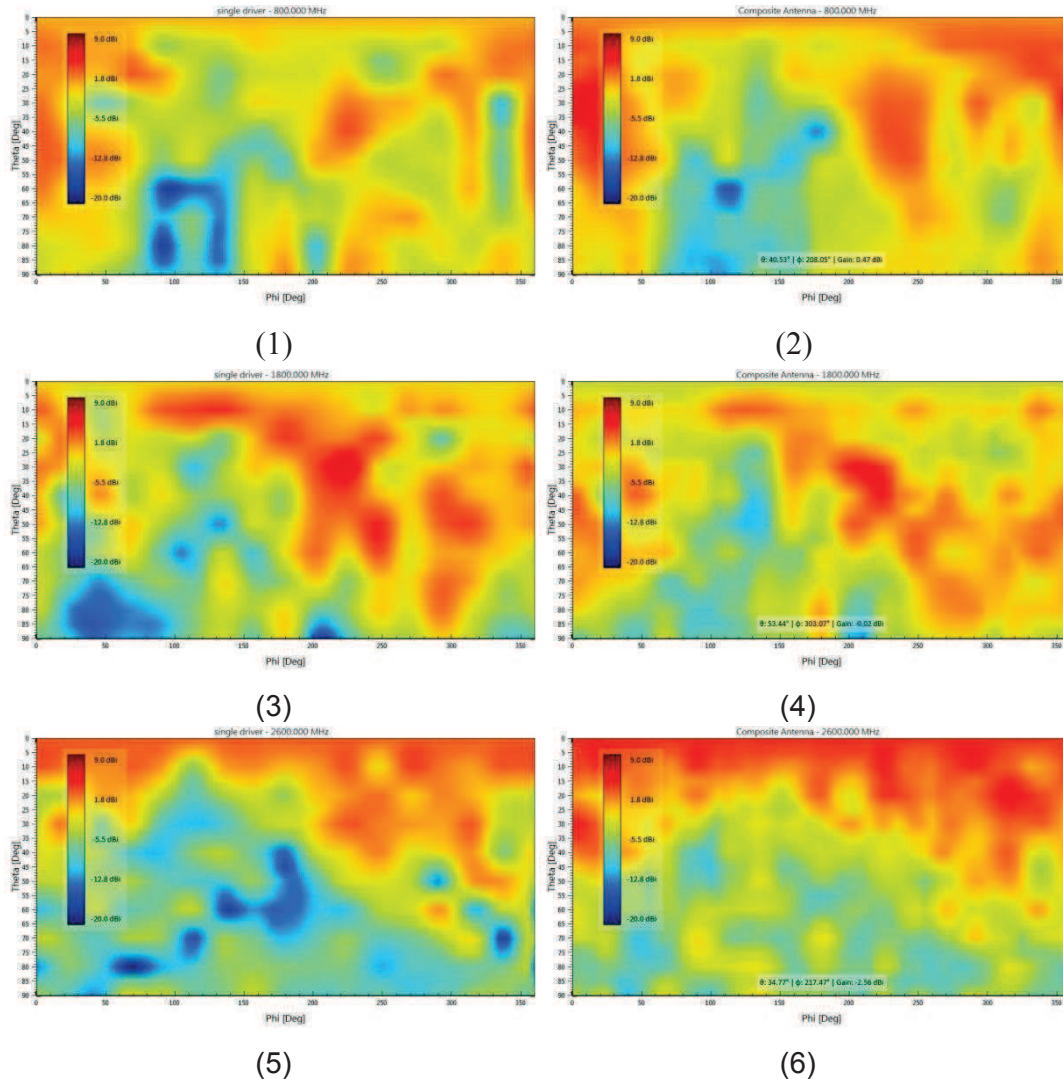


Figure 166: Gain improvement for the global system located on the dashboard at (1) single antenna 800MHz; (2) beam steering system 800MHz; (3) single antenna 1800MHz; (4) beam steering system 1800MHz; (5) single antenna 2600MHz; (6) beam steering system 2600MHz.

IV.4.3. Measured results of DRA located under the vehicle rooftop

The third location is to place the global system under the vehicle rooftop which is very close to the driver's head (Figure 167). The setup is completely reversed compared to the setup in the Section IV.4.1. The antenna is located in the middle of the rooftop area. There is no human in the vehicle during the efficiency measurement.

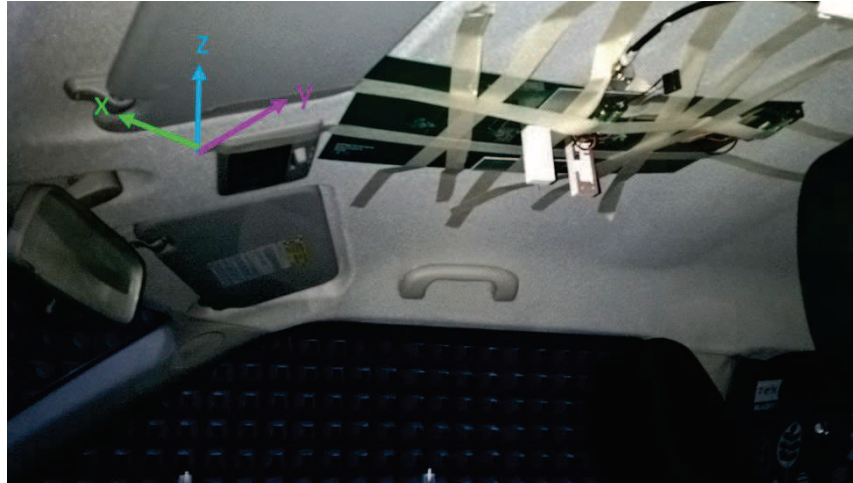


Figure 167: Photo of global system located under the vehicle rooftop.

IV.4.3.1. Beam steering system gain

As with the previous section, we selected 800MHz and 1800MHz to check the radiation pattern with different traces. From Figure 168, the radiation pattern is still steered by switching the traces. However, only low frequencies such as 800MHz can obtain radiation toward the front and the back of the vehicle.

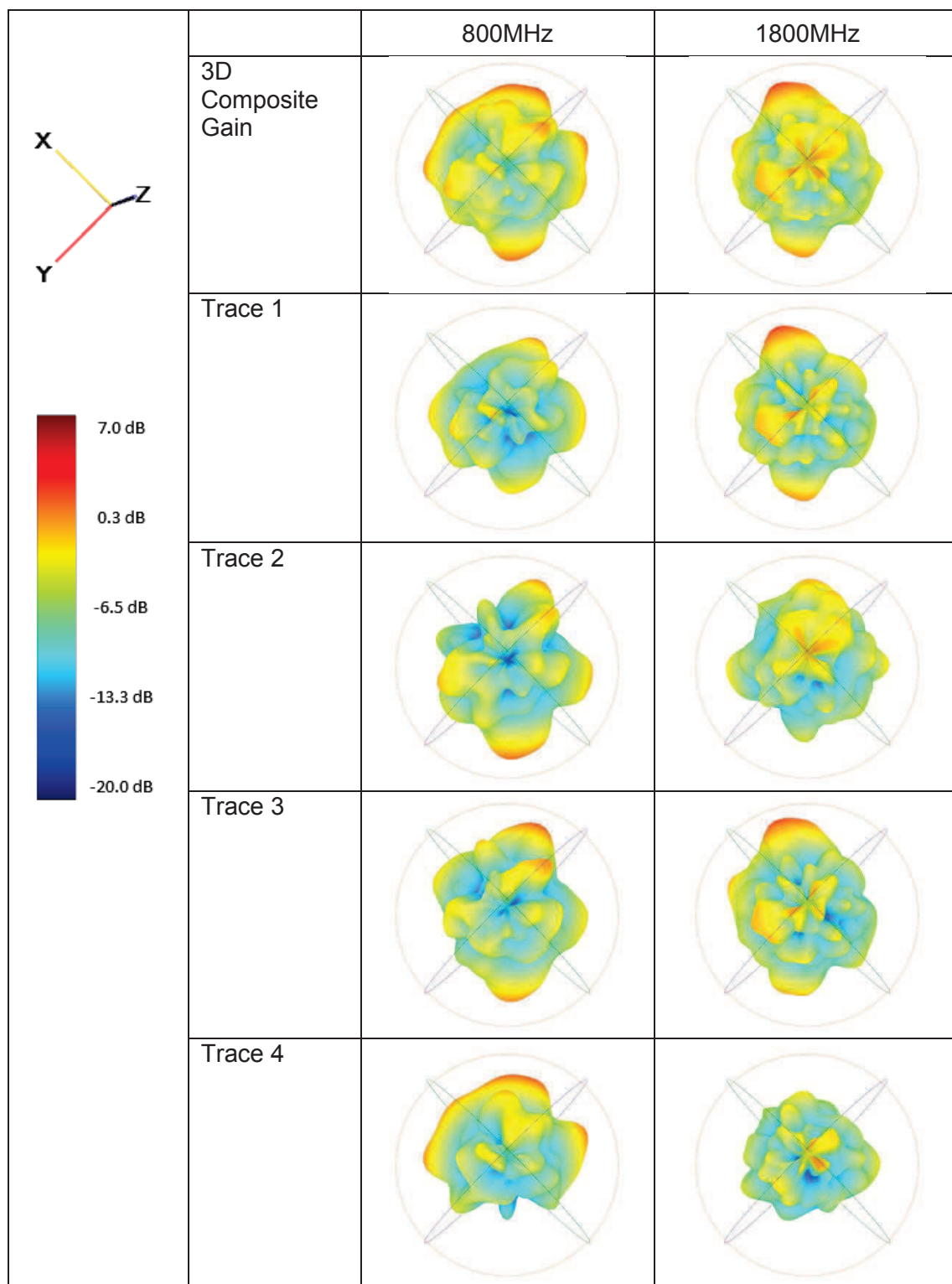


Figure 168: 3D radiation pattern and composite radiation pattern for the global system under the vehicle rooftop- 800MHz and 1800MHz.

IV.4.4. Summary for measurement in vehicle environment

To summarize all the different test conditions, Figure 169 demonstrates comparison of the active beam steering effect in different vehicle environments.

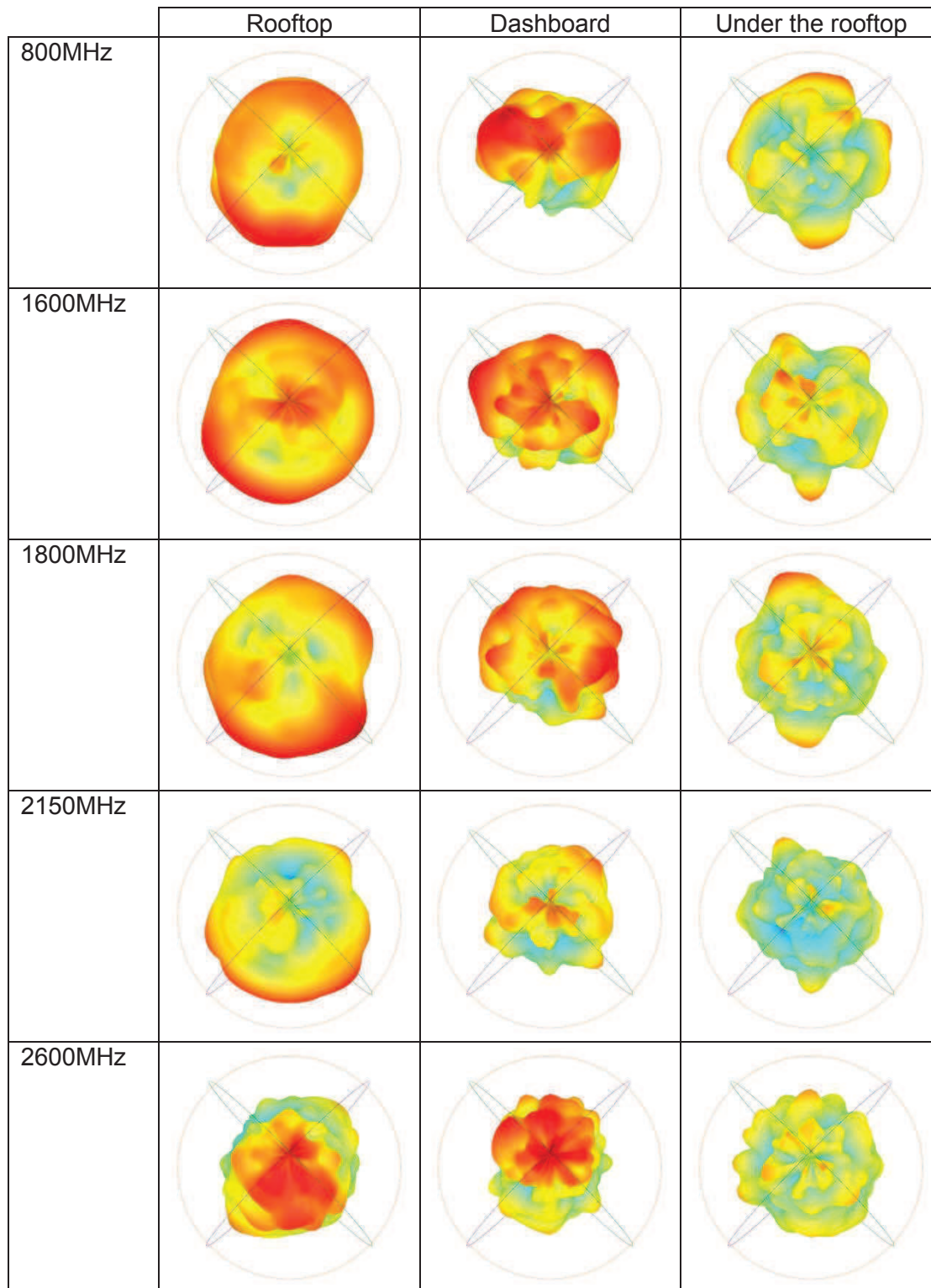


Figure 169: 3D composite gain for global system in automotive environment

From these results, we can plot the phase 0degree efficiencies chart with the composite efficiencies chart according to the frequency in Figure 170. The benefit of beam steering to improve the antenna system performance is demonstrated. It also indicates that the best placement for the antenna in the automobile is on the rooftop. The dashboard location can achieve acceptable results while below the rooftop represents the worst location to place the antenna system.

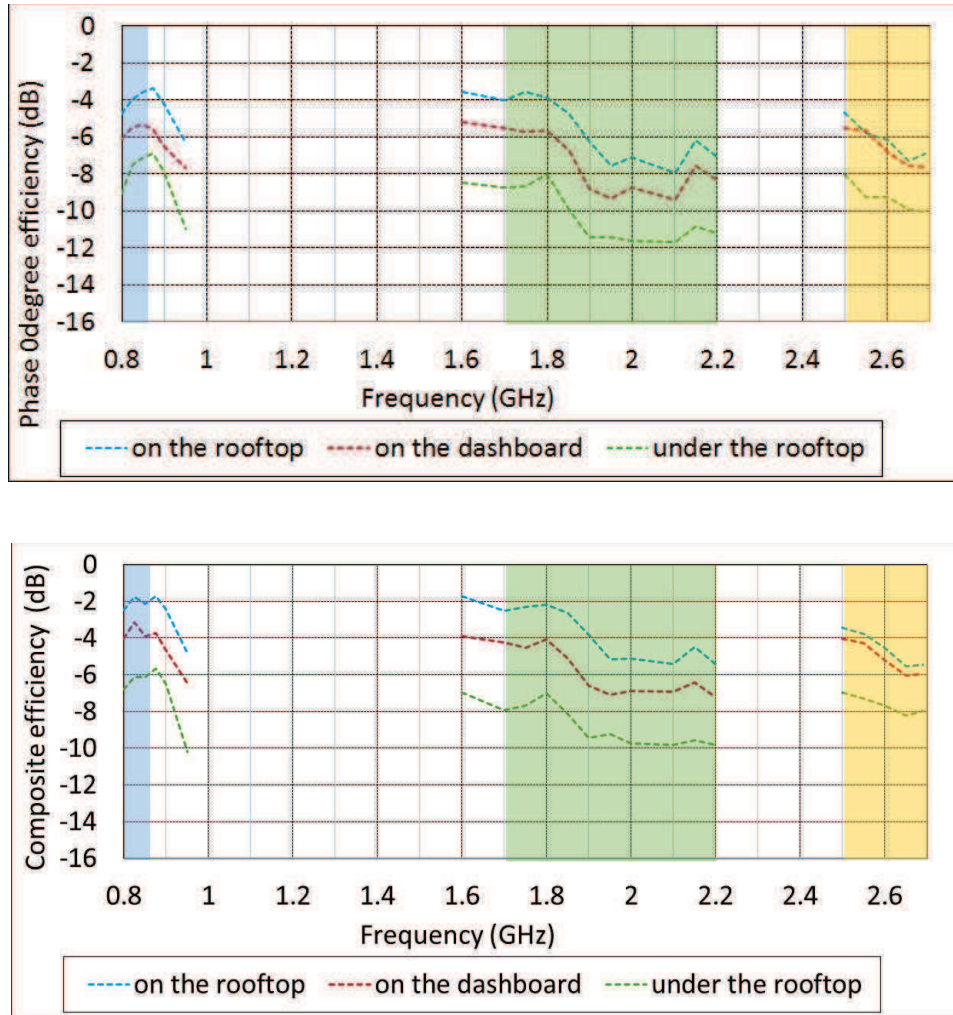


Figure 170: Efficiency of the global system location for all conditions (upper hemisphere).

IV.5. Conclusion

In this chapter, we have demonstrated the performance of a MIMO system. Indeed, the proposed compact and multiband DRA developed in Chapter Two exhibits the advantages of using a dielectric resonator as an antenna by covering LTE 800DD, LTE 1800+, LTE 2100 and LTE 2600. The DRA design satisfies the -6dB impedance bandwidth for the four distinct frequency bands. The antenna efficiency achieved 50% in LTE 800D and 75% in the higher frequency bands while being miniature as it had global dimensions of $\lambda_0/8 \times \lambda_0/17 \times \lambda_0/29$ at 790MHz. The MIMO system was composed of two DRAs placed within a small area. They presented a low ECC value (under 0.25) while exhibiting good performance with over 50% total efficiency. All the measurements are well matched with the simulations. The proposed antenna has a simple rectangular shape with only one surface printed with copper which can be easily fabricated. With these features, this antenna is very suitable for practical automotive MIMO applications.

To transfer this structure as a beam steering system, we provided signals with phase differences to both DRA feeds in order to get alternative radiation patterns. This antenna array has only two DRA elements and is able to achieve the performance of beam steering. This system combined the different types of beam steering system: switched-parasitic method and feeding phase different signal method. We used the MIMO DRA as the parasitic element in the beam steering system with the main DRA as the driven element.

We used the manual-switched phase shifter to evaluate the characteristics step by step. The system performed well and agreed with the simulated results, and exhibited beam steering.

Finally, we integrated the SP4T switches into the full system to auto-switch for practical applications. The global system can be easily controlled by programming the electrical control of the lines. Although the efficiency of the global system is impacted by the implementation of switches, the beam steering coverage can be kept similar to the manual-switched system. For frequencies higher than 1.5GHz, we can adjust the phase difference by changing the variable capacitance.

The SP4T-switched global system has been tested in the real vehicle environment and the advantages of the global system are demonstrated. By selecting the proper phase shifter trace the desired beam direction can be reached. The global system was also tested on the dashboard and under the rooftop where it is under a metalized surrounding. The system still presented beam steering behavior, and employing such a system clearly improved the composite efficiency.

Conclusion

The development of an “active” beam steering antenna system for automotive application was investigated. Since there is limited space available to place the antennas, the key subject of this research is the design of a miniaturized antenna system. Data connectivity will be one of the keys to enable autonomous car services. Ensuring reliable data connectivity over a cellular network is a challenge when the vehicle is moving fast and changing cells frequently. In an automotive environment, a directional antenna should have more benefits than a non-directional antenna. However, a directional radiation pattern must be toward the desired direction in order to improve the quality of the data throughput rate. Therefore, it is better if the antenna is able to steer the beam in the wanted direction.

Beamforming systems have already been investigated in recent years. Indeed, a lot of the papers focused on an improvement of the data throughput rate in WLAN 5GHz band or WLAN 2.4GHz. There are only a few studies talking about beam steering at such low frequencies as 800MHz which is normally the cellular networks frequency bands (2G, 3G or LTE communication system). There are several conventional methods used to achieve beam steering. Analog beamforming antenna with phase shifters and combiners can be fabricated at low cost. These solutions require at least two antennas to create an antenna array which leads to a bulky device. This kind of system brings design constraints regarding the location of the antenna or the cosmetic appearance of the device.

In this study, we also used the analog beamforming method as the basic system concept. To save system space, we proposed the use of the existing MIMO antenna as a 2nd antenna element to allow an “active steering” capability of the cellular system. We proposed to feed-in the phase difference signal to both antennas to achieve beam steering. Many commercial 4G LTE/3G/2G modules claim to use the MIMO technique, but this does not necessarily work. Sometimes the host only has 2G or 3G signal which does not support MIMO. In these cases an “active beam steering” system such as the one we propose can be beneficial.

We started by introducing and simply analyzing different beamforming systems. We provided the concept of our beamforming system consisting of a Main antenna and a MIMO antenna. We would like to use this method to achieve 360° radiation pattern coverage at frequencies as low as 800MHz. The radiation pattern must be steered if we provide a signal with a phase difference of 0°, 90°, 180° or 270° to the antennas.

Therefore, the antenna and phase shifter are the key components for our system.

All the components have to be miniaturized to be usable for an automotive application, particularly for placement on the vehicle rooftop. We decided to use DRA for our system. It could be made compact at the lowest desired frequency while covering higher frequencies. Also, we surveyed the existing phase shifters on the market. None of them are suitable to put in our global system. We decided to design an electronically controlled phase shifter which fit our test requirements.

To minimize the mechanical volume used by the solution, the main and MIMO antenna use dielectric resonator material. Both antennas are to be designed with the same geometry. For the first step, we focused on a multi band DRA with a shape for manufacture. There are several degrees of freedom that can be used for the DRA design. The most interesting features of DRA are the small size of the antenna and its broad range bandwidth. Also, the phase shifter is designed with some SMD components and ICs on a PCB, where thickness

can be a minimum. After that, all these key components were compatible for use in the vehicle environment so it was possible to develop the global active beam steering system for the automotive application.

In Chapter One, we illustrated the MIMO system in commercial communication designs. Then, a concept of the active beam steering global array system was introduced. The principles of several beamforming systems were introduced. The key components of a beam steering system (antennas, phase shifters ...) were presented.

We chose Dielectric Resonator Antennas for the rest of the study because of their ease to manufacture, their small size and wide band.

Several phase shifter structures have also been presented and compared in terms of performances and working frequency range. The desired functions for the phase shifter in this thesis are indicated as: good performance for the lowest LTE frequency of 800MHz, minimum fabrication cost, easy control with a 360° phase.

In Chapter Two, the antenna design aimed to miniaturize its size for a frequency as low as 800MHz and to obtain multi bands and broad bandwidth for LTE operation frequencies. We started to study several characteristics of dielectric resonators and wanted to employ their advantages. The rectangular shaped dielectric resonator antenna was developed and fabricated. The feed mechanism was selected by using a probe fed monopole metallic strip attached to one of the rectangular dielectric resonator surfaces.

Next, the correct dielectric material was chosen by analyzing the modes and resonant frequencies of rectangular DRAs. We need to consider that the antenna efficiency is affected by the losses when the dielectric permittivity increases. Also, the resonant frequency and the bandwidth of the antenna decrease when dielectric permittivity increases. The Q factor increases when bandwidth decreases. The final chosen dielectric material was the TMM10 material from Rogers with a relative permittivity of 9.2 and a loss tangent of 0.0022. It was the best trade-off between the Q factor, efficiency and physical antenna size for the lowest frequency of around 800MHz.

The MIMO system has to be integrated on the rooftop of a vehicle within a limited space of 120mm×70mm×65mm corresponding to $\lambda_0/3 \times \lambda_0/5 \times \lambda_0/6$ at 800MHz. To integrate two antennas within the allocated space, each radiating element needs to be miniaturized. In this framework, we set the dimensions of one dielectric resonator (DR) at 22mm×13mm×50mm, vertically placed on a finite FR4 substrate.

We proposed a DRA which covers the LTE 800DD, LTE 1800+, LTE 2100 and LTE 2600 frequency bands. The antenna satisfies an impedance bandwidth ($|S_{11}| < -6\text{dB}$) for four distinct frequency bands. The antenna efficiency is 50% in LTE 800D band and 75% in higher frequency bands. It is miniaturized since its overall dimension is $\lambda_0/8 \times \lambda_0/17 \times \lambda_0/29$ at 790MHz. Higher resonances are due to resonant modes inside the dielectric resonator. Moreover, the proposed antenna has a simple rectangular shape with only one surface printed with copper and can be easily fabricated. With these features, this antenna is very suitable for automotive applications.

In Chapter Three, the phase shifter, which is another key part to control the beam direction in our system, was studied. For type and size of the phase shifter, the automotive environment must be considered. Using a mechanical switched phase shifter is bulky and needs high

voltage control. The electronically controlled phase shifter is very suitable and more convenient in this case.

We looked for existing “off-the-shelf” devices able to answer our problem. It was hard to find one that was compact, low profile, with low insertion loss and phase shifts of 0° , 90° , 180° and 270° . We decided to design our own device using some active components on a PCB with low voltage requirement, low power consumption and easily controlled electronically.

We made a prototype with few active components integrated and we partially met the expectations. However, the measured results for insertion loss and return loss were worse than the simulations. We investigated the reasons for these differences. We found that the SP4T switches are critical components. Most of the interference in $|S_{11}|$ and $|S_{21}|$ were coming from the SP4Ts. Although the phase tuning result does not appear bad, the losses are too significant when the frequency is higher than 1.7GHz.

To reduce the losses from the circuit, we removed the SP4Ts and used different length microstrip lines to obtain the wanted phase shifters. This way we obtained phase shifts of 0° , 86° , 164° and 271° at 800MHz using different paths. We can also achieve a 20° minor phase tuning range at 800MHz, 70° at 1.7GHz and 58° at 2.7GHz. The insertion loss was reduced to within 1dB for 800MHz and within 4dB for frequencies higher than 1.7GHz.

Therefore, we adopted a manual-switched phase shifter design in our global active steering system.

In Chapter Four, we successfully demonstrated a low profile active beam steering antenna with simple geometry, of compact dimension and easy to manufacture.

First, the beam steering device used the previously conceived DRA as an array element.

The beam steering system is based on a simple MIMO design. The MIMO system is composed of two DRAs placed within a small area. The relative antenna locations were investigated to reach the best radiation pattern. For the whole system, the most challenging target is the lowest working band of 800MHz. The MIMO system presented a low ECC (Envelope Correlation Coefficient) value under 0.25 with a total efficiency over 50%. The obtained results prove that the proposed MIMO system works well in such a limited space and the whole system can be implemented on the vehicle rooftop.

Next, the active beam steering global system combined the DRAs, phase shifter and 3dB power divider. The distance and orientation between the array antenna elements were studied and optimized. The complete set of simulated results was presented in order to have the radiation pattern reach the largest coverage angle for all the target frequency bands. With a manual-switch phase shifter, the prototype of the system demonstrated good agreement between simulation and experiment. The system presents steered radiation patterns in all the LTE frequency bands – LTE 800DD, LTE 1800+, LTE 2100 and LTE 2600.

This system showed good performances for the 3D gain not only in free space, but also on the automotive rooftop. Lastly we measured the global system using a SP4T switch in the real vehicle rooftop. Even in the worse environments such as on the dashboard or below the rooftop of the vehicle, the system still performed well with beamforming ability. It presented beam steering behaviors, clearly improving the composite efficiency.

Here are the prospects for the study:



- The conceived DRA worked for multi bands of current cellular frequencies. However, the proposed antenna has a quite narrow bandwidth at low frequencies. To increase the bandwidth, it is possible to investigate band switching techniques or impedance matching. One of the band switching methods uses a switch IC to switch different parasitic elements to shift the frequency of the monopole fed DRA. Also, we can implement the switch IC at the feeding matching circuit to switch different matching paths or using variable capacitance to alter the antenna bandwidth.
- In the beam steering system, we provided different phase signals to the main and MIMO antennas. The phase shifter performances were impacted after switched IC implementation. We could work out the development of proper solutions to minimize the oscillations between the traces. This can improve the phase shifter characteristics. The system could be used in the real vehicle antenna box and could become more efficient.
- There are several types of SP4T and variable capacitor with different design concepts. We must seek to improve the performance of the SP4T using other components or topologies. After that, we can demonstrate improved performance of the higher frequencies in our active steering system.
- Since the DRA thickness can affect the yield rate of the fabrication, the manufacture cost can be reduced by minimizing the thickness of dielectric resonator. An idea is to use a dielectric with a higher permittivity and so a thinner resonator.
- To realize a full auto electrically controlled system, the switches have to be integrated. Therefore, we can minimize the whole system and realize the commercial package of the system with MIMO and active beam steering functions.

Reference

- [1] R. J. Langley and J. C. Batchelor, "Hidden antennas for vehicles," *Electronics & Communication Engineering Journal*, Vol. 14, no. 6, 2002, pp. 235-262.
- [2] Vason P. Srin, "A vision for supporting autonomous navigation in urban environments," *IEEE Vehicular Technology Magazine*, vol. 11, no. 1, pp. 25-28, 96, Mar. 2016.
- [3] C. Lim, T. Yoo, B. Clerckx, B. Lee and B. Shim, "Recent trend of multiuser MIMO in LTE-advanced", *IEEE Communications Magazine*, Vol. 51, no. 3, March 2013, pp. 127-135.
- [4] "Product technical specification and customer design guidelines- AirPrime EM7355", Sierra Wireless.
- [5] X. Xie, B. Huang, S. Yang and T. Lv, "Adaptive Multi-channel MAC protocol for dense VANET with Directional Antennas," *Consumer Communications and Networking Conference, CNCC 6th*, Las Vegas, 10-13 Jan. 2009.
- [6] S. Gao and Q. Luo, "Low-cost smart antennas for advanced wireless systems," *Antenna Technology: "Small Antennas, Novel EM Structures and Materials, and Applications" (iWAT)*, 2014 International Workshop on, Sydney, 4-6 March 2014.
- [7] C. Shannon, "The lattice theory of information," *Transactions of the IRE Professional Group on Information Theory*, Vol. 1, no. 1, February 1953, pp.105-107.
- [8] E. M. Rogers "Claude Shannon's cryptography research during World War II and the mathematical theory of communication," 1994 *Proceedings of IEEE International Carnahan Conference on Security Technology*, Albuquerque, NM, 1994, pp. 1-5.
- [9] P.F. Driessen and G.J. Foschini, "On the capacity formula for multiple input-multiple output wireless channels: a geometric interpretation," *Communications*, 1999. ICC '99. 1999 *IEEE International Conference on*, Vancouver, 6-10 June 1999.
- [10] C.A. Balanis, "Antenna theory – analysis and design (3rd Edition)," ed: John Wiley & Sons.
- [11] A. Raaza, A. Mehta, D. Mirshekar-Syahkal and P. J. Massey, "A Novel 8 Feed Beam Switched Antenna", 2008 *IEEE Antennas and Propagation Society International Symposium*, Jul 5-11 2008.
- [12] S.C. Panagiotou, T.D. Dimousios, S.A. Mitilneos and C.N. Capsalis, "Broadband switched parasitic arrays for portable DVB-T receiver applications in the VHF/UHF Bands", *IEEE Antennas and Propagation Magazine*, Vol. 50, no. 5, October 2008, pp. 110-117.
- [13] H. Scott and V. F. Fusco, "360o electronically controlled beam scan array", *IEEE Transactions on Antennas and Propagation*, Vol. 52, no. 1, January 2004, pp. 333-335.
- [14] M.K.A. Nayan, M.F. Jarnlos, M. Jusoh, M.I. Jais and T. Sabapaty, "Adaptive zero-interference of compact reconfigurable antenna for GPS application", *Wireless Technology and Applications (ISWTA)*, 2013 *IEEE Symposium on*, Sep 22-25 2013.
- [15] S. Ha, C.W. Jung, "Single patch beam steering antenna with U-slot for wearable fabric applications", *Antennas and Propagation (APSURSI)*, 2011 *IEEE International Symposium on*, Jul 3-8 2011.

- [16] S. Zhang, G. H. Huff, J. Feng, and J. T. Bernhard, "A pattern reconfigurable microstrip parasitic array", *IEEE Transactions on Antennas and Propagation*, Vol. 52, no. 10, October 2004, pp. 2773-2776.
- [17] W.-D. Wirth, "Beamforming", *Radar Techniques Using Array Antennas*, chapter 5, May 2013.
- [18] W.-D. Wirth, "Array antennas", *Radar Techniques Using Array Antennas*, chapter 4, May 2013.
- [19] Y. Li, M. F. Iskander, Z. Zhang and Z. Feng, "New low cost leaky wave coplanar waveguide continuous transverse stub antenna array using metamaterial-based phase shifters for beam steering", *IEEE Transactions on Antennas and Propagation*, Vol. 61, no. 7, July 2013, pp. 3511-3518.
- [20] W.L. Stutzman, J.H. Reed, C.B. Dietrich, B.-K. Kim, D.G. Sweeney, "Recent results from smart antenna experiments --Base station and handheld terminals", *Radio and Wireless Conference, 2000. RAWCON 2000. 2000 IEEE*, September 13 2000
- [21] S.-S. Jeon, Y. Wang, Y. Qian, and T. Itoh, "A novel planar array smart antenna system with hybrid analog-digital beamforming", *Microwave Symposium Digest, 2001 IEEE MTT-S International*, May 20-24 2001
- [22] D. M. Pozar "Microwave engineering (3rd Edition)," ed: John Wiley & Sons.
- [23] K. Chang, I. Bahl and V. Nair, "RF and microwave circuit and component design for wireless systems," ed: John Wiley & Sons.
- [24] Z. Li, D. Rodrigo, L. Jofre and B. A. Cetiner, "A new class of antenna array with a reconfigurable element factor," *IEEE Transactions on Antennas and Propagation*, Vol. 61, no. 4, July 2013, pp. 1947-1955.
- [25] R.D. Richtmyer, "Dielectric resonators," *Journal of Applied Physics*, Vol. 10, pp. 391-398, 1939
- [26] S.A. Long, M.W. McAllister and L.C. Shen, "The resonant dielectric cavity antenna", *IEEE Transactions on Antennas and Propagation*, Vol. 31, no. 3, March 1983, pp. 406-412
- [27] W.W.G. Hui, J.M. Bell, M.F. Iskander and J.J. Lee, "Low-cost microstrip-line-based ferrite phase shifter design for phased array antenna applications," *IEEE Antennas and Wireless Propagation Letters*, Vol. 6, March 2007, pp. 86-89.
- [28] J. Lampen, S. Majumder, C. Ji and J. Maciel, "Low-loss, MEMS based, broadband phase shifters," *Phased Array Systems and Technology (ARRAY), 2010 IEEE International Symposium on*, 12-15 October 2010.
- [29] Soon-Young Eom, "Broadband 180° bit phase shifter using a $\lambda/2$ coupled line and parallel $\lambda/8$ stubs," *IEEE Microwave and Wireless Components Letters*, Vol. 14, no.50, May 2004, pp. 228-230.
- [30] Q. Liu, H. Liu and Y. Liu, "Compact ultra-wideband 90° phase shifter using short-circuited stub and weak coupled line," *Electronics Letters*, Vol. 50, no. 20, September 2014, pp. 1454-1456.
- [31] R.V. Garver, "Broadband diode phase shifters," *Microwave Symposium Digest, 1971 IEEE GMITT International*, 16-19 May 1971.

- [32] A.M. Abbosh, "Compact tunable reflection phase shifters using short section of coupled lines," *IEEE Transactions on Microwave Theory and Techniques*, Vol. 60, no, 8, August 2012, pp. 2465-2472.
- [33] C. Ding, Y.J. Guo, P.-Y. Qin and Y. Yang, "A reconfigurable defected microstrip structure for applications in phase shifter," *Antennas and Propagation (EuCAP)*, 2014 8th European Conference on, 6-11 April 2014.
- [34] K.K. Tokgöz, Ç. Çetintepe and Ş. Demir, "1–6 GHz UWB phase shifter design and implementation with surface micromachining," *Antennas and Propagation (EUCAP)*, 2012 6th European Conference on, 26-30 March 2012.
- [35] X. Tang and K. Mouthaan, "Design considerations for octave-band phase shifters using discrete components," *IEEE Transactions on Microwave Theory and Techniques*, Vol. 58, no, 12, December 2010, pp. 3459-3466.
- [36] E. Ohlmer, G. Fettweis and D. Plettemeier, "MIMO system design and field tests for terminals with confined space - Impact on automotive communication," *Antennas and Propagation (EUCAP)*, Proceedings of the 5th European Conference on, 11-15 April 2011.
- [37] T. Lankes, P. Turban and F. Mierke, "Evaluation and optimization of LTE MIMO antenna configurations in automotive environment," *Antennas and Propagation (EuCAP)*, 2014 8th European Conference on, 6-11 April 2014.
- [38] L. Huitema and T. Monediere, "Dielectric materials for compact dielectric resonator antenna applications," *Dielectric Material, InTech*, chapter 2, pp. 27-56, October 2012
- [39] R.K. Mongia, A. Ittipiboon, "Theoretical and experimental investigations on rectangular dielectric resonator antennas," *IEEE Transactions on Antennas and Propagation*, Vol. 45, Iss. 9, Sep 1997, pp. 1348-1356
- [40] M.W. Mcallister, S.A. Long and G.L. Conway, "Rectangular dielectric resonator antenna," *Electronics Letters*, Vol. 19, no. 6, March 1983, pp. 218-219
- [41] Y.C. Chen, S.L. Yao, K.C. Chen, "Dual band hybrid CPW fed planar monopole/dielectric resonator antenna," *Communications (MICC)*, 2009 IEEE 9th Malaysia International Conference on, 15-17 Dec. 2009
- [42] A.S. Al-Zoubi, A.A. Kishk and A.W. Glisson, "Linear rectangular dielectric resonator antenna array fed by dielectric image guide with low cross polarization," *IEEE Transactions on Antennas and Propagation*, Vol. 58, no. 3, March 2010, pp. 697-705
- [43] M.T. K. TAM and R. D. MURCH, "Compact Circular Sector and Annular Sector Dielectric Resonator Antennas", *IEEE Transactions on Antennas and Propagation*, Vol. 47, no. 5, pp. 837-842, May 1999.
- [44] R.K. Mongia, A. Ittipiboon, M. Cuhaci and D. Roscoe, "Radiation Q-factor of rectangular dielectric resonator antenna: theory and experiment," *Antennas and Propagation Society International Symposium*, 1994. AP-S. Digest, 20-24 June 1994
- [45] L. Huitema, M. Koubeissi, M. Mouhamadou, E. Arnaud, C. Decroze, and T. Monediere, "Compact and multiband dielectric resonator antenna with pattern diversity for multistandard mobile handheld devices," *IEEE Transactions on Antennas and Propagation*, Vol. 59, Iss. 11, Nov 2011, pp. 4201-4208

- [46] M. Rotaru J.K. Sykulski, "Numerical investigation on compact multimode dielectric resonator antennas of very high permittivity," IET Science, Measurement and Technology, Vol. 3, no. 3, January 2009, pp. 217-22
- [47] NEDI technology Co., Ltd, MMIC GaAs Digital Phase Shifter, NDAC030 series, DC-4GHz
- [48] Analog Device, GaAs MMIC 6 bit digital phase shifters, HMC936ALP6E, 1.2 - 1.4 GHz
- [49] Mini-Circuits, surface mount phase shifters, SPHSA-152+, 800MHz- 1.5 GHz
- [50] Sigatek Microwave LLC, analog phase shifters, 360°, A7 series, 1MHz- 3.2 GHz
- [51] Fairview Microwave Inc., SMA Variable Phase Shifter, SMP1801, DC to 18 GHz
- [52] L3 Narda-ATM, motor driven phase shifters, P11XX-28, 360°/GHz
- [53] B. M. SCHIFFMAN, "A New Class of Broad-Band Microwave 90-Degree Phase Shifters," IRE Transactions on Microwave Theory and Techniques, Vol. 6, no. 2, April 1958, pp. 232-237
- [54] R.V. Garver, "Broadband diode phase shifters," Microwave Symposium Digest, 1971 IEEE GMTT International, 16-19 May 1971.
- [55] K.K. Tokgöz, Ç. Çetintepe and Ş. Demir, "1–6 GHz UWB phase shifter design and implementation with surface micromachining," Antennas and Propagation (EUCAP), 2012 6th European Conference on, 26-30 March 2012
- [56] P.S. Huang and H.C. Lu, "Broadband differential phase-shifter design using bridged T-type bandpass network," IEEE Transactions on Microwave Theory and Techniques, Vol. 62, no. 7, July 2014, pp. 1470-1479
- [57] X. Tang and K. Mouthaan, "Design considerations for octave-band phase shifters using discrete components," IEEE Transactions on Microwave Theory and Techniques, Vol. 58 no. 12, December 2010, pp. 3459-3466
- [58] Peregrine DTC, PE64904, 100 MHz to 3000 MHz.
- [59] RFMD, RFAC3612, 100 MHz to 3000 MHz.
- [60] Ethertronics AIRFDC™ and EtherChip™, 100 MHz to 3000 MHz.
- [61] Ethertronics Ether Switch&Tune™ and EC686, 100 MHz to 3000 MHz.
- [62] S.L. Preston, D.V. Thiel, J.W. Lu, S.G. O'Keefe and T.S. Bird, "Electronic beam steering using switched parasitic patch elements," Electronics Letters, Vol. 33, no. 1, January 1997, pp. 7-8.
- [63] M.K. Saleem, M. A. S. Alkanhal, A. F. Sheta, "Wide band hybrid dielectric resonator antenna with beam steering capability", Antenna Technology and Applied Electromagnetics (ANTEM), 2012 15th International Symposium on, 25-28 June 2012
- [64] M.R. Nikkhah, J. Rashed-Mohassel, A. A. Kishk, "Compact low-cost phased array of dielectric resonator antenna using parasitic elements and capacitor loading," IEEE Transactions on Antennas and Propagation, Vol. 61, no. 4, April 2013, pp. 2318-2321
- [65] J. Sun, W. Jiang and Z. Feng, "Design and investigation of a novel beam-steering cylindrical dielectric resonator antenna," Microwave, Antenna, Propagation and EMC

Technologies for Wireless Communications (MAPE), 2013 IEEE 5th International Symposium on, 29-31 October 2013

[66] N.R. Labadie, S.K. Sharma and G. Rebeiz, "Multimode antenna element with hemispherical beam peak and null steering," Antennas and Propagation Society International Symposium (APSURSI), 2012 IEEE, 8-14 July 2012

[67] A. Narbudowicz, M.J. Ammann and D. Heberling, "Switchless reconfigurable antenna with 360° steering," IEEE Antennas and Wireless Propagation Letters, Vol. 15, February 2016, pp.1689-1692

[68] S. Blanch, J. Romeu and I. Corbella, "Exact representation of antenna system diversity performance from input parameter description," Electronics Letters, Vol. 39, no. 9, pp.705-707, May. 2003

[69] R. G. Vaughan and J. B. Andersen, "Antenna diversity in mobile communications," in IEEE Transactions on Vehicular Technology, vol. 36, no. 4, pp. 149-172, Nov. 1987.

[70] M. S. Sharawi, "Current misuses and future prospects for printed multiple-input, multiple-output antenna systems," IEEE Antennas Propag. Mag., vol. 59, no. 2, pp. 162–170, Apr. 2017.

[71] D. M. Pozar "Microwave engineering (3rd Edition)," ed: John Wiley & Sons, Chapter 13.

[72] CTIA Certification Program, "CTIA test plan for wireless device over the air performance, Version. 3.6.2" CTIA – The Wireless Association, Appendix E.2, May. 2017

Annexes

Annex 1. Active steering result of SP4T-switched global system

Figure 171 demonstrates the beam steering results of the SP4T-switched global system.

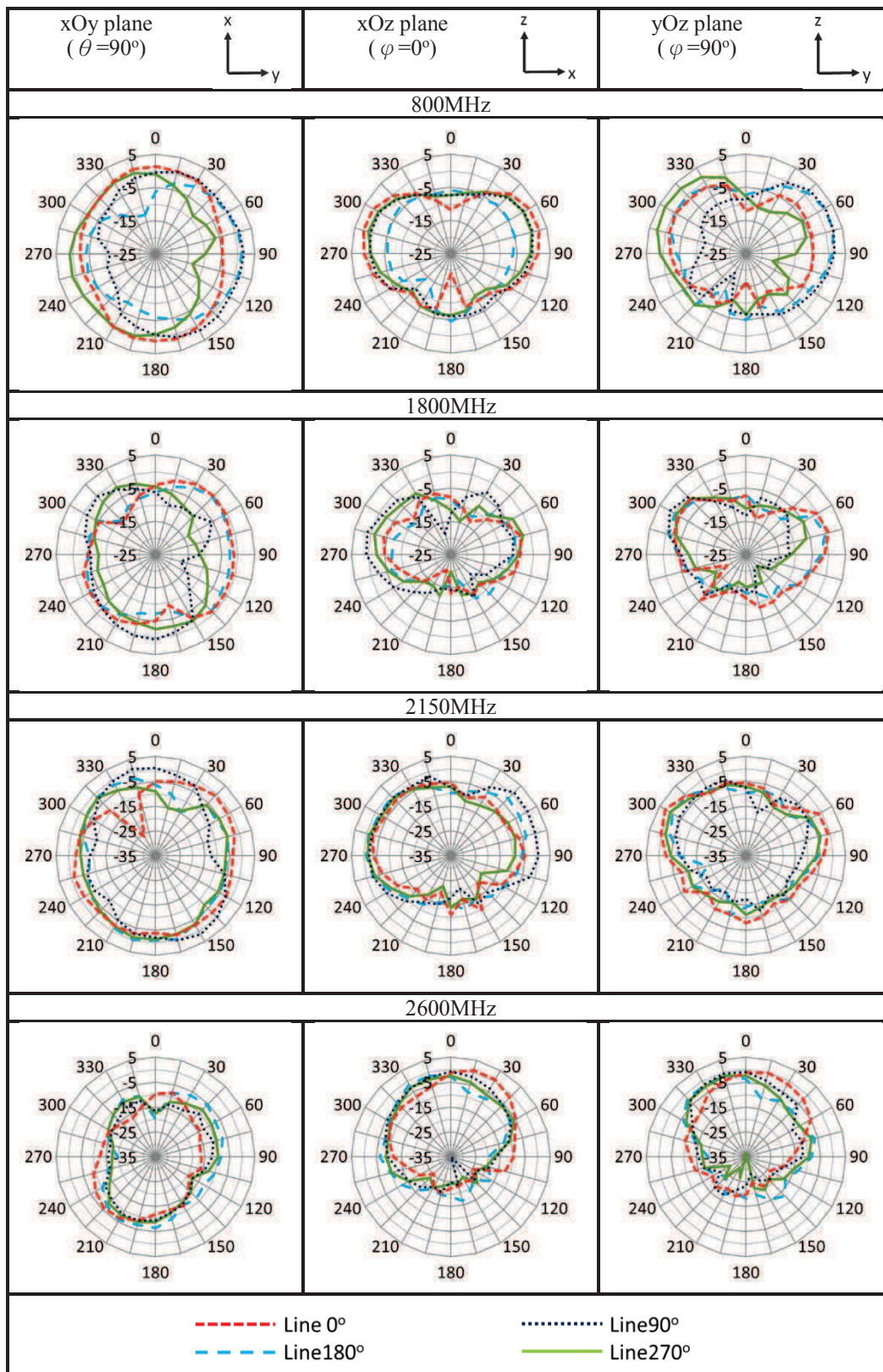


Figure 171: Performance of global system with SP4T-switched lines

For the beam steering result, the SP4T-switched global system can have a result similar to the manual-switched global system (Figure 172).

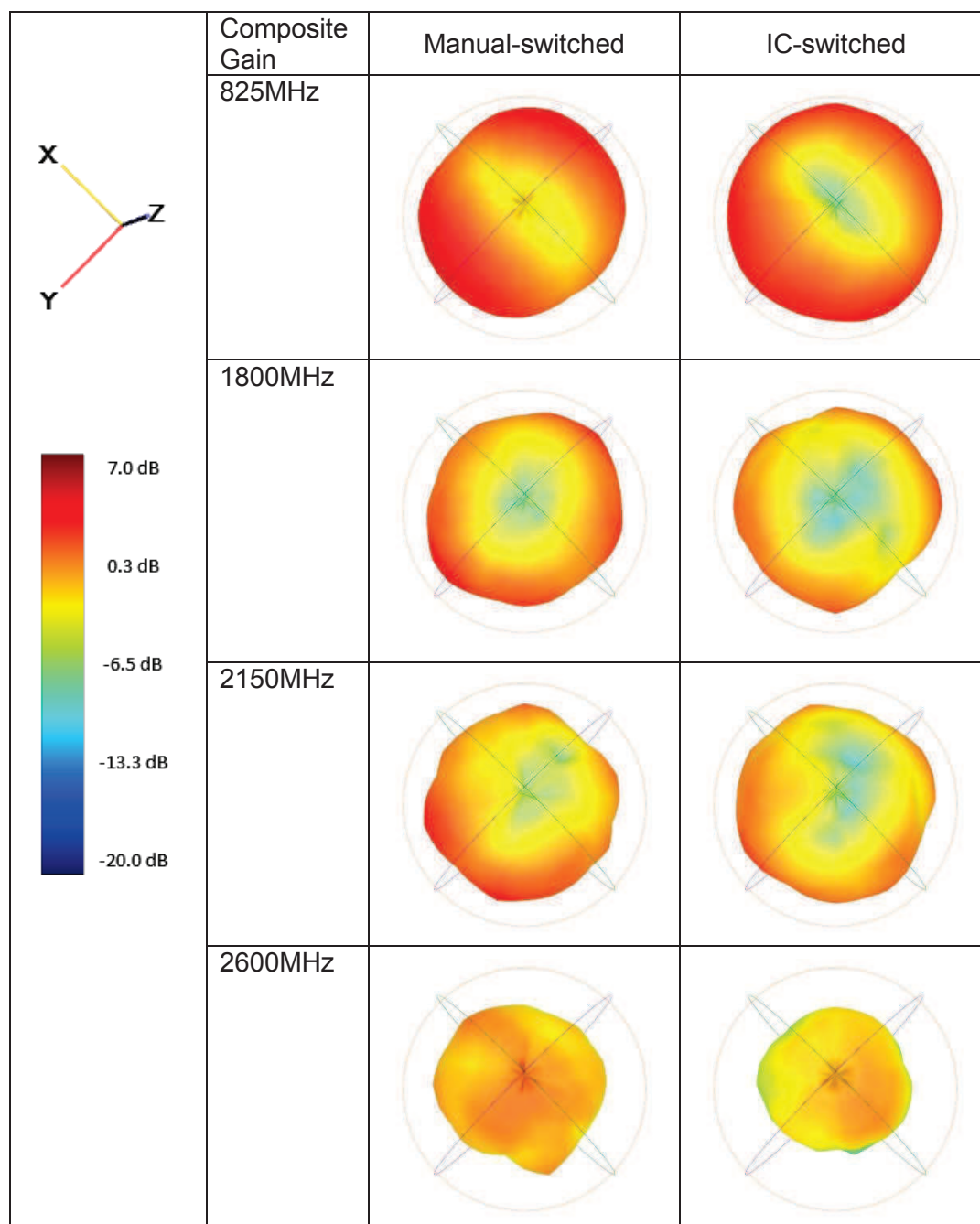


Figure 172: Manual-switched and SP4T-switched global system 3D composite radiation pattern comparison

In Figure 171, the radiation pattern at 800MHz is obviously steered by switching the lines of the phase shifter. Also, both manual-switched and SP4T-switched global systems have similar reconfigurable patterns at 800MHz. For higher frequency bands, the beam direction is not along the axis, changing 2D cut by different angles can achieve a better beam steering result as shown in Figure 173.

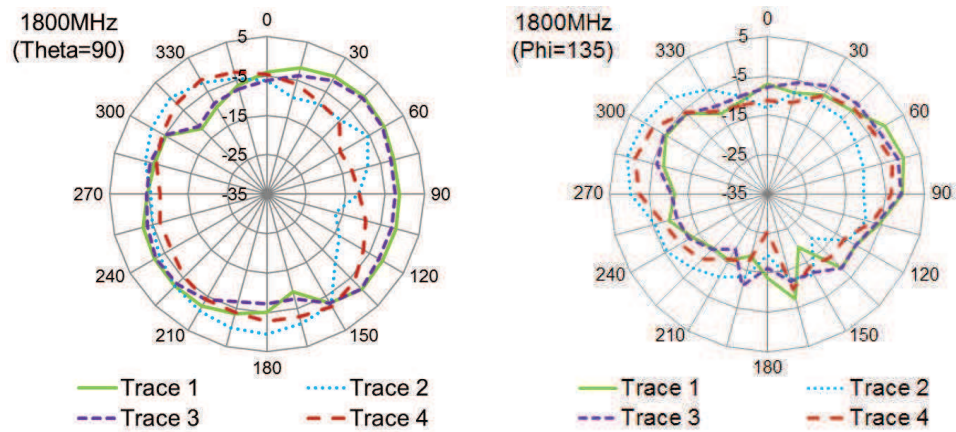


Figure 173: Beam steering pattern by line index for 1800MHz.

However, when the frequency is higher, the insertion loss becomes huge. The tunable phase shifter still has the ability for fine phase tuning. This is the advantage of using the SP4T-switched design.

Table of illustrations

Figure 1: General schematic of a MIMO system and modified concept for a beam steering system.....	10
Figure 2: LTE module connectors.....	11
Figure 3: Basic antenna structure for fitting LTE commercial module.	11
Figure 4: Architecture of the proposed antenna system.....	11
Figure 5: MIMO antenna system concept for LTE.....	12
Figure 6: Beamforming antenna system concept.....	13
Figure 7: Switch beam system.....	14
Figure 8: Switch feeding antenna system and 3dB radiation cone.....	14
Figure 9: switched parasitic elements in DVT-T antenna system.....	15
Figure 10: Switch loading elements antenna system and beam steer pattern.....	16
Figure 11: Geometry and radiation pattern of a reconfigurable GPS antenna.....	17
Figure 12: Geometry and radiation pattern of a reconfigurable patch antenna.....	17
Figure 13: Geometry and radiation pattern of a reconfigurable microstrip parasitic array.....	18
Figure 14: Comparison of radiation pattern: (a) switched beam scheme; (b) adaptive array scheme.....	18
Figure 15: Basic beamforming principle: phase alignment, amplitude weighting and summing.....	19
Figure 16: Central feed array.....	20
Figure 17: Beam steering by phase shifter element.....	20
Figure 18: Concept of digital-analog hybrid beamforming.....	21
Figure 19: Various antennas.....	22
Figure 20: (a) Wire dipole and monopole antenna, (b) E-and H-plane radiation patterns (c) 3D diagram of the radiation pattern	22
Figure 21: Configuration of full loop antenna and its equivalent magnetic dipole at the centre	23
Figure 22: Configuration of rectangular horn and 3D radiation pattern.....	23
Figure 23: Rectangular patch antenna and radiation pattern.	24
Figure 24: Geometry of dielectric resonator antenna.	24
Figure 25: Ferrite phase shifter. (a) Fabricated microstrip-line-based ferrite phase shifter prototype with a bias coil; (b) Feed network; (c) Bias vs. phase shift result.....	26
Figure 26: Example for switched line and phase shift result	26
Figure 27: Switched line phase shifter for 180°.....	26
Figure 28: Switched line phase shifter for 90°.....	27

Figure 29: Reflection type phase shifter for 270°	27
Figure 30: Reflection type phase shifter for 90°	27
Figure 31: Photo of loaded line phase shifter and phase shifter result.	28
Figure 32: Filter phase shifter with series-C filter configuration and three-stage all-pass filter configuration with phase shift result.	28
Figure 33: High-pass and low-pass hybrid phase shifter and phase shift result.	29
Figure 34: Adopted phase shifter structure.	29
Figure 35: Concept of MIMO system (a), transfer to beam steering antenna system (b).....	30
Figure 36: MIMO antenna system model in the thesis	31
Figure 37: Active steering antenna system model in the thesis.....	31
Figure 38: Dedicated space of the automotive antenna	33
Figure 39: Internal coaxial probe feed	35
Figure 40: External coaxial probe feed	35
Figure 41: Microstrip feeding and coplanar waveguide feeding	35
Figure 42: Aperture coupled feed	36
Figure 43: Dielectric image guide feed	36
Figure 44: Isolated rectangular dielectric resonator antenna.....	37
Figure 45: Rectangular DRA placed on a ground plane excited by a strip probe.	38
Figure 46: Adding extra metallic plate for hybrid mode [43].	38
Figure 47: Maximum dimensions of the antenna to be integrated within the dedicated space presented in Figure 38.....	40
Figure 48: E-field on the $y=11$ mm plane of an isolated DRA placed on FR4 copper coated substrate.	40
Figure 49: E-fields on the $y=11$ mm plane of a DRA placed on an FR4 copper coated substrate, with a metallic plate at $x=13$ mm (a) and with a partial metallic plate at $x=13$ mm ..	41
Figure 50: Input impedances with the modal analyses for three different cases.....	42
Figure 51: Final DRA cell dimensions.....	43
Figure 52: Input impedance variation of the final DRA alone and integrated on a $200 \times 200 \text{ mm}^2$ ground plane.	44
Figure 53: Input impedance with the modal analyses for the final design on $200 \times 200 \text{ mm}^2$ ground plane.	44
Figure 54: $ S_{11} $ parameters for the four studied cases.....	45
Figure 55: Final DRA matching circuitry.....	46
Figure 56: Photography for DRA cell.	47
Figure 57: Input impedance variation of DRA with matching circuitry.....	47
Figure 58: Measured and simulated $ S_{11} $ parameters of the DRA.....	48

Figure 59: 2D radiation pattern for the DRA.....	49
Figure 60: 3D radiation pattern for the DRA.....	50
Figure 61: Measured and simulated efficiency and maximum realized gain of the DRA	51
Figure 62: 3D anechoic chamber for the automobile.....	51
Figure 63: Top view of the antenna located on the rooftop	52
Figure 64: Photo of rooftop located DRA.	52
Figure 65: Measured 3D radiation patterns at different frequencies on vehicle rooftop.	53
Figure 66: 2D radiation patterns measured on vehicle rooftop compared with 200mm×200mm ground plane in free space.....	54
Figure 67: Comparison of measured maximum realized gain for the DRA.....	55
Figure 68: simulated $ S_{11} $ parameters of different ground plane size.	55
Figure 69: Photo of dashboard located DRA.	55
Figure 70: Photo of DRA located below the vehicle rooftop.	56
Figure 71: Measured 3D radiation patterns at different frequencies on the dashboard	57
Figure 72: Photo of the related DRA location below the vehicle rooftop.....	58
Figure 73: Measured 3D radiation patterns at different frequencies for the DRA under the vehicle rooftop.	59
Figure 74: Maximum realized gain comparing different locations.....	60
Figure 75: MMIC phase shifter: Insertion loss.....	62
Figure 76: Phase shifter pin definition for QFN package and MMIC die	62
Figure 77: Photo of surface mount phase shifter and its RF characteristics	62
Figure 78: Photo of surface mount phase shifter and its RF characteristics.....	63
Figure 79: (a) Beam steering architecture; Radiation pattern in different phases (b) 800MHz and (c) 1800MHz.....	64
Figure 80: Topology of differential phase shifter	64
Figure 81: The phase response for an example of a Schiffman phase shifter and differential phase response curve	65
Figure 82: Bridge T-type bandpass network and its magnitude response [56].	66
Figure 83: The plot for different return losses to the phase shifter bandwidth [56]	67
Figure 84: $ S_{11} $, $ S_{21} $ and phase shift of bridge T-type bandpass network for different k [56]	67
Figure 85: Initial simulation model for 90° phase shifter	68
Figure 86: Design characteristic of 90° phase shifter for 90° with phase error 10°.....	68
Figure 87: Initial model of the tunable 90° phase shifter	69
Figure 88: Characteristics of the initial tunable 90° phase shifter	70
Figure 89: Two stage and three stage tunable phase shifters.....	71

Figure 90: Characteristics of the two stage 180° tunable phase shifter	71
Figure 91: Characteristics of three stage 270° tunable phase shifter	71
Figure 92: Comparison of the different capacitor models in simulation	72
Figure 93: The resistor effect on $ S_{11} $ and $ S_{21} $ for 90° phase shifter	72
Figure 94: The resistor effect on $ S_{11} $ and $ S_{21} $ for 180° phase shifter	73
Figure 95: Initial diagram for the phase shifter	73
Figure 96: Characteristic of the initial tunable phase shifter for the antenna system	74
Figure 97: The topology of the 1 st prototype phase shifter.	74
Figure 98: The layout of the 1 st prototype phase shifter.	75
Figure 99: Measured results of the phase adjusting lines of the 1 st phase shifter design	75
Figure 100: Measured and simulated results for the paths between SP4T switches of 1 st design phase adjusting lines.....	76
Figure 101: Measured result to compare the $ S_{21} $ when two of the paths between SP4T and tunable phase shifter are removed	77
Figure 102: The difference between the initial and final phase shifter structure	78
Figure 103: Topology of final differential phase shifter for the thesis.....	78
Figure 104: Photograph of the final phase shifter and its reference line.....	78
Figure 105: Final circuitry for the tunable phase shifter.....	79
Figure 106: Simulated and measured result of reference line for SP4T-switched phase shifter	79
Figure 107: Phase shift result of SP4T-switched phase shifter with tunable phase shifter fixed at 90°.....	80
Figure 108: Simulated and measured results of SP4T-switched phase shifter in different paths	81
Figure 109: Schematic of the final SP4T-switched phase shifter	81
Figure 110: Performance of the SP4T-switched phase shifter at system target band	82
Figure 111: Measured port for the SP4T switch.....	82
Figure 112: Measured result for a single SP4T	83
Figure 113: The connection for switches and the paths	83
Figure 114: Topology of the four traces line only measurement.....	84
Figure 115: Simulated and measured result for delay lines only	84
Figure 116: Topology of the switched-line measurement.....	85
Figure 117: $ S_{11} $ and $ S_{21} $ Simulated and measured result for switches with lines	86
Figure 118: Measurement and simulation condition for tunable phase shifter only	86
Figure 119: Simulated and measured result of EC capacitance= 1.73pF @900MHz for tunable 90° phase shifter	87

Figure 120: All SMD phase shifter result from [56].....	87
Figure 121: variable capacitance chart and table for the SPI controlled by Hexadecimal code for EC1.0	87
Figure 122: $ S_{21} $ and phase measurement of the tunable 90° phase shifter with different values of the capacity	88
Figure 123: Topology of manual-switched phase shifter	89
Figure 124: Diagram of metal strip line connection at manual-switched phase shifter	89
Figure 125: Simulated and measured result of the reference line for manual-switched phase shifter	90
Figure 126: Simulated and measured results of the adjust line for manual-switched phase shifter	91
Figure 127: Simulated and measured result for the manual-switched phase shifter.....	91
Figure 128: Measured result of the manual-switched phase shifter by changing capacitance in tunable phase shifter part	92
Figure 129: Beam steering by switching parasitic patch elements	95
Figure 130: Beam steering by switched parasitic elements	96
Figure 131: Beam steering by switched capacitor loading	96
Figure 132: A single port of a cylindrical DRA and its radiation pattern.....	97
Figure 133: Dual ports of a cylindrical DRA and its radiation pattern with different phase differences.....	97
Figure 134: A three fed-in ports antenna system and its radiation pattern	98
Figure 135: A dual port with orthogonal excited fed-in system and its radiation pattern	98
Figure 136: The miniature antenna array for: (a) MIMO system working diagram; (b) beam steering working diagram	99
Figure 137: Relative distance of the antenna array elements in the system.....	99
Figure 138: MIMO antenna system in CST and prototype	100
Figure 139: (a) Measured and simulated $ S_{11} $ parameter. (b) Measured and simulated $ S_{22} $ parameter. (c) Measured and simulated $ S_{21} $ parameter.	101
Figure 140: Measured and simulated maximum realized gain and total efficiency for the proposed DRA in the MIMO system	101
Figure 141: Measured 3D radiation pattern at different frequencies for the MIMO system ..	102
Figure 142: ECC value of the MIMO system.....	103
Figure 143: Ideal radiation pattern of proposed global system.....	103
Figure 144: Setup for measuring different paths in the manual-switched global system	104
Figure 145: Performance of DRA with manual-switched lines.....	105
Figure 146: Geometry of the global system and its 3dB power divider.....	105

Figure 147: Measurement setup for manual-switched global system with fixed variant capacitance	106
Figure 148: Performance of global system with manual-switched lines	107
Figure 149: 3D radiation pattern and composite radiation pattern for manual-switched lines - 825MHz and 1800MHz	110
Figure 150: 3D radiation pattern and composite radiation pattern for manual-switched lines - 2150MHz and 2600Hz	111
Figure 151: Composite gain for manual-switched global system at 800MHz	112
Figure 152: Measurement setup for global system while varying the capacitance	112
Figure 153: Variable capacitance impact on 2D radiation	113
Figure 154: Setup for IC-switched global system	114
Figure 155: Photo of 3D chamber for measuring the global system	115
Figure 156: Photo of global system located on the rooftop	115
Figure 157: Gain improvement for global system located on the vehicle rooftop at 800MHz: (1) single antenna (2) beam steering system	116
Figure 158: Gain improvement for global system located on the vehicle rooftop at 1800MHz: (1) single antenna (2) beam steering system	116
Figure 159: Compared composite efficiency in free space and on vehicle rooftop	117
Figure 160: 3D radiation pattern and composite radiation pattern for global system on vehicle rooftop- 800MHz and 1600MHz	118
Figure 161: 3D radiation pattern and composite radiation pattern for global system on vehicle rooftop- 1800MHz and 1900MHz	119
Figure 162: 3D radiation pattern and composite radiation pattern for global system on vehicle rooftop- 2150MHz and 2600MHz	120
Figure 163: Composite maximum gain by trace index for global system on vehicle rooftop.	121
Figure 164: Photo of the global system located on the dashboard	121
Figure 165: 3D radiation pattern and composite radiation pattern for the global system on the dashboard- 800MHz and 1800MHz	122
Figure 166: Gain improvement for the global system located on the dashboard at (1) single antenna 800MHz; (2) beam steering system 800MHz; (3) single antenna 1800MHz; (4) beam steering system 1800MHz; (5) single antenna 2600MHz; (6) beam steering system 2600MHz.	123
Figure 167: Photo of global system located under the vehicle rooftop	124
Figure 168: 3D radiation pattern and composite radiation pattern for the global system under the vehicle rooftop- 800MHz and 1800MHz	125
Figure 169: 3D composite gain for global system in automotive environment	126
Figure 170: Efficiency of the global system location for all conditions (upper hemisphere). 127	

Figure 171: Performance of global system with SP4T-switched lines	139
Figure 172: Manual-switched and SP4T-switched global system 3D composite radiation pattern comparison.....	139
Figure 173: Beam steering pattern by line index for 1800MHz.....	140

Tables

Table 1: [Comparison between different electronic phase shifting technologies].....	29
Table 2: [Detailed dimensions of the DRA metal part (unit: mm)].....	43
Table 3: [Initial optimized values for bridged T-type bandpass filter 90° phase shifter].....	68
Table 4: [Final optimized values for the 90° tunable phase shifter]	79
Table 5: [Performance comparison of market available 360° phase shifter]	93
Table 6: [Beam steering range in different planes].....	106

Antenne multi-bandes à résonateur diélectrique et dépointage de faisceau pour applications automobiles

Les antennes à pointage électronique présentent des avantages significatifs dans les systèmes de communication sans fil. Malgré cela elles ne sont toujours pas implantées dans l'industrie automobile. En effet, l'espace limité et le toit en grande partie métallique freinent l'utilisation de ces aériens dans ce contexte contraint. De nombreux défis restent à relever pour concevoir un système efficace, peu encombrant, faible coût et permettant de rayonner sur 360°. L'objectif de cette thèse est donc la mise au point d'une antenne à balayage électronique pour application automobile fonctionnant dans la bande LTE. Un système de « type MIMO » est proposé. Une antenne à résonateur diélectrique efficace, multi-bandes et efficace est conçue selon une procédure de développement spécifique. Un déphaseur accordable est également mis au point et réalisé. Il utilise des commutateurs et un condensateur variable. Un déphasage de 360 degrés est obtenu, le dispositif est commandé électriquement. L'antenne et le déphaseur sont ensuite associés dans un système complet fonctionnant dans la bande LTE. Celui-ci utilise deux antennes identiques, une seule étant alimentée. Ce système complet est mesuré seul et sur le véhicule. Les résultats obtenus sont prometteurs et permettent d'envisager, moyennant quelques améliorations, une exploitation industrielle.

Les études menées pour aboutir à ce dispositif sont détaillées dans le manuscrit.

Mots-clés: antenne agile, dépointage de faisceau, applications automobiles, antenne à résonateur diélectrique, déphaseur, MIMO, antenne pour LTE.

Multiband DRA for automotive applications with beam steering

Even though beam steering technology has significant advantages in wireless communication systems, it is still not implemented in the automotive industry. Indeed, the limited space and the large metal sheet on the rooftop are the challenges for such system. This thesis is focused on the design of the LTE beam steering antenna based on a MIMO system for an automotive environment. An appropriate multiband, efficient and compact Dielectric Resonator Antenna is conceived using a specific development procedure. Also, a tunable phase shifter is designed and realized with switches and a variable capacitor. It has 360 degrees phase shift and can be electrically controlled. The proposed DRA and phase shifter are integrated in a global antenna system for automotive application in the LTE band. We finally propose a MIMO system with an active beam steering radiation pattern. It is very compact and can be implemented on the vehicle rooftop. Using the proposed phase shifter, a beam steering antenna is obtained with a global coverage close to 360° for the antenna alone or on the vehicle. Measurements are made in the using context of the antenna. Finally, the developed system is, with some improvement, powerful enough for "commercial" automotive applications. The studies carried out to develop this antenna are detailed in this manuscript.

Keywords: active steering, beamforming, automotive applications, dielectric resonator antennas (DRAs), phase shifter, MIMO, LTE antenna

